

# Balance of forces and torques in the mitotic spindle

---

Ivec, Arian

Doctoral thesis / Disertacija

2022

Degree Grantor / Ustanova koja je dodijelila akademski / stručni stupanj: **University of Zagreb, Faculty of Science / Sveučilište u Zagrebu, Prirodoslovno-matematički fakultet**

Permanent link / Trajna poveznica: <https://um.nsk.hr/um:nbn:hr:217:193843>

Rights / Prava: [In copyright](#)/[Zaštićeno autorskim pravom.](#)

Download date / Datum preuzimanja: **2024-12-22**



Repository / Repozitorij:

[Repository of the Faculty of Science - University of Zagreb](#)





University of Zagreb  
Faculty of Science  
Department of Physics

Arian Ivec

# **Balance of forces and torques in the mitotic spindle**

DOCTORAL THESIS

Supervisor:  
Professor Nenad Pavin, PHD

Zagreb, 2022



Sveučilište u Zagrebu  
Prirodoslovno-matematički fakultet  
Fizički odsjek

Arian Ivec

# **Ravnoteža sila i momenata sila u diobenom vretenu**

DOKTORSKI RAD

Mentor:  
prof. dr. sc. Nenad Pavin

Zagreb, 2022.

## Supervisor information

Nenad Pavin was born on the 5th of May in 1967 in Rijeka, Croatia. His elementary education begins in 1974 in Rijeka, and ends in 1982 in Zadar, where he also finishes high school in 1986. He enrolled in the Graduate Physics program at the University of Zagreb, where he first obtained his dipl. Ing. Phys. title in 1993., and afterwards becomes a mag. phys. in 1998. Afterwards, he defended his doctoral thesis named “Chaotic transients in a new population equation and their effect on the fractal structure of Arnold Tongues”, under the mentorship of professor Vladimir Paar in 1999. He continued his scientific career at the Faculty of Science of the University of Zagreb, where he became a docent in 2001. He worked as a guest scientist at the Max Planck Institute for the Physics of Complex Systems from 2007 to 2011, under the guidance of professor Frank Jülicher, where he broadened his scientific interests to include biophysics. He has since formed and led Pavin group, a research group for theoretical biophysics, based out of the Faculty of Science, University of Zagreb. He has published 54 papers in total, out of which 49 are represented in Current contents (CC), with some distinguish being: Cell – 2 papers (IF 33.116), Nature Cell Biology (IF 20.058) – 1 paper, Nature Communications – 2 papers (IF 12.124), Annual Review of Biophysics – 1 paper (IF 10.676), Developmental Cell – 2 papers (IF 9.174), Current Biology – 1 paper (IF 10.834), Cell Reports – 1 paper (IF 9.995), Physical Review Letters – 2 papers (IF 7.645). Nenad Pavin has mentored 5 doctoral students and 10 master students. He has presented at more than 25 conferences as an invited speaker. He has either led or worked as an associate on the following projects: ERC Synergy „Molecular origins of aneuploidies in healthy and diseased human tissues (ANEUPLOIDY)“ (10,000,000 EUR), numerous projects of the Croatian Science foundation (1,000,000 HRK), and the Scientific Center of Excellence for Quantum and Complex Systems, and Representations of Lie Algebras — QuantiXLie (36.956.624,09 HRK). He has received the following awards: (1) State Science award in 2015 (2)Yearly award for distinguished scientific accomplishments of the Faculty of Science,

University of Zagreb (2022) , (3) Award of the European society for microscopy in the category of life sciences for the article: “The mitotic spindle is chiral due to torques within microtubule bundles”, M. Novak, B. Polak, J. 78 Simunić, Z. Boban, B. Kuzmić, A. Thomae, I.M. Tolić, N. Pavin, Nat Commun 2018, where he was the senior PI. He taught 7 subjects on the undergraduate study program and 2 subjects on the graduate study program of the Department of Physics. He was the chair of the Doctoral Program, field Biophysics, and was chiefly responsible for developing and putting into operation a new study program “Professors of physics and computer science (in 2000)”, whose chair he was until 2005.

## Acknowledgements

I would like to express my gratitude to my supervisor Nenad Pavin for the opportunity to work on these exciting projects, for the knowledge I gained during these years and for the experience I gathered that will help me in my future challenges.

I thank all present and past members of Pavin and Tolić groups, particularly Monika Trupinić, Ivana Ponjavić, Marko Šprem, Lucija Kardaš, Maja Novak, Lucija Tomašić, Marcel Prelogović, Barbara Kuzmić, Ivana Šarić and Iva Tolić for making this work possible, as well as Matko Glunčić and Josip Tambača for providing me with key scientific insights.

I thank my family and friends, especially Tea Tipurić and Filip Kozlina, for enduring the long hours and erratic schedule that come with scientific work.

I acknowledge funding from the Croatian Science Foundation (HRZZ, projects IP-2019-04-5967 granted to N.P.), the QuantiXLie Scientific Center of Excellence, a project co-financed by the Croatian Government and European Union through the European Regional Development Fund — the Competitiveness and Cohesion Operational Programme (Grant KK.01.1.1.01.0004) and the "Young researchers' career development project – training of doctoral students" of the Croatian Science foundation.

# Abstract

In this thesis, I present results of my work over the last three years, carried out as a member of Pavin Group at the Faculty of Science, University of Zagreb. The mitotic spindle is a complex micro-machine composed of microtubules and associated proteins that must be highly ordered in space and time to function properly. A functional spindle has a distinct shape composed of curved bundles of microtubules twisted around the pole-to-pole axis. There is still a lack of understanding of how linear and rotational forces define the overall shape of the mitotic spindle, as well as how twisted shapes emerge as a result of interactions between microtubules and motor proteins. To answer this, we use a mean-field approach to model the entire spindle, describing the forces and torques along microtubule bundles throughout the spindle. We compare our theoretical modelling to experimentally observed bundle shapes in the mitotic spindle, including both unperturbed and compressed spindles. We conclude that rotational forces are primarily responsible for the observed spindle shape. Furthermore, we discover that the difference in bending forces explains the difference in the shapes of the inner and outer bundles, that the chirality of the spindle is caused by a constant twisting moment and that there exists a preferred direction from microtubules arising out of the centrosome.

Keywords: Spindle, Microtubule, Biophysics, Elasticity, Kirchhoff, Mitosis

## Prošireni sažetak

Diobeno vreteno je stanična struktura koja je odgovorna za raspodjelu genetskog materijala među stanicama kćeri, a sastoji se od mikrotubula i pridruženih proteina. Funkcionalno diobeno vreteno ima karakterističan oblik, sastojeći se od zakrivljenih svežnjeva mikrotubula, zakrenutih oko osi vretena. Potpuno razumijevanje linearnih i rotacionih sila, koje određuju cjelokupni oblik diobenog vretena te koje interakcije između mikrotubula i motornih proteina ih stvaraju, ostaje otvoreno pitanje. Predstavljamo metodu kojom je moguće izvući relevantne geometrijske parametre iz mikroskopskih slika diobenog vretena. Nadalje, uvodimo teorijski model diobenog vretena u kojem motorni proteini stvaraju sile i momente sila na polovima i duž svežnjeva mikrotubula, time regulirajući oblike svežnjeva mikrotubula. Iz modela dobivamo predviđanje oblika diobenog vretena, odnosno raspodjelu sila u diobenom vretenu, iz kojih možemo zaključiti da razlika u silama savijanja objašnjava razliku u obliku unutarnjih i vanjskih mikrotubula te da je cjelokupni oblik vretena većinski rezultat rotacionih sila. U prvom poglavlju opisana je struktura diobenog vretena, kao i njegova svojstva i uloga. Predstavljen je detaljni pregled biološke grade diobenog vretena i njegove strukture te je uloga diobenog vretena u staničnoj diobi i u stanici razjašnjena. Struktura diobenog vretena je razradena sa posebnim naglaskom na svežnjeve mikrotubula i motornih proteina, koji svojim djelovanjem stvaraju sile i momente sila u diobenom vretenu. Uvedena je fizikalna teorija elastičnosti, s istaknutim djelovima koji se koriste u radu za opis svežnjeva mikrotubula te je objašnjena opravdanost korištenja iste za opis stvarnih svežnjeva mikrotubula. Drugo poglavlje posvećeno je kiralnosti diobenog vretena, odnosno opisano je nedavno otkriće da se svežnjevi mikrotubula u diobenom vretenu namotavaju oko glavne osi diobenog vretena, tj. da nisu isključivo ravninski oblici. Objašnjena je pojava zavrnutih mikrotubula u diobenom vretenu, značaj tog uvrnuća za razumijevanje ravnoteže sila i momenta sila u diobenom vretenu te dosadašnji (neuspjeli) pokušaji kvantificiranja ovog uvrnuća. Navedeno ujedno služi i kao uvod za opis glavnog cilja radnje, koji uključuje konstrukciju sveobuhvatnog mod-



ela diobenog vretena, koristeći aproksimaciju srednjeg polja, te prethodnu potrebu razvijanja metode koja će moći adekvatno izmjeriti uvrnuće svežnjava mikrotubula u diobenom vretenu, kako bi se eksperimentalni podaci mogli dobro interpretirati te služiti za postavljanje, a potom i verifikaciju modela. U trećem poglavlju razvija se metoda kosog kruga (eng. Oblique Circle Method) koja se koristi služi za mjerenje uvinutosti mikrotubula. Prikazane su pretpostavke metode, ista je sistematički razradena te u konačnici primjenjena i validirana na stvarnim ljudskim stanicama. Metoda je potom korištena za dobivanje zaključaka o strukturi diobenog vretena u perturbiranim i ne-perturbiranim ljudskim tumorskim stanicama, kao i stanicama amebe. Iz primjene metode dobiveni su zaključci o okomitim i paralelnim silama i momentima sila u diobenom vretenu. U četvrtom poglavlju uvodi se fizikalni model diobenog vretena, koji za cilj ima opis svih svežnjeva mikrotubula u metafaznom diobenom vretenu. Predstavljen je opis sustava od prebrojivo mnogo svežnjeva mikrotubula te je potom aproksimacijom srednjeg polja taj broj pušten u beskonačnost, kako bi se dobio kontinuirani model koji opisuje cjelokupno diobeno vreteno. Iz kontinuiranog modela je izračunata ravnoteža sila i momenata sila u čitavom diobenom vretenu nakon čega su svežnjevi mikrotubula opisani Kirchhoffovom jednadžbom za tanke štapove. Predstavljeni su ulazni i izlazni parametri modela, istražen je parametarski prostor modela te je biološki relevantan dio parametarskog prostora identificiran. U petom poglavlju je teorijski model uspoređen s eksperimentalnim podacima bioloških diobenih vretena, koristeći za usporedbu informacije dobivene uporabom metode kosog kruga na mikroskopske slike diobenog vretena. Teorijski model je uspoređen s više staničnih linija te su za svaku staničnu liniju pronađeni parametri koji ju najbolje opisuju, odnosno, određene su optimalne distribucije sila i momenata sila u diobenom vretenu. Iz distribucije sila i momenata sile, pokazano je da unutarnji i vanjski mikrotubuli imaju znatno različite okomite sile, no slične paralelne sile. Nadalje, model pokazuje da mikrotubuli iz centrosoma izviru pod kutem, odnosno ne ravno poput zraka sunca, već su sve okrenute prema jednoj strani, što je dosad u polju nerazmatran detalj, ali za njega postoje eksperimentalni dokazi, stoga na taj način model sugerira daljnje eksperimente. U šestom poglavlju

su reiterirani glavni zaključci doktorskog rada, u vidu rezultata koji su dobiveni korištenjem samo metode kosog kruga, ali i teorijskog modela, te njegove usporedbe s eksperimentalnim podacijma.

Ključne riječi: diobeno vreteno, mikrotubul, biofizika, elastičnost, Kirchhoff, mitoza

## Extended abstract

Introduction. The mitotic spindle is a complex micro-machine composed of microtubules and associated proteins that must be highly ordered in space and time to function properly. A functional spindle has a distinct shape with curved bundles of stretching between the poles. Recent discoveries revealed that the mitotic spindle is a chiral object, which means that it can be distinguished from its mirror image, resulting in its constituent microtubule bundles being twisted around its long axis rather than being confined to a plane. This implies that, in addition to linear forces, torques play an important role in mitosis regulation. An in-depth understanding of how these forces define the overall shape of the mitotic spindle and how the twisted shapes arise as a result of interactions between microtubules and motor proteins is still unclear [1].

Methods. To answer this question, we first develop the Oblique Circle Method for measuring relevant geometrical parameters of mitotic spindle microtubule bundles. Then, we use a mean-field approach to model the entire spindle and compare the model results to our experimental data. Mean-field theory states that discrete microtubule bundles in a given region, as well as forces and torques, are approximated by averaged physical quantities. The central idea of our mean-field approach is to generalise the description of microtubule bundle spatial distribution by introducing a continuous density of these bundles. We assume that single bundles and centrosomes are in balance, thus in the model all forces and torques acting upon them are balanced. We also analyse spindle shapes from our experiments, by tracking single microtubule bundles, and extracting their twist and curvature.

Results. The model provides predictions for shapes of all microtubule bundles in the spindle, which we compared with our experiments [2, 3]. The model predicts that rotational forces dominate the shape of the entire spindle, and that a difference in bending forces explains the difference in the shapes of the inner and outer bundles. We can investigate general trends, such as dominating forces and torques, as well as their variability within

different cell populations, by comparing these parameters among different cells.

Discussion. The discovery that microtubule bundles in mitotic spindles are twisted in a helical fashion opens up a new line of inquiry into the potential biological roles of spindle chirality. To better understand the role and mechanism of spindle chirality, we created a spindle mean-field model that predicts the shape of all microtubule bundles in a mitotic spindle. We can infer the forces and torques acting on microtubule bundles and chromosomes during cell division by comparing the microtubule bundle shapes predicted by our model to measurements of experimental microtubule bundle curvature and twist. From this, we gain insight into how forces and torques shape the mitotic spindle, and how its chiral shape arises.

# Contents

<b>1</b>	<b>Introduction</b>	<b>1</b>
1.1	The role of the cell and its properties . . . . .	1
1.1.1	The cycle of cell division . . . . .	4
1.1.2	The mitotic spindle . . . . .	10
1.2	The structure and properties of the cytoskeleton . . . . .	15
1.2.1	Microtubules and other fibres . . . . .	17
1.2.2	Motor proteins . . . . .	24
1.2.3	Microtubule dynamics as force generators . . . . .	27
1.2.4	Motor proteins as force generators . . . . .	30
1.3	The current view on forces in the metaphase mitotic spindle . . . . .	30
1.3.1	Mapping the forces in the metaphase spindle . . . . .	35
1.4	Bridging fibres and their effect on metaphase force-balance . . . . .	39
1.4.1	The existence of bridging microtubules . . . . .	39
1.4.2	Bridging microtubules connect kinetochore pairs . . . . .	45
1.5	The theory of elasticity . . . . .	48
1.5.1	Theory of elasticity applied to thin elastic rods . . . . .	55
1.5.2	Torsion of thin elastic rods . . . . .	56
1.5.3	Bending of thin elastic rods . . . . .	58
1.5.4	Equilibrium of rods . . . . .	63
1.5.5	Boundary conditions at the ends of a bent rod . . . . .	65
1.6	Existing models of the mitotic spindle metaphase . . . . .	66
1.6.1	Slide and cluster models . . . . .	67
1.6.2	Liquid crystal models . . . . .	70
1.6.3	Elasticity models . . . . .	72
<b>2</b>	<b>Shapes and symmetries in the mitotic spindle</b>	<b>73</b>
2.1	The mitotic spindle is chiral . . . . .	73
2.2	Mitotic spindle chirality arises from the twisted shape of microtubule bundles	73
2.3	Effects of motor proteins on mitotic spindle chirality . . . . .	76
2.4	Role of mitotic spindle chirality . . . . .	79
<b>3</b>	<b>Quantifying the effects of spindle chirality</b>	<b>80</b>
3.0.1	Cell lines and microtubule visualization . . . . .	82
3.1	The Oblique Circle Method . . . . .	84
3.1.1	Image analysis and data tracking . . . . .	84
3.1.2	Choosing a coordinate system . . . . .	85
3.1.3	Fitting a circular arc to the microtubule bundle shapes . . . . .	85
3.1.4	Calculation of the curvature and twist from the fitting parameters . . . . .	87
3.1.5	Detailed worked example - synthetic spindle . . . . .	88

3.1.6	Fitting circular arcs to the bundles of the synthetic spindle . . . . .	90
3.1.7	Error analysis . . . . .	90
3.2	Application of the Oblique Circle Method to real spindles . . . . .	93
3.2.1	Knowledge gained from the Oblique Circle Method . . . . .	93
3.3	Measuring chirality of biological spindles . . . . .	98
3.3.1	Detailed analysis of unperturbed human spindles . . . . .	98
3.3.2	Spindle twist is most pronounced at anaphase onset in a cancer and a non-cancer cell line . . . . .	103
3.3.3	The <i>Naegleria gruberi</i> spindle twists from pole-to-pole in a righthanded fashion . . . . .	113
3.3.4	Compression of the spindle along the pole-to-pole axis increases the left-handed twist . . . . .	123
3.3.5	Motor proteins Eg5/kinesin-5 and Kif18A/kinesin-8 regulate spindle twist . . . . .	126
3.3.6	Depletion of PRC1 makes RPE1 spindles twist in a right-handed manner, whereas overexpression of PRC1 abolishes twist . . . . .	131
3.3.7	Depletion of augmin leads to zero twist in HeLa cells and right-handed twist in RPE1 cells . . . . .	132
3.3.8	Round spindles are more twisted than elongated spindles . . . . .	132
3.3.9	Mechanisms that generate spindle twist . . . . .	140
3.3.10	Physiological function of spindle twist . . . . .	145
<b>4</b>	<b>Mean-field model of the mitotic spindle</b>	<b>146</b>
4.1	Theory for force balance of mitotic spindle . . . . .	147
4.2	The mean-field approach . . . . .	149
4.3	Solving the mean-field model . . . . .	152
4.4	The balance of forces and torques . . . . .	154
4.5	Imposing symmetries . . . . .	155
4.6	The force and torque fields . . . . .	156
4.7	Taylor expansion of forces and torques . . . . .	159
4.7.1	Zeroth order expansion . . . . .	160
4.7.2	First order expansion . . . . .	160
4.7.3	Higher order terms . . . . .	162
4.7.4	Predictions of the theoretical model . . . . .	162
<b>5</b>	<b>Experimental verification of the mean-field model</b>	<b>177</b>
5.1	Comparison criteria and the loss function of choice . . . . .	177
5.2	Inferring the force and torque distributions in real spindles . . . . .	178
5.2.1	Perturbed and unperturbed HeLa cells . . . . .	178
5.2.2	Amoeba cells . . . . .	178

5.2.3	Compressed HeLa cells . . . . .	178
5.2.4	Independent verification of the model . . . . .	179
<b>6</b>	<b>Summary, conclusions and future expectations</b>	<b>183</b>
<b>A</b>	<b>Appendix</b>	<b>184</b>
A.1	Quantification of spindle chirality . . . . .	184
A.1.1	Cell lines . . . . .	184
A.1.2	Confocal microscopy . . . . .	184
A.1.3	Spindle twist calculation methods . . . . .	185
A.1.4	Tables with data breakdown from chirality quantification . . . . .	188
A.1.5	Detailed STLC analysis . . . . .	191
A.2	Additional Naegleria gruberi images . . . . .	191
A.3	Mean-field model . . . . .	196
A.3.1	Microtubule bundle density . . . . .	196
A.3.2	Additional symmetries for the torques . . . . .	198
A.3.3	Derivation of the force-balance equations . . . . .	199
A.3.4	Zeroth order . . . . .	207
A.3.5	first-order terms . . . . .	209
A.3.6	Mid-zone density . . . . .	212
A.3.7	Contour length of the bundle . . . . .	213
<b>B</b>	<b>Curriculum vitae</b>	<b>214</b>
B.1	Papers . . . . .	214
B.2	Conferences . . . . .	215

# 1 Introduction

In this thesis we model the mitotic spindle, a complex micro-machine responsible for the proper division of cells. We describe the functions of microtubule bundles, along with their corresponding active and passive motor proteins, and the functions of spindle poles, to obtain a comprehensive view into the forces and torques which the spindle uses to facilitate cell division. Microtubule bundles are important structural elements of the mitotic spindle, forces generated within microtubule bundles are responsible for proper centring of chromosomes in the equatorial plane during cell division, and their subsequent separation during the later stages of cell division. In the Introduction, we describe the cell, its structure and properties, and the cell cycle, with an emphasis on the mitotic spindle, providing an overview of the current state of the field from the literature. Next, we describe the chirality of the mitotic spindle, its recent discovery, how it arises as a consequence of microtubule bundle twist and how it effects cellular processes. In the section on Quantifying microtubule bundle twist, we introduce the Oblique Circle Method for measuring microtubule bundle twist. In the section for Theoretical model for chiral mitotic spindles, we introduce the basis of our theoretical model for the mitotic spindle, which we use to describe all microtubule bundles in the spindle. In the Quantitative experimental data and comparison with theoretical predictions section, we compare the model with experimentally imaged spindles, obtaining the distribution of forces and torques in the mitotic spindle. Finally, in the Conclusion section we provide a summary of all results and how they fit into the wider field of cytoskeletal biophysics.

## 1.1 The role of the cell and its properties

All living system are characterised by their ability to catalyse metabolic processes and their ability to transfer genetic information to their offspring. The cell is the basic building block of life, which can live as a fully functional organism or as the simplest component of a multicellular organism. An example of a metaphase mitotic spindle from a HeLa cell can be



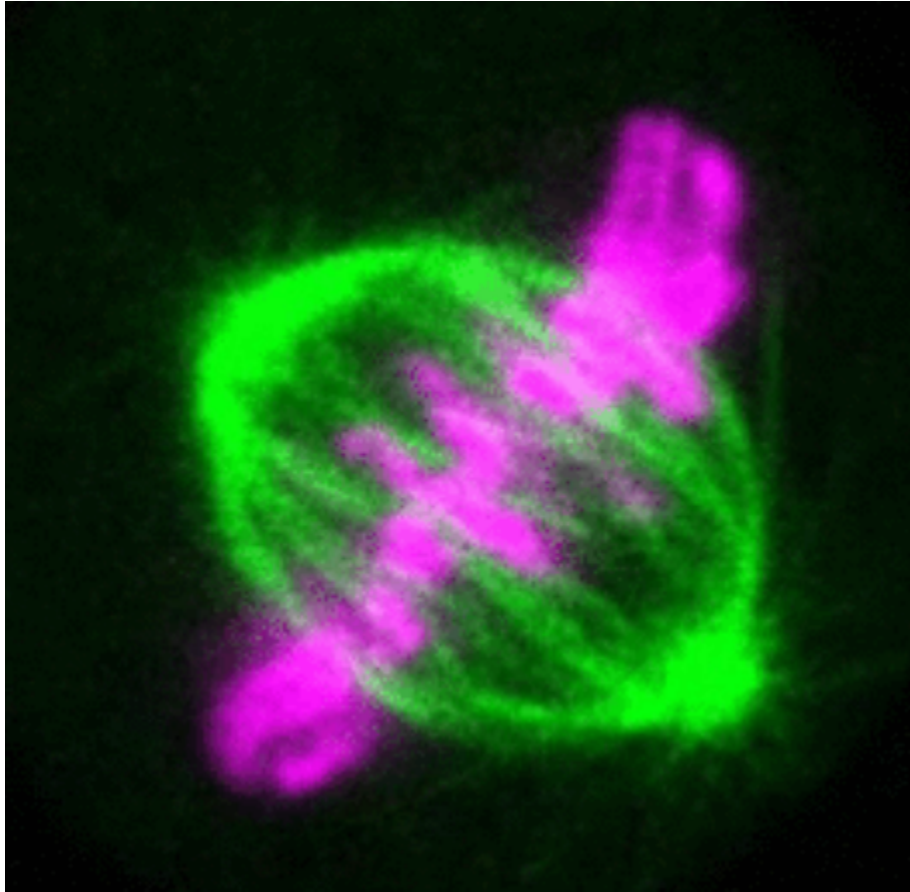


Figure 1: Microscopy picture of a live HeLa cell expressing PRC1-GFP. Images are property of Tolic Lab and used with permission.

seen in Fig. 1. Robert Hook, an architect, natural philosopher, and scientist, was the first to describe the cell, realising its importance as a fundamental building block of life. In 1665, while looking at thin slices of cork, he coined the term. His observations soon expanded to plants and woods, as well as flies' eyes. The ability of a living organism to proliferate by transferring copies of its genes into its offspring is its distinguishing feature. The most basic way to accomplish this fundamental task is to duplicate the cell's own genetic information, separate it evenly, and eventually divide into two genetically identical daughter cells, a process known as mitosis (Greek  $\mu\tau\omicron\sigma$  (mitos), meaning thread). Mitosis is thus a type of asexual reproduction in single cell organisms, occurring in bacteria, protists, algae, fungi, and plants.

Somatic cells in multicellular organisms, on the other hand, undergo mitosis not to reproduce, but to produce more cells during growth and repair processes. Despite working with cells that had been subjected to rather crude fixation and staining methods, Flemming was able to describe the bipolar shape of the spindle and its characteristic filamentous organization, in principle not much different from modern spindle seen under fluorescence microscopy Fig. 2, during the 1880s, laying the groundwork for all subsequent research of cell divisions and cells themselves.



Figure 2: Drawing of mitotic division as seen by Flemming with major components (chromosomes and microtubules) of the spindle. Adapted from [4].

### 1.1.1 The cycle of cell division

Mitosis is the division of a parent cell into two nascent daughter cells. This process is fundamental to all life, and the ability of cells to accurately duplicate and then precisely segregate their duplicated genetic material is critical [5]. This ensures the stability of a cell's genomic information, which is required for life to continue. This process must be extremely precise because any loss or gain of DNA material can be lethal to a single cell or cause severe complications for the cell, causing problems for the entire organism [6]. The importance of this process explains why the missegregation rate in human non-transformed cell lines is extremely low [7], and that controlled and timed cell divisions at the organismal level are required for cell type differentiation and thus complex organ development. In which case it is either not detected at the organismal level or causes severe complications for the cell. It is estimated that in single-cell organisms such as yeast, only one of its 16 chromosomes missegregates every 100 000 divisions [8]. A loss of controlled division is the most common defect observed in various cancers, infertility disorders and other congenital abnormalities [6]. Furthermore, aneuploidy, which is any deviation from a multiple of the haploid chromosome number, is the leading cause of spontaneous miscarriages and birth defects in humans [9] and represents a key hallmark of cancer [10].

The cell cycle Fig. 3 of most eukaryotic cells can be divided into the interphase and the mitotic phase (M phase), with its duration varying wildly between different types of organisms, but being around 24 hours for healthy human cells [11]. As interphase happens between two mitotic divisions, it is during interphase that the cell reorganizes its interior, grows and prepares for the next M phase.

The most prominent change of the cell cycles appears during the S phase of the interphase, during which DNA replication occurs. During the G1 and G2 phases the cell doubles its mass of proteins and organelles [11]. Additionally, cells can opt to enter the G0 phase, which is a resting period, in which the cell can remain before the cell cycle resumes. The majority of somatic cells return to the G1 phase from the G0 phase, but there exist *post-mitotic* cells,

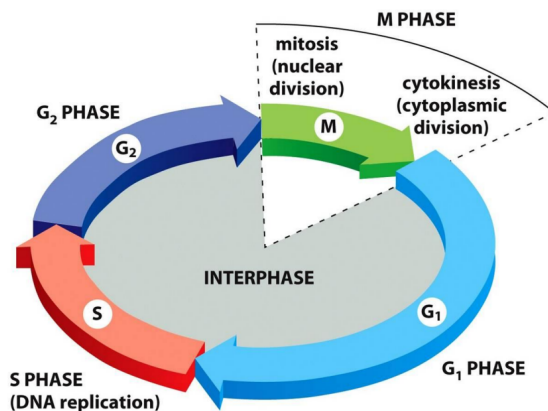


Figure 3: The phases of the cell cycle. Interphase consists of three distinct phases: the S phase which includes DNA replication, the G<sub>1</sub> phase as the gap between the M phase and the S phase, and the G<sub>2</sub> phase as the gap between the S phase and the M phase. The M phase consists of mitosis and cytokinesis. Adapted from [11].

like neurons, which remain metabolically active, but no longer divide [6]. These G phases thus form the gap phase between the S and M phases, giving the cell time to feed, grow and control the accuracy of on-going events. During the M phase, which consists of mitosis and cytokinesis, cell divides to form two identical daughter cells. M phase lasts for about 1 hour, the thus cell spends more than 95% of the time in the interphase [11] (Fig. 4).

For mitosis to proceed correctly, cells must first duplicate their microtubule organizing centres (MTOCs), in animal cells called centrosomes, in coordination with replication of chromosomes in the S phase.

The duplicated centrosomes separate in prophase of mitosis and will become two spindle poles of mitotic spindle [6], thus giving the spindle its characteristic bipolar form. It is important to note that this process has to be properly regulated because multipolar spindles that result from failure in this process contribute to missegregation of chromosomes leading to high genomic instability resulting in aneuploidy seen in many tumour cell lines [13]. Although mitosis is a continuous process, it has been commonly divided in five stages for ease of description [6] (Fig. 6).

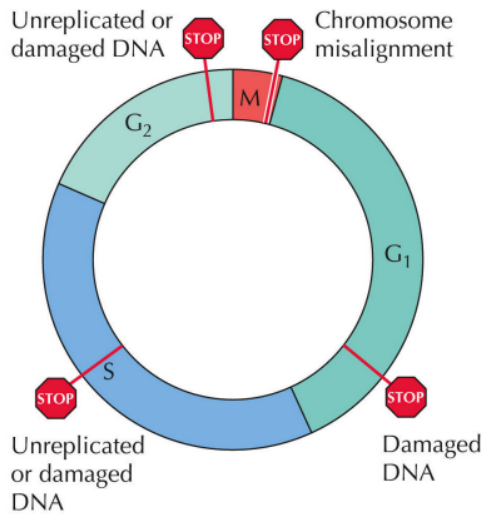


Figure 4: Four control points or checkpoints in the cell cycle - the G1 checkpoint at the G1/S transition, the S checkpoint during S phase, the G2 checkpoint at the G2/M transition during interphase. Adapted from [12].

The prophase, the first phase of the M phase, is distinguished by increased centrosome activity, as it is during prophase that they begin nucleating MTs, thereby replacing the interphase array of microtubules with mitotic asters, structures composed of a centrosome and its radial arrays of microtubules [14]. Furthermore, the rate at which microtubules grow at their plus ends accelerates, and two mitotic asters move to opposite sides of the nucleus due to the action of the bipolar kinesin-5 motor protein. The separated centrosomes will form two mitotic spindle poles Fig. 6. This pathway of centrosome separation in human cells is called the prophase pathway [15], because centrosomes can be also separated in prometaphase, which we will describe further on. Furthermore, during this phase, the internal order of the membrane system is disrupted, resulting in the cessation of endocytosis and exocytosis, as well as the rearrangement of actin microfilaments, resulting in the cell's characteristic round, football-like shape. Furthermore, it is when chromosomes condense, which means that each previously DNA duplex has its length reduced a thousand-fold, resulting in the tight structures known as chromosomes [5] (Fig. 6). The ultimate step has cohesin complexes

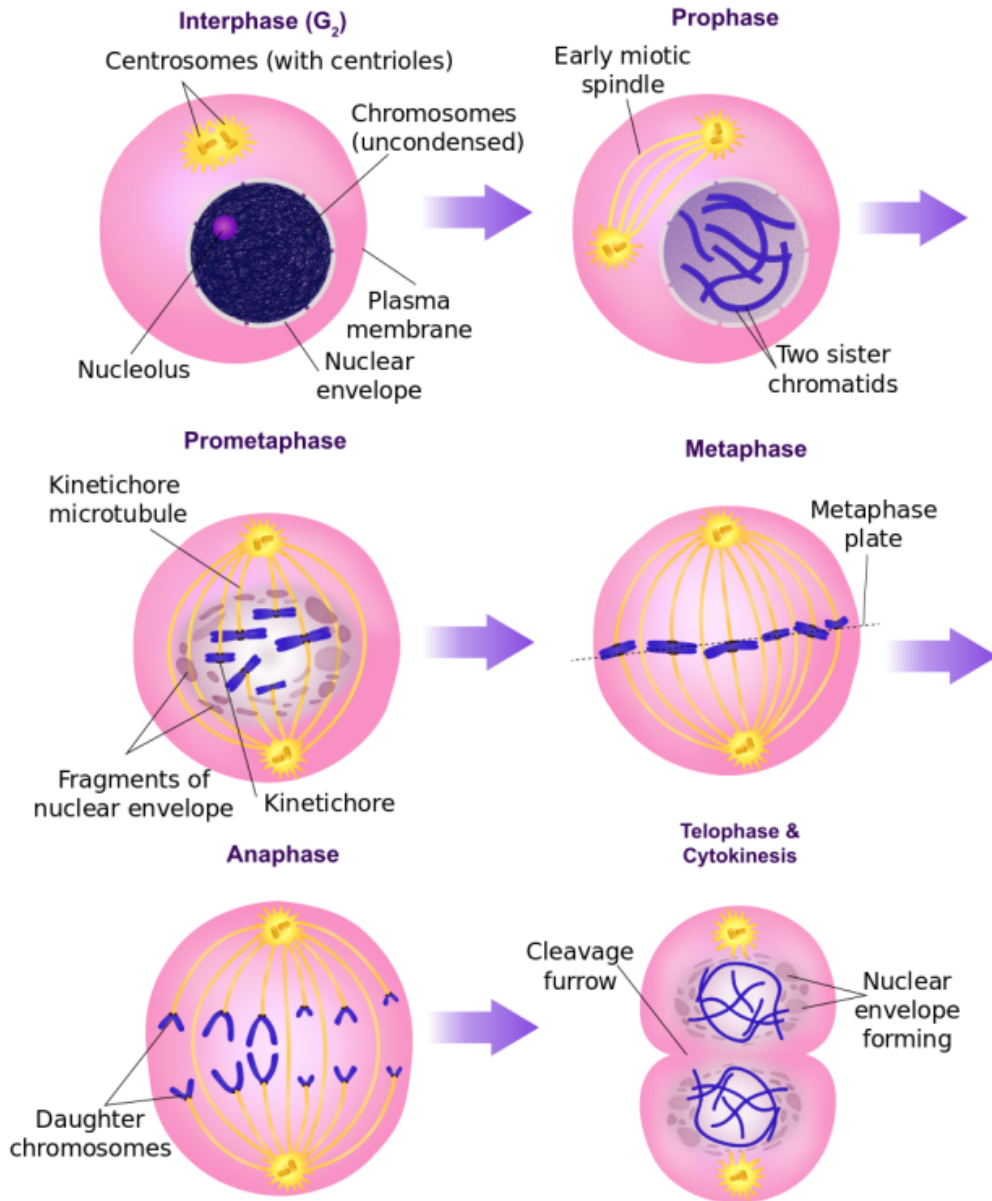


Figure 5: A diagram of the mitotic phases. The distinct phases of the cell cycles are shown, along with key events happening during each of the various phases. Adapted from original work by Ali Zifan under CC BY-SA 4.0.

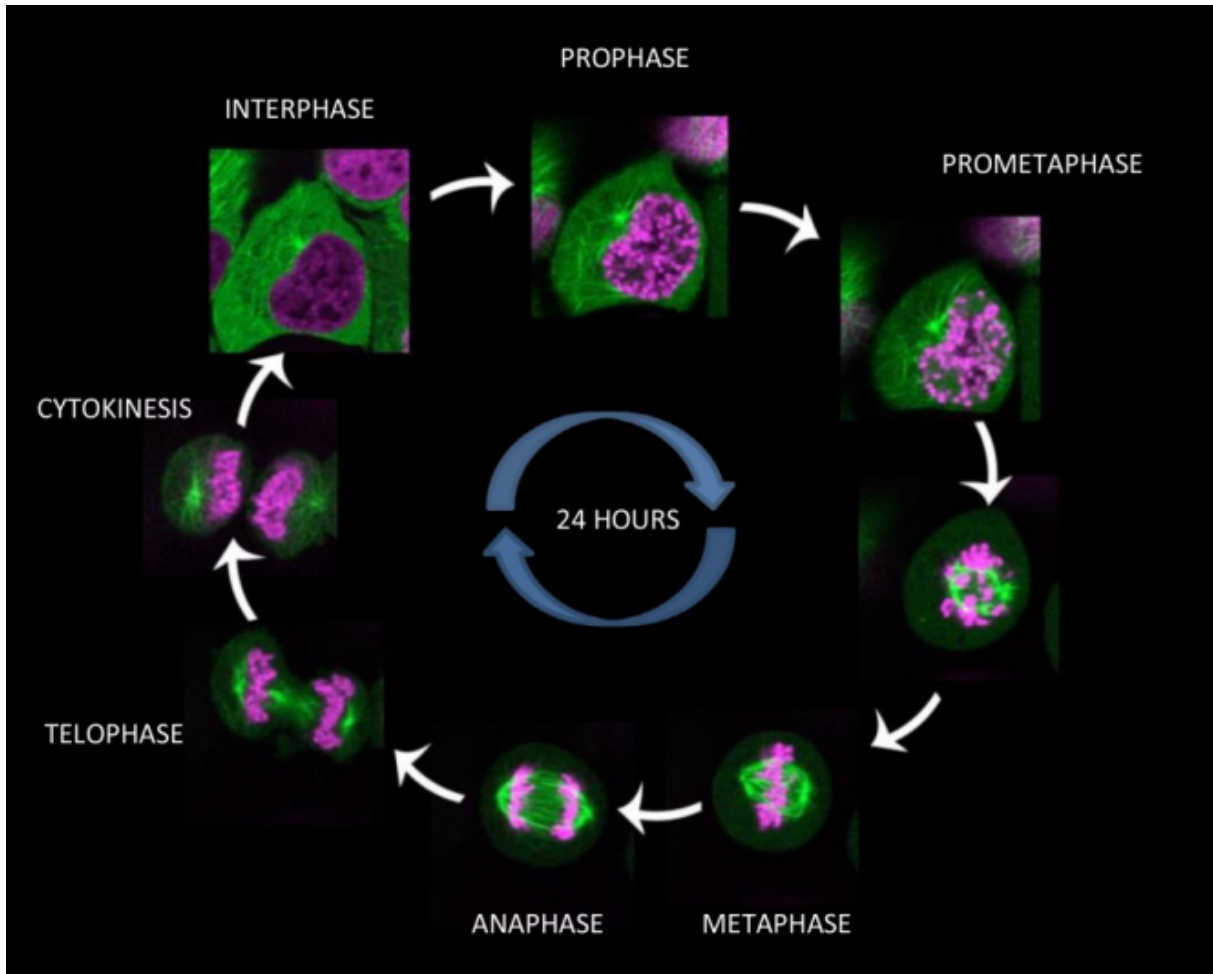


Figure 6: Mitotic stages are summarised in live cell images (Zeiss LSM 710 NLO inverted laser scanning confocal microscope, Zeiss, Germany). Beginning with interphase, stages of mitosis are depicted in a human HeLa cell (cervical cancer) expressing H2B-mCherry (chromosomes, magenta) and GFP-tubulin (microtubules, green): Condensation of chromosomes (prophase); nuclear envelope breakdown and attachment of chromosomes to spindle microtubules (prometaphase); alignment of chromosomes in spindle equatorial plane (metaphase); chromosome segregation (anaphase), contractile ring narrowing (telophase); cytoplasm division Tolic Lab photographs were used with permission.

at chromosome arms degrading, meaning that only those in centromeric region survive. These begin forming protein complexes called kinetochores, sites of future microtubule attachment, the centromeric region of each sister chromatid [16]. The nuclear envelope and nuclear pores degrade as the cell enters prometaphase, and the nuclear lamina disassembles. This nuclear envelope breakdown (NEBD) is what allows microtubules to associate with kinetochores and search for and capture pairs of chromosomes [17] (Fig. 6). This interaction between microtubules and chromosomes signals the beginning of assembling the mitotic spindle. After both sister chromatids are captured by opposite spindle poles they are said to be bi-oriented (amphitelic attachment) [14].

This allows these pairs to undergo the process of chromosome congression, leading to aligned sister chromatids in the equatorial plane and thereby defining the beginning of metaphase [18] (Fig. 6). Some types of cells separate their centrosomes extensively in this phase, meaning that the prometaphase pathway of centrosome separation is the main one [15]. Metaphase in human cells is defined by paired sister chromosomes oscillating at the centre of the spindle (Fig. 6). Metaphase is a biophysical steady state, which means that, while there are large fluctuations and directed fluxes in both physical and chemical processes during metaphase, their average is very close to being throughout metaphase [19].

Anaphase, the next stage of the cell cycle, occurs only when the cell's internal quality control system approves. This quality control process is carried out by the spindle assembly checkpoint (SAC), which delays chromosome segregation until chromosomes are attached to poles and kinetochores are under sufficient tension [20]. Only when these conditions are met will the anaphase-promoting complex/cyclosome (APC/C) be activated, causing cohesin complexes in the centromeric part of the cell to be broken and the chromosomes to be separated and pulled to different poles by the forces exerted by microtubule depolymerisation (anaphase A) (Fig. 6). Because of sliding by antiparallel microtubules, distinct movement occurs, with the spindle poles moving further away from each other, thereby elongating the spindle significantly (anaphase B) (Fig. 6).



In the penultimate phase, the telophase, which occurs after the chromosomes have been separated during anaphase, the nuclear envelope reforms and chromosomes once again de-condense (Fig. 6).

The final phase of the cell cycle, cytokinesis, is characterized by division of the cell cytoplasm through formation of a contractile ring [6] (Fig. 6).

### 1.1.2 The mitotic spindle

Equal division of the genetic material into two newly formed daughter cells is performed by the mitotic spindle, a complex micro-structure that consists of two poles, forming a bipolar cellular structure constructed from microtubule bundles extending between the poles, and a large number of associated proteins [5, 21–23]. The spindle is a mechanical assembly that generates and controls the forces required for chromosome segregation. This highly organised structure appears during prometaphase, and the mechanism by which it appears is unknown. Kinetochores will connect microtubule bundles to chromosomes. Sister kinetochores will form connections with microtubule bundles that emerge from opposing poles. All sister kinetochore pairs will be connected in this manner during the next phase of mitosis, the metaphase, allowing cell division to proceed in an orderly fashion. The mechanical properties of the spindle are determined by the mechanical properties of its fundamental building blocks, the microtubule bundles. Microtubules are thin elastic filaments that generate and balance forces acting on chromosomes caused by motor protein activity, as well as from polymerization and depolymerisation of the microtubule bundles [24]. In the 1950s, it was shown, using polarisation microscopy, that spindles are built from filaments that move parallel to chromosomes [25]. Later it was proposed that polymerisation dynamics of these filaments produce mechanical forces needed for powering chromosome motion during anaphase [26]. Through a combination of different techniques these filaments were identified as microtubules, non-covalent polymers of protein tubulin [27]. Because of its large size and central role in mitosis, the mitotic spindle's molecular components have been extensively

studied using various techniques, and many proteins required for mitosis have been identified [28]. The development of techniques like phase contrast microscopy enabled the first live-cell imaging of highly dynamic structures like the mitotic spindle [29]. Further, discovery and development of green fluorescent protein (GFP), and its related variants, made the quantification of molecular structures within the mitotic spindle much more readily available [30]. Furthermore, the discovery of micro-manipulation techniques [31] and laser ablation of some components of spindle gave us insight into mechanical principles of the mitotic spindle [32–34]. The development of inhibitors which target various molecular components of the spindle enabled using perturbations to elucidate the previously unknown roles of some proteins [35]. Sadly, despite all previous advances, our understanding of even the basic mechanical principles and architecture of this essential cellular structure remains rather rudimentary, since we cannot explain how the spindle maintains its structural and functional stability in the face of different forces [19, 36], and answering this is a key focus of modern biophysical research [37].

Centrosomes are cellular structures which act as the chief microtubule organisation centres in the cell. Every centrosome is made up of a pair of centrioles which are located in a pericentriol matrix [39].

Microtubules are microscopic protein tubes, formed by the polymerization of  $\alpha$ - and  $\beta$ -tubulin, organized into a bundle of microtubules, termed fibres, in the mitotic spindle [41]. Microtubule ends with  $\alpha$ -subunits exposed are named minus (-) ends, while microtubule ends with the  $\beta$ -subunits exposed are named plus (+) ends, respectively [11].

Depending on the orientation of a microtubule, it can be classify it as either parallel or antiparallel. Kinetochore fibres (k-fibres) are the most stable and important fibres, which attach with their (+) ends to the kinetochores, the protein complexes on the chromosome [16]. Amphitelic attachments enable chromosomes to link with the mitotic spindle. Electron microscopy (Fig. 9) has shown that k-fibres in human cancer cells contain 12-22 parallel MTs linked together [42].

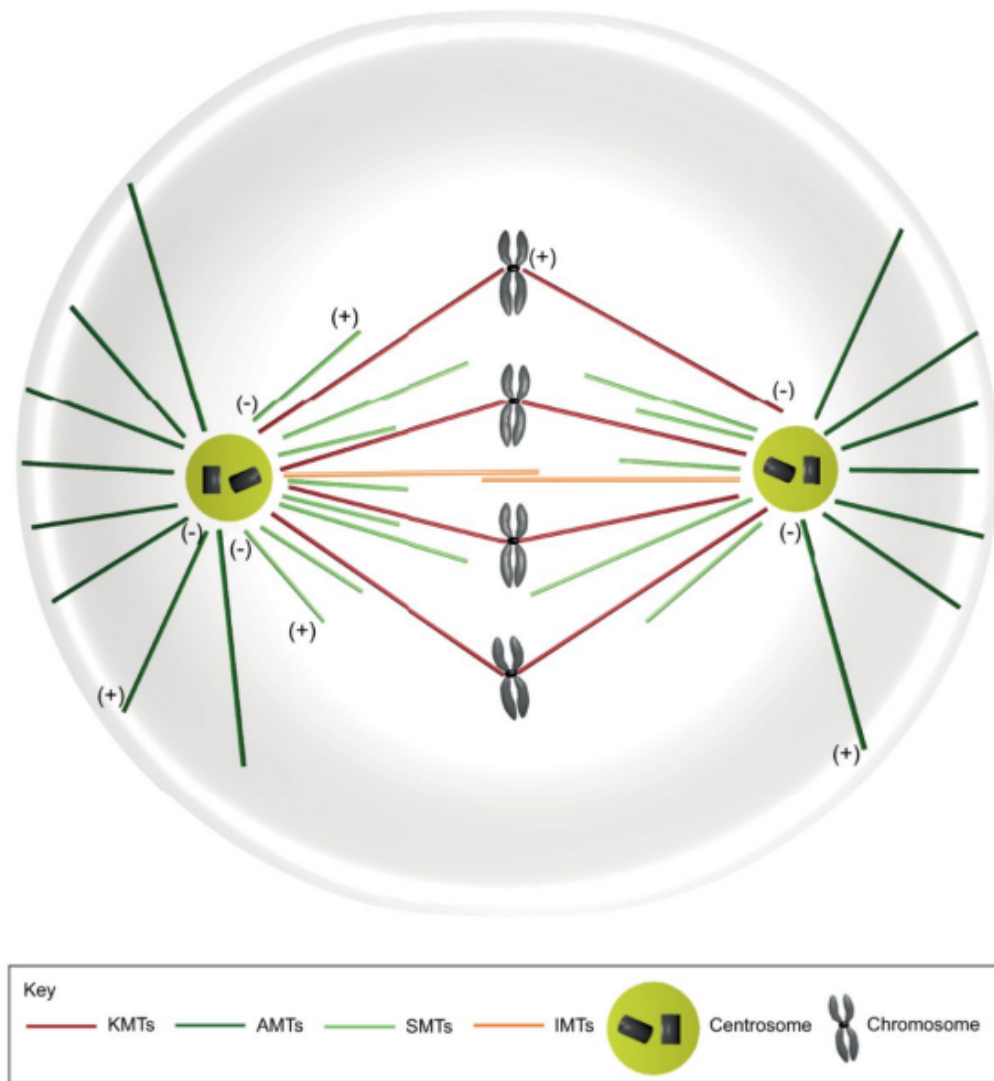


Figure 7: Schematic of the mitotic spindle architecture during metaphase. The metaphase spindle nucleates microtubules mainly from centrosomes (light green). Microtubules minus ends (-) anchor at the centrosome while their plus-ends (+) are growing toward different sites within the dividing cell. Kinetochore microtubules (KMTs) are depicted in red, and are attached to chromosomes, via kinetochores (black), astral microtubules are depicted in dark green and point towards the cell periphery. Spindle microtubules (SMTs) are depicted in light green, they are not in interaction with microtubules from the other pole, while interdigitating microtubules (IMTs), shown in orange, grow towards the spindle interior and interact in the middle of the spindle with microtubule from other pole, thus forming antiparallel overlaps. Adapted from [38].

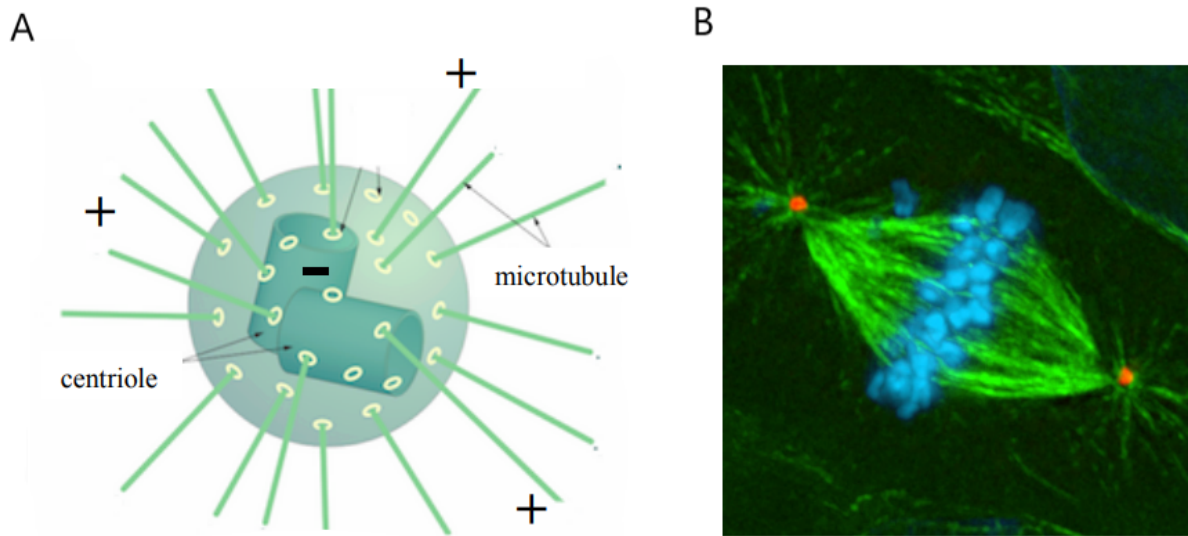


Figure 8: Schematic representation of a centrosome and its major components. Centrioles are the central structure, the light green circle represents the pericentriolar matrix and thin rods show newly nucleated microtubules. Minuses and pluses represent the (-) ends of microtubules embedded in the centrosome, while (+) represents growing the free ends. b) Confocal image of the mitotic cell in metaphase with centrosomes labelled red, microtubules green and chromosomes blue. Centrosomes in red represent two poles of the spindle [40].

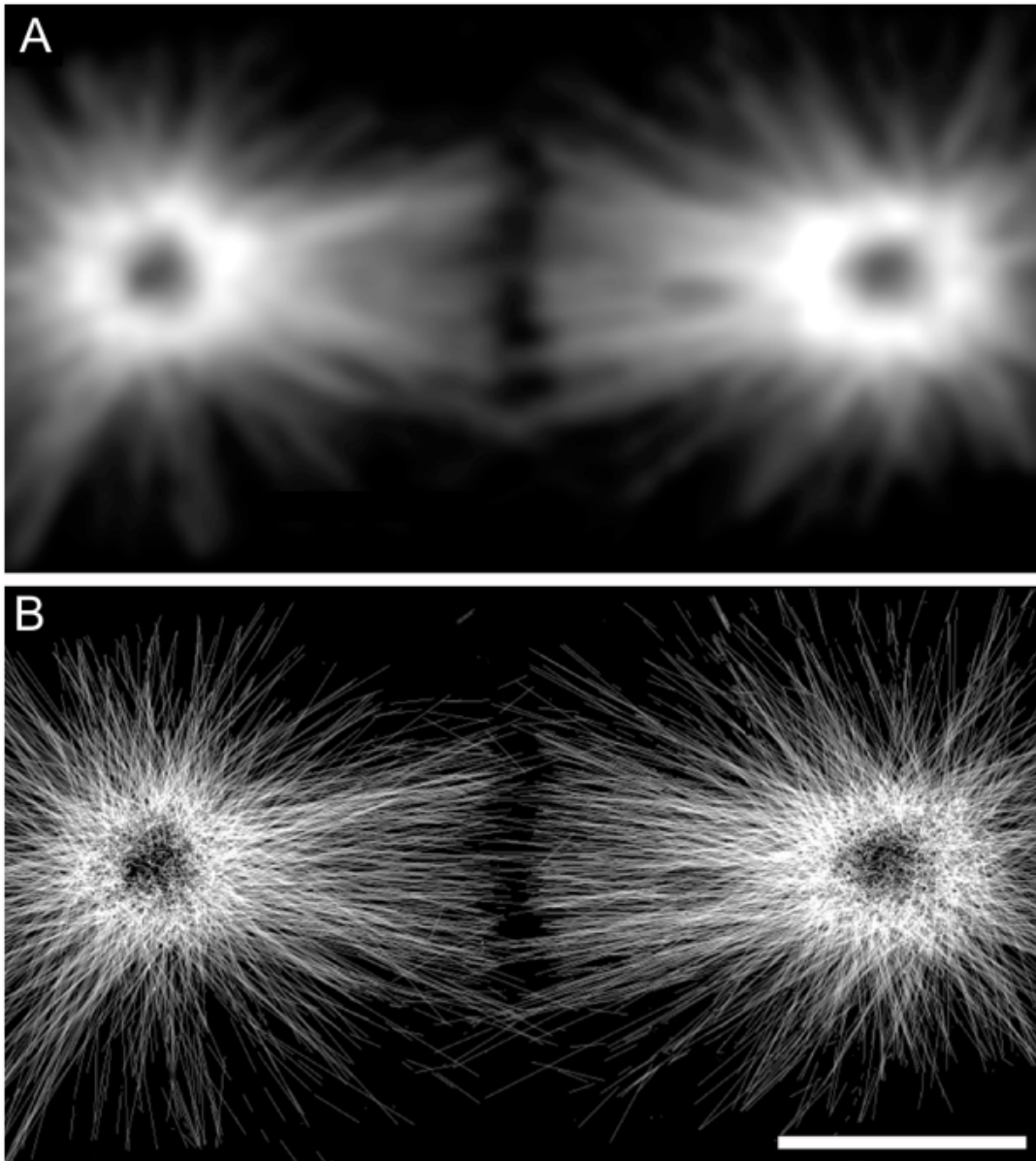


Figure 9: Organization of the mitotic spindle at metaphase in the early *C. elegans* embryo. (A) Level of resolution as expected from light microscopy. (B) Level of information obtained from electron microscopy. The density map of image A constructed from the data shown in B. The data comes from a 3D reconstruction of microtubules obtained from electron tomography, with microtubules simplified as straight lines. A was convolved with a two-dimensional Gaussian point-spread function with a full-width at half maximum (FWHM) equal to  $0.45\mu\text{m}$ . Scale bar:  $5\mu\text{m}$ . Adapted from [38].

In addition to k-fibres, the mitotic spindle contains two more kinds of microtubules – interpolar and astral microtubules (Fig. 10). Interpolar microtubules are organized into antiparallel bundles as they overlap at the centre of the spindle and astral microtubules extend from the spindle poles, through the cytoplasm, towards the cell cortex, thereby participating in spindle positioning inside the cell [11]. It has been shown, however, that the spindle is stable without the astral forces provided by astral microtubules anchored to the cell cortex [43].

## 1.2 The structure and properties of the cytoskeleton

Cytoskeletal filaments are classified into three types in eukaryotic cells. Actin filaments, also known as microfilaments, are cable-like structures with a diameter of approximately  $6nm$ . Intermediate filaments have a rope-like structure made up of several intertwined protein strands, with a diameter of about  $10nm$ . Microtubules have a pipe-like structure, with an outer diameter of approximately  $25nm$  and an inner diameter of approximately  $18nm$ . The cytoskeletal filaments were initially identified by electron microscopy [45–48]. The constituent proteins - actin, intermediate filament proteins, and tubulin - have been chemically purified and polymerised in the test tube to produce filaments that are virtually indistinguishable from those observed in both live and in vitro cells. These proteins' amino acid sequences, as well as those of many relatives from various organisms, have been determined. In addition, the actin and tubulin proteins have been crystallised and their structures have been studied at atomic resolution. These atomic structures were then used to create atomic models of the filaments as a whole. Given that actin filaments and microtubules can grow to lengths of tens of thousands of nanometres, it can be concluded that these filaments have the largest known atomic structures of any biomolecules. Although the atomic structure of the coiled protein that forms the backbone of the intermediate filament protein has been determined, the arrangement of the intermediate filament proteins within the filaments remains unknown. For more detailed information on the biochemical properties of filament proteins, their associated

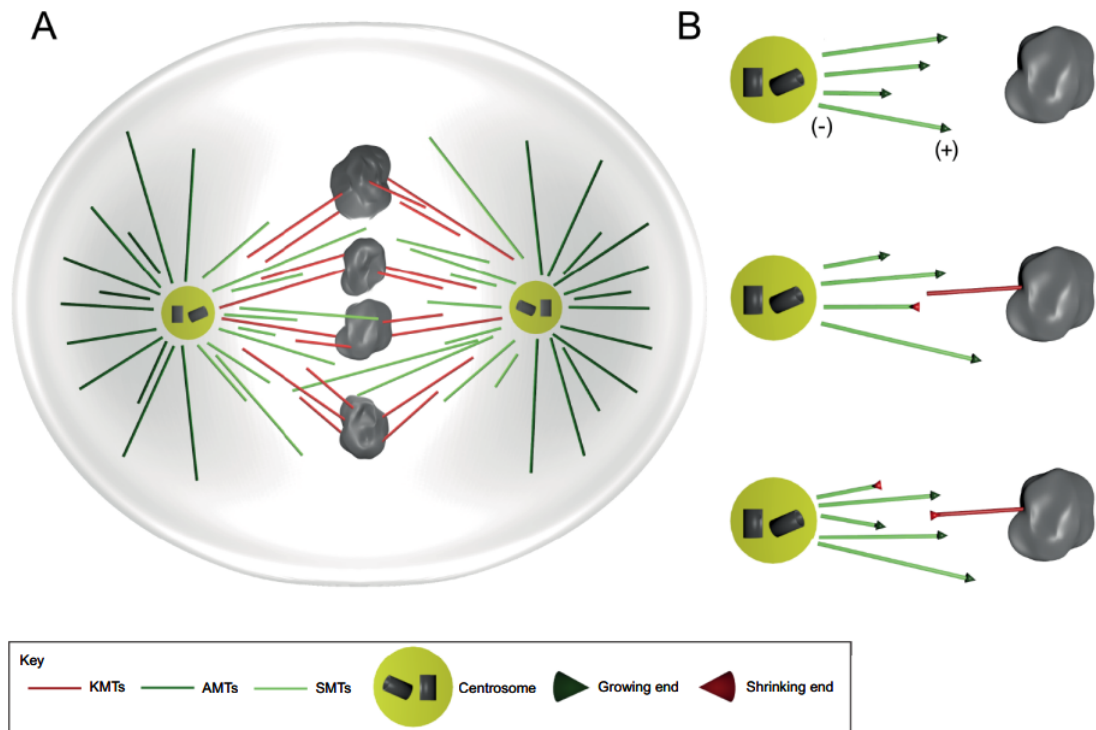


Figure 10: Metaphase spindle in an early *C. elegans* embryo. (A) Schematic representation of the growth of microtubules (AMTs, dark green; KMTs, red; SMTs, light green) from the centrosomes (light green spheres with centrioles). KMTs are attached with their plus-ends to the holocentric kinetochores of the chromosomes (gray). As schematically shown, the majority of KMT plus-ends in this mitotic spindle are not directly attached to the centrosomes. (B) Microtubules grow out from the centrosome (upper panel) and eventually attach to the holocentric kinetochore, thus converting into KMTs (mid panel). An attachment of the KMT plus-ends at the kinetochore (lower panel) causes a selective detachment of the KMT minus-ends from the centrosome, possibly because of mechanical stress. As a consequence, most of the KMT minus-ends are not directly attached to the centrosomes. Green arrows indicate microtubule growth, red arrowheads microtubule depolymerisation. Adapted from [38, 44].

proteins, and cytoskeletal filament systems see [49–51].

### 1.2.1 Microtubules and other fibres

Microtubules are the primary structural elements of the mitotic spindle. They are hollow polar tubes of varying lengths with well-defined ends that can be classified as plus (+) or minus (-). While (+) ends are free to interact with non-spindle elements such as chromosome kinetochores or cell cortex, (-) ends are embedded at specific points within the spindle. These are mostly microtubule organising centres (MTOCs), which serve as anchors for microtubule (-) ends. These spots not only act as anchors, but they also nucleate new microtubules, which grow with their (+) ends oriented away from the nucleation site from which they grew. The spindle's primary MTOCs are centrosomes, which nucleate the majority of microtubules beginning in prophase. Centrosomes are made up of two centrioles, as well as the pericentriolar matrix. They are duplicated in the centrosome cycle during the G2 phase of interphase. Centrosomes are duplicated and move to opposite sides of the nucleus, where they form the two poles of the future spindle. As the nuclear envelope degrades in an open mitosis, microtubules begin to form in all directions. The spindle formation and maturation will be led by microtubules that meet and interact mutually between centrosomes. Centrosomes and associated components determine the geometry of microtubules arrays throughout the cell cycle, and thus influence cell shape, polarity and motility, as well as spindle formation, chromosome segregation and cell division [5]. All centrosomes contain a structured core to which more than 50 copies of  $\gamma$ -tubulin ring complex ( $\gamma$ -TuRC) are connected [52]. Each  $\gamma$ -TuRC contains 13 copies of  $\gamma$ -isoform of tubulin that define the position of microtubule nucleation, the polar orientation of the polymer, and the lattice into which tubulin assembles [53]. As microtubules have their beginning at described spots they will form tubes as subunits are added in a defined structural order (Fig. 11).

The microtubule tubulin subunit is a heterodimer formed by two closely related globular proteins,  $\alpha$  and  $\beta$  tubulin. Non-covalent bonds hold them together, forming microtubules,



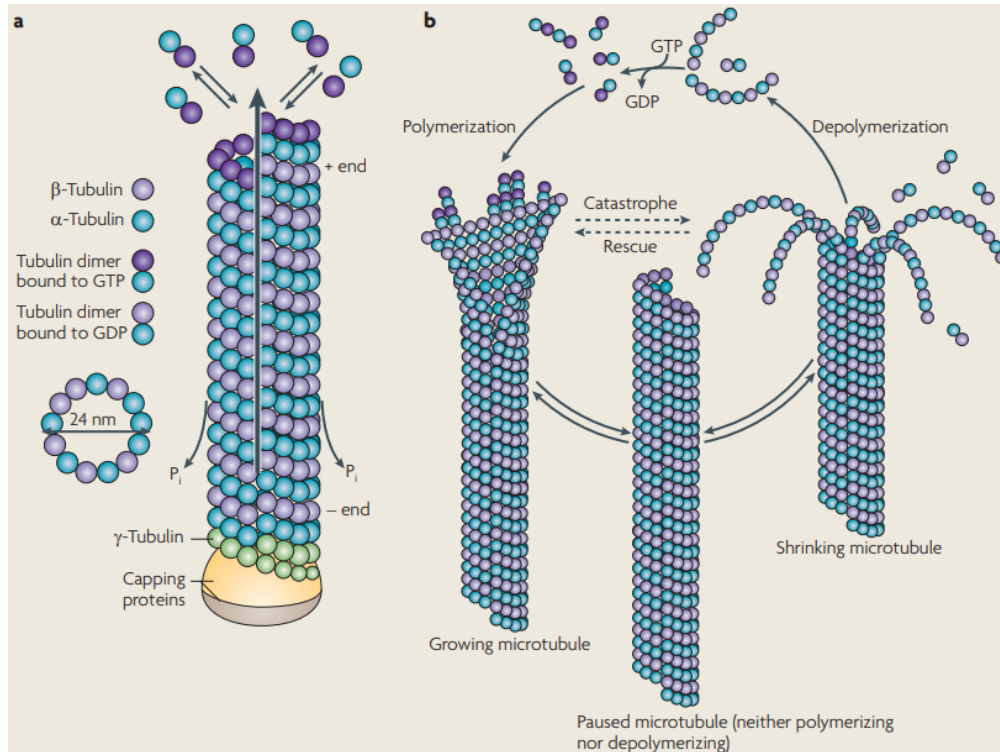


Figure 11: Microtubules are non-covalent cytoskeletal polymers that are found in all eukaryotic cells and play roles in mitosis, cell motility, intracellular transport, secretion, cell shape maintenance, and cell polarization. They are polarised structures made up of  $\alpha$ - and  $\beta$ -tubulin heterodimer subunits linked together to form linear protofilaments. A single microtubule is made up of 10-15 protofilaments (usually 13 in mammalian cells) that connect laterally to form a hollow cylinder 24 *nm* wide. Adapted from [54].

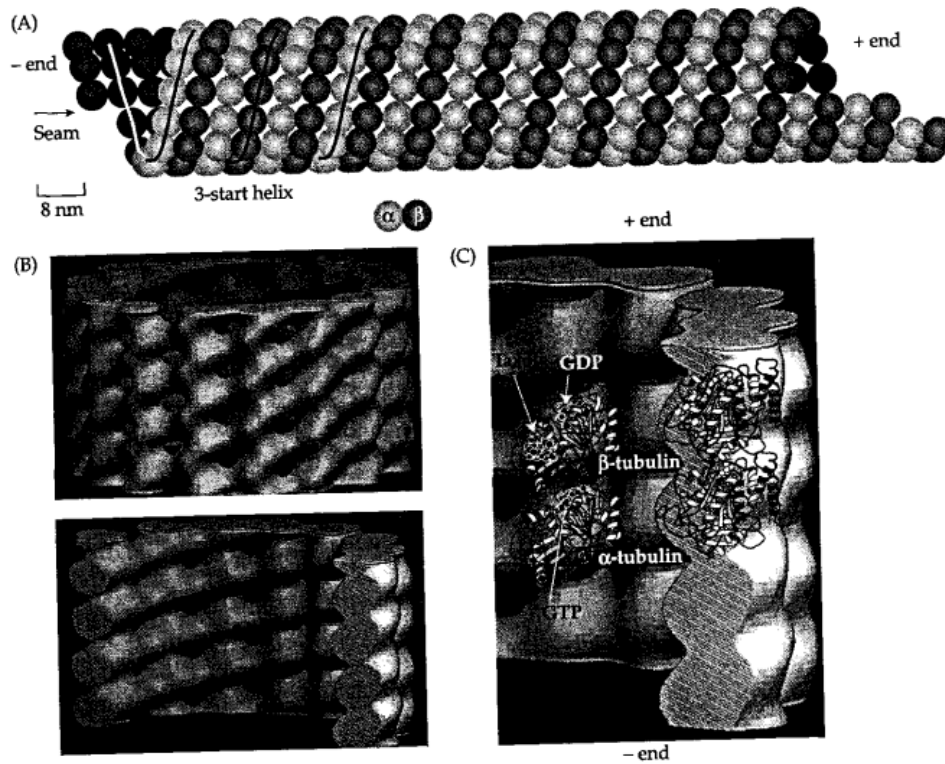


Figure 12: (A) A 3-start, 13-protofilament microtubule's lattice structure. The solid line represents one of the three-start helices. (B) Cryoelectron microscopy revealed a low-resolution structure of the microtubule. (C) A low-resolution atomic model of a microtubule showing the orientation of the dimer. Adapted from [24].

which are long, hollow tubes with an outer diameter of 25 nm. This cylindrical structure is made up of 13 protofilaments, each of which is made up of alternating  $\alpha$  and  $\beta$  tubulin molecules [55].

Both these monomers can bind one molecule of GTP. When bound to  $\alpha$  tubulin, GTP will never be exchanged or hydrolysed, while  $\beta$  tubulin bound GTP can undergo hydrolysis to produce GDP. This hydrolysis is important for microtubule dynamics Fig. 11. Both in interphase and mitosis microtubules often switch between phases of growth and shrinkage. This remarkable property was discovered in 1984 when Tim Mitchison and Marc Kirschner [56] deduced that microtubules switch from growth to shrinkage when they lose their GTP

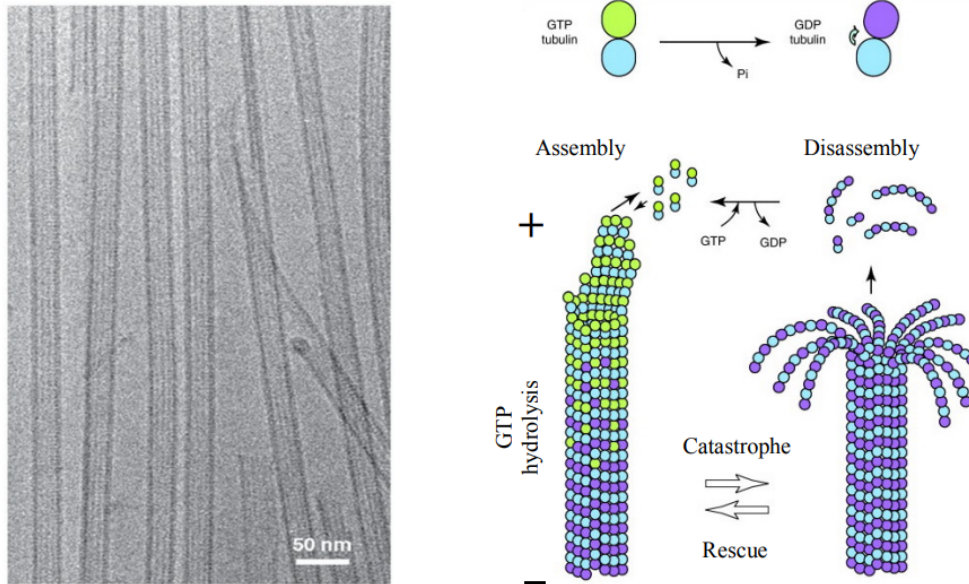


Figure 13: Left, microtubules as seen under electron microscope where their rod-like structure can be observed. Right, scheme of microtubules with depicted dynamic property. Exchange of GDP/GTP tubulin can be observed as process that determines switches between growth and shrinkage. Adapted from [57].

caps, that microtubules in vitro coexist in growing and shrinking populations, and that they change between growth and shrinkage only infrequently. This dynamic instability is a general property of microtubules and is thus fundamental in explaining cellular microtubule organization.

Microtubules possess intrinsic polarity with their minus ends embedded in MTOC, e.g. centrosome, while the (free) plus end is more dynamic and switches fast between growth and shrinkage, a.k.a. catastrophe, as can be seen in Fig. 11.

Microtubules grow when  $\alpha\beta$  tubulin collides with the end of a protofilament and forms a non-covalent bond. These collisions occur more frequently when the tubulin concentration is higher, and thus the growth rate increases linearly with more tubulin [58]. Microtubule ends with bound GTP are stable and polymerize, whereas ends containing GDP are unstable and depolymerise. In addition, there is a possibility for microtubules to switch from shrinkage

to growth in a process known as rescue (Fig. 11). Driving these processes are a host of microtubule-associated proteins (MAPs) that make microtubules grow faster, shrink slower, undergo catastrophe more often [59]. Dynamic instability is particularly frequent within microtubule populations that build up the mitotic spindle. Microtubules of the mitotic spindle are more dynamic than ones present in interphase, with complete exchange of spindle microtubules and soluble subunits occurring within seconds [60]. Already in 1950s Shinya Inoué [25] observed that spindles are made of aligned protein fibres that exist in rapid dynamic equilibrium with a pool of unassembled subunits. He proposed that spindle fibre disassembly generates force to move chromosomes. Indeed, once the nuclear envelope breaks down in prometaphase, chromosomes become free to establish contact with the growing microtubules via their kinetochores. These, kinetochore bound microtubules are called k-fibres and they generate forces on chromosomes throughout mitosis. During prophase, these forces direct the alignment of chromosomes to the metaphase plate and in anaphase they are directed to segregate chromosomes and pull them towards each pole of the spindle. There is also a way to modify the microtubule lattice which is important for microtubule behaviour. This group of reversible alterations is called postranslational modifications and has a role in structural variations of all newly synthesized proteins. These modifications affect protein's functional properties and for tubulin they occur on  $\alpha/\beta$  heterodimers of already polymerized stable microtubules. In this way dynamics, stability, distribution of microtubule populations in the spindle and interactions of microtubules with MAPS are finely tuned. For these variations some important modifications include polyamination, acetylation, methylation, phosphorylation and (de)tyrosination [55].

The length, strength, straightness, and polarity of a cytoskeletal filament are consequences of the packing of the subunits into the polymers. All three filaments are multi-stranded and high resolution electron micrographs show that there are extensive contacts between the protofilaments in actin filaments and microtubules. Intrastrand contact explains why filaments are so long, and why polymerisation and depolymerisation occur by monomer addition

and subtraction at the ends rather than by annealing and breakage of filaments. The actin and tubulin subunits fit snugly into their respective polymers such that the protein-protein interfaces in the filaments are well packed. As a result the filaments are stiff, with Young's moduli that approach the theoretical limit for materials held together by van der Waals bonds. The large, tubular cross-section of a microtubule suggests that this filament will have a much greater resistance to bending than the others. Measurements described in the next chapter show that this is indeed the case. The tubular arrangement also makes microtubules rather tolerant of lattice defects; an analogy can be made to a steel tube into which holes can be drilled without seriously weakening the structure. The filaments are straight because they are helically symmetrical (actin filaments, probably intermediate filaments) or nearly so (microtubules). Without this, filaments made of helical protofilaments would also be helical. With helical symmetry any intrinsic curvature in the individual protofilaments (i.e., any tendency to adopt a helical shape) is cancelled out. Although microtubules are not helically symmetrical due to the existence of seams, it and its subunits evidently have similar enough structures that the  $\alpha$ -type and  $\beta$ -type joins have similar mechanical properties and thus the filament can be regarded as quasi-symmetrical. Intermediate filaments may be helically symmetrical, though their structure is still uncertain. Actin filaments and microtubules are polar because the subunits are arranged head-to-tail in the protofilaments, and the protofilaments are parallel (rather than antiparallel). Polarity has two important consequences. First, polymerisation is expected to be kinetically faster at one end than the other: The end with the faster kinetics is called the plus end, whereas the other end is called the minus end. second, the surfaces of the filaments are asymmetrical. An analogy can be made to the coat of a short-haired cat which is smooth to stroke in one direction but rough in the other. The asymmetry of the actin filament is revealed by decoration with myosin head fragments in the absence of ATP (Fig. 14).

The "arrows" point away from the "barbed" plus end toward the "pointed" minus end. Asymmetry is essential for the unidirectional movement of motor proteins along actin fila-

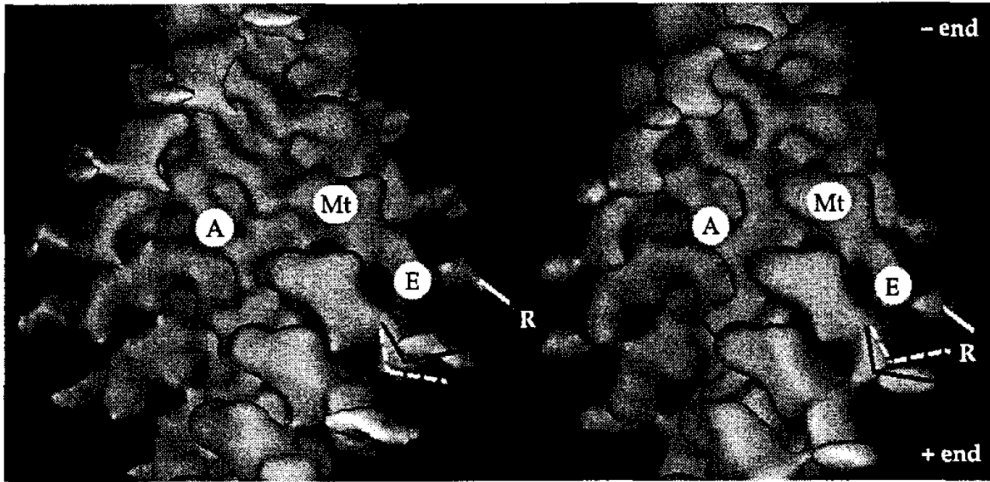


Figure 14: Rotation of myosin's light-chain binding domain. Cryoelectron micrographs of actin decorated with the S1 fragment of chicken smooth muscle myosin. The left-hand image is in the presence of ADP and the right-hand one is in the absence of nucleotide. The assignments of the actin monomer (A), the motor subdomain (microtubule), and the essential (E) and regulatory (R) light chains of the light-chain binding domain are made by fitting the atomic structures to the helically averaged electron microscopic images. The dissociation of ADP is associated with a movement of the distal tip of the light-chain binding domain through 35 nm toward the plus end of the actin filament (bottom). The black and dashed lines denote the positions of the essential and regulatory light chains in the two different nucleotide conditions. Adapted from [24].

ments and microtubules. Intermediate filaments may not be polar. Indeed, the homopolymeric intermediate filaments such as desmin and vimentin are almost certainly not polar because the antiparallel arrangement of the coiled-coil dimers in the tetramer produces a symmetrical protofilament, which in turn will lead to a symmetrical, monopolar filament. By the same argument the heteromeric keratin intermediate filaments are also likely to be nonpolar. The acidic and basic chains form a heterodimeric coiled coil but, like vimentin, the two coiled coils in the tetramer are arranged in an antiparallel fashion, while neurofilaments are polar. They are composed of three classes of neurofilament  $\alpha$ -protein, which form polar tetramers [61]. No intermediate filament motors are known, and this may be due to their lack of polarity. The structures of the cytoskeletal polymers reveal filaments that resemble cables (microfilaments), pipes (microtubules), and rope (intermediate filaments).

### 1.2.2 Motor proteins

Motor proteins are enzymes that convert the chemical energy derived from the hydrolysis of ATP into mechanical work used to drive cell motility. The widely accepted framework for understanding this chemomechanical transduction process is the rotating crossbridge model, shown in Fig. 15.

The model contains two key ideas: First, the motor cycles between attached and detached states. Second, while attached, the motor undergoes a conformational change (the working stroke) that moves the load-bearing region of the motor in a specific direction along the filament. If recovery takes place during the detached phase of the cycle, there will be a net displacement of the motor toward its next binding site on the filament. Motor proteins move across cytoskeleton and actively organize cell's interior. By using energy, they make traffic of all intracellular components possible. Transport inside the cell requires forces to move and position various molecular assemblies and organelles. These forces are mostly generated by motor proteins such as myosin, kinesin and dynein. To exert forces, motor proteins bind with one end to cytoskeletal filaments and with the other end to the cell

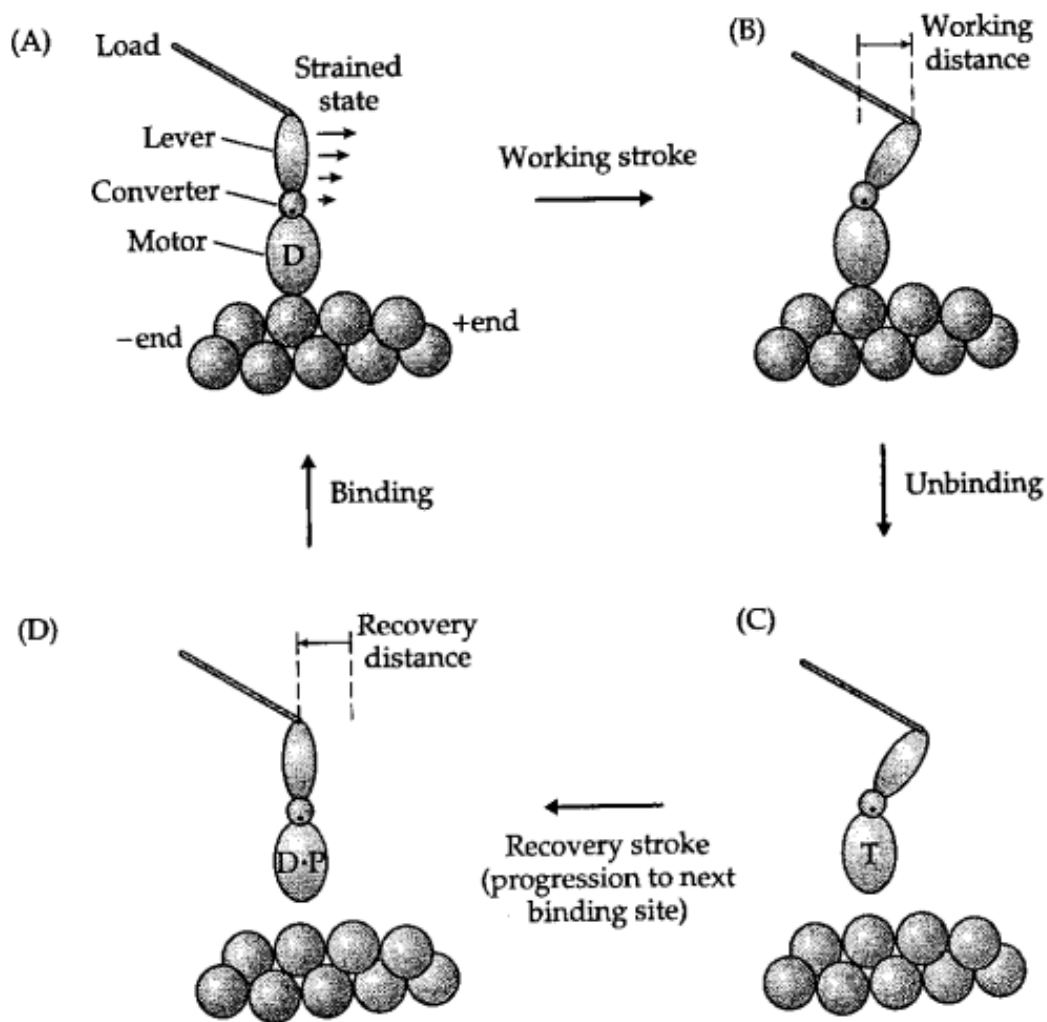


Figure 15: The rotating crossbridge model for myosin. (A) The binding of myosin to the actin filament catalyses the release of phosphate from the motor domain and induces the formation of a highly strained ADP state. (B) The strain drives the rotation of the converter domain, which is connected to a lever domain that amplifies the motion, moving the load through the working distance. (C) Following ADP release, ATP binds to the motor domain and causes dissociation of myosin from the actin filament. (D) while dissociated, the cross-bridge recovers to its initial conformation, and this recovery moves the motor toward its next binding site on the filament. T = ATP, D = ADP, P = Pi. Adapted from [24].



cortex, a vesicle or another motor [62] . Whilst myosins are associated with contractile activity in muscle and nonmuscle cells, kinesins and dyneins are microtubule motor proteins. Cytoskeletal motor proteins use structural changes in their nucleoside-triphosphate-binding sites to produce cyclic interactions with a partner protein. Further on, each cycle of binding and release must propel them forward in a single direction along a filament to a new binding site on the same filament. For such unidirectional motion, a motor protein must use the energy derived from ATP binding and hydrolysis to force a large movement in part of the protein molecule [55] (Fig. 16). The organization of microtubules into the highly ordered bipolar array of the mitotic spindle depends on activities of numerous motor and non-motor microtubule-associated proteins. Motor proteins have received significant attention because they generate force on microtubules during spindle formation and throughout mitosis. In that way, motor proteins actively walk across microtubule fibres and direct their active movement, thus, for example, controlling the separation of mitotic spindle poles. Some of the motor proteins form oligomers that can crosslink adjacent microtubules, and in that way, they can move one microtubule relative to the other, with the direction of movement dependent on the polarity of both motor protein and microtubules. Alternatively, such motor proteins can slide antiparallel microtubules past each other in the overlap zone of the spindle. There are approximately 14 families of kinesin-related proteins. Most of them walk towards plus end of the microtubule, but in addition to this behaviour, some walk towards the minus end, and some depolymerise microtubules. At the cellular level, kinesin motors perform a variety of functions during cell division and within the mitotic spindle where they help chromosomes get incorporated and segregated with the highest fidelity possible [63]. Their structure can roughly be summarized in having two heavy chains and two light chains per active motor, two globular head motor domains, and an elongated coiled-coil responsible for heavy chain dimerisation. Most kinesins have a binding site in the tail for either a membrane organelle or another microtubule, thus giving them specific roles in mitotic and meiotic spindle formation and chromosome separation during cell division. The fastest kinesins can

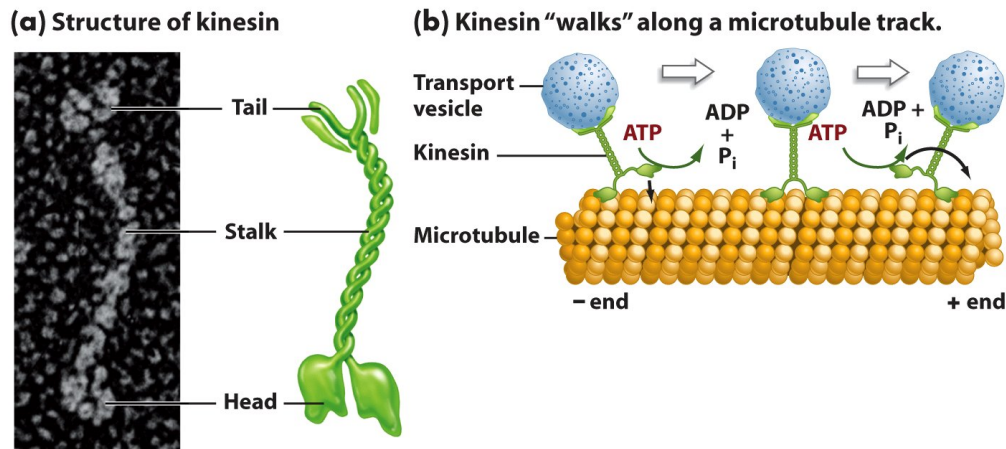


Figure 16: a) Electron microscope image of a kinesin motor with head and tail domain as it was walking along the microtubule [64]. b) Scheme of a microtubule with attached motor proteins kinesin and dynein and the preferred direction of their movement where + and - indicate the orientation of microtubule. Image in public domain, authored by Pearson Prentice Hall.

move their microtubules at about 2-3  $\mu\text{m}/\text{sec}$  [55]. Dyneins are a family of minus-end-directed microtubule motors and are unrelated to kinesin superfamily. They are composed of two or three heavy chains, including motor domain, and a large and variable number of associated light chains. The dynein family has two major branches. Cytoplasmic dyneins are found in, probably all eukaryotic cells. They have a role in vesicle trafficking and in localization of the Golgi apparatus near the centre of the cell. Other branch contains the axonemal dyneins which are highly specialized for the rapid and efficient sliding movements of microtubules that drive the beating of cilia and flagella, as well as of one's orchestrating mitosis. Dyneins are the largest of the known molecular motors, and they are also among the fastest with the ability to move their microtubules at the remarkable rate of 14  $\mu\text{m}/\text{sec}$  [55].

### 1.2.3 Microtubule dynamics as force generators

Chromosomes in the mitotic spindle take up a great deal of its volume, and they are susceptible to deformations. To correctly separate them during cell division, the spindle must

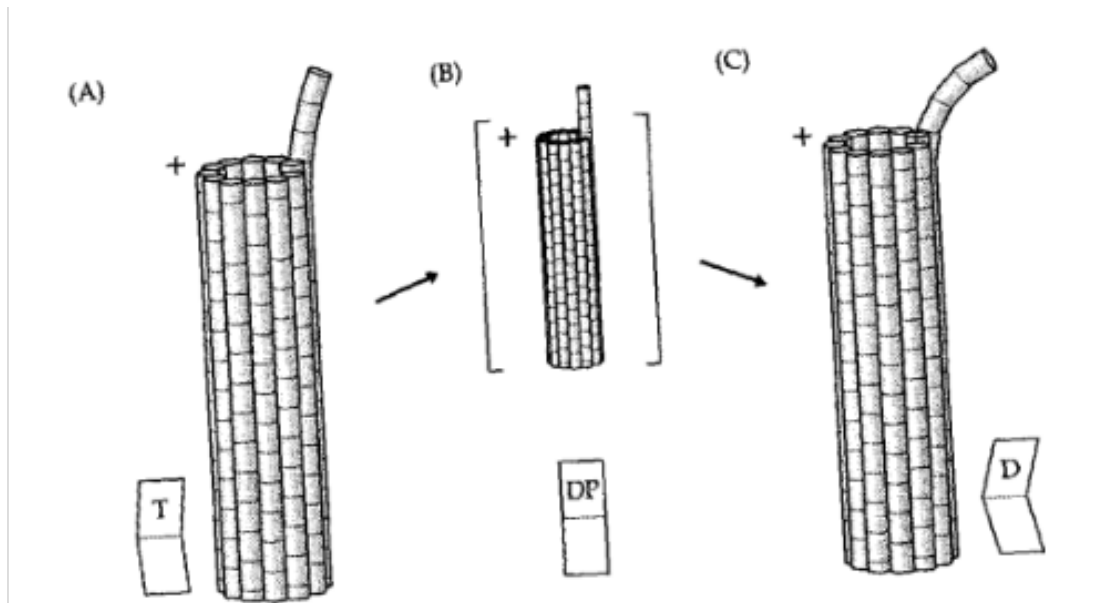


Figure 17: Structural changes accompanying GTP hydrolysis in microtubules. If the particular GTP-subunit is only slightly curved, the resulting protofilament need only be slightly deformed when it is in the straight wall of the microtubule (A). If, following polymerisation, the subunit changes to a very curved GDP-state, then it will be very unstable in the microtubule wall, and so the GDP-microtubule will tend to depolymerise (B). If, however, the GDP P subunit is straighter still, then it will be stabilised by being in the wall of the microtubule (C). Thus, the transduction from GTP to GDP P will be accelerated after closure. It is in this way that polymerisation catalyses hydrolysis, as required for a coupled mechanism. Adapted from [24].

precisely regulated the forces acting upon them throughout the entirety of the process. These forces are generated not just due to the polymerisation and depolymerisation of microtubules [11], but also due to the actions of molecular motors, which can broadly be split into kinesins and dineins [65].

Microtubules in the mitotic spindle are in constant flux, both shrinking and growing through (de-)polymerisation. During these processes, energy is released through GTP hydrolysis (Fig. 17), thereby producing forces acting on the organelles the microtubules are in contact with.

Microtubules, which polymerise, grow in length by adding  $\alpha\beta$  dimers from their surround-

ings. When adding these dimers, the microtubule simultaneously gains  $5 - 10k_B T$  of energy per dimer. Furthermore, this means that a microtubule also grows  $8 \mu\text{m}$ , and generates a force of around  $50pN$  on the object which it touches during the polymerisation process. When it loses a dimer during de-polymerisation, the system releases a similar amount of energy. In both directions of this process the microtubule uses energy which was previously stored in the form of GTP by the cell, meaning that both process can do net work on cellular structures.

The first quantitative experiments investigating the amount of work microtubules do were made on *in vitro* microtubules which pushed cellular organelles [66]. The canonical model of microtubule dynamics is based on the process of Brownian ratcheting [67]. In this mechanism thermal fluctuations stochastically add new dimers of tubulin, regardless of whether the microtubule is freely growing or pushing an object. This leads to the frequency of adding new dimers dropping, meaning that the microtubule grows slower, and even the growth of microtubules ceasing completely after a critical force has been passed. In case the microtubule bundle acts with a force coming from polymerisation, not all microtubules in the bundle will be able to do work, because only those microtubules which are in contact with an object can generate forces. The forces generated by the depolymerisation of microtubules are not understood as well as those which arise from polymerisation, because they are preconditioned by the existence of a mechanical link between the microtubules and the cellular object upon such a force would act [68]. It is well established that this dynamic growth and shrinkage of microtubules has a significant contribution to the forces exerted on the kinetochores [21, 68–70]. The precisely regulated transition between microtubule bundle growth and shrinkage induces oscillations in the kinetochore, due to the action of dynein on the kinetochores microtubule [71–74]. The mechanical link between microtubules and the kinetochore occurs on the microtubule bundle’s (+) end, where it binds via the Ndc80 molecular complex [75]. In yeast cells, microtubule dynamics directly influence the positioning of the cell nucleus before mitosis, with the microtubules growing from a nucleation site interacting with the cell membrane [76], or being towed by bound dynein motors [66].

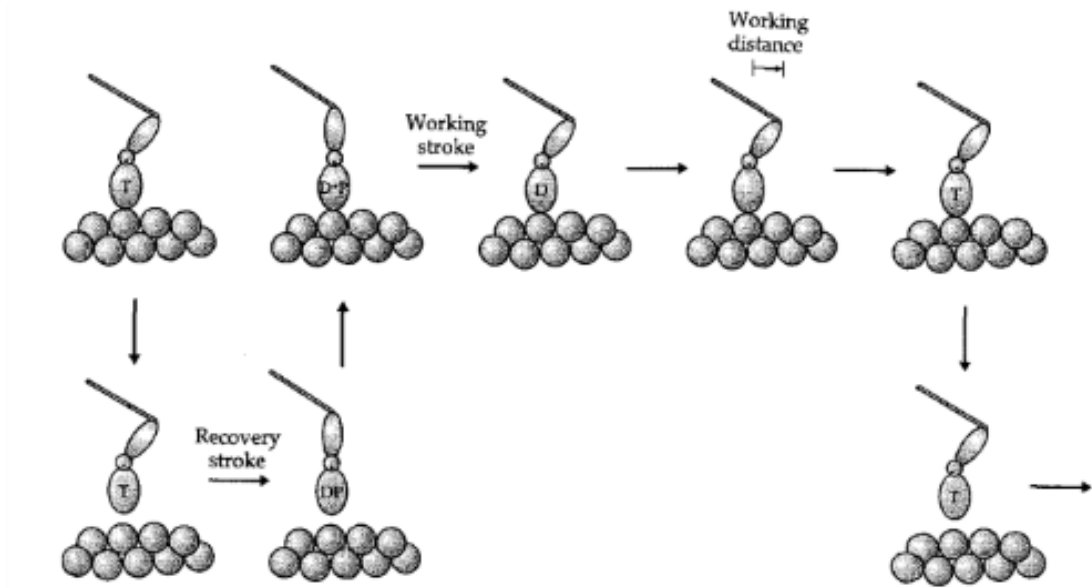


Figure 18: Structural model for myosin hydrolysis cycle. The working stroke occurs in the ADP state, and the recovery stroke occurs in the ADP.p, state. Adapted from [24].

#### 1.2.4 Motor proteins as force generators

The other main force generators are molecular motors, which can be broadly split into active and passive motors. Active motors use the energy released during ATP hydrolysis (Fig. 18) by moving neighbouring microtubules or other cellular organelles [65, 75]. Passive motor proteins, i.e., crosslinking proteins, connect with each other, but do not actively move themselves or other cellular structures. They are, effectively, a friction force for active molecular motors. The motor proteins can also regulate the speed of microtubule dynamics, which has been extensively studied on kinetochores and poles [76].

### 1.3 The current view on forces in the metaphase mitotic spindle

Metaphase, the state in which paired sister chromosomes balance at the centre of the spindle, is a natural starting point for a consideration of spindle biophysics because it is a stable steady-state. The metaphase spindle is highly dynamic, with large fluctuations and directed

fluxes in both physical and chemical processes, yet the average amount and position of all spindle components is constant over time. The stability of this steady-state is evident from the remarkable ability of metaphase spindles to correct transient fluctuations in morphology and position Fig. 19, and to recover from transient physical and chemical perturbations [31, 77–82].

The shape of the spindle and its likely filamentous organization was described by Flemming more than 125 years ago [83]. Polarization microscopy in the 1950s proved that spindles are built from filaments that run parallel to the direction of chromosome motion, which we will call the spindle axis [25].

Rapid assembly and disassembly of these filaments in response to physical and chemical perturbations lead Inoué and Sato to propose that their polymerization dynamics produce mechanical force, for example to power chromosome motion [84]. The filaments were identified as microtubules, non-covalent polymers of the protein tubulin, by a combination of biochemistry, pharmacology and electron microscopy [27, 85]. Today, it is known that the main structural element of the spindle is a lattice of oppositely oriented microtubules (Fig. 20) that undergo rapid polymerization and depolymerisation powered by GTP hydrolysis. Microtubules are made of 13 protofilaments. Spindle microtubules are organized in space, and their dynamics are regulated by proteins that include motor proteins [86] and microtubule-binding proteins [87].

The *term motor* protein refers to molecules in the kinesin and dynein families that use ATP hydrolysis energy to walk along microtubules. These generate sliding force between microtubules and other objects, and play a major role in force production (Fig. 21). The mitotic spindle in metaphase is in quasi-static equilibrium. The chromosomes maintain their position along the equatorial plane during the metaphase phase of the cell cycle, implying that there is a fixed distance between this plane and the poles. Meanwhile, the mitotic spindle remains nearly stationary in relation to the cell and its membrane [19, 88]. Because the metaphase spindle can be modelled as a static object, it is ideal for investigating the

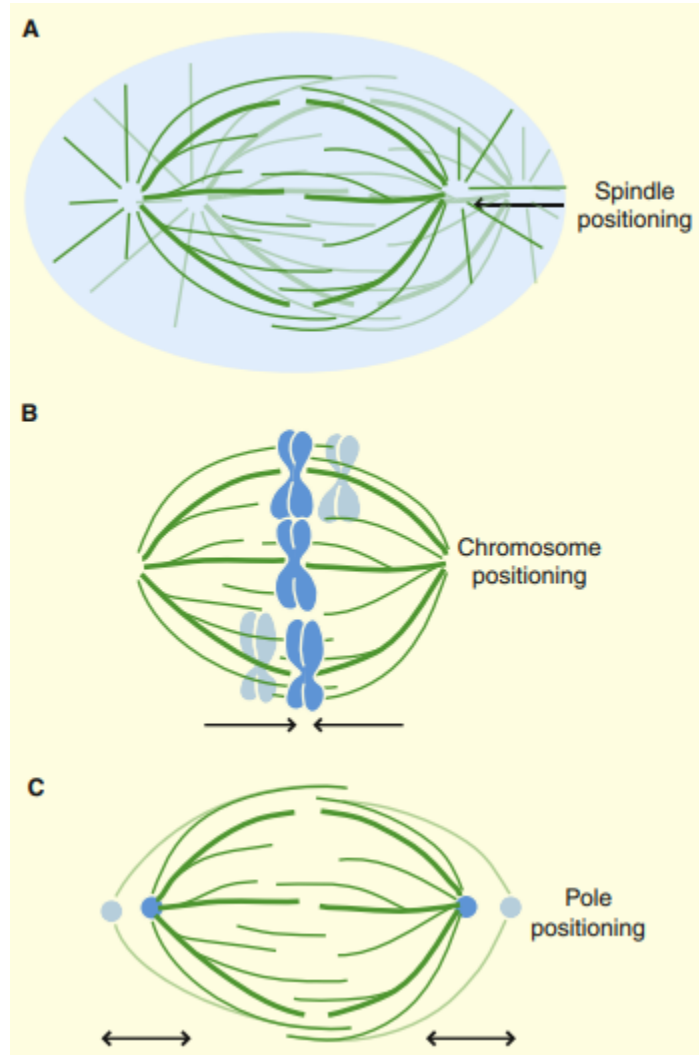


Figure 19: Three steady-states in position are reached during metaphase. Position-dependent forces (black arrows) must help reach the steady-state positions and correct any deviations (fainter colors) from them. (A) During symmetrical cell division, the spindle (green) must be positioned at the centre of the cell (blue). (B) The chromosomes (blue) must be placed in the middle of the two poles. (C) The spindle poles (blue) must be positioned a certain distance away from each other (and the chromosomes) to dictate spindle length. The three steady-state positions are critical in determining where the sister chromosomes will travel after anaphase and thus essential to accurate chromosome segregation. Adapted from [19].

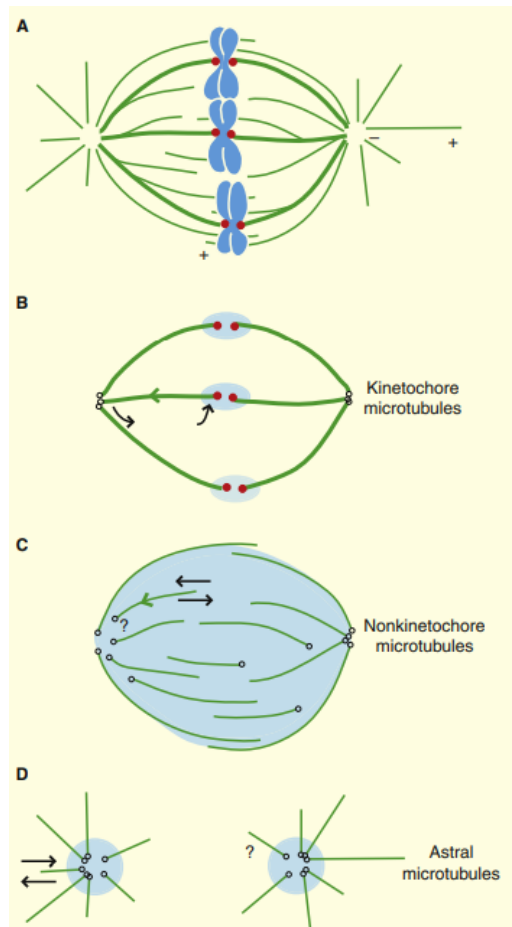


Figure 20: Microtubule architecture and dynamics in the mitotic metaphase spindle of mammalian cells. (A) Architecture of the mammalian mitotic spindle: microtubules (green), sister chromosomes (blue) and kinetochores (red) for attachment of chromosomes to microtubules. (B–D) Three classes of microtubules within the spindle, with different minus-end locations (empty black circles), dynamics (black arrows) and nucleation zones (blue). (B) Kinetochores microtubules continuously slide toward the pole (green arrow), polymerize at the kinetochore and depolymerise at the pole. Kinetochores microtubules form larger bundles (thicker green line) and have much longer lifetimes than the other two classes of microtubules. (C) Nonkinetochores microtubules are nucleated throughout the spindle, and continuously slide poleward (green arrow) with dynamic plus-ends and unprobed minus-ends. (D) Astral microtubules are nucleated at centrosomes, don't slide, have dynamic plus-ends and fixed minus-ends. Astral microtubules may also overlap with other microtubules (question mark). Adapted from [19].



balance of forces and torques in the mitotic spindle due to its stability in space and time [43, 89]. Metaphase forces are broadly classified as active, passive, and reaction forces. Because the metaphase mitotic spindle is static, forces acting on it must be balanced both locally and globally. The spindle is made of molecules (mostly proteins, but see [90, 91]) and subject to chemical influences, but here we will view it as an intrinsically mechanical object. Mechanical forces aid spindle assembly [92], move chromosomes within it [92, 93], stabilize [94] and correct [95] the attachment of chromosomes to microtubules, and regulate anaphase entry [96]. Spindle forces are produced by molecular motors, microtubule assembly dynamics, elastic elements, and friction (Fig. 20), because the structure is in a steady state, the action of these forces on any mechanically independent spindle component must integrate to zero. The majority of integrated spindle forces are position-dependent, allowing them to position objects in specific locations. At least three positioning tasks must be completed in order to generate the metaphase spindle: within the cell, the spindle positions (Fig. 19), typically near the centre of the longest axis [97–99] the chromosomes align at the centre of the spindle Fig. 19, generating the arrangement called the *metaphase plate* [100]; and the poles position a certain distance from each other (or perhaps from the chromosomes), thereby determining spindle length (Fig. 19).

Metaphase mitotic spindles of most biological cells have microtubules which group themselves into bundles of around 15-30 microtubules [38, 42, 101, 102], the kinetochore fibres or k-fibres for short, which connect to a single kinetochore. In other words, because a kinetochore has connecting k-fibres coming to it from both poles, and the interactions between different k-fibres are weak [31, 103], we can regard k-fibres as one continuous bundle extending from one pole to the other [16, 104]. In mammalian cell, interpolar microtubules group into interpolar fibres, made up of 2 - 7 microtubules [62, 105], which are crucial for maintaining the bipolarity of the spindle and a constant separation distance between the poles [19]. In the mammalian spindle, kinetochore-fibres (k-fibres) are bundles of microtubules [104–106] that connect chromosomes to spindles poles, ultimately moving chromosomes to poles and

future daughter cells. To do so, k-fibres must maintain their connection to the dynamic spindle. The k-fibre's connection (anchorage) to the spindle is mediated by a dense mesh-like network of non-kinetochore microtubules (non-kMTs) which connect to k-fibres along their length [62, 106] via both motor and non-motor proteins. Astral microtubules represent a small percentage of the total number of microtubules, and forming no bundles [19, 43].

To achieve force balance, the metaphase mitotic spindle must maintain a precise distribution of forces arising from polymerisation, depolymerisation, motor proteins, and fibre movements, which when added together vanishes, presenting an interesting conundrum for a living cell to solve [107].

### 1.3.1 Mapping the forces in the metaphase spindle

Even though in-depth knowledge of a great deal of motor proteins has been gained, how they function and the manner in which they produce forces has been gained, little is, however, known of how it all fits together and produces a balance of forces and torques in the whole mitotic spindle. During the metaphase, paired sister chromosomes balance at the centre of the spindle, making metaphase a natural starting point for exploring the physics of the spindle, because it is a stable steady-state. The metaphase spindle is highly dynamic, with large fluctuations and directed fluxes in both physical and chemical processes. If these fluctuations are averaged throughout time, however, they are almost constant. The stability of this steady-state is evident from the remarkable ability of metaphase spindles to correct transient fluctuations in morphology and position, and to recover from transient physical and chemical perturbations.

Most animal spindles can be thought of as a superposition of kinetochore, non-kinetochore and astral microtubules that differ in their architecture, dynamics and function, though they all assemble from the same pool of tubulin subunits Fig. 20.

Kinetochore microtubules (Fig. 22) have plus-ends embedded in kinetochores (protein structures where microtubules attach to chromosomes) and minus-ends at or near poles [104].

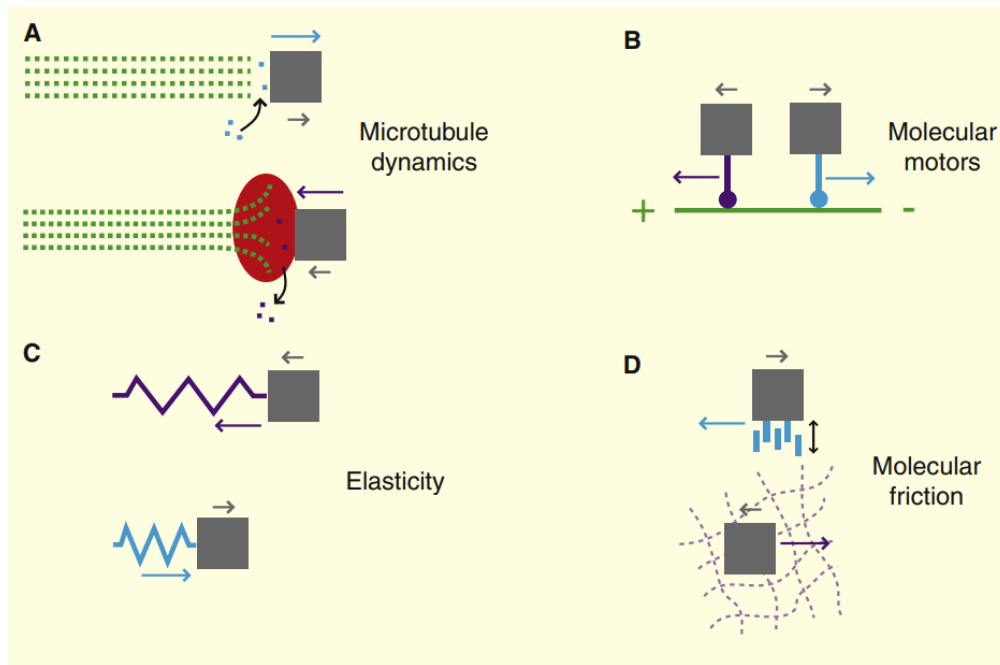


Figure 21: Molecular force generator locations in the metaphase spindle. Arrows represent the object's (square) direction, movement (small arrows) and knowledge force (large arrows) (large arrows). Microtubules (A) (green) assembling (top) and disassembling (bottom) can either push or pull an object. To connect disassembly and object movement, it is necessary to include a connecting element (red ellipse). (B) A molecular motor can provide power to an object, movement toward the plus-ends of microtubules (blue) or minus-ends (blue). (C) A stretchy spring element can pull objects inward, when stretched or pushed outward when compacted. (D) Friction forces are in opposition, movement. They can be produced by bonding, breakage (top, blue bonds moving up and to the right) down) as well as mesh reorganisation (bottom) necessary for object movement. Adapted from [19].

Their main functions are to exert pulling forces on chromosomes at kinetochores and to silence the spindle assembly checkpoint signal that is generated by unattached kinetochores. Some types of spindles may lack one of the other microtubule classes, but K-MTs appear to be indispensable to spindle function. In mammalian cells, each chromosome has one kinetochore that binds to the plus-ends of 10–30 K-MTs [33, 108, 109], and most extend continuously from kinetochore to pole [104]. The K-MTs attached to a single kinetochore tend to bundle with each other and with an approximately equal number of nonkinetochore microtubules [104], to form a kinetochore fibre (k-fibre) that is prominent in light level micrographs. Within a k-fibre, microtubules are evenly spaced, 50–100 nm apart [104], and they behave as one mechanical unit upon physical manipulation [110]. Interactions between k-fibres are weak, except at the poles where they converge [31, 103, 111]. K-MTs probably have two origins, capture of plus-ends of microtubules from the other two classes [112], and direct nucleation at kinetochores followed by integration into the spindle [113]. The blue zones in Fig. 20 illustrate the K-microtubule nucleation potential. K-MTs turnover much more slowly than the other microtubule classes, presumably because both ends are capped, with a half-life of around 7 min in metaphase spindles [114]. Complete replacement of K-MTs presumably requires that their plus-ends detach from the kinetochore. K-MTs turnover while remaining attached by polymerizing at kinetochores (Fig. 20), sliding toward the pole at  $0.5 \mu\text{m}/\text{min}$  (green arrow) [115], and depolymerizing at poles (black arrow). In mammalian spindles, the instantaneous polymerization rate at kinetochores is quite variable, because chromosomes oscillate around their mean position on the metaphase plate. Sliding and depolymerisation rates appear rather constant from published data [116], though they have yet to be measured with high accuracy. Polymerisation, sliding and depolymerisation must precisely balance at steady-state, but how precisely this occurs is an unsolved part of the question of spindle length regulation.

Nonkinetochore microtubules (nK-MTs), depicted in Fig. 20, collectively span the region from one spindle pole to the other and comprise all microtubules other than K-MTs

(nK-MTs have also been referred to as interpolar microtubules) [62]. The nK-MTs comprise the majority of microtubules in mammalian spindles that have been studied by electron microscopy. During metaphase, they bundle together 30–50 nm apart in groups of 2–6, with anti-parallel interactions apparently preferred [62]. The function of nK-MTs is poorly understood. Since they are the majority class of microtubules and interact in an anti-parallel fashion, they are thought to help integrate the whole spindle and keep the poles apart, i.e. to ensure its bipolarity. Arguing in favor of this role, bipolar meiotic spindles can assemble from nK-MTs alone in *Xenopus* egg extract [117]. Contrary to many textbook models, the minus-ends of most nK-MTs are not simply located at poles, but rather throughout the spindle [63]; many nK-MTs have minus-ends embedded in k-fibres, where they presumably couple mechanically to K-MTs [62]. Most of our understanding of nK-microtubule dynamics comes from *Xenopus* egg extract spindles, where nK-MTs comprise over 90% of all microtubules. Nucleation of nK-MTs is thought to occur throughout the spindle [118], as indicated by the blue shaded zone in Fig. 20. nK-MTs turnover very rapidly [119], presumably by dynamic instability of plus-ends. Sliding velocities in *Xenopus* extract spindles have been measured by speckle imaging and single molecule imaging. All nK-MTs slide poleward at an average velocity of 2  $\mu\text{m}/\text{min}$ , though sliding velocities vary greatly even between nearby microtubules, [120], indicating that lateral cross-links in the spindle must be weak and/or dynamic. Sliding velocity decreases away from the metaphase plate, implying that poles may form where the sliding velocity reaches zero [121]. A velocity gradient of this magnitude is only possible if nK-MTs are short in comparison to the length of the *Xenopus* meiotic half-spindle, which is most likely the case, though quantitative electron microscopy data are lacking. Much less is known about the dynamics of nK-microtubules in mammalian spindles, in part due to their rapid turnover, which makes photo-marking difficult.

The minus ends of astral microtubules are attached to centrosomes, where they are nucleated. Many of their plus-ends extend toward the cortex and are thought to mediate one of  $\alpha$ -MTs' key functions, which is to position the spindle within the cell [122], and  $\alpha$ -MTs

presumably extend into the spindle as well. These are very obvious in *Caenorhabditis elegans* embryonic spindles that lack nK-MTs [123], However, they are difficult to distinguish from nK-MTs in mammalian cells.  $\alpha$ -MTs turnover at a rate comparable to nK-MTs, and turnover by dynamic instability of plus-ends has been visualised for the subset of  $\alpha$ -MTs that elongate away from the spindle, with growth and shrinkage rates of 10-15  $\mu\text{m}/\text{min}$  [124].  $\alpha$ -microtubule minus-ends are thought to be capped by  $\gamma$ -tubulin complexes at the centrosomes and do not appear to slide [125].

## 1.4 Bridging fibres and their effect on metaphase force-balance

### 1.4.1 The existence of bridging microtubules

Interpolar microtubules are located in the vicinity of k-fibres, which suggested that they interact with neighbouring k-fibres [36, 62, 110, 138, 139]. It has been also proposed that some level of mechanical coupling between these two types of microtubules exists [140–142]. The present textbook picture of the spindle still depicts these two subsets of microtubules as spatially separate and puts the origin of the pulling force on the k-fibres [11]. Recently, these interpolar microtubules were the focus of a study that discusses their interaction with k-fibres and might explain the spindle force distribution paradox. In [33] a bundle of antiparallel non-kinetochore microtubules, named the 'bridging fibre', was shown to link sister k-fibres in metaphase (Fig. 25).

The bridging fibre moves together with the sister k-fibres it is adjacent to, implying that they form a single mechanical entity whose role is to balance the tension between sister kinetochores and the compression at the spindle pole [33, 143, 144]. The postcut relaxation of the interkinetochore tension is dependent on the size of the released k-fibre stub, according to laser ablation at various distances from the kinetochore [33, 144].

Longer stubs maintain tension because they remain connected to the bridging fibre, whereas shorter stubs relax tension because they lose their connection to the bridging fi-

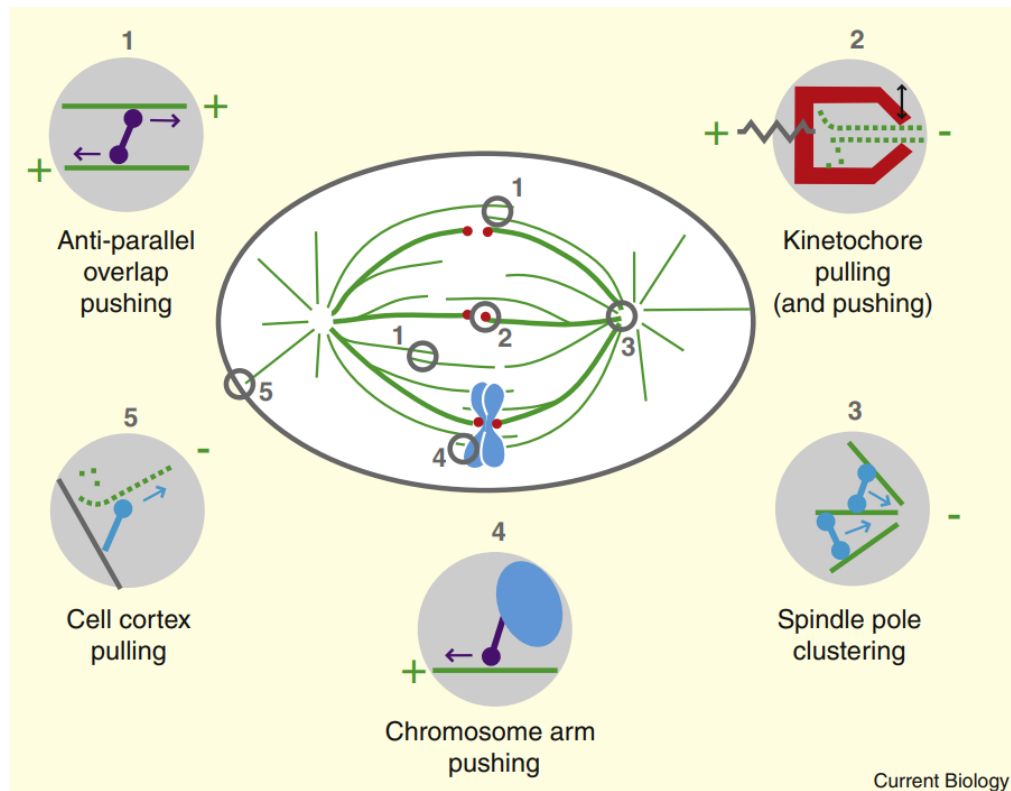


Figure 22: Molecular force generator action sites in the metaphase spindle (1) Microtubule cross-linking motors are active wherever anti-parallel microtubules overlap. This location is shown both near and far from the metaphase plate. Kinesin-5 family members push microtubules apart: this is the best understood outward force and is required for the establishment of bipolarity in most spindles. [121, 126]. *C. elegans* embryonic spindles largely lack nK-MTs and do not require this force [127]. (2) At kinetochores, where microtubules disassemble and pull (and assemble and may push), and Ndc80 (red arms) is thought to provide microtubule attachment. The elastic centromere (spring) is deformed [128] in this region and friction (double arrow) occurs. Plus- and minus-end motors (e.g., Cenp-E and Dynein) can also operate here, as can microtubule depolymerases (e.g., MCAK and Kif18) and other end-binding proteins [86, 92, 129–131]. (3) At the poles, dynein and/or minus-end kinesins organize and focus minus-ends, presumably by holding on to one microtubule while moving on another [132]. K-MTs depolymerise at poles (depolymerases may be involved [133]), and whether this generates pulling forces has been suggested [116, 134] but not directly measured. (4) On chromosome arms, plus-end-directed chromokinesins (e.g., Kid [135]) push microtubules, exerting away-from-the-pole force (polar ejection force [136]). (5) At the cortex, dynein pulls on  $\alpha$ -MTs, and may be the main spindle-centering force in mammalian cells [137]. How motor activity is coupled to depolymerisation (and polymerisation) at the cortex is unclear. Adapted from [19].

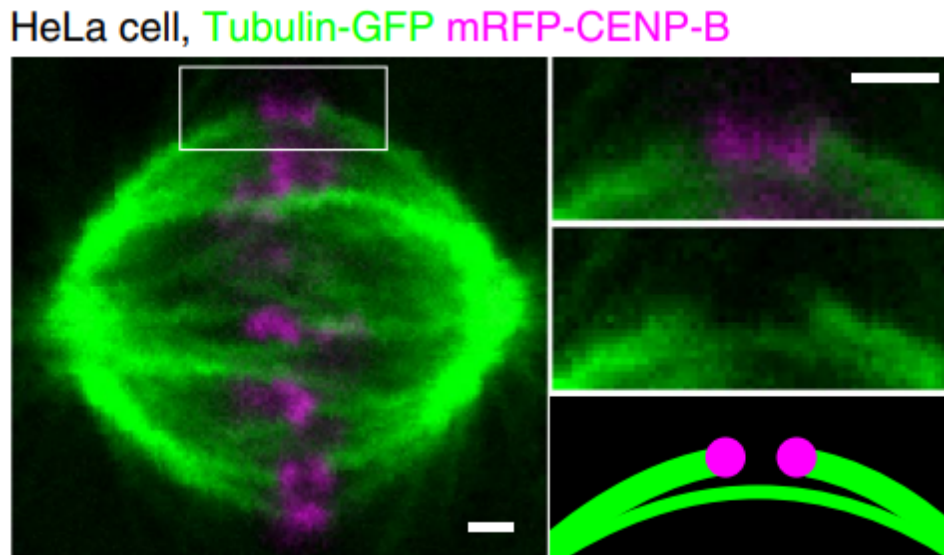


Figure 23: Spindle in a HeLa cell expressing tubulin-GFP (green) and mRFP-CENP-B (magenta). Enlargements of the boxed region (top: merge, middle: GFP, bottom: scheme) show a bridging fibre connecting sister k-fibres. Adapted from [33].

bre. This explained the disparity in previously published data reporting different responses of interkinetochore tension to laser ablation in various cell types [113, 145, 146].

The discovery of the bridging fibre and its potential contribution to force organisation in the metaphase spindle raises the question of how and when this complex mechanical entity made up of k-fibres, bridging fibres, and sister kinetochores is assembled.

The known mechanisms for spindle assembly and chromosome movements during prometaphase can be described with the two general scenarios of how this structure can be assembled, named the 'Bridge first' and 'K-fibre first' scenarios, because these three elements first come into contact in prometaphase following nuclear envelope breakdown [147]. (Fig. 27).

In the 'Bridge first' scenario, kinetochores first interact with overlapping bundles that become bridging fibres before attaching to sister kinetochores and becoming bioriented. Kinetochores are bioriented by k-fibres prior to the assembly of the bridging fibre in the 'K-fibre first' scenario. The observation that not all chromosomes establish an interaction with spindle mi-



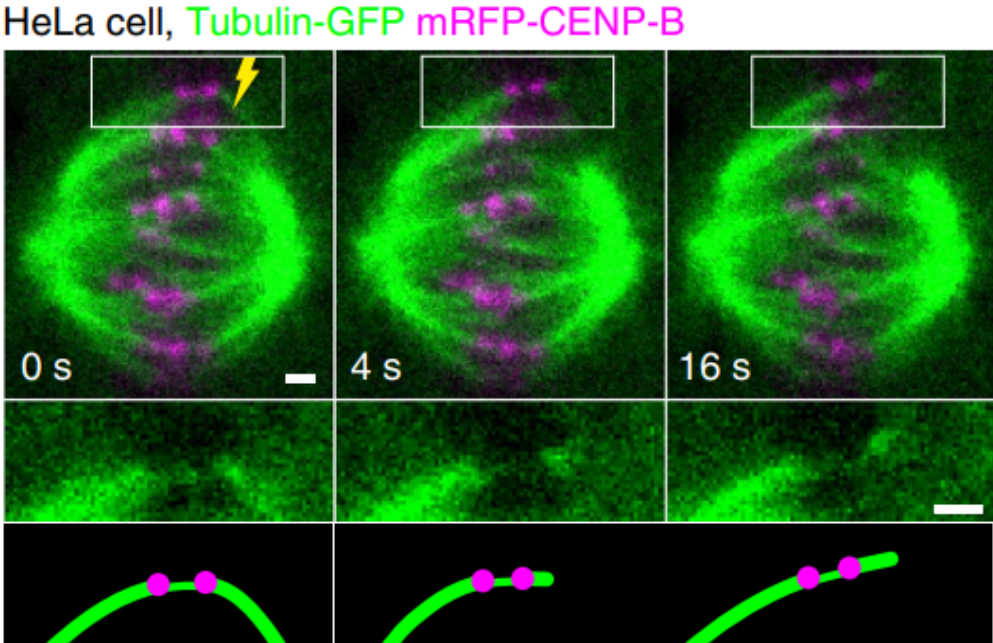


Figure 24: Time-lapse images of the spindle (top) in a HeLa cell as in Fig. 23, and enlargements of the boxed region (middle: GFP, bottom: schemes). After the cut (yellow), the bridging fibre moved together with sister kinetochores Adapted from [33].

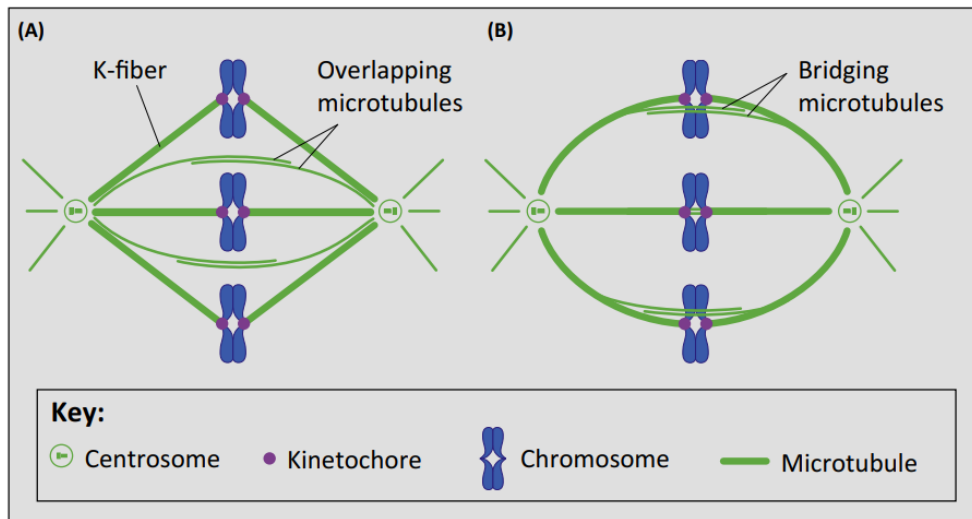


Figure 25: Diagrams of the Classic and New Views of the Mitotic Spindle (A) The k-fibres in the tensed k-fibre model of the mitotic spindle are expected to be straight, originate at the poles, and terminate at the kinetochores. Interpolar microtubules are curved, originate at opposite poles, and form antiparallel overlap zones in the spindle's centre, where they do not interact with k-fibres. (B) Along the length of the spindle, k-fibres interact with interpolar microtubules in the new model discussed here. Interpolar microtubules are referred to as "bridging fibres" because they serve as a link between sister k-fibres. The outer k-fibres and their bridging fibre are curved, whereas the inner ones are straight. For clarity, nonbridging interpolar microtubules have been omitted. Adapted from [143].

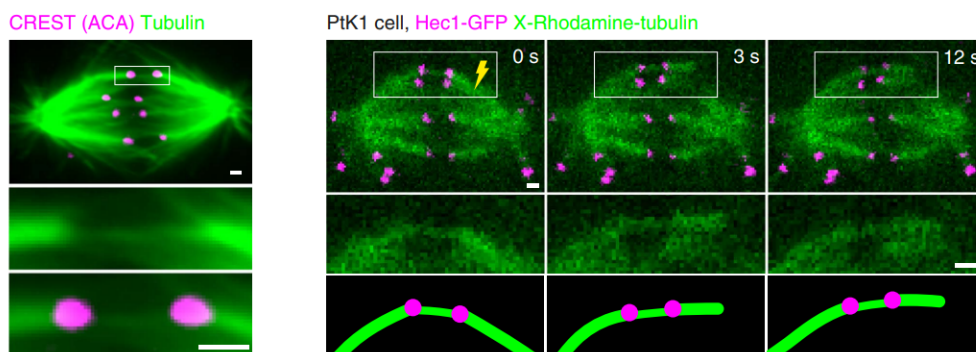


Figure 26: Spindle in a PtK1 cell (top) immunostained for tubulin (green) and kinetochores (magenta). Enlargements of the boxed region (middle: tubulin, bottom: merge) show a bridging fibre between sister kinetochores. Laser-cutting in a PtK1 cell with Hec1-GFP (magenta) and X-Rhodamine-tubulin (green). Adapted from [33].

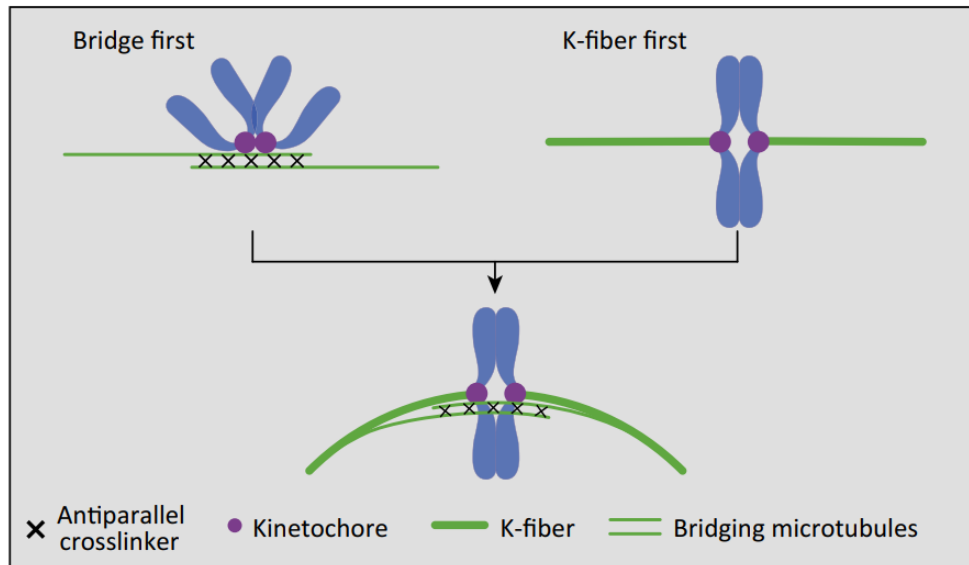


Figure 27: The chromosome first interacts with an overlap bundle in the 'Bridge first' scenario. After the chromosome is attached by two sister k-fibres, this bundle will become the bridging fibre. The chromosome is first bioriented by two k-fibres in the 'K-fibre first' scenario, and then the bridging fibre is acquired. Adapted from [143].

Microtubules from the same starting position relative to the spindle poles is also important for our discussion; some chromosomes are closer to one of the poles, whereas others are closer to the future metaphase plate [148]. This initial position impacts how the chromosome interacts with the microtubules, which could determine which of the described scenarios is more plausible. In contrast, it has been demonstrated that chromosomes in the equatorial plane can become bioriented without CENP-E or dynein activity, implying that rapid end-on attachment of k-fibres is the mechanism for their congression [102, 148]. Moreover, the inhibition of k-fibre formation resulted in decreased stability of the kinetochore– microtubule attachment, with kinetochores tumbling during congression and chromosomes periodically moving poleward during metaphase [149]. However, rapid biorientation by k-fibres in a crowded space such as the central part of the spindle with many chromosomes shielding each other from direct contact with microtubules does not seem to be likely, making the 'bridge-first' scenario a more likely candidate [150, 151]. For a more detailed analysis of the origins of bridging

fibres, see [143].

### 1.4.2 Bridging microtubules connect kinetochore pairs

The tension on the kinetochore is balanced by compression in the bridging fibre. Theory and experiments predict the force balance in the k-fibre and the bridging fibre. The segment of the k-fibre between the junction and the kinetochore (magenta) is under tension, while the bundle consisting of the segment of the k-fibre and the bridging fibre between the pole and the junction (black), as well as the central part of the bridging fibre between the two junctions (green), is under compression. The central part of the bridging fibre balances the forces acting at the pole and at the kinetochore, allowing tension and compression to coexist within a single k-fibre. (Fig. 28). Rods can represent microtubule bundles because they are stiff, and the rope to symbolize the feeble chromatin. The current paradigm, in which sister k-fibres are linked by chromatin, is represented by a model in which two rods are linked by a rope. A construction of this type, however, cannot be bent. If a third rod is added as a link between these two rods, the entire structure can curve under compression. The bridging fibre is a third microtubule bundle that forms a bridge between sister k-fibres, hence the name [33] Fig. 28. A similar conclusion can be drawn from some electron micrographs of spindles such as in plant endosperm [152]. Yet, even if microtubule bundles lie close to each other, they do not necessarily interact. By severing a k-fibre with a laser [113], it has been demonstrated that the bridge fibre moves in tandem with sister k-fibres, indicating that these three fibres are closely coupled and hence capable of withstanding large physical perturbations such as k-fibre cutting. The bridging fibre is attached laterally to the k-fibres in the region away from the kinetochore, but these fibres separate from each other near to the kinetochore, according to Severing of a k-fibre at distinct locations. The bridging fibre is composed of 10-15 anti-parallel microtubules, with the anti-parallel overlap measured by PRC1-GFP extending over 5  $\mu\text{m}$ : 1  $\mu\text{m}$  between sister kinetochores and 2  $\mu\text{m}$  along each sister k-fibre. The presence of anti-parallel overlaps in bridge fibres shows that these fibres represent

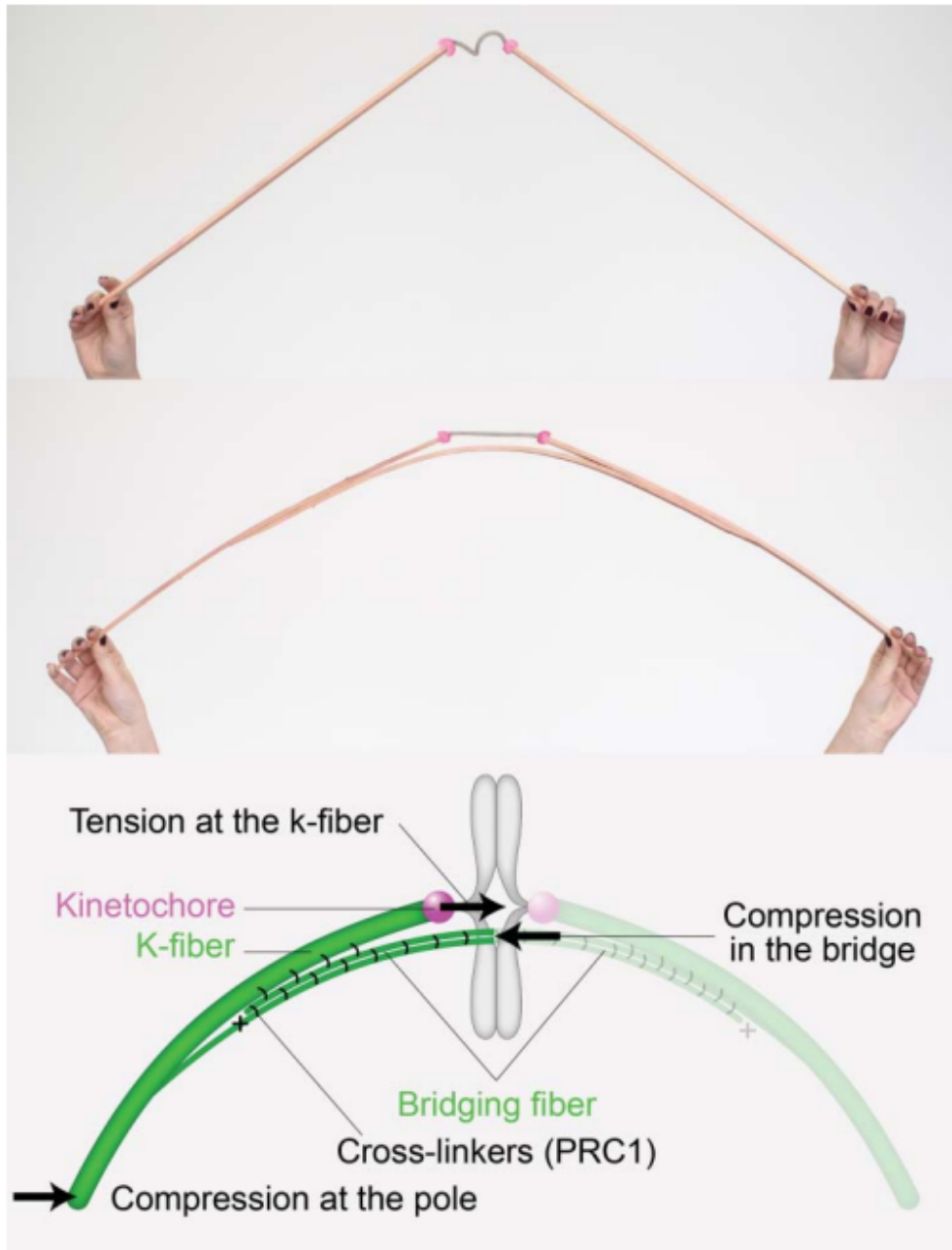


Figure 28: Bridging fibre links sister k-fibres and balances the tension on kinetochores. Macroscopic models made of wooden rods and a rope illustrate that the structure with two rods is not curved and the rope is relaxed, whereas the structure with 3 rods curves under compression and the rope gets tensed. The scheme shows the bridging fibre and forces in the spindle. Adapted from [143].

a subset of overlap microtubules, also known as interpolar or interdigitating microtubules. These microtubules branch from opposite spindle poles and connect at the spindle equator. The fraction of overlap microtubules that bridge k-fibres, as well as the location of the plus and minus ends of microtubules in the bridging fibre, are still unknown. Our experiments yielded a mathematically precise yet simple model [33]. In this model, microtubule fibres in the spindle are elastic rods, which bend under compressive force [153]. Their curvature reveals information about the forces that bend the k-fibres. At the same time, this model describes how kinetochores' tension is balanced: The tension at the kinetochore and the compression at the spindle pole are balanced by compression in the bridging fibre (Fig. 28). Thus, the k-fibre is under tension close to the kinetochore and under compression close to the pole [31]. The wooden model with three rods provides a visual representation of this force balance. According to our model, the force balance can be established if the bridging fibre splits from the k-fibres about 1 mm away from the kinetochore. In trials, if the kinetochore is cut close to the kinetochore, the kinetochore will move toward its sister because the bridging fibre is now separated from the severed k-fibre and cannot balance stress between sister kinetochores. If the cutting is performed far away from the kinetochore, the bridge fibre stays connected to the severed k-fibre and continues to balance the inter-kinetochore tension and therefore their distance. Experiments have revealed that the kinetochore response varies depending on the site of the cut [33].

Linkers between k-fibres and the bridge fibre maintain this microtubule arrangement with bridging fibres together. Key motor proteins and passive cross-linkers are being identified in order to better understand how this structure is maintained [86], as well as to define their geographic distribution in the spindle. Combining these experiments with new models incorporating bridging fibres will help researchers understand how spindle forces are generated, how they drive chromosome segregation, and how k-fibres, kinetochores, and bridging fibres self-assemble into a metaphase spindle.

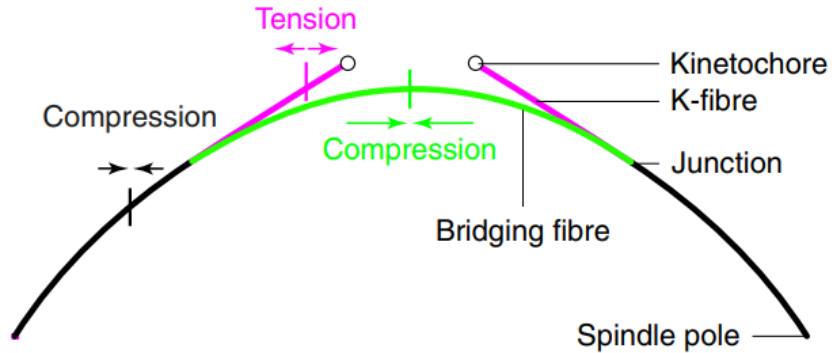


Figure 29: Compression in the bridging fibre balances the tension on the kinetochore. Theory and experiments predict the force balance in the k-fibre and the bridge fibre. The k-fibre segment between the junction and the kinetochore (magenta) is under tension, whereas the bundle (black) and the central part of the bridging fibre between the two junctions (green) are under compression. The bridging fibre’s central portion balances the forces acting at the pole and the kinetochore, allowing tension and compression to coexist within a single k-fibre. Adapted from [33].

## 1.5 The theory of elasticity

Because of the elastic features described in earlier chapters, the system we explore in this thesis, microtubule bundles in the mitotic spindle, can be thought of as stiff, continuous filaments that are thus suited for modelling using the theory of elasticity [154]. Elasticity theory is based on the mechanics of solid substances, which are considered continuous media. When subjected to applied forces, solid bodies deform to some extent, changing shape and volume. A body’s deformation is mathematically described as follows. The radius vector  $r$  in some co-ordinate system defines the position of any point in the body. When the body is deformed, every point in it is in general displaced. Let the radius vector of a particular point before the deformation be  $r$ , and after the deformation have a different value  $r'$  (with components  $x'_i$ ). The displacement of this point due to the deformation is then given by the vector  $r' - r$ , which we shall denote by the  $\mathbf{u}$ :

$$\mathbf{u} = \mathbf{x}' - \mathbf{x} \quad (1.5.1)$$

The vector  $\mathbf{u}$  is called the displacement vector. The co-ordinates  $x'_i$  of the displaced point are, of course, functions of the co-ordinates  $x_i$  of the point before displacement. The displacement vector  $u_i$  is therefore also a function of the co-ordinates  $x_i$ . If the vector  $\mathbf{u}$  is given as a function of  $x_i$ , the deformation of the body is entirely determined. When a body is deformed, the distances between its points change. Up to the second order, this distance is given by [154] (using the general summation rule):

$$dl'^2 = dl^2 + 2u_{ik}dx_id x_k, \quad (1.5.2)$$

where we have utilised the *strain tensor*  $u_{ik}$  defined as Eq. (1.5.2)

$$u_{ik} = \frac{1}{2} \left( \frac{\partial u_i}{\partial x_k} + \frac{\partial u_k}{\partial x_i} + \frac{\partial u_l}{\partial x_i} \frac{\partial u_l}{\partial x_k} \right). \quad (1.5.3)$$

Except in special cases, the displacement vector for a small deformation is itself small. It is evident that a three-dimensional body (i.e., one whose dimension in no direction is small) cannot be deformed in such a way that parts of it move a considerable distance without the occurrence of considerable extensions and compressions in the body, so for small deformations, we can therefore neglect the last term in the general expression, as being of the second order of smallness. Thus, the strain tensor is given by

$$u_{ik} = \frac{1}{2} \left( \frac{\partial u_i}{\partial x_k} + \frac{\partial u_k}{\partial x_i} \right) \quad (1.5.4)$$

Let us consider the total force on some portion of the body. Firstly, this total force is equal to the sum of all the forces on all the volume elements in that portion of the body, i.e. it can be written as the volume integral  $\mathbf{F} = \int_V \mathbf{f} dV$ , where  $\mathbf{f}$  is the force per unit volume and  $\mathbf{f}dV$  the force on the volume element  $dV$ . Secondly, the forces with which various parts of the



portion considered act on one another cannot give anything but zero in the total resultant force, since they cancel by Newton's third law. The required total force can therefore be regarded as the sum of the forces exerted on the given portion of the body by the portions surrounding it. From above, however, these forces act on the surface of that portion, and so the resultant force can be represented as the sum of forces acting on all the surface elements, i.e. as an integral over the surface  $S$  bounding the volume  $V$   $\int_V \mathbf{f} dV = \oint_S \sigma d\mathbf{A}$ . Application of the divergence theorem yields

$$f_i = \frac{\partial \sigma_{ik}}{\partial x_k}. \quad (1.5.5)$$

The tensor  $\sigma_{ik}$  is called the *stress tensor*.

In equilibrium the internal stresses in every volume element must balance, i.e. we must have

$$\mathbf{f} = 0 \Rightarrow \frac{\partial \sigma_{ik}}{\partial x_k} = 0 \quad (1.5.6)$$

If the body is in an external field, e.g., a gravitational field, the sum  $\mathbf{F} + \rho \mathbf{g}$  of the internal stresses and the force of gravity ( $\rho \mathbf{g}$  per unit volume) must vanish ;  $\rho$  is the density and  $\mathbf{g}$  the gravitational acceleration vector, directed vertically downwards. In this case the equations of equilibrium are

$$\frac{\partial \sigma_{ik}}{\partial x_k} + \rho \mathbf{g} = 0 \quad (1.5.7)$$

The moment of the forces on a portion of the body follows from the above equations. The moment of the force  $\mathbf{F}$  can be written as an anti-symmetrical tensor of rank two, whose components are  $F_i x_k - F_j x_i$ , where  $x_i$  are the co-ordinates of point where the force is applied. Like the total force on any volume

$$\mathbf{M} = \int_V \mathbf{x} \times \mathbf{f} dV = \oint_S \mathbf{G} d\mathbf{A}, \quad (1.5.8)$$

or, separated into components

$$\mathbf{x} \times \mathbf{f} = \frac{\partial \sigma_{il}}{\partial x_l} x_k - \frac{\partial \sigma_{kl}}{\partial x_l} x_i = \frac{\partial(\sigma_{il}x_k - \sigma_{kl}x_i)}{\partial x_l} - \sigma_{il} \frac{\partial x_k}{\partial x_l} + \sigma_{kl} \frac{\partial x_i}{\partial x_l}. \quad (1.5.9)$$

Because Cartesian components are independent, the relation  $\frac{\partial x_k}{\partial x_l} = \Delta_{kl}$  holds. In the first term in Eq. (1.5.9), the integrand is the divergence of a tensor; the integral can be transformed into one over the surface. If  $M_{ik}$  is to be an integral over the surface only, the second term must vanish identically, i.e. we must have  $\sigma_{ik} = \sigma_{ki}$ . Thus the important result that the stress tensor is symmetrical is obtained. The moment of the forces on a portion of the body, if the body is to be in balance, must also vanish:

$$\mathbf{x} \times \mathbf{f} = 0 \Rightarrow \frac{\partial \sigma_{il}}{\partial x_l} x_k - \frac{\partial \sigma_{kl}}{\partial x_l} x_i = 0. \quad (1.5.10)$$

In order to be able to apply the general formulae of thermodynamics to any particular case, the free energy  $F$  of the body as a function of the strain tensor must be known. This expression is easily obtained by using the fact that the deformation is small and expanding the free energy in powers of  $u_{ik}$ , especially if we consider only isotropic bodies. The free energy  $F$  is defined as:

$$\sigma_{ik} = \partial F / \partial u_{ik}. \quad (1.5.11)$$

The external forces applied to the surface of the body (which are the usual cause of deformation) appear in the boundary conditions on the equations of equilibrium. Let  $\mathbf{P}$  be the external force on unit area of the surface of the body, so that a force  $\mathbf{P}dA$  acts on a surface element  $dA$ . In equilibrium, this must be balanced by the force  $-\sigma_{ik}dA_k$  of the internal stresses acting on that element. Thus we must have  $\mathbf{P}_i dA - \sigma_{ik}dA_k = 0$ . Writing  $dA_k = n_k dA$ , where  $\mathbf{n}$  is a unit vector along the outward normal to the surface, we find

$$\sigma_{ik}n_k = P_i. \quad (1.5.12)$$

This is the condition which must be satisfied at every point on the surface of a body in equilibrium. To derive a formula giving the mean value of the stress tensor in a deformed body, we multiply equation Eq. (1.5.6) by  $x_k$  and integrate over the whole volume, obtaining

$$\sigma \mathbf{n} = \mathbf{P}. \quad (1.5.13)$$

The undeformed state of the body is one where there is an absence of external forces. Thus if  $u_{ik} = 0$  holds, so does  $\sigma_{ik} = 0$ . Since  $\sigma_{ik} = \partial F / \partial u_{ik}$ , it follows that there is no linear term in the expansion of  $F$  in powers of  $u_{ik}$ . Next, since the free energy is a scalar, each term in the expansion of  $F$  must be a scalar also. Two independent scalars of the second degree can be formed from the components of the symmetrical tensor  $u_{ik}$ : they can be taken as the squared sum of the diagonal components  $u_{ii}^2$  and the sum of the squares of all the components  $u_{ik}^2$ . Expanding  $F$  in powers of  $u_{ik}$  we therefore have, as far as terms of the second order,

$$F = F_0 + \frac{1}{2} \lambda u_{ii}^2 + \mu u_{ik}^2. \quad (1.5.14)$$

This is the general expression for the free energy of a deformed isotropic body. The quantities  $\lambda$  and  $\mu$  are called Lamé coefficients. The change in volume in the deformation is given by the sum  $u_{ii}$ . If this sum is zero, then the volume of the body is unchanged by the deformation, only its shape being altered. Such a deformation is called a pure shear. The opposite case is that of a deformation which causes a change in the volume of the body but no change in its shape. Each volume element of the body retains its shape also. We have seen that the tensor of such a deformation is  $u_{ik} = \text{constant} \times \Delta_{ik}$ . Such a deformation is called a *hydrostatic compression*. Any deformation can be represented as the sum of a pure shear and a hydrostatic compression. To do so, we need only use the identity

$$u_{ik} = \left( u_{ik} - \frac{1}{3} \Delta_{ik} u_{ll} \right) + \frac{1}{3} \Delta_{ik} u_{ll} \quad (1.5.15)$$

The first term on the right is evidently a pure shear, since the sum of its diagonal terms is zero ( $\Delta_{ii} = 3$ ). The second term is a hydrostatic compression. As a general expression for the free energy of a deformed isotropic body, it is convenient to replace Eq. (1.5.14) by another formula, using this decomposition of an arbitrary deformation into a pure shear and a hydrostatic compression. We take as the two independent scalars of the second degree the sums of the squared components of the two terms in Eq. (1.5.15). Then  $\mathbf{F}$  becomes

$$F = \mu(u_{ik} - \frac{1}{3}\Delta_{ik}u_{ll})^2 + \frac{1}{2}Ku_{ll}^2. \quad (1.5.16)$$

The quantities  $K$  and  $\mu$  are called respectively the bulk modulus or modulus of hydrostatic compression (or simply the modulus of compression) and the shear modulus or modulus of rigidity.  $K$  is related to the Lamé coefficients by

$$K = \lambda + \frac{2}{3}\mu. \quad (1.5.17)$$

In a state of thermodynamic equilibrium, the free energy is a minimum. If no external forces act on the body, then  $\mathbf{F}$  as a function of  $u_{ik}$  must have a minimum for  $u_{ik} = 0$ . This means that the quadratic form (Eq. (1.5.16)) must be positive. If the tensor  $u_{ik}$  is such that  $u_{ll} = 0$ , only the first term remains in Eq. (1.5.16) ; if, on the other hand, the tensor is of the form  $u_{ik} = \text{constant} \times \Delta_{ik}$ , then only the second term remains. Hence it follows that a necessary (and evidently sufficient) condition for the form (Eq. (1.5.16)) to be positive is that each of the coefficients  $K$  and  $\mu$ , is positive. Thus we conclude that the moduli of compression and rigidity are always positive  $K > 0$  and  $\mu > 0$ . We now determine the stress tensor. To calculate the derivatives  $\partial F / \partial u_{ik}$ , we write the total differential  $d\mathbf{F}$  (for constant temperature)

$$dF = Ku_{ll}du_{ll} + 2\mu(u_{ik} - \frac{1}{3}\Delta_{ik}u_{ll})d(u_{ik} - \frac{1}{3}\Delta_{ik}u_{ll}) \quad (1.5.18)$$

In the second term, multiplication of the first parenthesis by  $\delta u_{ik}$  gives zero, leaving

$$dF = K u_{ll} du_{ll} + 2\mu(u_{ik} - \frac{1}{3}\Delta_{ik}u_{ll})d(u_{ik}), \quad (1.5.19)$$

where we have used the identity  $du_{ll} = \Delta_{ik}du_{ik}$ . From this equation, by dividing with  $d(u_{ik})$ , we have obtained the stress tensor:

$$\sigma_{ik} = K u_{ll} \Delta_{ik} + 2\mu(u_{ik} - \frac{1}{3}\Delta_{ik}u_{ll}). \quad (1.5.20)$$

This expression determines the stress tensor in terms of the strain tensor for an isotropic body. It shows, in particular, that, if the deformation is a pure shear or a pure hydrostatic compression, the relation between  $\sigma_{ik}$  and  $u_{ik}$  is determined only by the modulus of rigidity  $\mu$  or of hydrostatic compression  $K$  respectively.

Let us consider some simple cases of what are called homogeneous deformations, i.e. those in which the strain tensor is constant throughout the volume of the body. For example, the hydrostatic compression already considered is a homogeneous deformation. We first consider a simple extension (or compression) of a rod. Let the rod be along the  $z$ -axis, and let forces be applied to its ends which stretch it in both directions. These forces act uniformly over the end surfaces of the rod ; let the force on unit area be  $p$ . Since the deformation is homogeneous, i.e.  $u_{ik}$  is constant through the body, the stress tensor  $\sigma_{ik}$  is also constant, and so it can be determined at once from the boundary conditions Eq. (1.5.12). There is no external force on the sides of the rod, and therefore  $\sigma_{ik}n_k = 0$ . Since the unit vector  $\mathbf{n}$  on the side of the rod is perpendicular to the  $z$ -axis, i.e.  $n_z = 0$ , it follows that all the components  $\sigma_{ik}$  except  $\sigma_{zz}$  are zero. On the end surface we have  $\sigma_{zi}n_i = p$ , or  $\sigma_{zz} = p$ . From the general expression Eq. (1.5.16) which relates the components of the strain and stress tensors, we see that all the components  $u_{ik}$  with  $i \neq k$  are zero. For the remaining components we find

$$u_{xx} = u_{yy} = -\sigma u_{zz}, \quad u_{zz} = p/E, \quad (1.5.21)$$

where  $E$  is called *Young's modulus*,  $\sigma$  is called the *Poisson ratio*, and they are given by

$$E = 9K\mu/(3K + \mu), \quad \sigma = \frac{1}{2}(3K - 2\mu)/(3K + \mu). \quad (1.5.22)$$

*Young's modulus* is a measure of the ability of the material to resist compression in the transverse direction, while the *Poisson ratio* is the ratio of the transverse compression to the longitudinal extension. These two constants have been measured for a wide variety of materials, and are thus more common in the literature than hydrostatic compression and shear constants. The *Poisson ratio* can only take values between  $-1 \leq \sigma \leq \frac{1}{2}$ . The relationship between the stress and strain tensors is given by [154]:

$$\sigma_{ik} = \frac{E}{1 + \sigma} \left( u_{ik} + \frac{\sigma}{1 - 2\sigma} u_{ll} \Delta_{ik} \right). \quad (1.5.23)$$

A very important case is that where the deformation of the body is caused, not by body forces, but by forces applied to its surface. The equation of equilibrium then becomes, in vector notation, [154]:

$$(1 - 2\sigma)\Delta \mathbf{u} + \mathbf{grad} \operatorname{div} \mathbf{u} = 0. \quad (1.5.24)$$

### 1.5.1 Theory of elasticity applied to thin elastic rods

Let us now consider the deformation of thin rods. This differs from all the cases hitherto considered, in that the displacement vector  $\mathbf{u}$  may be large even for small strains, i.e. when the tensor  $u_{ik}$  is small. For example, when a long thin rod is slightly bent, its ends may move a considerable distance, even though the relative displacements of neighbouring points in the rod are small. There are two types of deformation of a rod which may be accompanied by a large displacement of certain parts of it. One of these consists in bending the rod, and the other in twisting it. We shall begin by considering the latter case.

### 1.5.2 Torsion of thin elastic rods

A torsional deformation is one in which, although the rod remains straight, each transverse section is rotated through some angle relative to those below it. If the rod is long, even a slight torsion causes sufficiently distant cross-sections to turn through large angles. The generators on the sides of the rod, which are parallel to its axis, become helical in form under torsion. Let us consider a thin straight rod of arbitrary cross-section. We take a co-ordinate system with the  $z$ -axis along the axis of the rod and the origin somewhere inside the rod. We use also the *torsion angle*  $\xi$ , which is the angle of rotation per unit length of the rod. This means that two neighbouring cross-sections at a distance  $dz$  will rotate through a relative angle  $d\phi = \xi dz$  (so that  $\xi = \frac{d\phi}{dz}$ ). The torsional deformation itself, i.e. the relative displacement of adjoining parts of the rod, is assumed small. The condition for this to be so is that the relative angle turned through by cross-sections of the rod at a distance apart of the order of its transverse dimension  $\mathbf{R}$  is small, i.e.,  $\xi R \ll 1$ . For the strain tensor, it can be shown [154] that the non-zero components are

$$u_{xz} = \frac{1}{2} \left( \frac{\partial \psi}{\partial x} - y \right), \quad u_{yz} = \frac{1}{2} \left( \frac{\partial \psi}{\partial y} + x \right), \quad (1.5.25)$$

where  $\psi$  is the *torsion function*, defined by  $u_z = \xi \psi(x, y)$ . Since we have  $u_{ll} = 0$ , torsion does not result in a change in volume, i.e. it is a pure shear deformation. The non-zero components of the stress tensor are similarly

$$\sigma_{xz} = 2\mu\xi \left( \frac{\partial \psi}{\partial x} - y \right), \quad \sigma_{yz} = 2\mu\xi \left( \frac{\partial \psi}{\partial y} + x \right) \quad (1.5.26)$$

Since only  $\sigma_{xz}$  and  $\sigma_{yz}$  are different from zero, the general equation Eq. (1.5.6) reduces to

$$\frac{\partial \sigma_{xz}}{\partial x} + \frac{\partial \sigma_{yz}}{\partial y} = 0. \quad (1.5.27)$$

From this, we conclude that the torsion function must satisfy  $\Delta\psi = 0$ , where  $\Delta$  is the two-dimensional Laplacian. The total elastic energy for the rod can be obtained, and it is equal to

$$F_{\text{rod}} = \frac{1}{2} \int \tau \xi^2 dz \quad (1.5.28)$$

where  $\tau$  is the *torsional rigidity* of the rod. Let us consider now a more usual case of torsion, where one of the ends of the rod is held fixed and the external forces are applied only to the other end. These forces are such that they cause only a twisting of the rod, and no other deformation such as bending. In other words, they form a couple which twists the rod about its axis. The moment of this couple will be denoted by  $M$ . We should expect that, in such a case, the torsion angle  $t$  is constant along the rod. This can be seen, for example, from the condition that the free energy of the rod is a minimum in equilibrium. The total energy of a deformed rod is equal to the sum  $F_{\text{rod}} + U$ , where  $U$  is the potential energy due to the action of the external forces. Substituting in  $\xi = d\phi/dz$  and varying with respect to the angle  $\phi$ , we find

$$\Delta \frac{1}{2} \int \tau \left(\frac{d\phi}{dz}\right)^2 dz + \Delta U = \int \tau \frac{d\phi}{dz} \frac{d\Delta\phi}{dz} dz + \Delta U = 0. \quad (1.5.29)$$

Integrating the above equation by parts, one obtains

$$- \int \tau \frac{d\xi}{dz} \Delta\phi dz + \Delta U + [\tau \xi \Delta\phi] = 0 \quad (1.5.30)$$

The last term on the left is the difference of the values at the limits of integration, i.e. at the ends of the rod. One of these ends, say the lower one, is fixed, so that  $\Delta\phi = 0$  there. The variation  $\Delta U$  of the potential energy is minus the work done by the external forces in rotation through an angle  $\Delta\phi$ . As we know from mechanics, the work done by a couple in such a rotation is equal to the product  $M\Delta\phi$  of the angle of rotation and the moment of the



couple. Since there are no other external forces,  $\Delta U = -M\Delta\phi$ , and we have

$$\int \tau \frac{d\xi}{dz} \Delta\phi dz + [\Delta\phi(-M + \tau\xi)] = 0. \quad (1.5.31)$$

The second term on the left has its value at the upper end of the rod. In the integral over  $z$ , the variation  $\Delta\phi$  is arbitrary, and so we must have

$$\tau \frac{d\xi}{dz} = 0, \quad (1.5.32)$$

from which the result

$$\xi = \text{constant}, \quad (1.5.33)$$

immediately follows. Thus the torsion angle is constant along the rod. The total angle of rotation of the upper end of the rod relative to the lower end is  $\xi l$ , where  $l$  is the length of the rod. In Eq. (1.5.31), the second term also must be zero, and we obtain the following expression for the constant torsion angle

$$\xi = \frac{M}{\tau}. \quad (1.5.34)$$

### 1.5.3 Bending of thin elastic rods

A bent rod is stretched at some points and compressed at others. Lines on the convex side of the bent rod are extended, and those on the concave side are compressed. As with plates, there is a neutral surface in the rod, which undergoes neither extension nor compression. It separates the region of compression from the region of extension. Let us begin by investigating a bending deformation in a small portion of the length of the rod, where the bending may be supposed slight; by this we here mean that not only the strain tensor but also the magnitudes of the displacements of points in the rod are small. We take a co-ordinate system with the origin on the neutral surface in the portion considered, and the  $x$ -axis parallel to the axis of

the undeformed rod. Let the bending occur in the  $zx$ -plane. As in the bending of plates and the twisting of rods, the external forces on the sides of a thin bent rod are small compared with the internal stresses, and can be taken as zero in determining the boundary conditions at the sides of the rod. Thus we have everywhere on the sides of the rod  $\sigma_{ik}n_k = 0$ , or, since  $n_z = 0$ ,  $\sigma_{xx}n_x + \sigma_{xy}n_y = 0$ , and similarly for  $i = y, z$ . We take a point on the circumference of a cross-section for which the normal  $\mathbf{n}$  is parallel to the  $x$ -axis. There will be another such point somewhere on the opposite side of the rod. At both these points  $n_y = 0$ , and the above equation gives  $\sigma_{xx} = 0$ . Since the rod is thin, however,  $\sigma_{xx}$  must be small everywhere in the cross-section if it vanishes on either side. We can therefore put  $\sigma_{xx} = 0$  everywhere in the rod. In a similar manner, it can be seen that all the components of the stress tensor except  $\sigma_{zz}$  must be zero. That is, in the bending of a thin rod only the extension (or compression) component of the internal stress tensor is large. A deformation in which only the component  $\sigma_{xx}$  of the stress tensor is non-zero is just a simple extension or compression. Thus there is a simple extension or compression in every volume element of a bent rod. The amount of this varies, of course, from point to point in every cross-section, and so the whole rod is bent. It is easy to determine the relative extension at any point in the rod. Let us consider an element of length  $dz$  parallel to the axis of the rod and near the origin. Upon being bent, the length of this element becomes  $dz'$ . The only elements which remain unchanged are those which lie in the neutral surface. Let  $R$  be the radius of curvature of the neutral surface near the origin. The lengths  $dz$  and  $dz'$  can be regarded as elements of arcs of circles whose radii are respectively  $R$  and  $R + x$ ,  $x$  being the co-ordinate of the point where  $dz'$  lies. Hence

$$dz' = \frac{R + x}{R} dz = \left(1 + \frac{x}{R}\right) dz. \quad (1.5.35)$$

Thus we obtain the expression for the relative extension  $(dz' - dz)/dz = x/R$ . The relative extension of the element  $dz$ , however, is equal to the component  $u_{zz}$  of the strain tensor, meaning that  $u_{zz} = (dz' - dz)/dz = x/R$ . Since for a simple extension the relationship

between the strain and shear tensors is given by the Young modulus  $\sigma_{zz} = E u_{zz}$ , we obtain

$$\sigma_{zz} = E \frac{x}{R}. \quad (1.5.36)$$

The position of the neutral surface in a bent rod has now to be determined. This can be done from the condition that the deformation considered must be pure bending, with no general extension or compression of the rod. The total internal stress force on a cross-section of the rod must therefore be zero, i.e. the integral  $\int \sigma_{zz} df$ , taken over a cross-section, must vanish. Using the expression Eq. (1.5.36) for  $\sigma_{zz}$ , we obtain the condition

$$\int x df = 0. \quad (1.5.37)$$

We can now bring in the centre of mass of the cross-section, which is that of a uniform flat disc of the same shape. The co-ordinates of the centre of mass are, as we know, given by the integrals  $\int x df$ ,  $\int y df$  and  $\int u df$ . Thus the condition Eq. (1.5.37) signifies that, in a co-ordinate system with the origin in the neutral surface, the  $x$  co-ordinate of the centre of mass of any cross-section is zero. The neutral surface therefore passes through the centres of mass of the cross-sections of the rod. Two components of the strain tensor besides  $u_{zz}$  are non-zero, since for a simple extension we have  $u_{xx} = u_{yy} = -\sigma u_{zz}$ . Knowing the strain tensor, we can easily find the displacement

$$u_{zz} = \partial u_z / \partial z = x/R, \quad \partial u_x / \partial x = \partial u_y / \partial y = -\sigma x/R \quad (1.5.38)$$

$$\begin{aligned} \frac{\partial u_z}{\partial x} + \frac{\partial u_x}{\partial z} &= 0, \\ \frac{\partial u_x}{\partial y} + \frac{\partial u_y}{\partial x} &= 0, \\ \frac{\partial u_z}{\partial y} + \frac{\partial u_y}{\partial z} &= 0. \end{aligned} \quad (1.5.39)$$

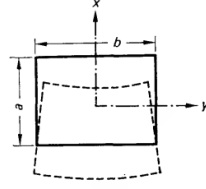


Figure 30: Bending of a rod as a result of a force. Adapted from [154].

Integration of these equations gives the following expressions for the components of the displacement

$$\begin{aligned}
 u_x &= -\frac{1}{2R}[z^2 + \sigma(x^2 - y^2)] \\
 u_y &= -\sigma xy/R \\
 u_z &= xz/R
 \end{aligned}
 \tag{1.5.40}$$

It is seen from formulae Eq. (1.5.40) that the points initially on a cross-section  $z = \text{constant} = z_0$  will be found, after the deformation, on the surface  $z = z_0 + u_z = z_0(l + x/R)$ . We see that, in the approximation used, the cross-sections remain plane but are turned through an angle relative to their initial positions. The shape of the cross-section changes, however; for example, when a rod of rectangular cross-section (sides  $a$ ,  $b$ ) is bent, the sides  $y = \pm\frac{1}{2}b$  of the cross-section become  $y = \pm\frac{1}{2}b + u_y = \pm\frac{1}{2}b(1 - \sigma x/R)$ , i.e., no longer parallel but still straight. The sides  $x = \pm\frac{1}{2}a$  however, are bent into the parabolic curves Fig. 30:

$$x = \pm\frac{1}{2}a + u_x = \pm\frac{1}{2}a - \frac{1}{2R}[z_0^2 + \sigma(\frac{1}{4}a^2 - y^2)]
 \tag{1.5.41}$$

The free energy per unit volume of the rod is

$$\frac{1}{2}\sigma_{ik}u_{ik} = \frac{1}{2}\sigma_{zz}u_{zz} = \frac{1}{2}Ex^2/R^2.
 \tag{1.5.42}$$

Integrating over the cross-section of the rod, we obtain the equation

$$\frac{1}{2}E/R^2 \int x^2 df \quad (1.5.43)$$

This is the free energy per unit length of a bent rod. The radius of curvature  $R$  is that of the neutral surface. However, since the rod is thin,  $R$  can here be regarded, to the same approximation, as the radius of curvature of the bent rod itself, regarded as a line (often called an "elastic line"). In the expression Eq. (1.5.43) it is convenient to introduce the moment of inertia of the cross-section. The moment of inertia about the  $y$ -axis in its plane is defined

$$I_y = \int x^2 df \quad (1.5.44)$$

analogously to the ordinary moment of inertia, but with the surface element  $df$  instead of the mass element. Then the free energy per unit length of the rod can be written

$$\frac{1}{2}EI_y/R^2 \quad (1.5.45)$$

We can also determine the moment of the internal stress forces on a given cross-section of the rod (the bending moment). A force  $\sigma_{zz}df = (xE/R)df$  acts in the  $z$ -direction on the surface element  $df$  of the cross-section. Its moment about the  $y$ -axis is  $\sigma_{zz}df$ . Hence the total moment of the forces about this axis is given by

$$M_y = EI_y/R \quad (1.5.46)$$

Thus the curvature  $\kappa = 1/R$  of the elastic line is proportional to the bending moment on the cross-section concerned.

### 1.5.4 Equilibrium of rods

To derive the equations of equilibrium for a bent rod, consider an infinitesimal element  $dl$  bounded by two adjoining cross-sections of the rod, and calculate the total force acting on it. We denote by  $\mathbf{F}$  the resultant internal stress on a cross-section. The components of this vector are the integrals of over the cross-section. If we regard the two adjoining cross-sections as the ends of the element, a force  $\mathbf{F} + d\mathbf{F}$  acts on the upper end, and  $-\mathbf{F}$  on the lower end; the sum of these is the differential  $d\mathbf{F}$ . Next, let  $\mathbf{K}$  be the external force on the rod per unit length. Then an external force  $\mathbf{K}dl$  acts on the element of length  $dl$ . The resultant of the forces on the element is therefore  $d\mathbf{F} + \mathbf{K}dl$ . This must be zero in equilibrium. Thus the equation

$$\frac{d\mathbf{F}}{dl} = -\mathbf{K}, \quad (1.5.47)$$

holds. A second equation is obtained from the condition that the total moment of the forces on the element is zero. Let  $\mathbf{M}$  be the moment of the internal stresses on the cross-section. This is the moment about a point (the origin) which lies in the plane of the cross-section. We can calculate the total moment, on the element considered, about a point  $O$  lying in the plane of its upper end. Then the internal stresses on this end give the resulting moment  $\mathbf{M} + d\mathbf{M}$ . The moment about  $O$  of the internal stresses on the lower end of the element is composed of the moment  $-\mathbf{M}$  of those forces about the origin  $O'$  in the plane of the lower end and the moment about  $O$  of the total force  $\mathbf{F}$  on that end. This latter moment is  $-d\mathbf{l} \times \mathbf{F}$ , where  $d\mathbf{l}$  is the vector of the element of length of the rod between  $O'$  and  $O$ .

The moment due to the external forces  $\mathbf{K}$  is of a higher order of smallness. Thus the total moment acting on the element considered is  $d\mathbf{M} + d\mathbf{l} \times \mathbf{F}$ . In equilibrium, this must be zero:

$$d\mathbf{M} + d\mathbf{l} \times \mathbf{F} = 0. \quad (1.5.48)$$

If, however, additionally an external torque, given as  $\mathbf{m}$  per unit length  $dl$ , acts upon the

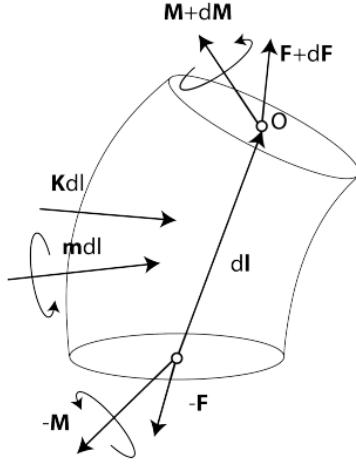


Figure 31: Geometry of an infinitesimally thin rod and the forces and torques acting upon it. Figure authored by Maja Novak and used with permission.

rod, the equilibrium equation will change to

$$d\mathbf{M} + d\mathbf{l} \times \mathbf{F} = -\mathbf{m}d\mathbf{l}. \quad (1.5.49)$$

This can be seen in Fig. 31.

Dividing this equation by  $d\mathbf{l}$  and using the fact that  $d\mathbf{l}/d\mathbf{l} = \mathbf{t}$  is the unit vector tangential to the rod (regarded as a line), we obtain

$$d\mathbf{M}/d\mathbf{l} = \mathbf{F} \times \mathbf{t} - \mathbf{m}. \quad (1.5.50)$$

Equations Eq. (1.5.47) and Eq. (1.5.50) form a complete set of equilibrium equations for a rod bent in any manner. If the external forces on the rod are concentrated, i.e. applied only at isolated points of the rod, the equilibrium equations at all other points are much simplified. For  $\mathbf{K} = \mathbf{0}$  we have from Eq. (1.5.47):

$$\mathbf{F} = \text{const}, \quad (1.5.51)$$

i.e., the stress resultant is constant along any portion of the rod between points where forces are applied. The values of the constant are found from

$$\mathbf{F}_{i+1} - \mathbf{F}_i = -\mathbf{K}_i, \quad (1.5.52)$$

where the sum is over all forces applied to the segment of the rod between the two points. It should be noticed that, in the difference  $\mathbf{F}_{i+1} - \mathbf{F}_i$ , the point  $i + 1$  is further from the point from which  $l$  is measured than is the point  $i$ . In particular, if only one concentrated force  $\mathbf{f}$  acts on the rod, and is applied at its free end, then  $\mathbf{F} = \mathbf{const} = \mathbf{f}$  at all points of the rod.

The Eq. (1.5.50) can in this case also be simply integrated, obtaining

$$\mathbf{M} = \mathbf{F} \times r + \mathbf{const} - \int \mathbf{m} dl. \quad (1.5.53)$$

If concentrated forces also are absent, and the rod is bent by the application of concentrated moments, i.e. of concentrated couples, then  $\mathbf{F} = \mathbf{const}$  at all points of the rod, while  $\mathbf{M}$  is discontinuous at points where couples are applied, the discontinuity being equal to the moment of the couple. Analogue to forces, the differences between infinitesimally close points are given by

$$\mathbf{M}_{i+1} - \mathbf{M}_i = -\mathbf{m}_i. \quad (1.5.54)$$

### 1.5.5 Boundary conditions at the ends of a bent rod

The end of the rod is said to be clamped Fig. 32 if it cannot move either longitudinally or transversely, and moreover its direction (i.e. the direction of the tangent to the rod) cannot change. In this case the boundary conditions are that the co-ordinates of the end of the rod and the unit tangential vector  $\mathbf{t}$  there are given. The reaction force and moment exerted on the rod by the clamp are determined by solving the equations.

If the end of the rod is fixed to a hinge, it cannot be displaced, but its direction can vary.



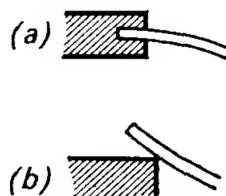


Figure 32: Types of ends of rods. (a) Clamped. It cannot move either longitudinally or transversely, and moreover its direction cannot change. (b) Free end, whose position and direction are arbitrary. Adapted from [154].

In this case the moment of the forces on the freely turning end must be zero. Finally, if the rod is supported Fig. 32, it can slide at the point of support but cannot undergo transverse displacements. In this case the direction  $\mathbf{t}$  of the rod at the support and the point on the rod at which it is supported are unknown. The moment of the forces at the point of support must be zero, since the rod can turn freely, and the force  $\mathbf{F}$  at that point must be perpendicular to the rod; a longitudinal force would cause a further sliding of the rod at this point. The boundary conditions for other modes of fixing the rod can easily be established in a similar manner. A rod of arbitrary cross-section undergoing large deflections is in general twisted also, even if no external twisting moment is applied to the rod. An exception occurs when a rod is bent in one of its principal planes, in which case there is no torsion. For a rod of circular cross-section no torsion results for any bending, if there is no external twisting moment, of course.

## 1.6 Existing models of the mitotic spindle metaphase

We end the introduction by providing an overview of the existing models for the mitotic spindle metaphase. The 'Slide-and-cluster' model is considered representative for the metaphase of the meiosis of the frog *Xenopus Laevis* [121, 155], the liquid crystal model for the mitosis of the worm *C. Elegans* [156, 157], while a model based on the theory of elasticity is appropriate for the modelling of the *Drosophila* fly embryo [158]. All three models, though different in

their fundamentals and the biological organisms in question, explain the balance of forces in the spindle metaphase and thus answer key questions about how the mitotic spindle works.

### 1.6.1 Slide and cluster models

After nucleation, microtubules are moved continuously outward by motors or other forces, as can be seen in Fig. 33. The outward motion is balanced by microtubule loss due to dynamic instability or other means, as well as microtubule resupply at the equator by means of new nucleation. Microtubules slow down as they move, their density increases, and their minus ends can begin to pile up. If the velocity gradient is steep enough, microtubules can overtake those that were nucleated earlier, and the minus ends form a sharp, highly clustered pole. The loss due to microtubule depolymerisation eventually balances out the increase in minus-end density at the poles, and a steady-state is reached. It should be noted that the model only considers interpolar MTs. Kinetochore MTs have different dynamics, but experiments show that they are not required for the assembly of stable, bipolar astral spindles [117] and usually represent a minority of the microtubules in a spindle. Regardless of how microtubules are nucleated, lost, moved, or slowed, the slide-and-cluster model makes several strong predictions: First, spindles achieve a steady state in length through intrinsic spindle mechanisms. Because their length is determined independently, they can be as small as the cell in which they form, as seen in eggs (and egg extracts). Second, some minus ends will be found throughout the spindle (though the majority will be at the poles), and nucleation sites must not be restricted to the poles. Both are true in non-astral spindles in *Xenopus* egg extracts [63, 117, 118]. Third, microtubules at the equator will slide toward the poles with their minus ends leading. Exogenous, stabilized MTs added to *Xenopus* extract spindles do this [117], and all detectable endogenous microtubules slide bidirectionally at the equator [159, 160], presumably toward their minus ends. However, in order to critically test this prediction, the dynamics of endogenous minus ends must be visualized. Fourth, because interpolar microtubules move more slowly near the poles, the measured rate of microtubule

sliding decreases as distance from the chromosomes increases. In contrast to models in which microtubules stretch throughout the spindle and flux is produced by forces concentrated at the poles, this is a significant departure [161–163], because such models predict a constant microtubule velocity throughout the spindle. Microtubules at the pole will have an average velocity of zero (though they may jiggle due to stochastic effects), and any MTs found beyond the pole will have an inward average velocity. Fifth, because the pole position in the slide-and-cluster scenario is determined by the average microtubule velocity (rather than the position of a nucleating and organizing centre), changes in global flux rates or the positional dependence of microtubule velocities should affect the pole positions and thus the spindle length. Sixth, changing the mechanism that generates the microtubule velocity gradient will affect the degree to which poles are clustered. Spindles with unfocused or non-existent poles will result from inhibiting the gradient. To provide more-detailed predictions of spindle responses to perturbations and other features, a more-specific model for how microtubules are moved and slowed is required.

The slide and cluster model has microtubule motion being controlled by the interactions of two types of simple motors with the MTs. Each is biologically inspired: A sliding motor represents the plus-end-directed motor kinesin-5 [164], and a clustering motor represents the minus-end-directed dynein-dynactin complex [165] or ncd [166], as can be seen in Fig. 34. When the sliding motor links a pair of antiparallel MTs, it walks toward the plus ends of each, pushing the MTs such that their minus ends slide apart (Fig. 34). This function has been widely hypothesized for kinesin-5 on the basis of its tetrameric structure [166–168]. By contrast, when a sliding motor links a pair of parallel MTs, it simply resists relative motion between the two. The specific effect of each sliding motor depends on the position and velocities of the two microtubules it connects, but on average, sliding motors in the spindle contribute an outward component to each microtubules velocity( Fig. 34). A clustering motor moves toward the minus ends of the two microtubules that it links. It pauses upon reaching the minus end of one microtubule while continuing to move along the other. As noted in the

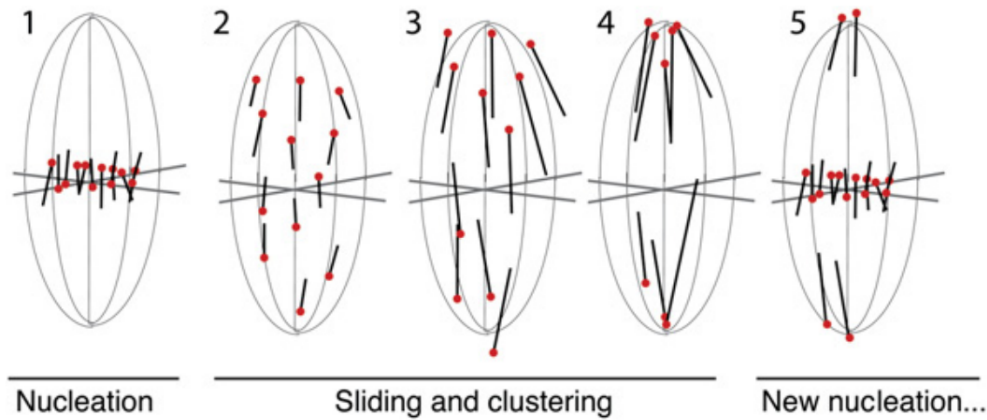


Figure 33: Slide-and-Cluster Scenario MTs are nucleated in the middle of the spindle (1). They then slide outward (2 and 3) but slow down as their minus ends are moved further. Where the minus ends stop sliding (on average), they pile up and form the pole (4). microtubules are lost continuously through depolymerisation at plus and/or minus ends. Meanwhile, new nucleation replenishes the population at the centre of the spindle (5). All the activities in 1 through 5 are continuous and simultaneous. Adapted from [121].

literature [169, 170], a motor with this behaviour will slide the parallel microtubules such that their minus ends move toward each other, i.e., it clusters them (Fig. 34). In a group of parallel MTs, the clustering motors work to pull each microtubule's minus end toward the average position of the minus ends in the group. In a spindle, microtubules of each orientation have their minus ends spread out predominantly in one half of the spindle, with left-pointing microtubules having their minus ends in the right half of the spindle and vice-versa [63]. Thus, the minus ends of each orientation have an average position somewhere between the chromosomes and the pole they are moving toward. By pulling minus ends toward the average position, the clustering motor contributes an outward component to the velocity of microtubules near the chromosomes but an inward component to those near the poles. At the chromosomes, then, the two motors cooperate to pull microtubules outward (Fig. 34). Away from the chromosomes, they compete, and microtubules move more slowly. If and where the velocity contributions from the two motor types balance, the microtubules

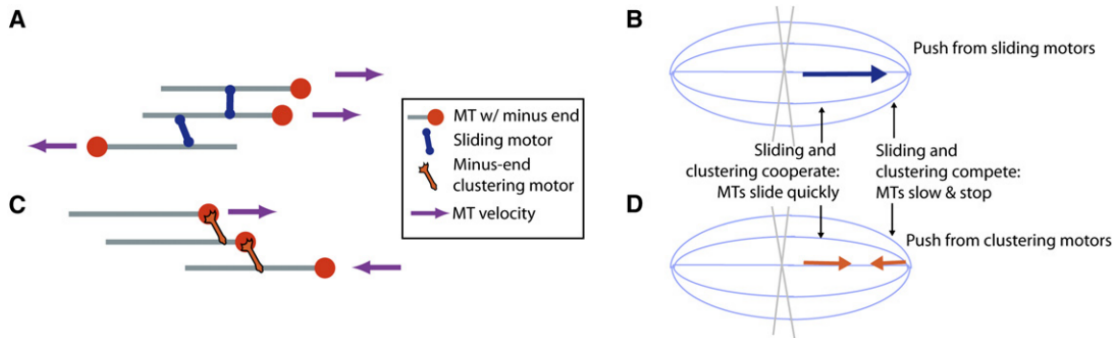


Figure 34: Sliding- and Clustering-Motor Activity (A) A sliding motor walks toward the plus ends of MTs. A motor linking antiparallel microtubules slides them so that their minus ends move apart, while one linking parallel microtubules resists their relative motion. (B) The effect of the sliding motor, throughout the spindle, is to move microtubules toward the pole. (C) A minus-end clustering motor walks toward the minus ends of two parallel MTs. When it reaches the end of one microtubule, it sticks there and slides the other microtubule to make their minus ends move together. (D) The effect of the clustering motors is to pull together the minus ends of parallel MTs. Near the chromosomes, this pulls microtubules outward, so both motor types work together. Near the poles, the clustering pulls microtubules inward, so the motors are antagonistic. Adapted from [121].

stop moving entirely, and their minus ends clump together to form poles (Fig. 34).

### 1.6.2 Liquid crystal models

The liquid crystal model for the mitotic spindle adequately models the spindle of the *Xenopus Laevis* frog [156, 157] The mitotic spindle of the *Xenopus Laevis* frog does not have well defined microtubule bundles, as is typical for human cells, but an almost continuous distribution of microtubule bundles throughout the spindle, which still connect the kinetochores with the poles. The liquid crystal model gets its name from the fact that such spindles really resemble liquid crystals.

The model is complex, and uses force balance equations, along with fluctuation correlations of the microtubule density throughout the volume of the spindle. The active liquid

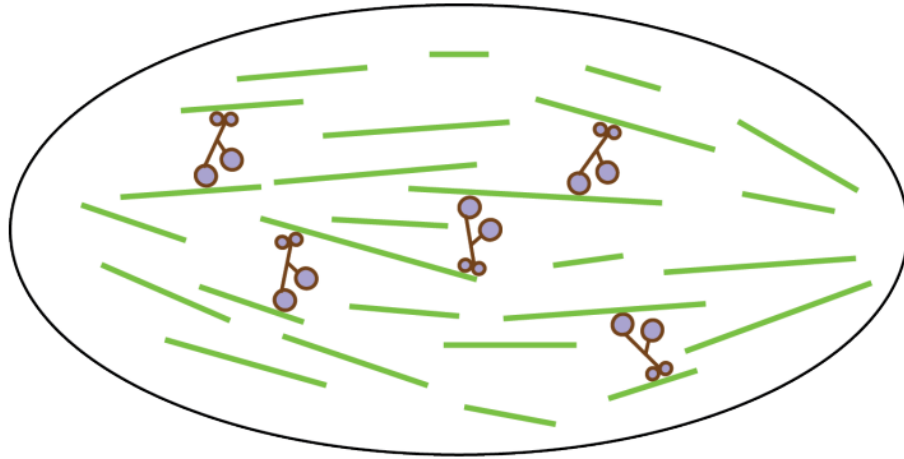


Figure 35: Schematic of the liquid crystal model. Microtubules are depicted as green rods, while molecular motors are multi-headed proteins in purple. Unlike human spindles, spindles suitable for a description with the liquid crystal model have microtubule bundles distributed throughout the spindle space. Adapted from [157].

crystal theory provides a basis for investigating the wide range of spindle phenomenology that has been observed, such as the fusion of two spindles [171] or the response of the spindle to physical perturbations [172]. Molecular perturbations should cause the theory's parameters, such as  $K$ , the orientational elasticity, or  $W$ , the strength of the active stress, to change, potentially resulting in changes in spindle structure and dynamics. While more research is needed to predict which parameters will be affected by specific molecular perturbations, this could be investigated empirically by measuring how molecular perturbations influence the theory's parameters using fluctuations. More broadly, the success of such a simple description shows that, despite spindles' extreme molecular complexity [28], their structure and dynamics at cellular scales are quantitatively accounted for using just a few effective parameters and argues that active liquid crystal theories are a promising route for developing predictive theories of cell biology [173].

### 1.6.3 Elasticity models

Mechanically, polymers are stiff rods with an elastic modulus comparable to that of plexiglass [24]. In vivo, microtubule associated proteins and mechanical stresses in the cell can affect the microtubule mechanics [174, 175]. In particular, microtubules are often bundled by various cross-linking proteins [176], which presumably increases the effective microtubule stiffness further [177]. Each microtubule is a thin elastic rod with high flexural rigidity. In theory, the bundle's rigidity can vary along its length due to a variety of factors such as spatial variation in the number of microtubules, cross-linking density, and local mechanochemistry of the cell. In this case, the flexural rigidity is assumed to be constant. A flexible, hinge-like connection between the microtubule bundles and the centrosome (spindle pole), according to the model, is not robust and is an ineffective method of transducing the motors' signals. forces in the spindle: in this case, the tightly cross-linked bundle of 10 microtubules is equivalent to a weak spring with  $K = 1pN/mum$ , so just one more molecular motor could significantly deform the spindle. Furthermore, a force change in the narrow range of 25-35 pN per bundle would significantly deform the spindle aspect ratio from 10 to 1, which was never observed. If the microtubules are clamped at the spindle poles, the spindle's mechanical properties improve: each microtubule bundle can withstand up to 50 pN of pushing or sliding force before buckling. The microtubule bundles act as effective compressed springs in this regime. The stiffness of these 'elastic springs' is on the order of  $K = 30pN/mum$ , so only a few tens of motors would noticeably deform the spindle. The model predicts a characteristic inflection point in the middle of a bundle when it buckles at forces greater than 50 pN. In summary, our model suggests that the microtubule bundles in the spindle can be considered as a series of springs compressed by molecular motors.



Figure 36: A macroscopic example in which a sponge is deformed by hand, illustrating the relationship between the rotational force and shape. The sponge can be bent in two different ways (left and middle) and twisted (right). Adapted from [178].

## 2 Shapes and symmetries in the mitotic spindle

### 2.1 The mitotic spindle is chiral

Rotational forces can deform an elastic object in different ways, where the shape of the object provides information about the force direction. The relationship between the rotational force and shape can be illustrated by a macroscopic example in which we deform a sponge by hand Fig. 36.

### 2.2 Mitotic spindle chirality arises from the twisted shape of microtubule bundles

Recent mathematical models [43, 178] confirm the hints obtained from the macroscopic example with the sponge. The two-dimensional shapes resembling the letter 'S' appear in the theoretical model when rotational forces act perpendicular to the pole-to-pole axis Fig. 37.

Rotational forces in any other direction, on the other hand, result in three-dimensional shapes with a helical twist, according to [43]. When a component of the rotational force parallel to the pole-to-pole axis exists, helical shapes of microtubule bundles in the spindle form. A typical spindle side view provides a wealth of information about the complex shapes of microtubule bundles, but it is insufficient to determine whether these shapes lie in a single plane or extend in three dimensions, as helical shapes do. Looking at the spindles along the



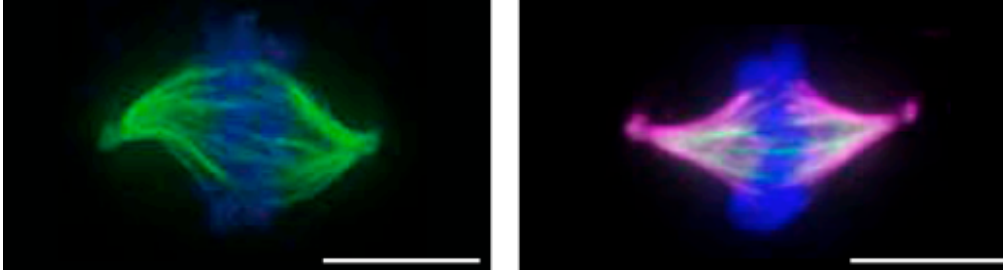


Figure 37: Left: S-shaped spindle in a lung cancer cell line. Microtubules are shown in green and DNA in blue. Right:  $\alpha$ -shaped spindle in a HeLa cell overexpressing HSET (kinesin-14). Microtubules are shown in magenta, HSET in green, and DNA in blue Adapted from [178].

pole-to-pole axis helps to visualize helical shapes. (end-on view in Fig. 38).

Interpolar microtubule bundles look like petals of a flower, whereas in a spindle without helical shapes, the bundles look like an aster (compare end-on view in Fig. 38). The difference between is most pronounced in the central part of the bundles (dark green segments in Fig. 38), where real bundles have an arc-like shape, in contrast to straight lines in the spindle with and without helical bundles, respectively. The handedness of the bundles can be determined by connecting the end points of each arc by an arrow, following the bundle in the direction towards the observer (Fig. 38). If an arrow rotates clockwise with respect to the spindle pole (as in the end-on view in Fig. 38), the handedness of the bundle is left. Such bundle and its mirror image are not superimposable, thus, the bundle is chiral. If the bundles in an individual spindle predominantly show the same handedness, the spindle is chiral (Fig. 38). To explore the three-dimensional contours of microtubule bundles in the spindle, we looked at the spindles along the pole-to-pole axis. Microtubule bundles, which appear as spots in a cross-section of the spindle, were tracked through the  $z$ -stacks [43] Fig. 39.

Surprisingly, it was discovered that the arrows connecting the end points of the central part of each bundle rotate clockwise, implying that bundles follow a left-handed helical path along the pole-to-pole axis Fig. 39. Thus, the spindle is a chiral object. The experimentally measured three-dimensional shapes of microtubule bundles can be used to deduce linear and

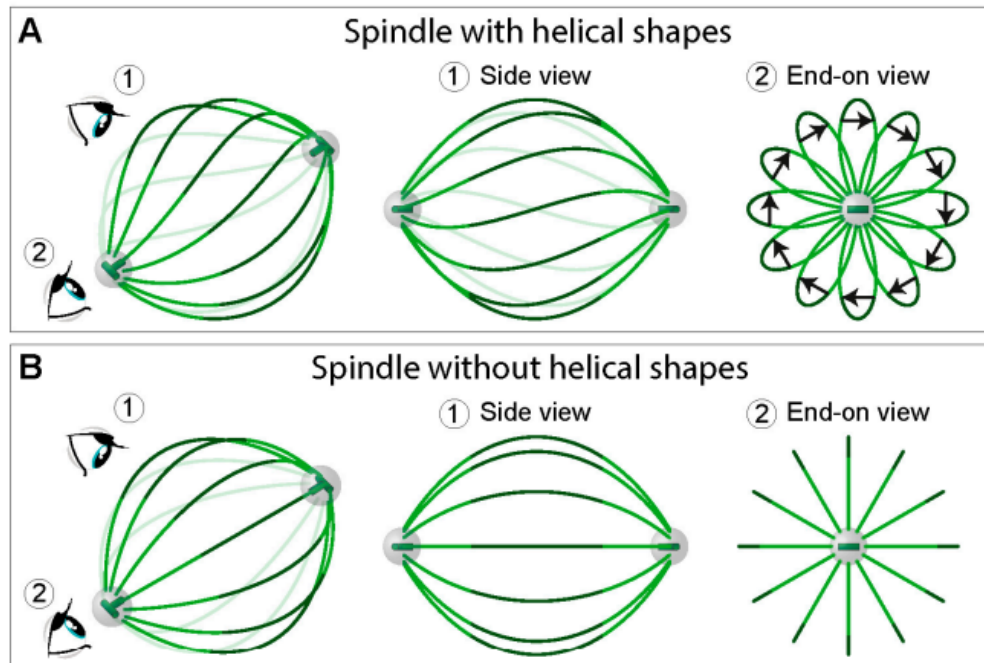


Figure 38: The chirality of the spindle is caused by a twisting moment in the spindle. A simplified scheme of a spindle (A) with and without helical microtubule bundle shapes. In each panel, an arbitrary angle view of the spindle is shown on the left, along with eye signs indicating the view angle for the side view (1) and the end-on view (2), which are shown in the middle and on the right, respectively. Green lines represent interpolar microtubule bundles, with the central portion highlighted in a darker shade. The arrows in (A) connect the end points of each bundle's central part, following the bundle in the direction of the observer. Centrosomes are represented by grey spheres with centrioles (green) inside. Adapted from [178].

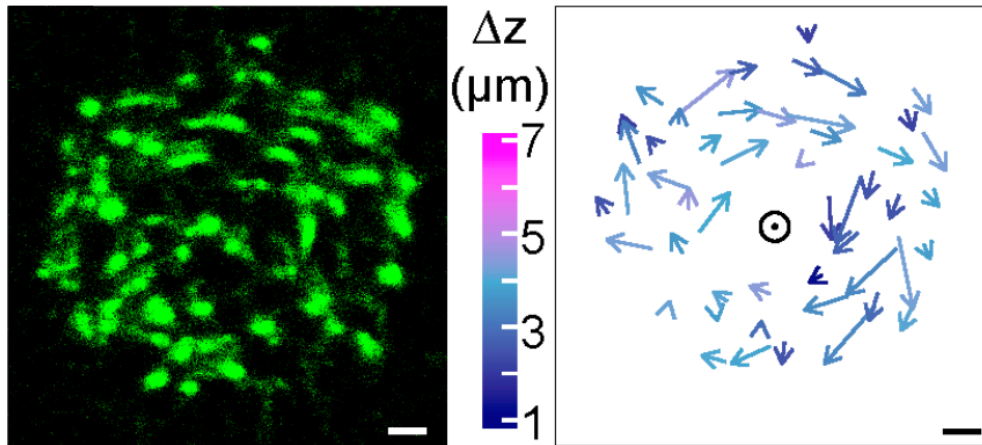


Figure 39: Left, cross section of a spindle in a HeLa cell expressing PRC1-GFP (green), which marks the central part of interpolar bundles, i.e., bridging fibres [179]. Right, arrows connecting starting and ending points of PRC1-GFP bundles traced in the direction towards the observer. Longer arrows roughly correspond to larger twist around the spindle axis (circle) and colors show z-distance between starting and ending points (see colour bar). Scale bars,  $1 \mu\text{m}$ . Adapted from [178].

rotational forces in the spindle by comparison with a theoretical model [43]. The model predicts that a twisting moment of roughly  $-10pN \times \mu\text{m}$  can explain the measured twist of the bundles, which turn by about  $-2 \text{ deg} \times \mu\text{m}^{-1}$  around the spindle axis.

### 2.3 Effects of motor proteins on mitotic spindle chirality

The twist of microtubule bundles is potentially generated by motor proteins that, in addition to linear forces, exert rotational forces on microtubules by switching protofilaments with a bias in a certain direction [180–190]. The first molecular motor discovered to generate torque was the single-headed axonemal dynein. In *in vitro* gliding motility assays, surface-attached dynein motors rotated the microtubules around their axis in a clockwise motion, when viewed from the minus-end of the microtubules, while translocating them in a linear fashion [180]. The same type of assay was used to show that the minus-end directed motor kinesin-14 (Ncd) generates torques which rotate microtubules in a clockwise direction as viewed from

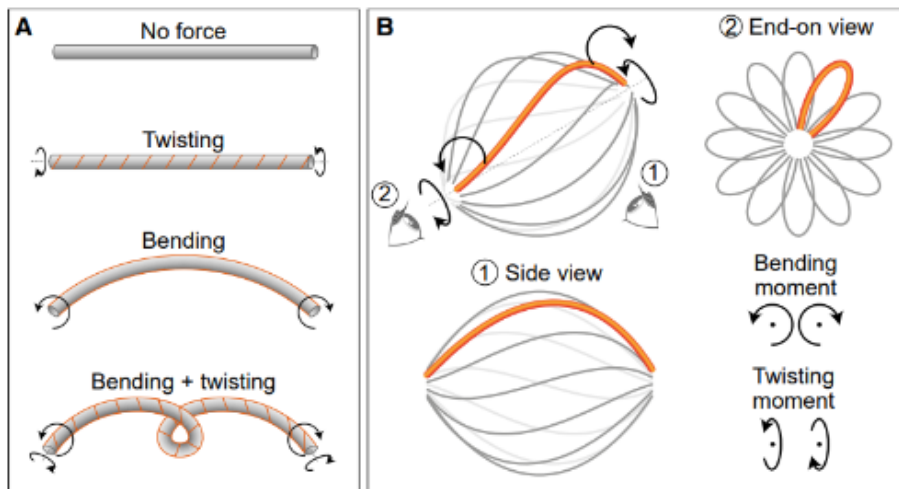


Figure 40: Rotational forces and spindle chirality bend and twist. (A) A relaxed elastic rod (grey) is straight. When the twisting moment is applied, it becomes twisted (orange line), bent when the bending moment is applied, and achieves a complex shape when both moments, bending and twisting, are applied. (B) Three projections of a simplified spindle that demonstrate its chiral structure. A view of a spindle from any angle (top, left), with eye signs indicating the view angle for the side view (1) and the end-on view (2). Gray lines represent interpolar microtubule bundles, with one bundle highlighted in orange. The observed chiral shapes are produced by bending and twisting moments (curved arrows) acting on the bundle. Adapted from [70].

their minus-ends [183], and similar results were obtained with kinesin-14 in an assay in which microtubules glide along each other, where the transport microtubule moves in a helical motion in a clockwise direction [182]. Counter-clockwise rotation direction has been found for the plus-end-directed motor protein kinesin-5 (Eg5), which was observed as a corkscrew motion of a sliding microtubule on surface-attached motors [184]. Gliding motility assays, as well as motility assays on freely suspended microtubules, showed a counter-clockwise rotation for the plus-end-directed motor protein kinesin-8 (Kip3) [181, 187], while another study found that kinesin-8 can switch protofilaments in both directions [189]. Several other motor proteins also exhibit rotational movements, including kinesin-130,36, kinesin-232, cytoplasmic dynein [188], and kinesin-6 (MKLP1) [191]. In contrast to this vast body of knowledge on chiral motor stepping in vitro, little is known about the role of motor proteins and their asymmetric stepping in the generation of torques within microtubule bundles in vivo, and thus spindle twist.

The left-handed twist of the bundles disappears when kinesin-5 (Kif11/Eg5) motor is inactivated during metaphase, suggesting that this motor is important for the maintenance of helical shapes [43]. This motor is known to be crucial for spindle assembly [164, 192], yet dispensable for spindle maintenance in many human cell lines [193].

Motors are often characterised in terms of linear forces, which can be pulling or pushing forces depending on the direction. Motors can also exert rotating pressures on the microtubule. In vitro studies have shown that axonemal dynein [180], kinesin-14 (Ncd) [183], kinesin-5 (Eg5) [184], kinesin-8 (Kip3) [187], and cytoplasmic dynein [188] can generate rotational forces on the microtubule by stepping sideways while walking along the microtubule. For example, Kip3 motors wick microtubule protofilaments with a bias toward the left, and molecular modelling suggests that this bias is due to the asymmetric geometry of the motor neck linker complex [190]. Unlike these motors, kinesin-1 walks along the microtubule protofilament as it moves from one tubulin dimer to the next. However, according to a recent study, kinesin-1 can generate rotational forces on the microtubule by rotating around an axis

perpendicular to the microtubule [190]. The rotational forces produced by this method can reach  $1.65pN$ . If the motors required for spindle chirality generate similar rotational forces, 10-100 motors per microtubule bundle could generate helical shapes based on the bundle's estimated bending and twisting moments. We hypothesise that motors can generate rotational forces in two areas of the spindle: the overlap zone of antiparallel microtubules and the spindle pole. Motors in the overlap zone may turn antiparallel microtubules around each other while sliding them, resulting in helical twisting of the bundle. Motors attached to the pole can rotate microtubules as they walk along them towards the spindle equator. To understand how rotational forces are generated and balanced in the spindle, new experiments and theoretical models are required.

## 2.4 Role of mitotic spindle chirality

When the bridging fibre model is used to describe the three-dimensional architecture of the entire spindle, surprising results emerge. In this case, rotational forces can act in any direction rather than just within a plane. According to this model, the microtubule bundles in the spindle extend in three dimensions and have a twisted shape rather than lying in a plane like meridians on Earth. [43]. Motivated by this unusual prediction, experiments showed that the bridging fibres indeed display a twisted shape [43]. When the spindle is observed along the axis, the twisted shape is visible as the rotation of bridging fibres around the spindle axis. The fibres have a left-handed twist, making the entire spindle chiral. Twist has also been observed in yeast rod-shaped spindles, where individual microtubules within the bundle twist around each other. [194, 195]. Recent 3D reconstructions of the microtubule organization in spindles of human cells show an occasional twist of microtubules within a bundle [106].

The twisted shapes of microtubule bundles are most likely generated by motor proteins, given that motors exert rotational forces on the microtubule in addition to linear forces. In vitro studies have shown that the mitotic motors kinesin-14 (Ncd) [182, 183, 196], kinesin-5 (Eg5) [184], kinesin-8 (Kip3) [181, 187, 189], and cytoplasmic dynein [188], can generate ro-

tational forces on the microtubule by stepping sideways while moving along the microtubule. In the spindle, the twisted shape of the bundles depends on kinesin-5 [43] and likely also on other motors, which may generate rotational forces in the overlap zone of antiparallel microtubules and at the spindle pole. In the overlap zone, motors may twist the antiparallel microtubules around each other, while the motors attached to the pole may rotate the microtubules as they walk along them [178]. To explore these hypotheses, new experiments and theoretical models are needed with the aim to understand how rotational forces are generated and balanced in the spindle. Furthermore, the biological function of spindle chirality is unknown at the moment. The discovery of rotational forces on the scale of individual motor proteins and the entire spindle opens up an exciting new field of study into the mechanisms and biological roles of rotational forces in mitosis. Microtubule bundles twist as a result of internal torques as well as linear forces. The experimentally measured three-dimensional shapes of microtubule bundles, primarily bridging fibres that laterally link sister kinetochore fibres and are marked by protein regulator of cytokinesis 1 (PRC1), were used to calculate spindle forces and torques by comparing them to a theoretical model [43]. Left-handed twist was also observed in spindles lacking NuMA and kinesin-5 activity in RPE1 cells during anaphase [197]. Another organism whose spindles are prominently twisted is a unicellular eukaryote, amoeba *Naegleria gruberi*. The amoeba spindles are predominantly twisted in a right-handed fashion [3].

How precisely to quantify, and even measure microtubule bundle twist is an open question, and we shall see in the next chapter how this has been tackled.

### **3 Quantifying the effects of spindle chirality**

Because of the mystery surround spindle chirality, many efforts have been made to try and quantify it, but none have been comprehensive. Understanding spindle chirality will allow us to understand the forces and torques which It is possible to directly measure the forces

exerted on microtubule bundles, [198], but it is difficult due to the small scales involved. To supplement such experiments, the forces can be measured indirectly by inferring them from the shape of the microtubule bundle.[21, 199, 200]. This method is based on the fact that microtubules are naturally straight but can change shape depending on the forces acting on them. This method was used to calculate the bending rigidity of single microtubules [200] and microtubule polymerization forces [199]. Similarly, methods to characterize the shape of cytoskeletal filaments, such as actin and microtubule bundles, together with relevant forces have been developed based on open active contours [201–203] or by directly calculating the Frenet frame [204, 205]. A shape-based approach to force quantification can also be applied to spindle microtubule bundles. Individual microtubule bundle shapes shape the entire spindle, similar to mitotic spindles in human cells, as the spindle shapes of most metazoans are similar [206]. Even in spindles without centrosomes, e.g. in some protozoan organisms such as amoebas, a similar spindle shape is present [207]. The same is the case for plant spindles [208]. In some lower eukaryotes, e.g. yeasts, this type of spindle shape is absent as their spindles consist of a single straight microtubule bundle [209]. Because the spindle shape reflects the forces within it, precise measurement and characterization of microtubule bundle shapes is critical for understanding the forces that act on chromosomes during mitosis. It was recently discovered that the spindle in human cells is chiral, with bundles following a left-handed helical path. [2, 43]. Chirality is also present in the spindles of amoeba *Naegleria gruberi*, though the twist is right-handed [3]. The chirality of the spindle is best visualized by looking at the spindle end-on, i.e., along the pole-to-pole axis, to observe the three-dimensional shapes with a helical twist Fig. 41. This view allows for visualization of microtubule bundles as flower petals. By following the bundles in the direction towards the observer, the petals rotate clockwise if the bundles follow a left-handed helical path, which corresponds to negative values of twist Fig. 41. Vice versa, the petals rotate counter-clockwise, and have a positive value of twist, if the bundles follow a right-handed helical path. The reason for this chirality may be the action of the motor proteins that exert rotational



forces on the microtubules, such as kinesin-5 (Kif11/Eg5) [184], whose inhibition leads to the abolishment of left-handed twist [43]. Motor proteins generate these forces by 'walking' along a microtubule and performing side-steps while switching protofilaments along the same microtubule [187, 188, 190].

We develop a method for the analysis and measurement of the geometrical properties of microtubule bundles within the spindle. To extract information about the shape of a microtubule bundle from experimental data containing a small number of points per bundle, we introduce a robust approach, in which we consider the bundle as a part of a circular arc, leading to two parameters characterizing the bundle. This description allows us to faithfully represent the microtubule bundle and extract the relevant geometrical information, i.e., the curvature and the twist, but it is also simple enough to be done systematically on a wide variety of microtubule bundles.

### **3.0.1 Cell lines and microtubule visualization**

Twist can be measured in every cell line that has labelled microtubule bundles. This label can be a fluorescent protein tag on a microtubule bundle (e.g., on tubulin) or on proteins that are associated with microtubule bundles in a way that they cover most of the length of the bundle (e.g., PRC1, Fig. 41). Tags can be inserted into the cells on a plasmid by transfection or endogenously expressed after CRISPR/Cas-9 manipulation. The chosen tags should also allow for the visualization of the spindle poles. It is possible to measure twist both in live and fixed cells. In fixed cells it is important to perform an appropriate fixation method. Fixation with methanol can often cause spindles to shrink along the  $z$ -direction, yielding measurements that are not relevant for live cells, thus care should be taken that the shapes of spindles in fixed cells closely resemble spindles in live cells. In fixed cells, fluorescently labelled antibodies can also be used for tubulin visualization. The spindle in Fig. 41 was imaged as described in [2]. Further examples of imaging both live and fixed cells for purpose of measuring twist can be found in [43]. Examples of microscope settings for the purpose of

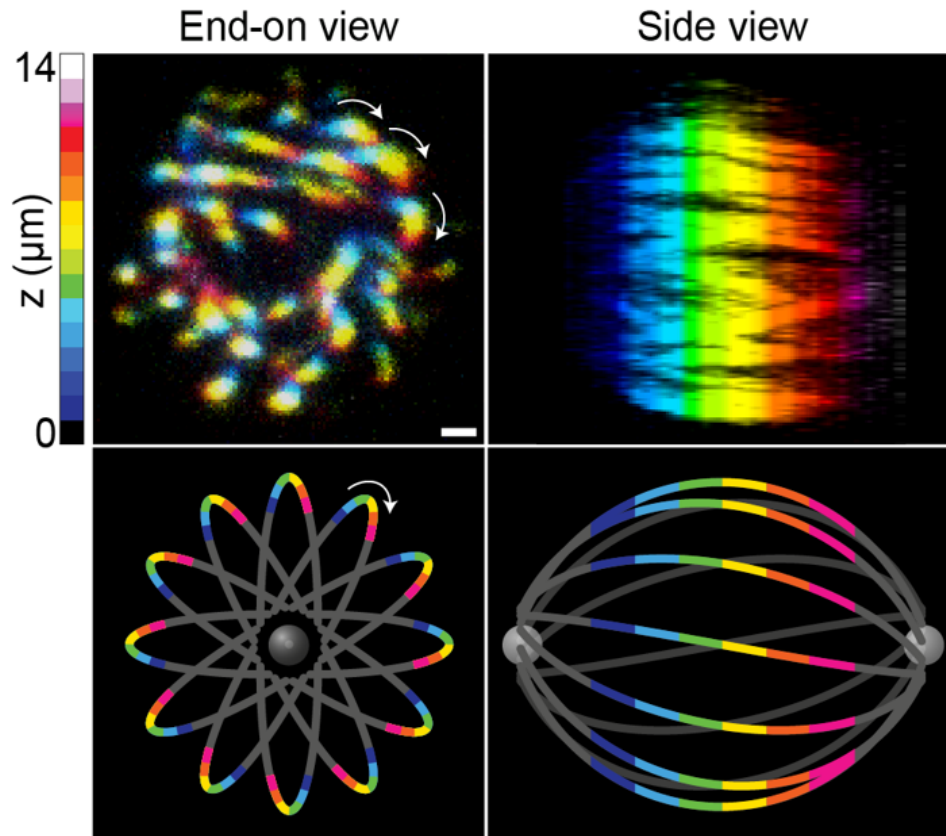


Figure 41: End-on view and side view of a human mitotic spindle. Top, projections of confocal images, colour coded for the position along the pole-to-pole axis (see colour bar), of the metaphase spindle in a live HeLa cell expressing PRC1-GFP shown in the end-on view (left) and side view (right). Scale bar,  $1 \mu\text{m}$ . Bottom, schematic representations of spindle microtubule bundles shown in the end-on view (left) and side view (right). The arrows show the direction of the bundle twist along the pole-to-pole axis, when looking towards the observer. The clockwise direction of the arrows indicates left-handed twist. Adapted from [1].

imaging spindles for measuring twist can be found in Section 3.0.1, as well as in [2].

### 3.1 The Oblique Circle Method

During cell division, the mitotic spindle divides the genetic material of the mother cell into two equal parts. Precisely regulated forces within the spindle are required for the proper movement of chromosomes and the functional spindle shape. The focus of most research in the field is on tension forces acting on kinetochores, whereas forces that regulate spatial organization of the whole spindle remain poorly understood. The recent discovery of twisted shapes of microtubule bundles suggests that the bundles extend along curved paths in three dimensions, meaning that rotational forces, in addition to linear forces, exist in the spindle. We develop a robust method to measure the curvature and twist of microtubule bundles, which represent information characteristic for each bundle, to facilitate understanding of linear and rotational forces in the spindle.

#### 3.1.1 Image analysis and data tracking

Individual microtubule bundles need to be tracked in order to acquire their  $x$ ,  $y$ ,  $z$  coordinates in each  $z$ -plane of the entire  $z$ -stack. Examples of such microtubule tracking can be found in [43]. Each spindle has two poles positioned along the pole-to-pole axis, along with  $N$  microtubule bundles denoted by index  $i = 1, \dots, N$ . The  $i$ -th bundle is represented by set of  $n_i$  tracked points  $T_{ij} = (x_j, y_j, z_j)_i$  where  $j = 1, \dots, n_i$  is the index of individual points Fig. 42. Each bundle is tracked through all  $z$ -planes in the direction from left centrosome towards the right centrosome (the left centrosome represents the bottom  $z$ -plane, while the right centrosome represents the highest tracked  $z$ -plane in the stack). The positions of the centrosomes are the starting and end points of the spindle, so we include this information by extending the coordinates of each single bundle with the centrosome coordinates, with the left centrosome as the starting data point,  $T_{i0}$ , and the right centrosome as the ending

data point,  $T_{in_{i+1}}$  (sample data for the spindle from Fig. 41 is given in Table S1 [1]), and thus coordinates of the  $i$ -th bundle are indexed  $j = 0, \dots, n_i + 1$ . The  $z$ -plane refers to the imaging plane, which we convert to its corresponding  $z$ -coordinate by multiplying with the distance between successive planes set during image acquisition and by a factor of 0.81 to correct for the refractive index mismatch [43]. In the example case in Fig. 41 the distance between  $z$ -planes is equal to  $405nm$  after correction.

### 3.1.2 Choosing a coordinate system

During imaging, spindles have an arbitrary location and orientation with respect to the laboratory coordinate system. To make tracks of microtubule bundles suitable for analysis, we transform the laboratory coordinate system so that the left centrosome is positioned at the origin of the new coordinate system and the right centrosome is positioned on the  $z$ -axis Fig. 42, which we term the spindle coordinate system. The spindle coordinate system is obtained by two transformations: (i) translation  $T'_{ij} = T_{ij} - T_0$ , where  $T'_{ij}$  is transformed coordinate and  $T_0$  is position of the left centrosome ( $T_0$  is given by the first row of Table S1 [1]), and (ii) subsequent rotation  $T''_{ij} = MT'_{ij}$ , where  $T''_{ij}$  are coordinates in the spindle coordinate system and  $M$  is the rotation matrix which aligns the pole-to-pole axis with the  $z$ -axis of the spindle coordinate system and the unit vector  $\hat{z} = (0, 0, 1)$ . The rotation matrix is a textbook problem and it can be calculated, e.g., as the Rodrigues rotation [210] matrix. A Python implementation is provided with the accompanying paper [1]. Finally, it is convenient to parametrise points by using cylindrical coordinates,  $T''_{ij} = (d_j \cos \phi_j, d_j \sin \phi_j, z_j)_i$ , where  $d_j$ ,  $\phi_j$ , and  $z_j$  are, respectively, the radius, azimuth and axial position.

### 3.1.3 Fitting a circular arc to the microtubule bundle shapes

To characterize complex three-dimensional shapes of microtubule bundles from noisy experimental data requires a robust approach. In our method, curvature and twist, which measure the extent the bundles extend along curved paths in three dimensions, are the geometrical

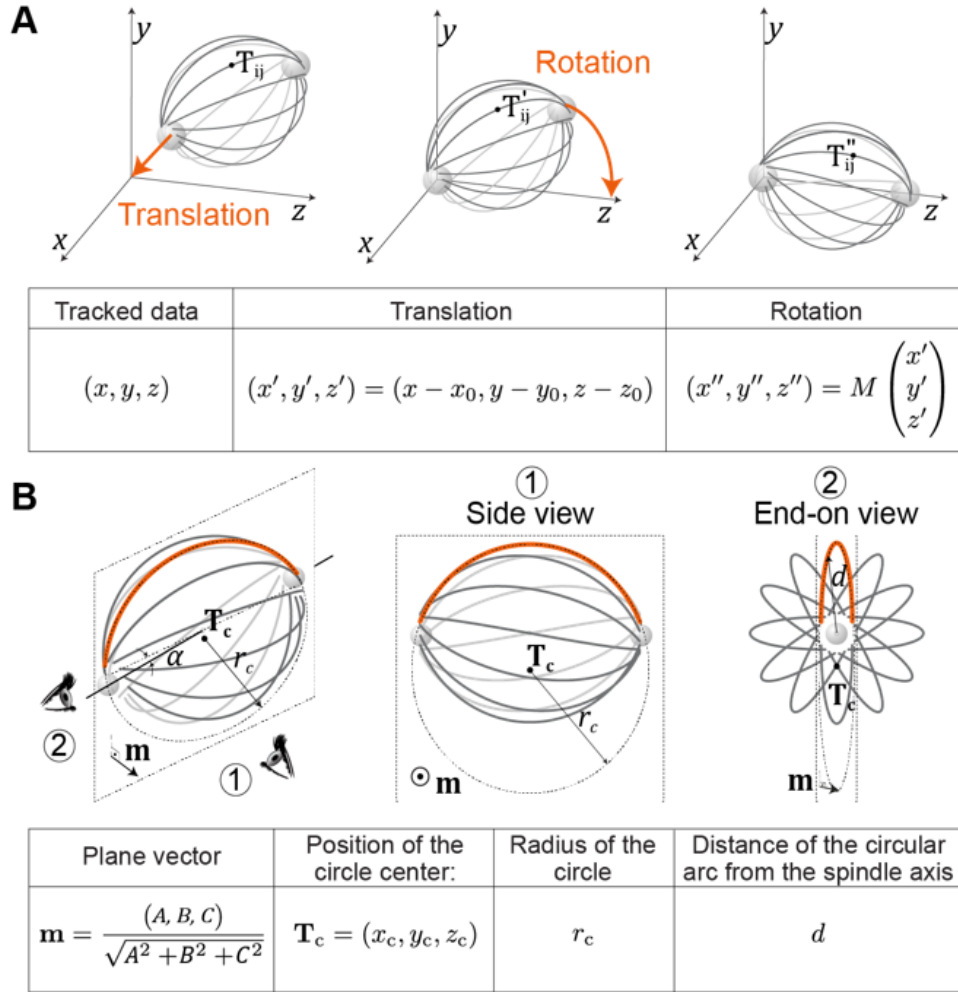


Figure 42: Overview of method. (A) The spindle, along with the centrosomes and the marked traced bundle point  $T_{ij}$ , is positioned at an arbitrary angle and distance from the origin of the coordinate system (left). The spindle is translated so that the left centrosome is located at the origin of the coordinate system (middle). The spindle is rotated so that the pole-to-pole axis, along with the right centrosome, aligns with the  $z$ -axis of the coordinate system (right). (B) A view of the spindle from an arbitrary angle (left) where eye signs mark the view angle for the side view (1) and the end-on view (2), which are shown in the middle and on the right, respectively. A microtubule bundle (orange curved line) is fitted by a circle of radius  $r_c$ . The angle between the central spindle axis (solid line) and the plane in which the fitted circle lies (dashed parallelogram) is denoted. The parameters used to calculate the twist and curvature are named at the bottom of the scheme. Adapted from [1].

quantities that represent the information about the bundle shapes. To obtain these quantities from the experimental traces, we fit a circular arc extending through three dimensions to these data. To fit a circular arc in an easily reproducible way, we first fit a plane, and then fit a circle that lies in this plane Fig. 42. In the rest of this section, we focus on one microtubule bundle only, thus we omit the bundle index  $i$ . In the first step, we fit the best-fitting least squares distance plane  $Ax + By + Cz + D = 0$ , where  $A$ ,  $B$ ,  $C$ , and  $D$  are the parameters of the general form equation of the plane, which we term the bundle plane, to the traced data. We solve the total least squares problem by using the singular value decomposition method ([211]). The normal unit vector of the bundle plane is given by  $m = (A, B, C)/\sqrt{A^2 + B^2 + C^2}$ . We denote the angle of vector  $\mathbf{m}$  with respect to the pole-to-pole axis as  $\alpha$ , which we calculate from the scalar product  $\cos \alpha = m\hat{z}$ . In the second step, we fit a circle to the data by choosing only from those circles that lie in the bundle plane. We calculate the projection of the traced bundle points onto the bundle plane and fit a circular arc to them. Here we use the HyperLS algorithm [212], because fitting a circle with standard methods [213] is not suitable for straight bundles. The fitting parameters are the radius of the circle,  $r_c$ , and the position of the circle centre,  $T_c = (x_c, y_c, z_c)$ . These parameters, together with the normal vector of the bundle plane, determine the geometry of our traced bundle.

### 3.1.4 Calculation of the curvature and twist from the fitting parameters

Based on the fitting parameters, we can infer the curvature and twist of the microtubule bundle. The curvature of the bundle can be directly calculated from the radius of the fitted circle,

$$\kappa = 1/r_c \tag{3.1.1}$$

The twist, however, cannot be calculated in a such straightforward manner. We define the twist value,  $\omega$ , as a change of the azimuthal angle with respect to the axial position

$$\omega = d\phi/dz. \quad (3.1.2)$$

Please note that this value corresponds to the reciprocal value of the helical pitch multiplied by  $2\pi$ . The right-hand side of Eq. (3.1.2) can be calculated from the slope of the microtubule bundle with respect to the pole-to-pole axis as

$$\tan(\pi/2 - \alpha) = d\frac{d\phi}{dz}, \quad (3.1.3)$$

where we utilized the fact that the bundle plane vector  $\mathbf{m}$ , which defines the angle  $\alpha$ , is perpendicular to the tangent of the microtubule bundle. Here,  $d$  corresponds to the radial coordinate in the spindle coordinate system Fig. 42. For our case of discrete tracked bundle data points, we average the radius over all traced points  $\langle d \rangle = 1/n_i \sum_{j=1}^{n_i} d_j$ , and thus Eq. (3.1.2) can be written as

$$\omega = f \cot \alpha / \langle d \rangle, \quad (3.1.4)$$

where  $f$  is a dimensionless corrective factor, which we introduce to take into account the approximative approach of the method due to fitting a circular arc to the bundle segment. The corrective factor depends on the geometry of the bundle, but for bundle segments significantly shorter than the spindle length one can use  $f = 1$ , as shown in the section Error analysis. A Python implementation is provided in File S2 in [1].

### 3.1.5 Detailed worked example - synthetic spindle

To demonstrate the workings of our method, we provide a detailed worked example on a made-up mitotic spindle in a spindle coordinate system, which mimics the one shown in the schematic in Fig. 42, but also includes noise to make it closer to experimental data. We construct a synthetic spindle as a series of mathematically defined curves, which are evenly

distributed around the  $z$ -axis. Furthermore, to mimic discrete imaging planes, we choose to assign to the  $z$ -coordinates discrete values of  $z_j = L_0 + j\Delta L$ , where  $j = 1, \dots, n$ . Here,  $L_0 + \Delta L$  and  $L_0 + n\Delta L$  denote the starting point and ending  $z$ -coordinates of the synthetic bundle segments. Because all bundles are composed of the same number of points, parameter  $n$  has the same value for all bundles. To do this, we first define a bundle as a twisted circular arc:

$$B(z_j) \equiv \begin{bmatrix} \cos(\omega_0 z_j) & \sin(\omega_0 z_j) & 0 \\ -\sin(\omega_0 z_j) & \cos(\omega_0 z_j) & 0 \\ 0 & 0 & 1 \end{bmatrix} \begin{pmatrix} \sigma \eta_x(z_j) \\ \sqrt{R_0^2 - (z_j - L/2)^2} + y_0 + \sigma \eta_y \\ z_j \end{pmatrix} \quad (3.1.5)$$

The first term is a matrix which twists the bundle by twist parameter  $\omega_0$  around the  $z$ -axis. The second term is a vector that defines the bundle as a circular arc with added noise, where  $R_0 = 1/\kappa_0$  is radius of the circular arc,  $\kappa_0$  is the corresponding curvature,  $L$  is the pole-to-pole length of the spindle and constant  $y_0 = -\sqrt{(R_0^2 - (L/2)^2)}$  is chosen so that that the circular arc extends from one pole to the other. The two independent components of noise,  $\eta_x(z_j)$  and  $\eta_y(z_j)$ , are unit Gaussian white noises, and  $\sigma$  is the intensity of the noise. To obtain a spindle, we evenly arrange the  $N$  bundles around the pole-to-pole axis, so that the  $i$ -th bundle,  $T_i$ , is given by

$$T_i(z_j) \equiv \begin{bmatrix} \cos(\frac{2\pi i}{N}) & \sin(\frac{2\pi i}{N}) & 0 \\ -\sin(\frac{2\pi i}{N}) & \cos(\frac{2\pi i}{N}) & 0 \\ 0 & 0 & 1 \end{bmatrix} B(z_j) \quad (3.1.6)$$

The first term represents a matrix which rotates the  $i$ -th bundle, in order to obtain a spatial configuration of bundles distributed around the  $z$ -axis. Finally, positions of spindle poles are given by



$$T_{i,0} = \begin{pmatrix} 0 \\ 0 \\ 0 \end{pmatrix}, T_{i,n+1} = \begin{pmatrix} 0 \\ 0 \\ L \end{pmatrix} \quad (3.1.7)$$

Our method will determine the defined twist of this curve  $\omega$ , as well as its curvature  $\kappa$ .

### 3.1.6 Fitting circular arcs to the bundles of the synthetic spindle

We fit a circular arc to the synthetic bundles by using the approach described in the section Fitting a circular arc to the microtubule bundle shapes. In the first step, we obtain parameters of the bundle plane,  $A, B, C$ , and  $D$ . In the second step, we fit the circular arc which lies in the bundle plane and the corresponding radius  $r_c$ . To test our method, we apply the method to four different synthetic spindles shown in Fig. 43. The first and second spindles have short bundle segments, with and without noise, whereas the third and fourth spindles have long bundle segments, also with and without noise. In the case with short bundle segments the twist and curvature obtained from the method closely matches the parameters that define the synthetic spindle, both with and without noise Fig. 43. This agreement is expected because the fitting curve closely follows the synthetic bundle segments in the case without noise. In the case with long bundle segments, the obtained twist is slightly smaller than the defined one and the difference between the fitted curve and the synthetic bundle segments becomes visible Fig. 43.

### 3.1.7 Error analysis

Because in the case of long bundle segments the twist we obtain from our method underestimates the value of the twist parameter Fig. 43, we explored how the discrepancy changes with the length of the bundle segment, normalized by the length of the spindle  $\ell = n\Delta L/L$ , for noise intensity set to zero,  $\sigma = 0\mu\text{m}$ . We determine the twist of synthetic spindles by our method, for segment lengths ranging from  $0.2 - 10\mu\text{m}$  and plot the value of the twist  $\omega$

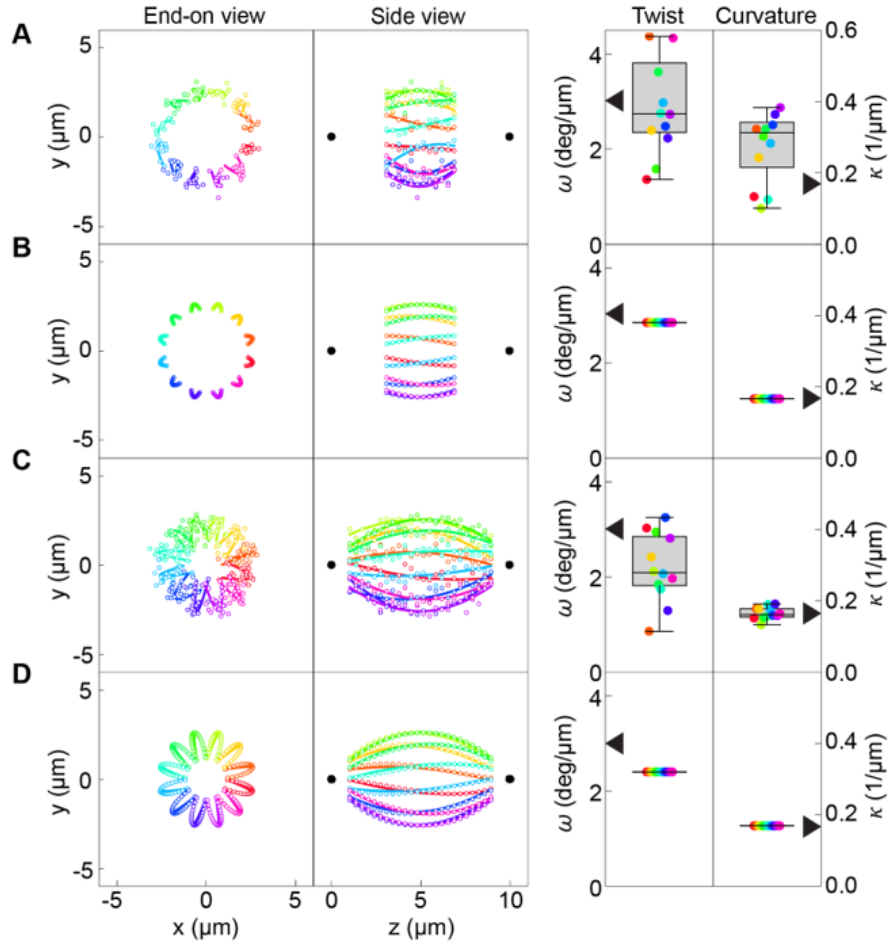


Figure 43: Application of method to four synthetic spindles. Synthetic spindles (colored circles) together with poles (black points), fits to them (colored lines) in the side view (left) and in the end-on view (middle), along with corresponding values of twist and curvature (right). The first two spindles have short bundle segments, in which 40% of central bundles were calculated, both with noise (A) and without noise (B). The last two spindles have long bundle segments, in which 80% of central bundles were calculated, with noise (C) and without noise (D). Short segments are comprised of  $n = 12$  points, with noise  $\sigma = 0.25\mu\text{m}$  in (A) and  $\sigma = 0\mu\text{m}$  in (B). Long segments are comprised of  $n = 24$  points, with noise  $\sigma = 0.25\mu\text{m}$  in (C) and  $\sigma = 0\mu\text{m}$  in (D). For all spindles, the values of the other parameters are  $\Delta L = 0.33\mu\text{m}$ ,  $\omega_0 = 3 \text{ deg}/\mu\text{m}$ ,  $L = 10\mu\text{m}$  and  $R_0 = 6\mu\text{m}$ , which corresponds to the curvature of  $\kappa_0 = 0.188\mu\text{m}^{-1}$ . Twist and curvature are shown with individual points and box and whisker plots (median and interquartile range, whiskers extending to 1.5 of the interquartile range). Black arrowheads show the values of parameters  $\omega_0$  and  $\kappa_0$ . Adapted from [1].

obtained from our method, divided by the twist parameter, as shown in Fig. 44. The other parameters have a smaller influence on the method. In particular, varying the value of  $\omega_0$  from 0 to 9 deg/ $\mu\text{m}$  Fig. 44 and  $R_0/L$  from 0.6 to 4 Fig. 44, we find that the difference in the twist ratios for different values of  $R_0$  does not exceed 5% and that the difference in the twist ratio for different values of  $\omega_0$  does not exceed 4.5%. In real spindles the twist of bundle ranges from 0 to 20 deg/ $\mu\text{m}$  and the width-length ratio  $R/L$  from 0.6 – 0.8 [2], making it possible to treat the error solely as a function of the bundle segment length  $\ell$ . The value of the twist obtained by our method systematically underestimates the exact value for longer bundle segments, which we can use to remedy this discrepancy. To obtain, by our method, a value of the twist close to the actual value, we need to calculate the corrective factor  $f$  in Eq. (3.1.4). Approximatively, this function is given by

$$f(\ell) = 1 - 0.178\ell^2 - 0.178\ell^4. \quad (3.1.8)$$

Since the synthetic spindle is similar to spindles found in HeLa cells, this phenomenological function can be used for all bundles in HeLa spindles, and also for spindles that have shapes similar to HeLa cells. For the majority of bundles this correction will be less than 5% [2, 3, 43]. To explore whether we can use our method to detect twist and curvature in noisy experimental data, we apply our method to the synthetic spindle and estimate for which noise intensity values twist and curvature are detectable. Here we calculate the relative dispersion of a measured twist as  $\text{RSD}_{\omega_0} = 1/\omega_0 \sqrt{1/N \sum_{i=1}^N (\omega_i - \omega_0)^2}$ , for different values of the noise intensity and twist (Fig. 44). We found that for a broad range of noise intensity values around 80nm, which is equivalent to the pixel size of the confocal microscope, and twist values around 3 deg/ $\mu\text{m}$ , the relative dispersion was significantly below 1. A value of RSD below 1 signifies that the twist is detectable, i.e.,  $\text{RSD} = 1$  is the detection limit. Similarly, we calculate the relative dispersion of the curvature as  $\text{RSD}_{(\kappa_0)} = R_0 \sqrt{(1/N \sum_{i=1}^N (1/R_i - 1/R_0)^2)}$ . We have found that for a broad range of values typical for spindles the curvature was detectable

Fig. 44. Based on these results, we conclude that the method can reliably detect twist and curvature in noisy experimental data.

## 3.2 Application of the Oblique Circle Method to real spindles

To apply our method to real spindles and compare the results with the method from [43], we first *analysed* the HeLa cell spindle from Fig. 41 (Table S2 in [1]) and obtained fits and values for the curvature and twist Fig. 45 (Table S3 in [1]). The resulting twist is  $\omega = -2.3 \pm 0.3 \text{ deg}/\mu\text{m}$  (*mean*  $\pm$  *s.e.m.*) and the curvature is  $\kappa = 0.08 \pm 0.01 \text{ deg}/\mu\text{m}$ . The value of twist is consistent with the value of obtained by using the method from [43],  $\omega = -2.3 \pm 0.4 \text{ deg}/\mu\text{m}$ . The value of curvature is similar to the value obtained from SOAX [203],  $\kappa = 0.07 \pm 0.01 \text{ deg}/\mu\text{m}$ , with SOAX parameters chosen in such a way that number of converged snakes is similar to the number of tracked bundles (File S3 in [1]).

Furthermore, to explore how the Oblique Circle Method performs on a wide range of test cases, we applied it to spindles from the HeLa cell line, including live and fixed cells, stained with different methods, and with applied STLC and Lat A treatments, from [43]. The obtained results are similar to those from [43], even though the obtained values were slightly lower Fig. 46.

### 3.2.1 Knowledge gained from the Oblique Circle Method

Curvature and twist provide geometrical information about the shape of the bundle. Based on these geometrical parameters, we can infer information about rotational forces, i.e., bending and twisting moments. Curvature can provide an estimate of the bending moment acting upon the bundle  $M_{bend} = EI/r_c$ , where  $r_c$  is the radius of curvature measured for a microtubule bundle and  $EI$  is its flexural rigidity given as Young's modulus times the second moment of inertia of the cross-section (Eq. (1.5.46)). In the case of bundles with multiple microtubules, the flexural rigidity depends on the number of microtubules in microtubule

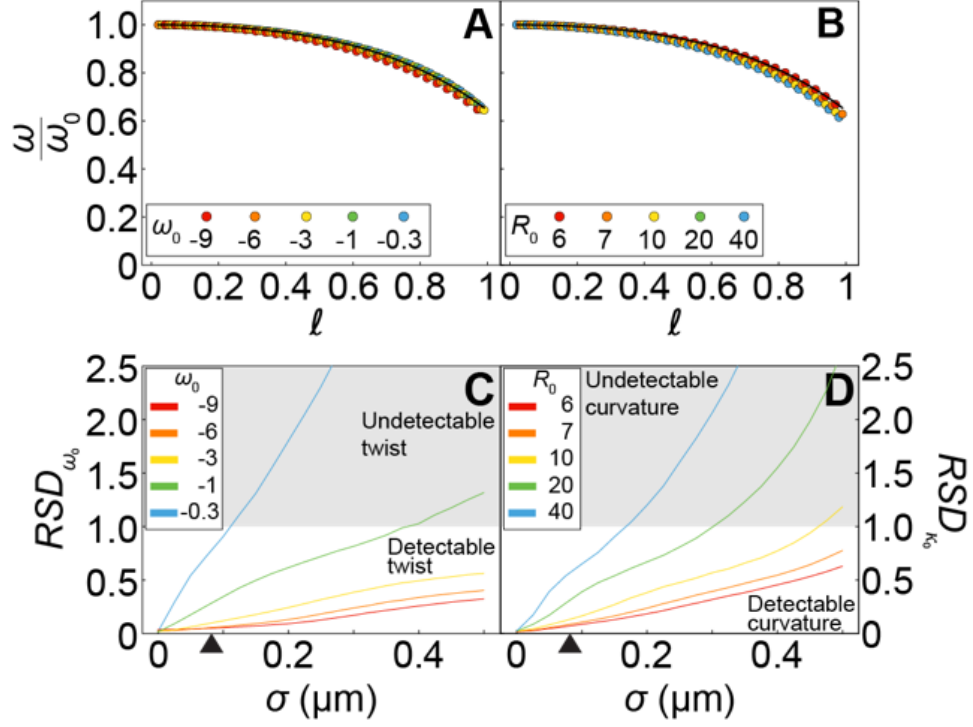


Figure 44: Error analysis for twist and curvature of synthetic spindles. (A), the dots show the dependence of the twist ratio for a spindle with  $\omega_0 = 3 \text{ deg}/\mu\text{m}$  and five different values of  $R_0$ , shown in the legend, as a function of the normalized bundle segment length. The values for  $R_0 = 20 \mu\text{m}$  are not visible, because they overlap with values for  $R_0 = 40 \mu\text{m}$ . (B), the dots show the dependence of the twist ratio for a spindle with  $R_0 = 6 \mu\text{m}$  and five different values of  $\omega_0$ , shown in the legend, as a function of the normalized bundle segment length. In both (A) and (B) the thick black line shows the function  $f(\ell)$  from Eq. (3.1.8) and there is no noise,  $\sigma = 0 \mu\text{m}$ . (C), the lines show the relative dispersion of the curvature, for a spindle with  $\omega_0 = 3 \text{ deg}/\mu\text{m}$  and five different values of  $R_0$ , shown in the legend, as a function of the noise intensity. (D), the lines show the relative dispersion of the method for twist, for a spindle with  $R_0 = 6 \mu\text{m}$  and five different values of  $\omega_0$ , shown in the legend, as a function of the noise intensity. In both (C) and (D)  $\ell = 0.6$ , the undetectable region is shaded grey and black arrowheads denote  $\sigma = 0.08 \mu\text{m}$ . In all panels  $L = 10 \mu\text{m}$ ,  $N = 20000$  and  $n = 18$ . Adapted from [1].

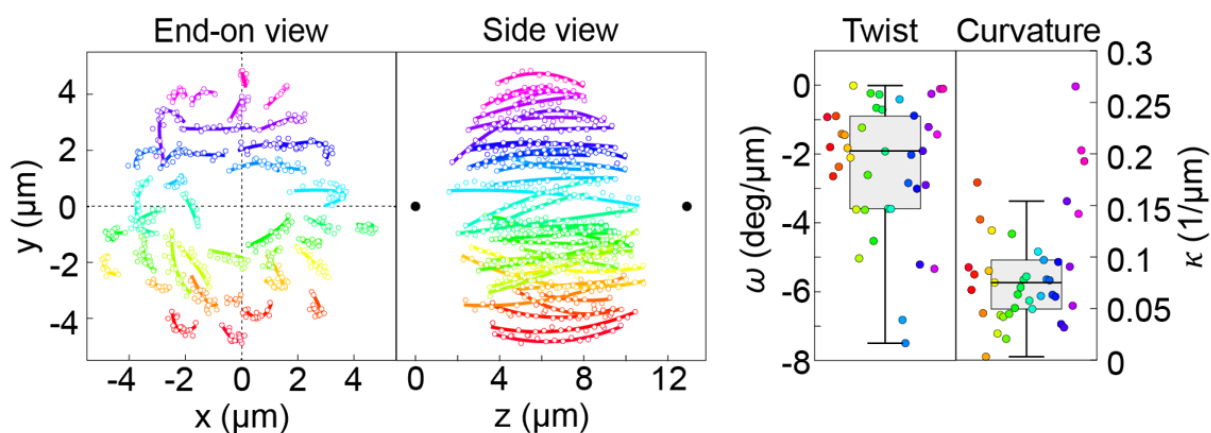


Figure 45: Application of the Oblique Circle Method to the HeLa cell mitotic spindle from Fig. 41. Tracked microtubule bundles are shown in the end-on view (left) and side view (right). Each bundle is represented by a different colour, thin circles mark the manually traced points along the bundle, and thick lines show circular arcs of the fitted circles. The spindle poles are represented as black dots in the side view. Box and whisker plots (median and interquartile range, whiskers extending to 1.5 of the interquartile range) of the twist and curvature of each bundle. This HeLa cell spindle shows a strong left-handed twist. Adapted from [1].

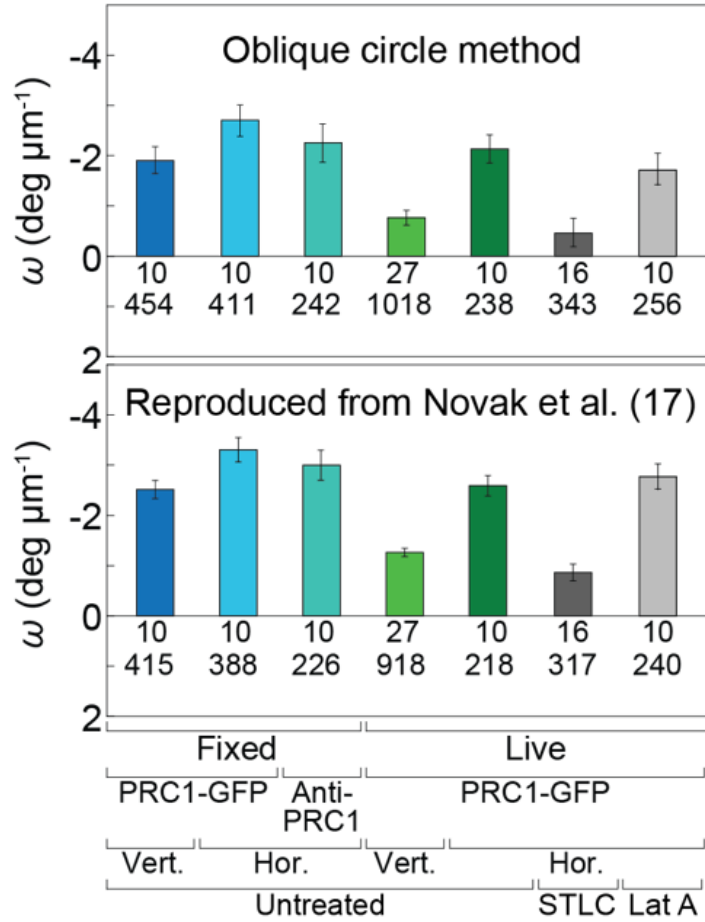


Figure 46: Calculation of the twist of spindles in HeLa cells from [43]. The average twist of spindles in different conditions, including vertical and horizontal spindles, fixed and live cells, untreated and treated cells, analysed with the Oblique Circle Method (top) and reproduced from [43] (bottom). Error bars, s.e.m. Cell lines were: HeLa cells expressing PRC1-GFP (1st, 2nd, 4th, 5th, 6th, 7th bars), unlabelled HeLa cells immunostained for PRC1 (3rd bar). Numbers below the bars represent the number of cells (top) and bundles (bottom). Note that the number of bundles is larger for twist measured by the Oblique Circle Method because the method includes all bundles. Bottom graph reproduced with permission from [43], from Fig. 41 and Fig. 42. Adapted from [1].

bundles and how tightly they are linked [153]. From fluorescence analysis the number of microtubules in bundles was estimated to be between 14 and 21 k-fibres [33, 109]. Twist characterizes to which extent bundles rotate around the spindle pole-to-pole axis. Intuitively, one can expect that twist is related to twisting moment within these bundles. This is indeed the case for spindles described by model from [43], in which microtubule bundles, that are intrinsically straight, extend radially from spindle poles. In this case, we can obtain an estimate for the twisting moment acting upon the microtubule bundle  $M_{twist} = \omega\tau$ , where  $\omega$  is the measured twist and  $\tau$  is the torsional rigidity of the microtubule bundle (Eq. (1.5.34) [43, 154]). In [43] twist was calculated for short bundles, calculating twist for finite segments  $\Delta z$  using only the starting and ending points of the bundle, where we excluded bundle data points close to the poles and entire bundles close to the pole-to-pole axis. With the Oblique Circle Method, we calculated  $\omega$  by utilizing all data points, including those with longer bundle segments and bundles closer to the pole-to-pole axis. By doing this, we replicated all key findings, though the obtained twist was slightly lower. The Oblique Circle Method has the advantage of being more robust and applicable to a greater variety of microtubule bundles. Fitting the simple shape of a circular arc is a straightforward approach to extract the most important geometrical parameters from the data obtained from confocal microscopy, namely from microtubule bundles which have a low number of data points, and which make less than one helical turn. The Oblique Circle Method cannot be applied to microtubule bundles that make several helical turns, because such shapes cannot be approximated by a circular arc. The usual techniques of signal processing are designed for working with microtubule bundles that make several helical turns [1, 214, 215], but for the same reason they are less suitable for fitting microtubule bundles in spindles. Our method could also be applied to data of bundle shapes obtained from super-resolution or electron microscopy, and provide more accurate information about the curvature and twist of microtubule bundles. High-resolution microscopy data might also allow for the use of more complex fitting techniques [201–203], making it possible to obtain not only the twist and curvature, but also other geometric parameters.



Further comparison of different fitting methods would be necessary to identify an optimal approach for spindle microtubule bundle characterization.

### **3.3 Measuring chirality of biological spindles**

We will now utilise the OCM to measure spindle chirality, and try to ascertain the biological role and the molecular origin of spindle chirality. We analyse the twist of human cell lines. We show that spindle twist changes through different phases of mitosis and peaks around anaphase onset in a cancer, non-cancer cell line and a non-human cell line. To test the idea that the chiral shape may help the spindle to absorb mechanical load, we compressed vertically oriented spindles along the pole-to-pole axis, which led to an increase in spindle twist. Thus, we propose a biological function of spindle chirality in promoting the flexibility of the spindle and its mechanical response to external forces, thereby decreasing the risk of spindle breakage under high load. By performing a candidate screen in which we depleted or inactivated motor proteins that step in a chiral manner and other microtubule-associated proteins, we identified several molecular players involved in the regulation of spindle chirality, leading us to suggest that the main mechanism generating spindle chirality is the action of motor proteins that rotate microtubules around one another within the antiparallel overlaps.

#### **3.3.1 Detailed analysis of unperturbed human spindles**

We can look at the data presented in Fig. 46 in more detail. For the 10 spindles from the first bar from Fig. 46, we can obtain Figs. 47 to 49

We can also look at U2OS cells, more specifically U2OS, stained with Anti-PRC1, held fixed and imaged horizontally, from data publicly available at [216], and they are shown in Figs. 50 to 52.

We can also look at U2OS cells, more specifically U2OS, stained with Anti-PRC1, live and imaged imaged vertically, from data publicly available at [216], and they are shown in

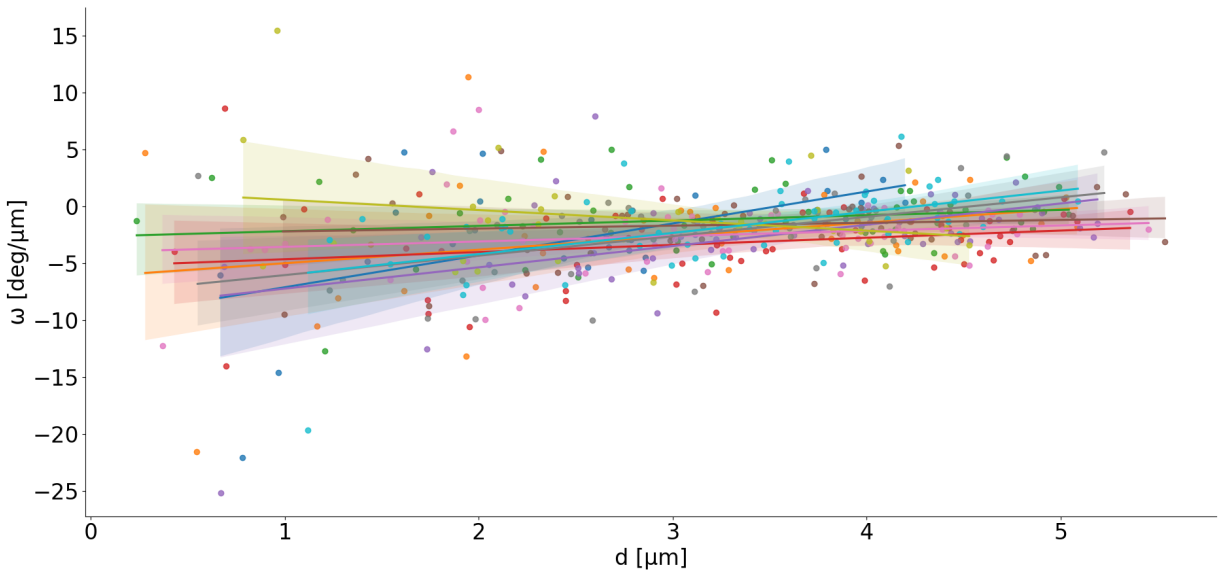


Figure 47: Calculation of the twist of spindles in HeLa cells using the OCM ( $N_{\text{spindles}} = 10$  and  $N_{\text{bundles}} = 454$ ). Data corresponds to the first bar in Fig. 46. Dots show the measured twist (y-axis) and distance from the pole-to-pole axis (x-axis) from each bundle. The line is a linear regression fit, with the shaded region corresponding to a confidence interval of 95%. Colours corresponds to different cells from the experiment.

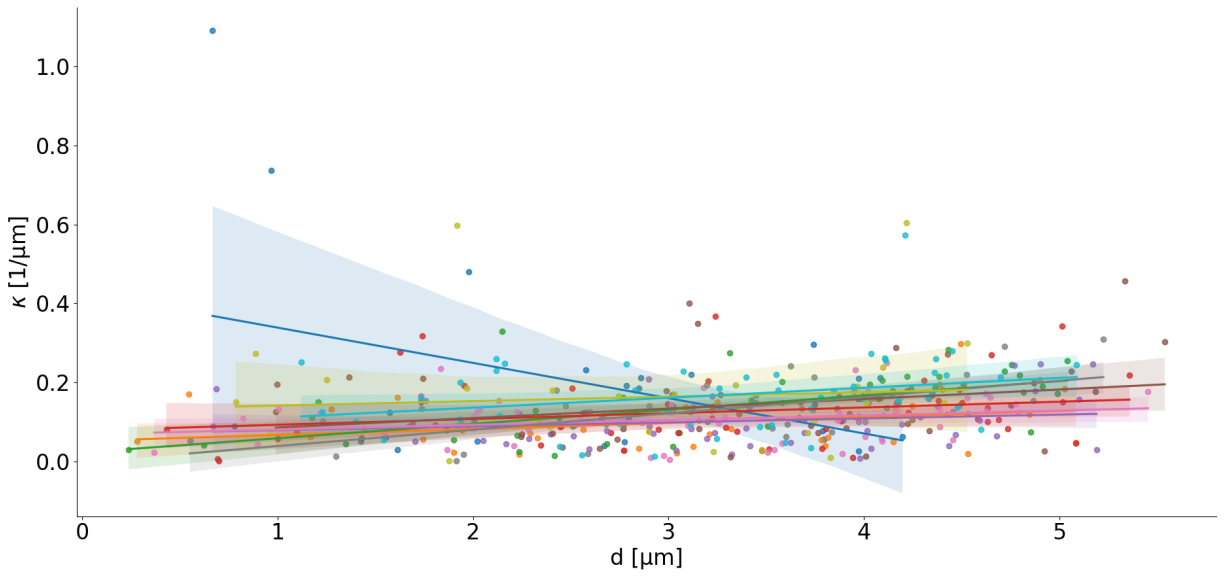


Figure 48: Calculation of the twist of bundles in HeLa cells spindles using the OCM ( $N_{\text{spindles}} = 10$  and  $N_{\text{bundles}} = 454$ ). Data corresponds to the first bar in Fig. 46. Dots show the measured curvature (y-axis) and distance from the pole-to-pole axis (x-axis) from each bundle. The line is a linear regression fit, with the shaded region corresponding to a confidence interval of 95%. Colours corresponds to different cells from the experiment.

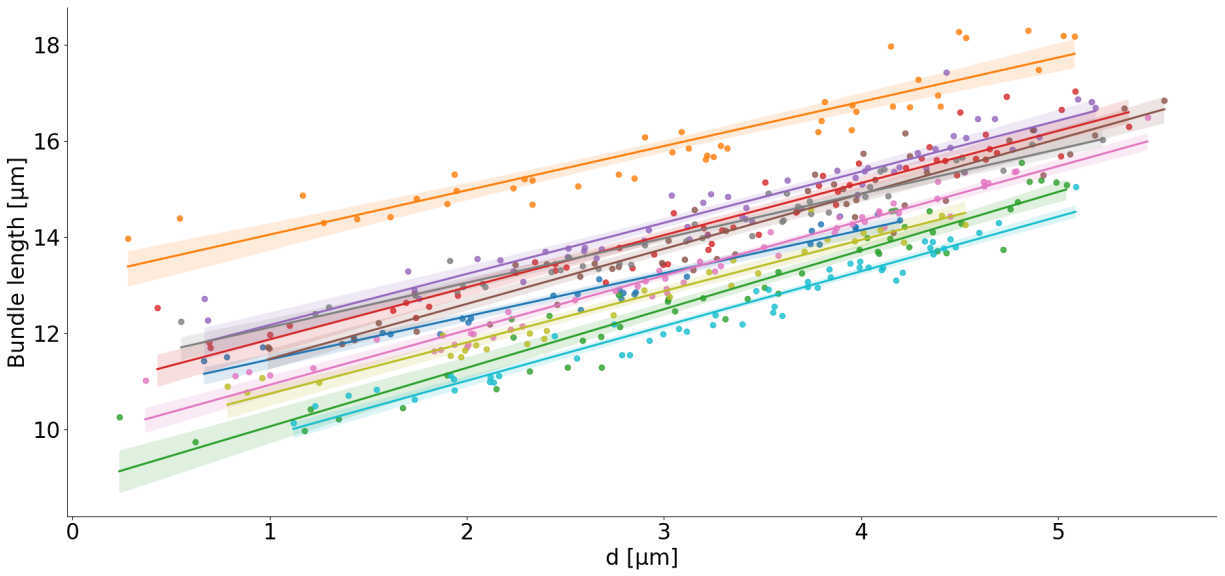


Figure 49: Calculation of the length of bundles in HeLa cells spindles using the OCM ( $N_{\text{spindles}} = 10$  and  $N_{\text{bundles}} = 454$ ). Data corresponds to the first bar in Fig. 46. Dots show the measured bundle length (y-axis) and distance from the pole-to-pole axis (x-axis) from each bundle. The line is a linear regression fit, with the shaded region corresponding to a confidence interval of 95%. Colours corresponds to different cells from the experiment.

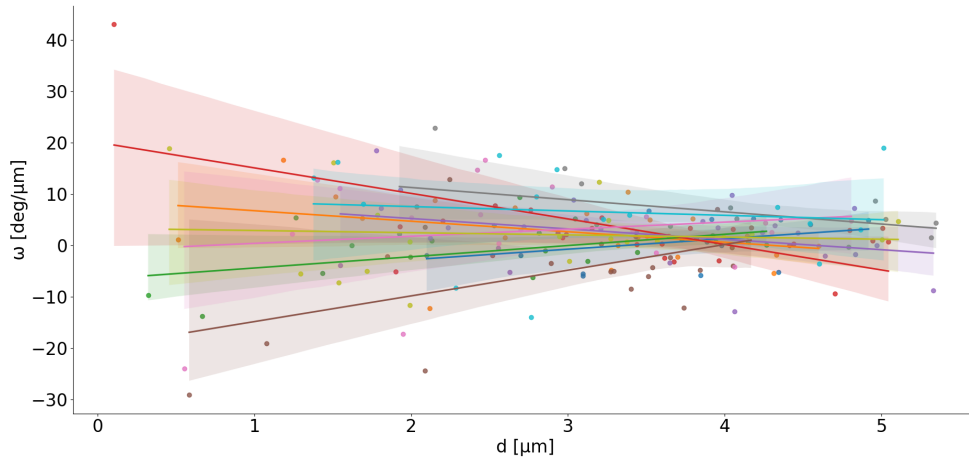


Figure 50: Calculation of the twist of bundles in U2OS cell spindles using the OCM ( $N_{\text{spindles}} = 10$  and  $N_{\text{bundles}} = 199$ ). Dots show the measured twist (y-axis) and distance from the pole-to-pole axis (x-axis) from each bundle. The line is a linear regression fit, with the shaded region corresponding to a confidence interval of 95%. Colours corresponds to different cells from the experiment.

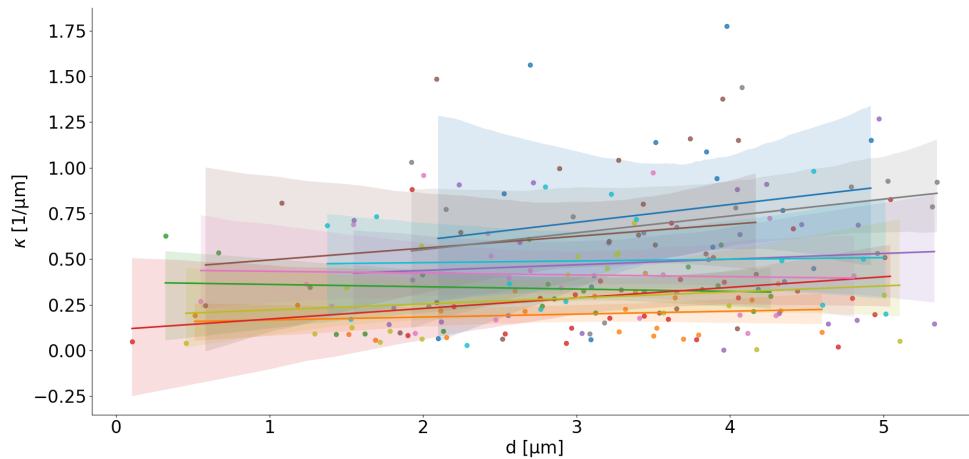


Figure 51: Calculation of the curvature of bundles in U2OS cell spindles using the OCM ( $N_{\text{spindles}} = 10$  and  $N_{\text{bundles}} = 199$ ). Dots show the measured curvature (y-axis) and distance from the pole-to-pole axis (x-axis) from each bundle. The line is a linear regression fit, with the shaded region corresponding to a confidence interval of 95%. Colours corresponds to different cells from the experiment.

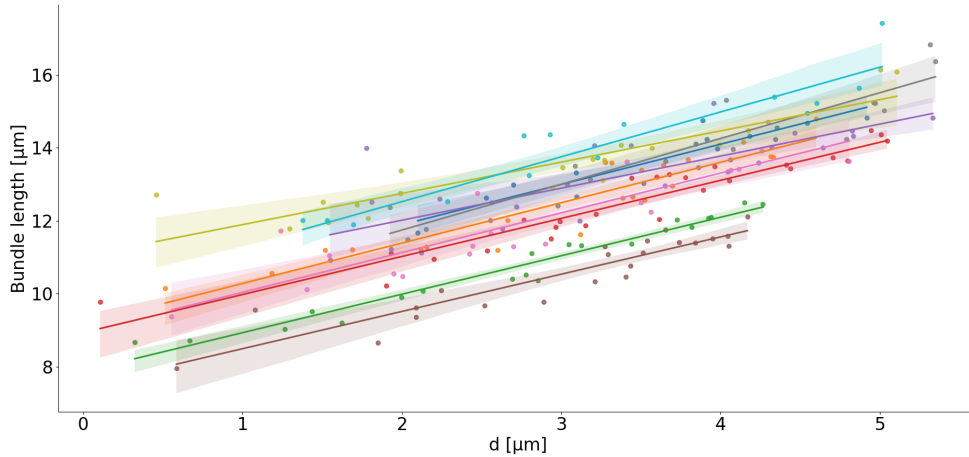


Figure 52: Calculation of the length of bundles in U2OS cell spindles using the OCM ( $N_{\text{spindles}} = 10$  and  $N_{\text{bundles}} = 199$ ). Dots show the measured bundle length (y-axis) and distance from the pole-to-pole axis (x-axis) from each bundle. The line is a linear regression fit, with the shaded region corresponding to a confidence interval of 95%. Colours corresponds to different cells from the experiment.

Figs. 53 to 55.

From these graphs, we can see clear trends - there is a slight decrease in measured twist from inner to outer bundles, the curvature increases from inner to outer bundles, and the contour length of the bundles also increases from inner to outer bundles. This provides us with a basis for constructing a theoretical model, and will be revisited at that point.

### 3.3.2 Spindle twist is most pronounced at anaphase onset in a cancer and a non-cancer cell line

To explore the twist of the spindle, the first step was to obtain end-on view images covering the whole spindle from pole to pole because this view allows for the visualization of the twist of microtubule bundles Fig. 56. A signature of the twisted shape is that microtubule bundles look like flower petals in the end-on view. In contrast, the twisted shape is not easily recognized in the side-view of the spindle Fig. 56. If the spindle is standing vertically with respect to the imaging plane, a  $z$ -stack of images directly provides an end-of view of the

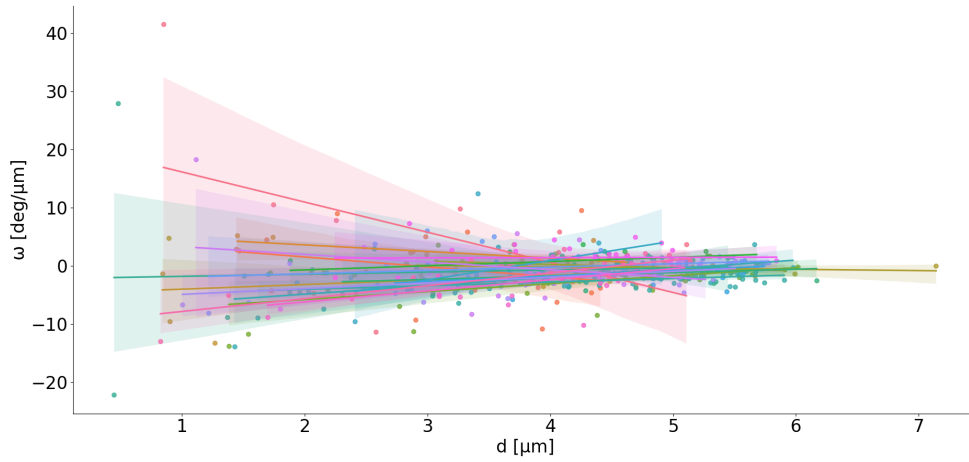


Figure 53: Calculation of the twist of bundles in U2OS cell spindles using the OCM ( $N_{\text{spindles}} = 20$  and  $N_{\text{bundles}} = 473$ ). Dots show the measured twist (y-axis) and distance from the pole-to-pole axis (x-axis) from each bundle. The line is a linear regression fit, with the shaded region corresponding to a confidence interval of 95%. Colours corresponds to different cells from the experiment.

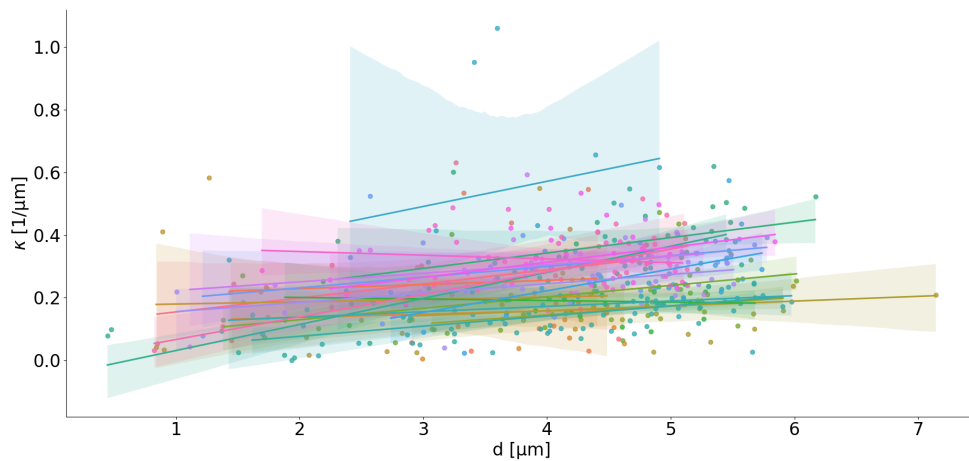


Figure 54: Calculation of the curvature of bundles in U2OS cell spindles using the OCM ( $N_{\text{spindles}} = 20$  and  $N_{\text{bundles}} = 473$ ). Dots show the measured curvature (y-axis) and distance from the pole-to-pole axis (x-axis) from each bundle. The line is a linear regression fit, with the shaded region corresponding to a confidence interval of 95%. Colours corresponds to different cells from the experiment.

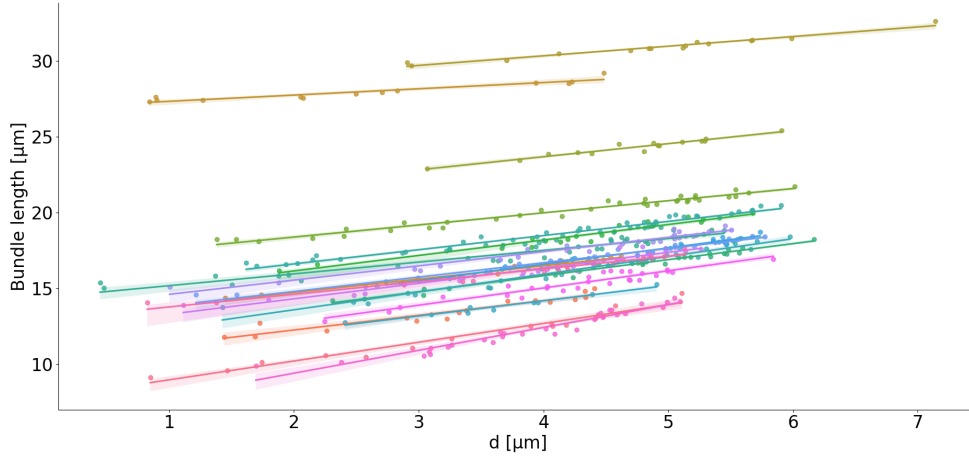


Figure 55: Calculation of the length of bundles in U2OS cell spindles cells ( $N_{\text{spindles}} = 20$  and  $N_{\text{bundles}} = 473$ ). Dots show the measured bundle length (y-axis) and distance from the pole-to-pole axis (x-axis) from each bundle. The line is a linear regression fit, with the shaded region corresponding to a confidence interval of 95%. Colours corresponds to different cells from the experiment.

spindle, but if the spindle is lying horizontally, a  $z$ -stack needs to be transformed into the end-on view.

To quantify spindle twist, we used 3 complementary approaches: visual assessment, optical flow, and bundle tracing Fig. 57.

As it is still an open question in the field what method is the most appropriate to measure spindle twist [1, 43, 197], visual assessment is useful as a quick and rough estimate of the twist and as a control for other methods. In the visual assessment method, the spindle is observed end-on and the rotation of microtubule bundles around the pole-to-pole axis is estimated visually. If the bundles rotate clockwise when moving along the spindle axis in the direction towards the observer, the twist is left-handed, and vice versa Fig. 57. We score the twist as left-handed, right-handed, weak left-handed, weak right-handed, or no visible twist. Weak twists correspond to a range of approximately  $-1$  to  $-2 \text{ deg}/\mu\text{m}$  in Oblique Circle Method(Fig. 58. This is visible as a total rotation of  $5 - 10$  :  $\text{deg}$  in the clockwise (left-handed) or counter-clockwise (right-handed) direction in the end-



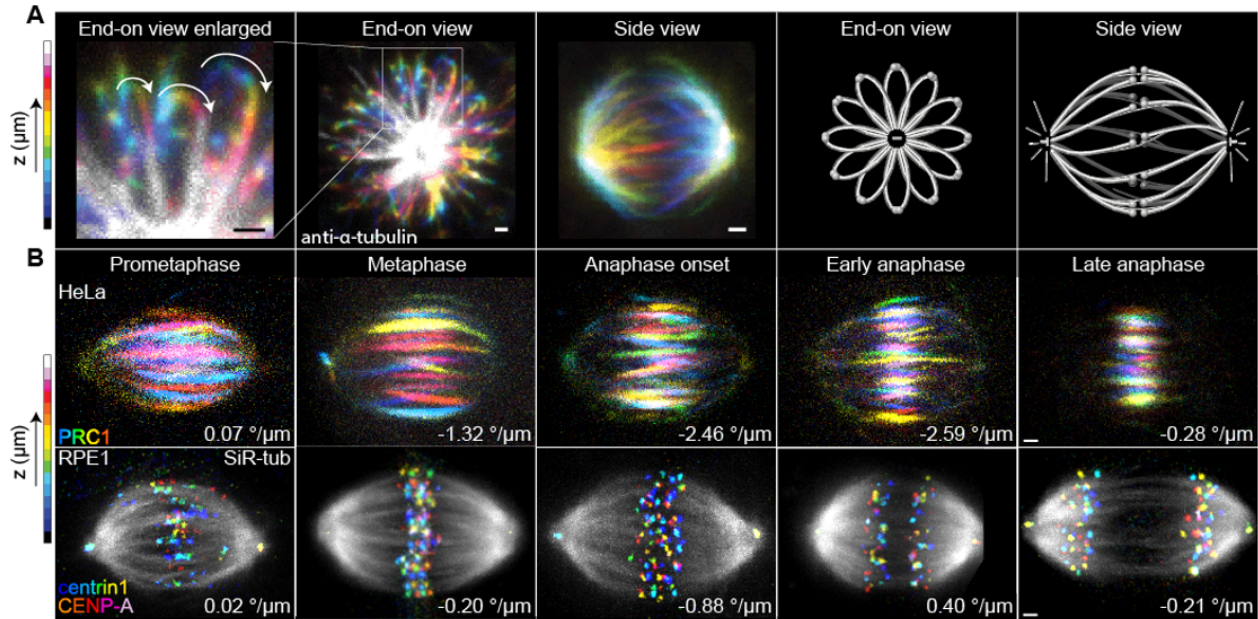


Figure 56: Spindle twist culminates at the beginning of the anaphase. (A) Images of spindles immunostained for  $\alpha$ -tubulin in a HeLa-Kyoto BAC cell line stably expressing PRC1-GFP (PRC1-GFP signal is not shown). Left, enlarged section of the image showing microtubule bundles from the end-on view, rotating in a clockwise direction (arrows) through  $z$ -planes when moving towards the observer. The end-on view and the side view of a spindle are shown next. Images are colour-coded for depth using ImageJ temporal colour coding Lookup Table '16 colors' (see colour bar). Scale bar, 1  $\mu\text{m}$ . Right two panels show schemes of a spindle from the end-on view and side view. (B) Top row, images of spindles in HeLa-Kyoto BAC cells stably expressing PRC1-GFP, shown in different phases of mitosis. Bottom row, images of spindles in hTERT-RPE1 cells expressing CENP- $\alpha$ -GFP and centrin1-GFP, shown in different phases of mitosis. Microtubule bundles of HeLa spindles (PRC1-GFP signal) are colour-coded for depth using ImageJ temporal colour coding Lookup Table '16 colors' and microtubules of RPE1 spindles are shown in grey (SiR-tubulin dye) while kinetochores/centrosomes are colour-coded for depth using the same colour coding as described above (see colour bar). Scale bars, 1  $\mu\text{m}$ . Additional examples of HeLa cell spindles are shown in Fig. 107. Adapted from [2].

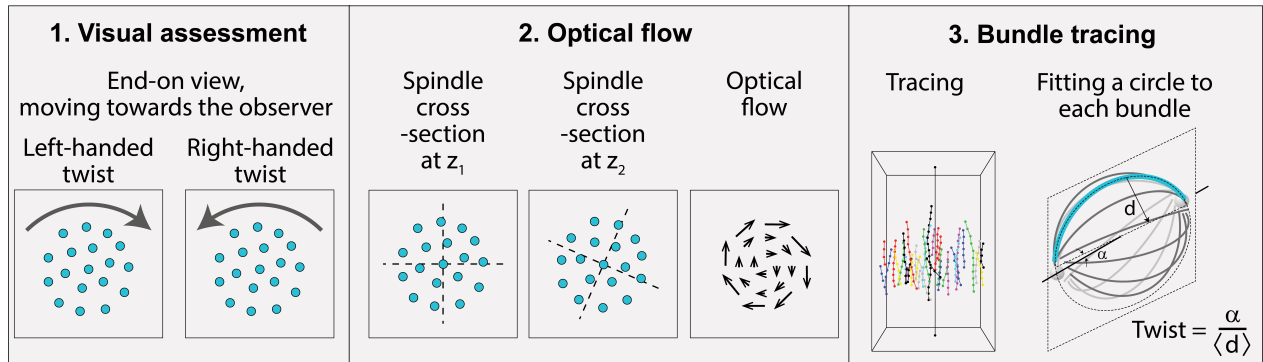


Figure 57: Methods for calculating twist during mitosis. Schemes of three methods used to measure spindle twist: visual assessment (1), optical flow (2) and the Oblique Circle Method (3). Adapted from [2].

on view of the spindle when moving towards the observer along the bundle length, which is typically  $5\mu\text{m}$ . Accordingly, left and right twists correspond to a rotation of more than  $10^\circ$  in the end-on view (Fig. 58). In the optical flow method, the movement of the signal coming from microtubule bundles is estimated by comparing the signal from one  $z$ -plane to the next Fig. 57. This method provides a value for the average twist of all bundles in a spindle and is optimal for experiments on a large number of spindles because it is automated.

As a label for microtubule bundles, SiR-tubulin we used to observe all microtubule bundles, or, alternatively, PRC1-GFP to observe the bridging fibres [33, 179]. To compare the results of the three methods, we analysed twist of 10 metaphase spindles in HeLa cells stably expressing PRC1-GFP Fig. 59.

All three methods yielded a left-handed twist, which is expressed by negative values, for all 10 spindles. The spindles that were visually assessed as having a strong left twist had, on average, a higher left twist value also in the bundle tracing and optical flow method, than those with a weak left twist. The absolute values of twist of individual spindles obtained by bundle tracing and optical flow were similar, with optical flow yielding smaller negative values ( $-1.32 \pm 0.29 \text{ deg}/\mu\text{m}$ ,  $n = 10$ ; all data are given as  $\text{mean} \pm \text{sem}$ ) than bundle tracing ( $-2.07 \pm 0.29 \text{ deg}/\mu\text{m}$ ,  $n = 10$ ). This difference is likely due to the sensitivity of the optical

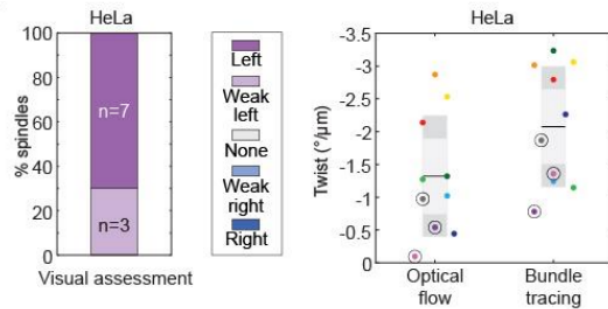


Figure 58: Twist differences throughout the cell cycle. On the left, representation of microtubule bundle movements along the  $z$ -axis of the same spindle in HeLa cells viewed from the end-on view in different phases of mitosis; each microtubule bundle is represented by a circular arc of the circle fitted on the traces and arrowheads which point at the rotation direction, the colour of the bundle shows its length along the depth axis (shared colour bar on the right, bottom is shortest bundle, top is longest); black dot represents the pole-to-pole axis; each colour represents one phase of the mitosis; scale bar,  $1 \mu\text{m}$ . On the right, graph shows the change of twist values for five HeLa cells over time; the beginning of anaphase (visible chromosome separation) was set as time zero; each colour represents one cell and thick black line represents mean values with error bars showing SEM; data shown in orange originate from the cell whose bundles' movements are shown on the left and images are shown in Fig. 106. Experiments were performed on the HeLa-Kyoto BAC cells stably expressing PRC1-GFP. Other examples of spindle images are shown in Fig. 106. Adapted from [2].

flow method to all signals including the background. Based on this cross-check between the three methods, we conclude that they provide comparable values of spindle twist. Thus we use optical flow for experiments in which we test changes in the overall spindle twist in a large number of cells, and bundle tracing for experiments where high spatial precision is required. Spindles in cancer cell lines are twisted in a left-handed manner in metaphase [43], but it is not known whether the twist is present already when the spindle assembles in prometaphase or it arises as the spindle matures. Furthermore, it is unknown how the twist changes during anaphase. To examine the development of spindle twist throughout mitosis Fig. 59 (Movies S2-S6 in [2]), we first measured twist in individual live HeLa cells expressing PRC1-GFP as they progressed through mitosis, shown in Figs. 59 and 106.

The average twist of the spindle in prometaphase was close to 0, it was left-handed (negative) during metaphase, culminated at anaphase onset reaching a value of  $-1.88 \pm 0.3 \text{ deg}/\mu\text{m}$  ( $n = 5$ ), and decreased afterwards Fig. 59. In agreement with this result, experiments in which different spindles were imaged in different phases showed a peak of spindle twist around anaphase onset, with a value of  $-1.98 \pm 0.26 \text{ deg}/\mu\text{m}$  ( $n = 6$ ) Figs. 59, 61 and 107 and Movies S2-S6 in [2], Tables 3 and 4. Expression of PRC1-GFP in this cell line did not influence the twist, as non-transfected HeLa cells stained with SiR-tubulin showed similar twist values in metaphase (Tables 3 and 4;  $p = 0.47$ , Student's t-test).

To test whether the time spent in metaphase affects spindle twist, we accelerated entry into anaphase by inhibiting Mps1 kinase, one of the main components of the spindle assembly checkpoint [217]. Treatment of HeLa cells expressing PRC1-GFP with the inhibitor AZ314642 during prometaphase shortened the time to anaphase from 40 minutes to 8 – 10 minutes, on average. We measured the twist at the beginning of anaphase or in early anaphase and found it to be significantly smaller than in control cells,  $-0.17 \pm 0.21 \text{ deg}/\mu\text{m}$  ( $n = 17$ ) ( Fig. 60 Tables 3 and 4. This result suggests that the reduction of time needed to enter the anaphase may also mean a reduction of time to build up spindle twist.

To explore whether spindle twist and its variation over time is specific to cancer cell

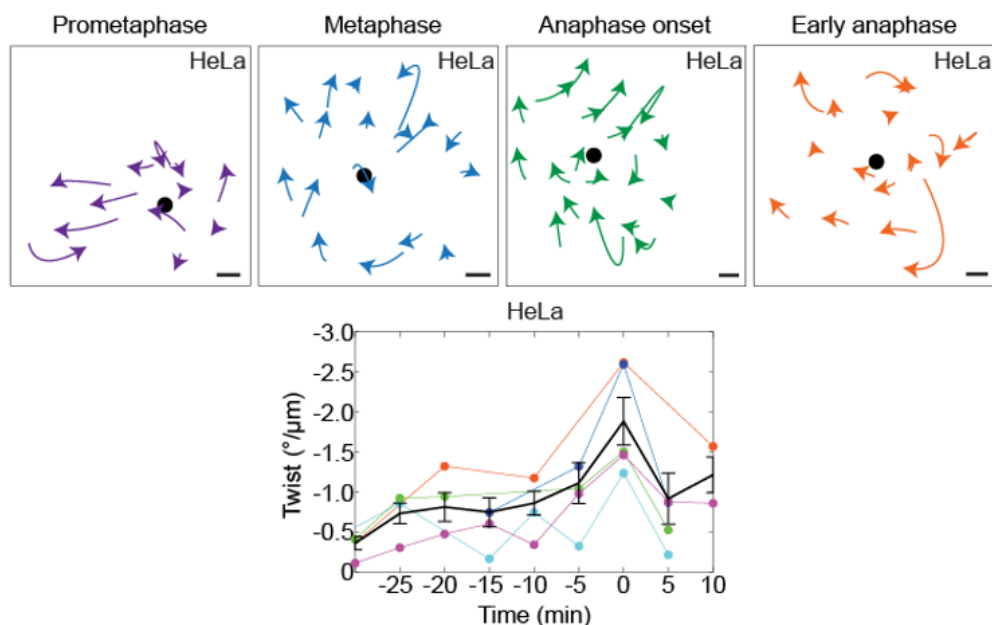


Figure 59: Twist differences throughout the cell cycle. On the left, representation of microtubule bundle movements along the  $z$ -axis of the same spindle in HeLa cells viewed from the end-on view in different phases of mitosis; each microtubule bundle is represented by a circular arc of the circle fitted on the traces and arrowheads which point at the rotation direction, the colour of the bundle shows its length along the depth axis (shared colour bar on the right, bottom is shortest bundle, top is longest); black dot represents the pole-to-pole axis; each colour represents one phase of the mitosis; scale bar,  $1\mu\text{m}$ . On the right, graph shows the change of twist values for five HeLa cells over time; the beginning of anaphase (visible chromosome separation) was set as time zero; each colour represents one cell and thick black line represents mean values with error bars showing SEM; data shown in orange originate from the cell whose bundles' movements are shown on the left and images are shown in Fig. 106. Experiments were performed on the HeLa-Kyoto BAC cells stably expressing PRC1-GFP. Other examples of spindle images are shown in Fig. 106. Adapted from [2].

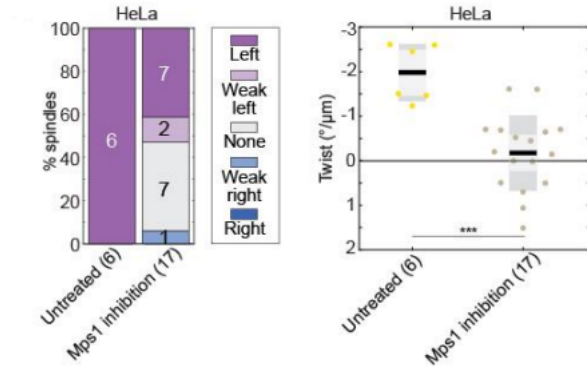


Figure 60: Graphs showing twist values after the inhibition of Mps1 in HeLa cells. On the left, visual assessment graph represents percentages of spindles showing left, right, weak left, weak right or no twist as described in the legend. On the right, graph shows twist calculated with the optical flow method. The black line shows the mean; the light and dark grey areas mark 95% confidence interval on the mean and standard deviation, respectively.  $***p < 0.001$  (Student's t-test). Experiments were performed on the HeLa-Kyoto BAC cells stably expressing PRC1-GFP. Adapted from [2].

lines, we measured twist in the non-cancer immortalized epithelial cell line hTERT-RPE1 (shortened to just RPE1) Fig. 59 and found that spindles in these cells also show a left-handed twist, but the values are smaller than in HeLa cells Fig. 61. Moreover, the temporal pattern of twist in RPE1 cells was similar to that in HeLa cells. Twist was absent in prometaphase, it was very weak left-handed in metaphase, had a peak value at anaphase onset, decreased during anaphase, and vanished in late anaphase (Fig. 61). The value at anaphase onset was  $-0.53 \pm 0.15 \text{ deg}/\mu\text{m}$  ( $n = 26$ ), which indicates a weaker left-handed twist than in HeLa cells. Taken together, our results show that spindles are born without twist. The left-handed twist in HeLa cells arises as the spindle acquires its metaphase shape, peaks at the start of chromosome segregation, and declines afterwards. In RPE1 cells, the twist shows a similar trend, but the values are much less pronounced and the twist is mostly noticeable only in early anaphase.

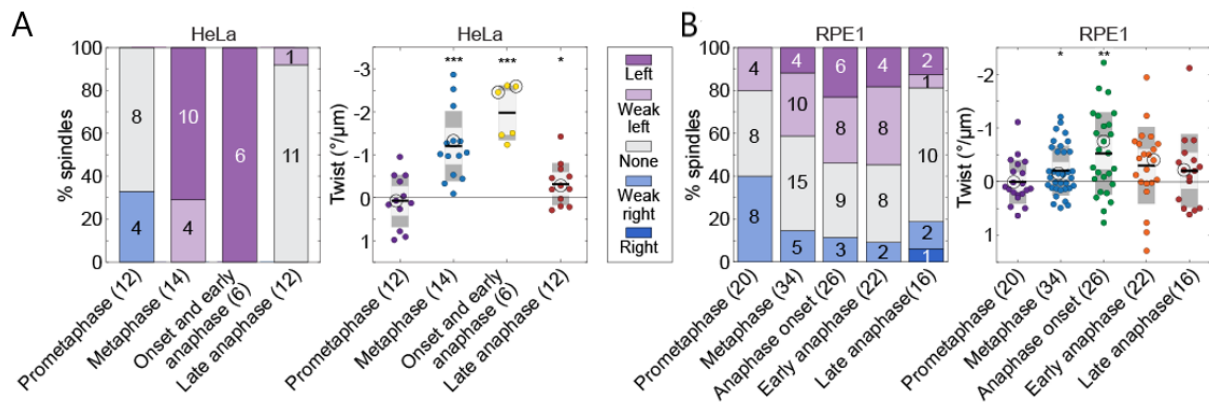


Figure 61: Twist differences throughout the cell cycle. Twist in different phases of mitosis in HeLa-Kyoto BAC cells stably expressing PRC1-GFP. On the left, visual assessment graph represents percentages of spindles showing left, right, weak left, weak right or no twist, as described in the legend, in different phases of mitosis (numbers on the graph and in the brackets show the number of cells). On the right, graph shows twist values calculated with the optical flow method in different phases of mitosis. The black line shows the mean; the light and dark grey areas mark 95% confidence interval on the mean and standard deviation, respectively;  $***p < 0.001$ ,  $**p < 0.01$ ,  $*p < 0.05$  (Student's t-test for the mean twist value different from 0). Non-significant differences were not shown on the graph. Circled dots represent the cells that are shown on the images above. Raw data of 10 out of 14 metaphase spindles was taken and re-calculated from [43] and also used in Fig. 58. Twist in different phases of mitosis in hTERT-RPE1 cells expressing CENP- $\alpha$ -GFP and centrin1-GFP; legend as in (D). Adapted from [2].

### 3.3.3 The *Naegleria gruberi* spindle twists from pole-to-pole in a righthanded fashion

*Naegleria gruberi* is a unicellular eukaryote whose evolutionary distance from animals and fungi has made it useful for developing hypotheses about the last common eukaryotic ancestor. *Naegleria* amoebae lack a cytoplasmic microtubule cytoskeleton and assemble microtubules only during mitosis and thus represent a unique system for studying the evolution and functional specificity of mitotic tubulins and the spindles they assemble. Previous studies show that *Naegleria* amoebae express a divergent  $\alpha$ -tubulin during mitosis, and we now show that *Naegleria* amoebae express a second mitotic  $\alpha$ - and two mitotic  $\beta$ -tubulins. The mitotic tubulins are evolutionarily divergent relative to typical  $\alpha$ - and  $\beta$ -tubulins and contain residues that suggest distinct microtubule properties. These distinct residues are conserved in mitotic tubulin homologs of the 'brain-eating amoeba' *Naegleria fowleri*, making them potential drug targets. Using quantitative light microscopy, we find that *Naegleria*'s mitotic spindle is a distinctive barrel-like structure built from a ring of microtubule bundles. Similar to those of other species, *Naegleria*'s spindle is twisted, and its length increases during mitosis, suggesting that these aspects of mitosis are ancestral features. Because bundle numbers change during metaphase, we hypothesize that the initial bundles represent kinetochore fibres and secondary bundles function as bridging fibres.

Cells from across the eukaryotic tree use microtubules for a variety of functions during both interphase and mitosis. Interphase microtubules contribute to cell shape, polarity, and intracellular trafficking. During cell division, a microtubule based spindle mediates chromosome segregation. [5, 218]. Interphase and mitotic microtubule functions are emergent properties of microtubule-associated proteins as well as the subunit composition and post-translational modifications of tubulin. Eukaryotic cells typically express multi-functional tubulins used for both interphase and mitotic functions [219]. For example, human embryonic kidney cells express high levels of one  $\alpha$ -tubulin and two  $\beta$ -tubulins (80% identical)[220], while budding yeast express one  $\beta$ -tubulin and two  $\alpha$ -tubulins (88% identical), and each uses



these tubulins in both interphase and mitosis [221]. As an extreme example, the unicellular algae *Chlamydomonas* has one  $\alpha$ - and one  $\beta$ -tubulin gene that are used for all microtubule functions [221]. Other eukaryotes, however, express unique tubulin isotypes for specific functions, including meiotic spindle assembly in *Drosophila* oocytes [222], axoneme formation in diverse systems [223] and touch receptor neurons in worms [224]. These specialized tubulins support the 'multi-tubulin hypothesis' that posits that different tubulins can specify distinct cellular functions [225, 226]. *Naegleria gruberi* is a single-celled eukaryote that diverged from the 'yeast-to-human' lineage over a billion years ago with the unusual ability to differentiate from a crawling amoeba to a swimming flagellate [227]. This stress response involves the assembly of an entire microtubule cytoskeleton—centrioles, flagella, and a cortical microtubule array—including transcription and translation of flagellate-specific  $\alpha$ - and  $\beta$ -tubulins along with associated microtubule-binding proteins [228]. The flagellate form is transient, and cells return to crawling amoebae within 2–300 min [229] after which the flagellate microtubules are disassembled and tubulin is degraded. The *Naegleria* flagellate microtubules, and the  $\alpha$ - and  $\beta$ -tubulins that comprise them, are specific for these non-mitotic microtubule functions, an idea that stimulated the development of the multi-tubulin hypothesis [226]. Unlike other eukaryotes, interphase *Naegleria* amoebae lack tubulin transcripts [230, 231] and have no observable microtubules as visualized by immunofluorescence [207, 232] or electron microscopy [233]. *Naegleria* amoebae, however, assemble microtubules within the nucleus for closed mitosis [207, 230–232]. Previous studies have shown that *Naegleria* expresses a divergent  $\alpha$ -tubulin specifically during mitosis [231] that is incorporated into the mitotic spindle. [207, 231, 232] *Naegleria*, therefore, represents a unique test of the multi-tubulin hypothesis. The most well-studied spindles are those of animal cells, which contain functionally distinct populations of microtubules, including (1) kinetochore fibre microtubules that bind to kinetochores to connect each chromosome to a single spindle pole; [234] (2) non-kinetochore microtubules that extend from the poles and overlap at the midzone, linking the two halves of the spindle; [5, 62, 106, 235] and (3) astral microtubules that extend from spindle poles to-

ward the cell cortex. During anaphase, kinetochore microtubules shorten (anaphase A) [236] while midzone microtubules elongate to drive chromosome segregation (anaphase B) [237]. A subset of midzone microtubules, called bridging fibres, closely approach kinetochore fibres in each half spindle [33]. Bridging fibres contribute to the balance of tension and compressive forces in the spindle [33], chromosome alignment, and chromosome motion in anaphase [34, 238, 239]. Spindle microtubules are organized by mitotic motor proteins that promote microtubule dynamic turnover, spindle pole organization, chromosome congression during prometaphase, and poleward motion in anaphase [23]. The influence of motor proteins in spindle structure is highlighted by the twist they introduce in spindles of human cell lines [43]. Outside of animals, there exists a wide diversity of spindle architecture and molecular mechanisms driving chromosome segregation [240]. While some organisms break down the nuclear envelope to facilitate microtubule-chromosome interaction (open mitosis), others nucleate microtubules in the cytoplasm that pass through holes in the nuclear envelope to interact with chromosomes (semi-open mitosis), or, like *Naegleria*, assemble microtubules within an intact nuclear envelope (closed mitosis). [207, 232, 241]. Spindle-microtubule-organizing centres also vary widely, from centriole-containing centrosomes that nucleate spindle microtubules in the cytoplasm of animal cells, to spindle pole bodies that nucleate mitotic microtubules from the surface of the nuclear envelope in yeast, to diffuse microtubule-organizing centres in land plants, as well as a wide variety of microtubule-organizing centres and spindle architectures found in protist lineages. [242–245]. Even though this wide diversity of spindle organization, eukaryotic chromosome segregation generally requires three activities: (1) a regularly structured, microtubulebased spindle apparatus. No eukaryotic species has yet to be reported that does not use microtubules to segregate its chromosomes, and each species assembles a characteristic spindle structure prior to mitosis. (2) Chromosome interaction with microtubules. This usually occurs via attachment of kinetochores to the ends of microtubules as in cultured mammalian cells [234]. or lateral interactions as in *C. elegans* meiosis [246]. (3) Microtubule dynamics. Mitotic microtubules are nucleated and grow to form the

spindle and are subsequently disassembled after chromosome segregation. In line with its unusual  $\alpha$ -tubulin, the architecture of the *Naegleria* spindle is also unconventional; *Naegleria*'s spindle is barrelshaped and lacks obvious microtubule-organizing centres and homologs of many proteins found in conventional kinetochores. [233, 247–251]. We test whether, in the absence of the evolutionary constraints imposed by interphase microtubule functions, *Naegleria*'s mitotic microtubule system has diverged from canonical systems. In addition to the previously reported mitotic  $\alpha$ -tubulin, *Naegleria* expresses a second mitotic  $\alpha$ -tubulin along with two mitotic  $\beta$ -tubulins. In contrast to the *Naegleria* tubulins expressed during the flagellate stage that closely resemble tubulins from heavily studied species, the protein sequences of the *Naegleria* mitotic tubulins have diverged significantly, consistent with the original multi-tubulin hypothesis [226]. Mitotic tubulins are used to build an unusual spindle composed of a ring of regularly spaced microtubule bundles that twists end-to-end. As mitosis proceeds, additional microtubule bundles form in the equatorial region of the spindle and-as in other eukaryotes-the spindle elongates to facilitate chromosome segregation. The organization and dynamics of the *Naegleria* spindle highlight both core aspects of mitosis as well as variable features of cell division.

The 3D reconstructions of vertically oriented spindles revealed that the microtubule bundles curved and appeared to twist from one end of the spindle to the other (Figs. 62 and 63; Videos S1 and S2 in [3]).

Such twist has so far been documented only in HeLa, U2OS, and RPE1 cells, where it is generated through the activity of the spindle kinesins Eg5/kinesin-5 and Kif18A/kinesin-8 and regulated by other microtubule-binding proteins. [2, 43, 197]. To quantify the degree of twist in the *Naegleria* spindle, we traced individual metaphase bundles Fig. 63 and measured their curvature and twist by fitting a plane to the points representing the bundle and a circle that lies in this plane to the same points. We then estimated bundle curvature as the inverse of the radius of the fit circle, and the twist as the angle between the plane and the  $z$  axis divided by the mean distance of these points from the  $z$ -axis using the OCM Section 3.1

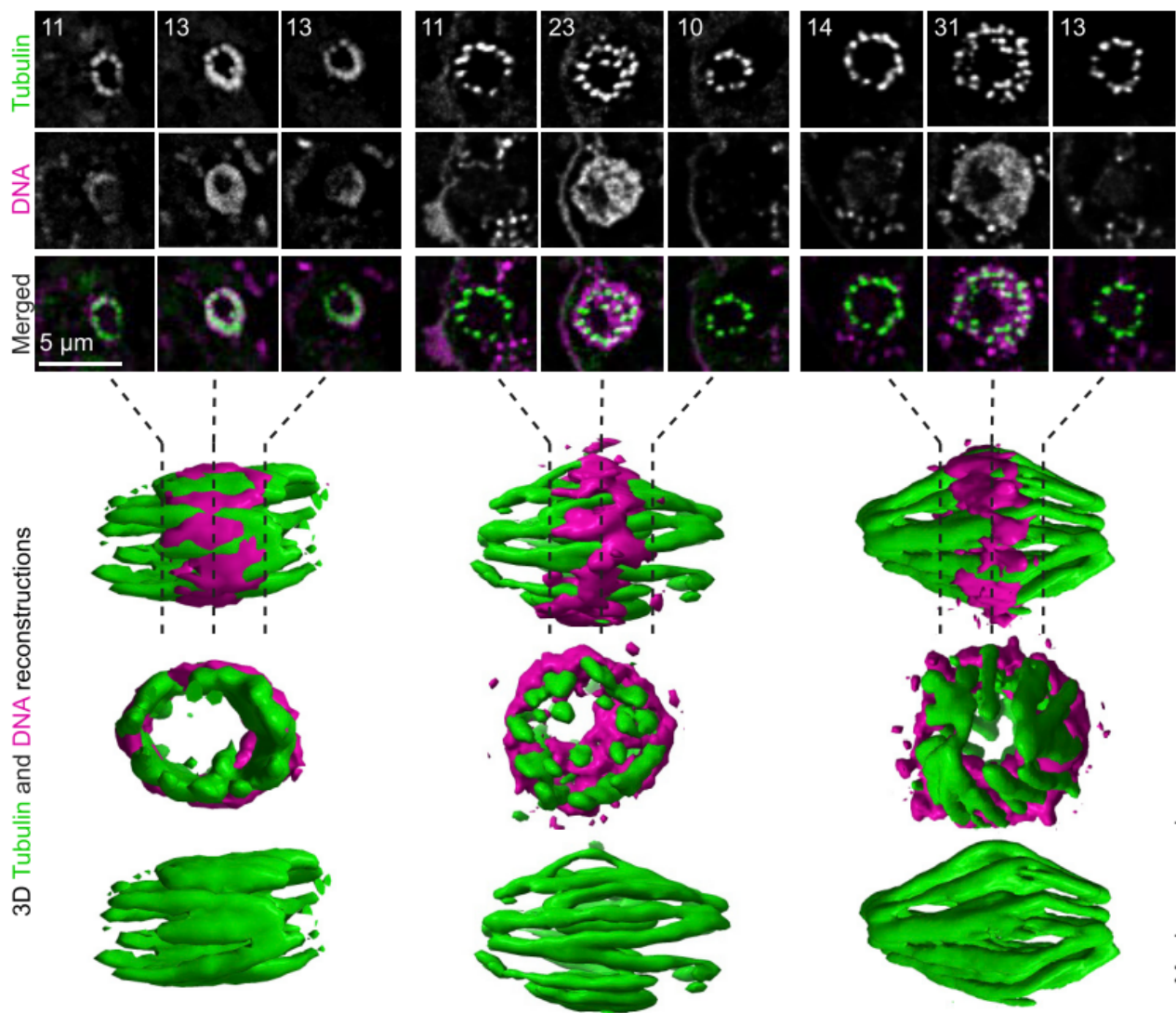


Figure 62: The number of microtubule bundles changes as mitosis proceeds (A) Cells were fixed and stained with antibodies (anti- $\alpha$ -tubulin clone DM1A, green) to detect microtubules and DAPI to label DNA (magenta). Cells with spindles perpendicular to the coverslip were imaged using confocal microscopy and deconvolved using Autoquant software (top panels), and 3D reconstructions were rendered using ChimeraX software (bottom panels, not to scale). Individual z planes are shown for slices approximately 25%, 50%, and 75% through the spindle for three representative cells. Numbers (upper left) indicate the number of distinct microtubule bundles in that position of the spindle Adapted from [3].

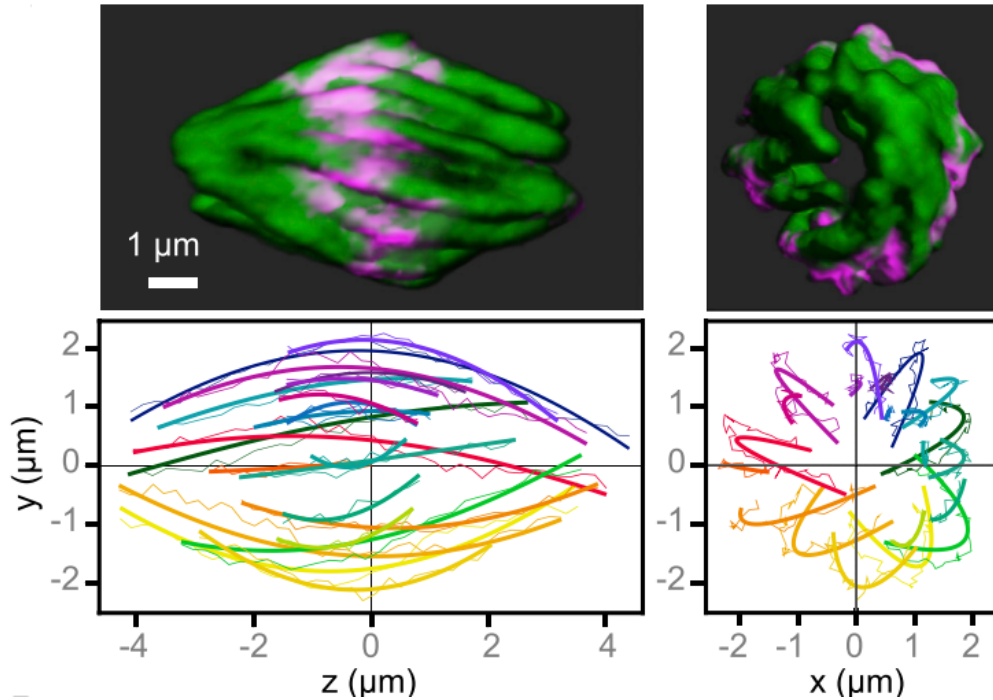


Figure 63: Naegleria mitotic spindles are twisted (A) A 3D reconstructed spindle (the same spindle shown in Fig. 62, right) is shown from side and end-on view viewpoints. Microtubules are shown in green, and DNA is in magenta. Microtubule bundles were quantified from the side view (left graph) and end-on view (right graph). Each bundle is represented by a different colour, thin lines mark the manually traced points along the bundle, and thick lines show circular arcs of the fitted circles. Adapted from [3].

and Fig. 42.

The resulting data show that microtubule bundles in the Naegleria spindle are curved  $0.146 \pm 0.009/\text{mm}$  Fig. 64. and twisted  $0.873 \pm 0.316/\text{mm}$ ; Fig. 64, with shorter bundles having more curve and twist than longer bundles Fig. 64. This result was corroborated by visual assessment of the handedness of the spindle twist (if the bundles rotate counter-clockwise when moving along the spindle axis toward the observer, the twist is right-handed). We found a mixture of left- and right-handed twist, with the majority of spindles showing a strong right-handed twist Fig. 64E.

Analysing early metaphase (defined for this analysis as cells with  $< 20$  bundles) separate

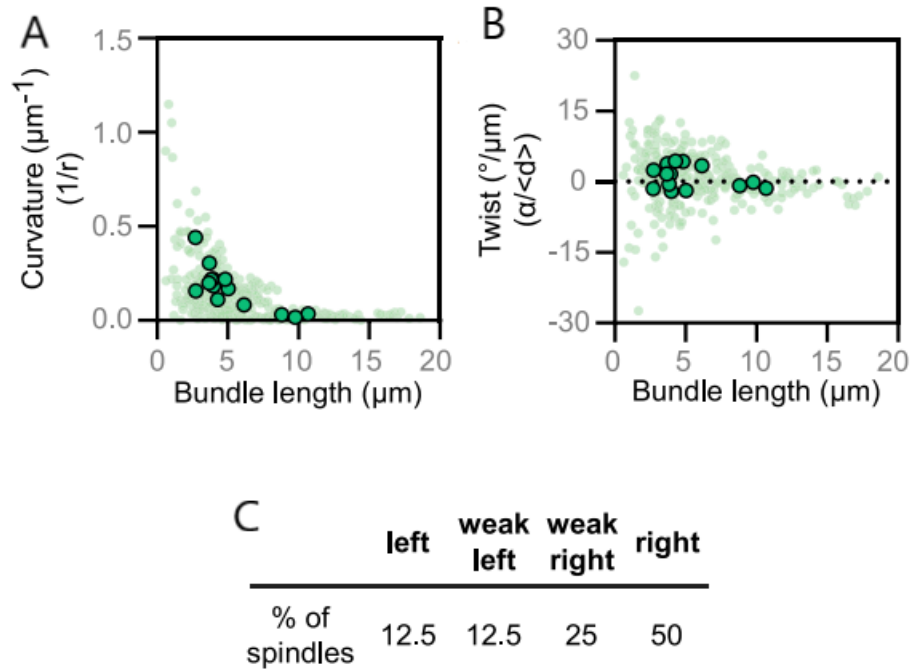


Figure 64: (A) The curvature of microtubule bundles is shown as a function of bundle length (measured along its pole-to-pole axis). Each small dot represents a single bundle within a spindle, while each larger dot represents the average for a spindle. (B) The twist of microtubule bundles is shown as a function of bundle length. Each small dot represents a single bundle within a spindle, while each larger dot represents the average for a spindle. The data in (A) and (B) are from 4 experimental replicates, encompassing 14 cells and 301 bundles. (C) The percentage of spindles with right, weak right, left, or weak left handedness are shown (see Fig. 65 for a breakdown of this analysis). Data were analysed for 40 cells from 4 experimental replicates. See also Fig. 66, Video S1 in [3], and Tables S1 and S2 in [3]. Adapted from [3].

from late metaphase (cells with  $>20$  bundles) suggests that bundles increase in length and decrease in curvature during metaphase Fig. 65.

Right-handed twist was dominant for vertically and horizontally oriented spindles and for cells in early and late metaphase Fig. 65, suggesting that the handedness of spindle chirality does not depend on mitotic stage or spindle orientation during imaging. The microtubule bundles of the *Naegleria* spindle are less curved than those of HeLa cells, as the radius of curvature is larger for *Naegleria*,  $6.9 \pm 0.4\text{mm}$ , than for the outermost bundles in HeLa cells,  $5.1 \pm 0.3\text{mm}$  [252] Moreover, the radius of curvature normalized to the spindle half-length, which is equal to 1 for bundles shaped as a semicircle, is  $1.26 \pm 0.05$  for *Naegleria* and  $0.90 \pm 0.05$  for HeLa cells [43]. The twist of *Naegleria* spindles is more eye-catching than in HeLa cells, however, due to the smaller number of microtubule bundles, which are well defined and have a uniform shape, in contrast to the less ordered distribution and shapes of bundles in HeLa cells. Together, these data indicate that the microtubule bundles that comprise the *Naegleria* spindle are physically linked and under rotational forces.

Similar to results from human cell lines, [2, 43, 197] the microtubule bundles in *Naegleria* spindles twist. This observation implies that *Naegleria*'s mitotic microtubule bundles are physically connected, a hypothesis that may explain their regular spacing within the spindle. The function of spindle chirality in human cells may be a passive mechanical response to spindle forces that decreases the risk of spindle breakage under high load [2, 70]. In contrast to the left-handed chirality observed in human cell lines, [2, 43, 197] the majority of *Naegleria* spindles are right-handed. When RPE1 cells are depleted of components of the key spindle regulator augmin, the spindle twist reverses and becomes right-handed [2], indicating that the chirality of twist is modulated by microtubule-associated proteins. Intriguingly, *Naegleria* lacks homologs of the entire augmin complex, [253] in line with the reversed chiral-

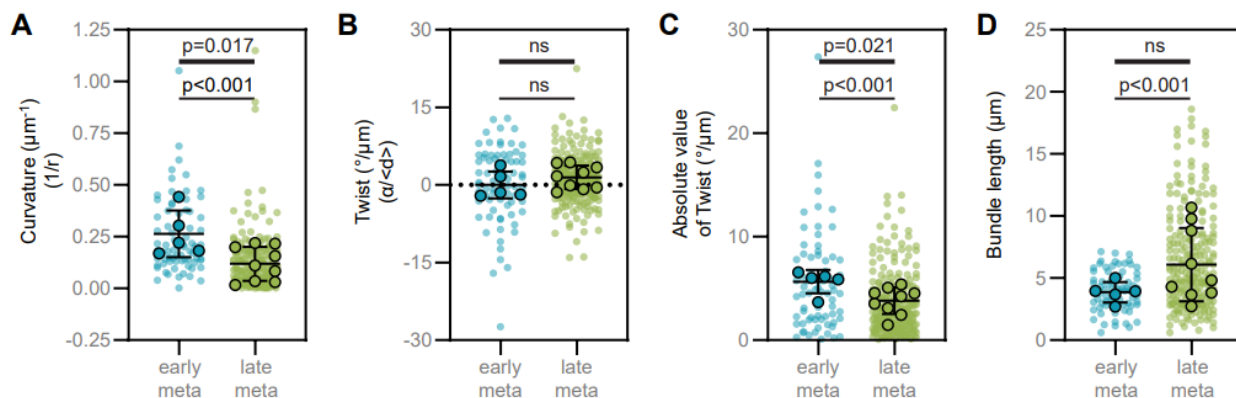


Figure 65: Curvature, twist, and arrangement of microtubule bundles. Related to Fig. 62 and Fig. 63. (A) Curvatures were calculated for individual bundles (smaller data points) and averaged for each spindle (larger data points). Lines indicate the mean and standard deviation calculated from spindle averages. Early metaphase bundles are significantly more curved when analysed per bundle (indicated by thin line, Mann-Whitney test), or when spindle averages are compared (indicated by thick line, unpaired t test). (B) Bundle twists were calculated and compared, and are displayed as in A. The mean twist is different from 0 in late metaphase ( $p = 0.0003$ ), but not in early metaphase ( $p = 0.94$ ). To determine whether spindles are statistically different in early versus late metaphase, we compared the twist of both individual bundles and whole spindles and found no statistically supported difference (individual bundles:  $p = 0.233$ , unpaired t test, whole spindles:  $p = 0.325$ , unpaired t test). (C) The twist values in panel B were converted to absolute values. These values support more total twist in early metaphase than late for individual bundles (Mann-Whitney test) and whole spindles (unpaired t test). (D) Bundle lengths were measured and data are displayed for individual bundles and spindle averages as in A. Late metaphase spindles have longer bundles when all individual bundles are considered (Mann-Whitney test), but not when averaged by spindle ( $p = 0.061$ , unpaired t test). Data were taken from 4 experimental replicates. Adapted from [3].



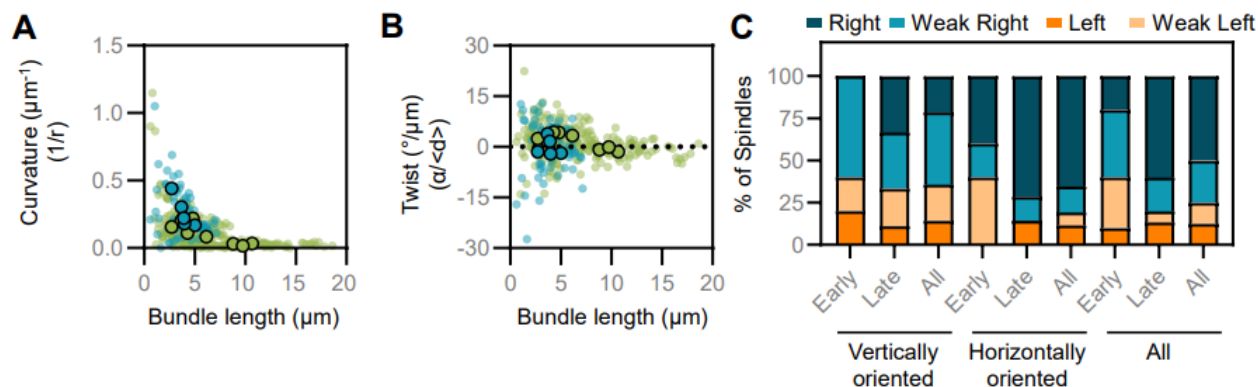


Figure 66: Curvature, twist, and arrangement of microtubule bundles. (A) The curvature of microtubule bundles is shown as a function of bundle length. Each small dot represents a single bundle within a spindle, while each larger dot represents the average for a spindle. Teal dots indicate bundles within early metaphase spindles, while green dots indicate late metaphase. (B) The twist of microtubule bundles is shown as a function of bundle length. Each small dot represents a single bundle within a spindle, while each larger dot represents the average for a spindle. Teal dots indicate bundles within early metaphase spindles, while green dots indicate late metaphase. For panels  $\alpha$ –F, data were quantified from 4 experimental replicates, encompassing 14 cells and 301 bundles. (C) The percentage of spindles with right, weak right, left, or weak left handedness are shown. Spindles are grouped according to the stage of mitosis (early or late metaphase) and their orientation (vertical or horizontal), as indicated. The twist was determined visually by moving through end-on  $z$ -stacks from the bottom plane towards the top plane, where bundle rotation clockwise and counter-clockwise implies a left-handed and right-handed twist, respectively. For horizontally oriented spindles,  $z$ -stacks were first rotated to obtain the end-on view. Data were taken from 4 experimental replicates. Adapted from [3].

ity of *Naegleria* spindles relative to that of augmin-expressing hTERT-RPE1 cells. Because spindle chirality in these human cell lines requires kinesin-5 (Eg5) and kinesin-8 (Kif18A) motor activity, we hypothesize that *Naegleria* spindle twist also relies on mitotic motor-generated torque. [2, 43]. In support of this idea, we mined previous transcriptional analyzes of *Naegleria* differentiation [254] and found several kinesins whose expression was up to 8-fold enriched in asynchronously dividing amoebae compared with non-dividing flagellates, including homologs of spindle-associated kinesin-5 and kinesin-14 (Table S1 in [3]). *Naegleria*'s evolutionary position makes it well suited for identifying features of mitotic spindles that may be deeply conserved, including their bi-polarity, elongation, and twist. *Naegleria*'s position also highlights features that may be lineage specific due to their absence in this distant species. For example, features of animal cell spindles that are missing from *Naegleria* include obvious microtubule-organizing centres and astral microtubules that contribute to spindle position and to cytokinesis. Moreover, the unique properties of *Naegleria* mitotic tubulins may have practical value. Although *Naegleria gruberi* is innocuous, the related *Naegleria fowleri* is the infamous 'brain-eating amoeba' that causes an infection that is both devastating and usually lethal [255]. Because the divergent residues we have identified in the *Naegleria* mitotic tubulins are conserved in both *Naegleria* species but not in human tubulins, these residues represent specific, potential targets for therapeutics to disrupt *Naegleria* cell division and growth.

### **3.3.4 Compression of the spindle along the pole-to-pole axis increases the left-handed twist**

The biological role of spindle chirality is still unknown. Although chirality may be simply a side effect of the activity of torque-generating motors, the twisted shapes of microtubule bundles may contribute to spindle physiology by allowing changes of spindle shape as a mechanical response to external forces. To test this idea, we gently compressed vertically oriented HeLa cell spindles in metaphase along the pole-to-pole axis for 1.5 minutes, fol-

lowing the compression protocol from a previous study [31] Fig. 67; Movie S7 in [2] ). We used the bundle tracing method to measure spindle twist, which allowed us to graphically reconstruct spindles from the end-on view and side view (Fig. 67). Traces of the microtubule bundles in the end-on view after 1 minute of compression were more rounded than before compression, indicating an increase in twist, and the mitotic spindle shortened (Fig. 67). Spindle shortening was used as a measure to confirm successful compression, showing that spindle length decreased from  $14.07 \pm 0.55 \mu\text{m}$  before compression to  $12.75 \pm 0.80 \mu\text{m}$  after 1 minute of compression ( $p = 0.013$ ; a paired t-test was used to compare the values before and after compression,  $n = 6$  spindles) (Fig. 68). Spindle width increased after compression in some cases, e.g., for the spindle shown in Fig. 67, but overall this change was not significant ( $p = 0.18$ ) (Fig. 68).

Compression resulted in a 2.3-fold increase of the left-handed spindle twist, from  $-0.63 \pm 0.28 \text{ deg}/\mu\text{m}$  before compression to  $-1.42 \pm 0.50 \text{ deg}/\mu\text{m}$  after 1 minute of compression ( $p = 0.040$ ) (Figs. 68 and 69) and Movie S7 in [2] . Histograms of twist values show that the distribution shifted towards more negative values upon compression (Fig. 70). To quantify this shift, we analysed the fraction of bundles having a strong left-handed twist with a value smaller than  $-2.8 \text{ deg}/\mu\text{m}$ , which is one standard deviation away from the mean twist before compression. The twist was smaller than  $-2.8 \text{ deg}/\mu\text{m}$  for 9 out of 80 bundles  $11.3\% \pm 3.5\%$  before compression, whereas after compression this was the case for 21 out of 73 bundles  $28.8\% \pm 5.3\%$ . The difference was significant ( $p = 0.0064$ ; two-proportions  $z$ -test), suggesting that compression resulted in a higher proportion of bundles having a strong left-handed twist. Contour length of the microtubule bundles did not change significantly after compression ( $p = 0.99$ ) (Figs. 68 and 69).

We were unable to detect changes in bundle curvature after compression ( $p = 0.41$ ), Figs. 68 to 70, which is consistent with the non-significant change in spindle width. Thus, as the spindle was compressed end-on by an external force, which resulted in spindle shortening, the microtubule bundles did not shorten substantially, but instead became more twisted.

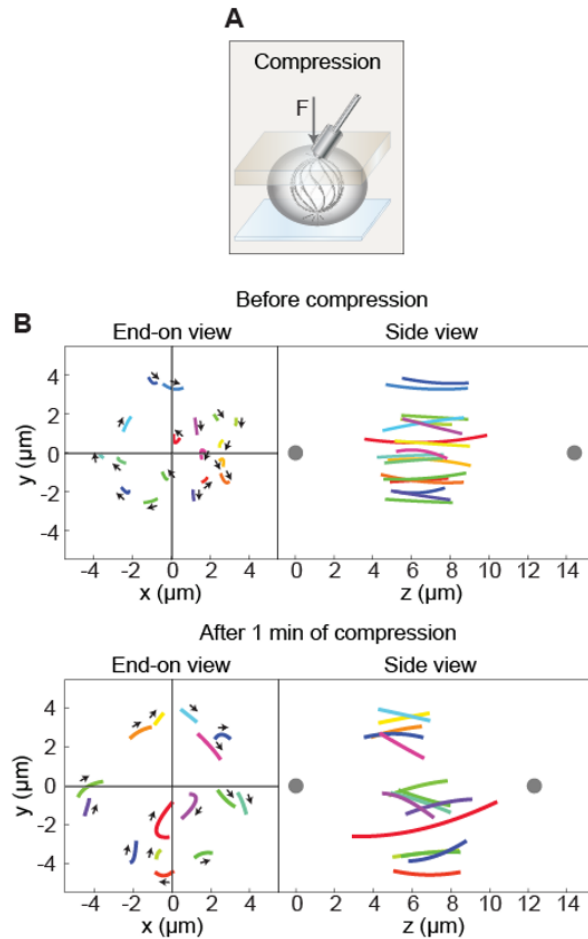


Figure 67: Spindles compressed by an external force have stronger twist. (A) Scheme of the experimental method for spindle compression. Blue layer represents the dish; spindle is shown inside a cell with microtubule bundles in grey; grey layer represents the gel with a metal rod on top; arrow shows the direction of force. (B) Microtubule bundles in a spindle shown from the end-on view and side view before compression and after 1 minute of compression, as indicated. Each bundle is represented by a different colour; lines show circular arcs of the fitted circles and arrows represent the rotation direction of each bundle. Grey dots in the side view represent spindle poles. Adapted from [2].

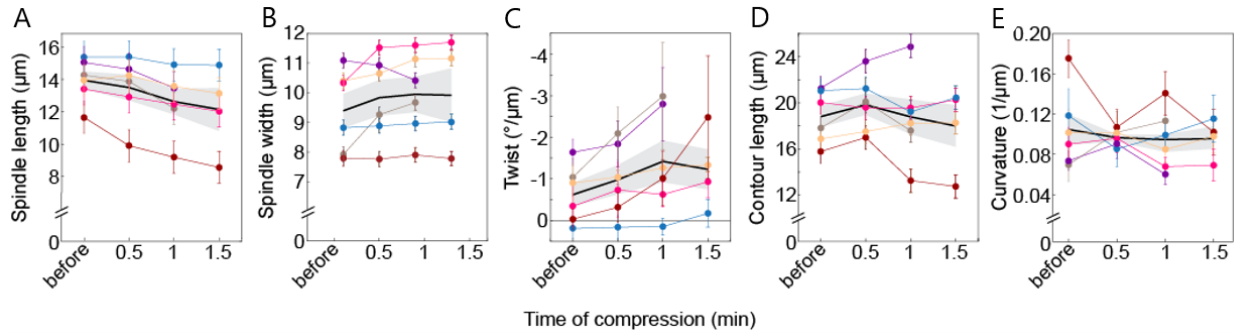


Figure 68: (C)-(G) Graphs showing the change of spindle parameters from before compression up to 1.5 min of compression: spindle length (C), spindle width (D), twist of microtubule bundles (E), length of the bundle contours (F), and bundle curvature (G). Each colour represents one cell; dots represent mean values; error bars in (C) and (D) show the estimated errors in the determination of spindle length and width,  $1 \mu\text{m}$  and  $0.25 \mu\text{m}$ , respectively; error bars in other graphs represent SEM. Thick black line shows the mean of all data with grey area representing SEM. Experiments were performed on the HeLa-Kyoto BAC cells stably expressing PRC1-GFP. Successful compression was performed on 6 spindles from 5 independent experiments. Individual data points are shown in Fig. 69 Adapted from [2].

These results support the idea that the twist within the bundles allows a mechanical response to external forces.

### 3.3.5 Motor proteins Eg5/kinesin-5 and Kif18A/kinesin-8 regulate spindle twist

To explore the molecular origins of torques in the spindle and thus its twisted shape, we consider the following molecular activities. First, motors that exert torque on the microtubule may generate the twisted shape of the bundle by twisting the microtubules within the bundle around each other, or by twisting the microtubules with respect to the spindle pole. Second, proteins that crosslink neighbouring microtubules or link microtubules with the pole may prevent free rotation of the microtubules, thereby allowing for twisting of the bundles. Third, nucleation of new microtubules within the bundle may affect the bundle twist. To test the role of these activities in the regulation of spindle twist, we performed a

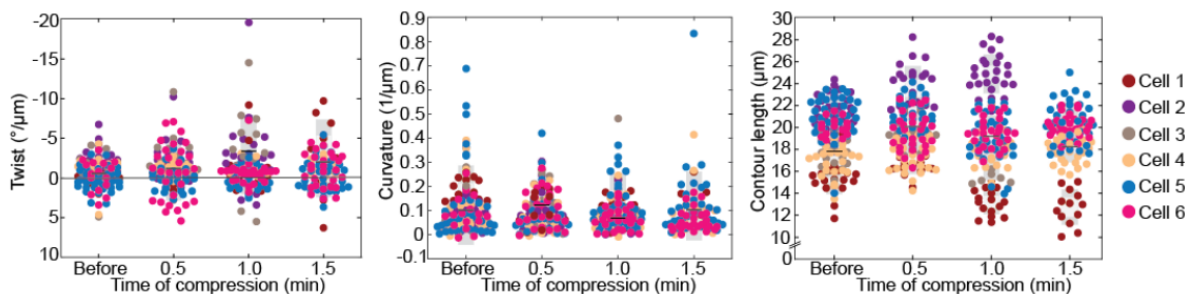


Figure 69: Twist, curvature and contour length of microtubule bundles in spindles compressed by an external force. On the left, graph show the change of the twist before and up to 1.5 min after the compression. In the middle, graph shows the change of the curvature before and up to 1.5 min after the compression. On the right, graph shows the change of length of the bundle contours before and up to 1.5 min after the compression. Each colour represents one cell, as described in the legend; dots represent bundles; the black line shows the mean; the light and dark grey areas mark 95% confidence interval on the mean and standard deviation, respectively. Experiments were performed on the HeLa-Kyoto BAC cells stably expressing PRC1-GFP. Adapted from [2].

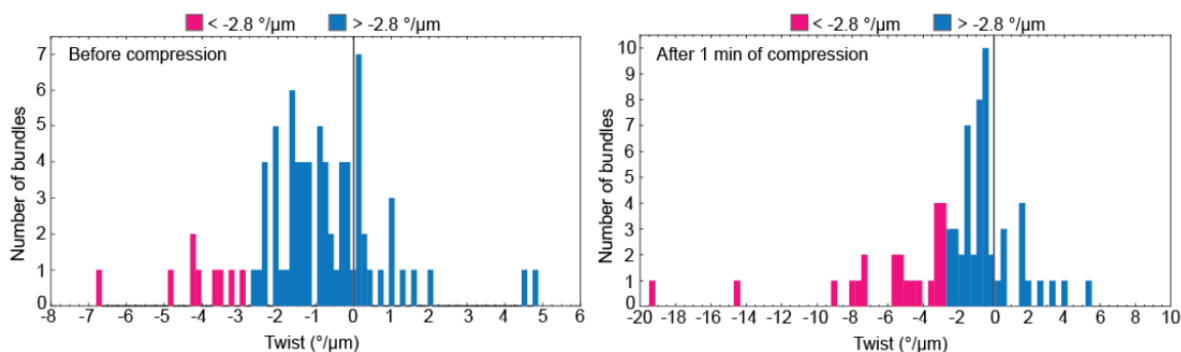


Figure 70: Histograms of twist values before (left) and 1 minute after the compression (right). Colors magenta and blue represent bundles with twist values lower than  $-2.8 \text{ deg}/\mu\text{m}$  and above  $-2.8 \text{ deg}/\mu\text{m}$  (one standard deviation away from the mean twist before compression), respectively. Note that the distribution shifted towards more negative values upon compression. The twist was smaller than  $-2.8 \text{ deg}/\mu\text{m}$  (corresponding to strong left-handed twist) for 9 out of 80 bundles ( $11.3\% \pm 3.5\%$ ) before compression, whereas after compression this was the case for 21 out of 73 bundles ( $28.8\% \pm 5.3\%$ ). Adapted from [2].

candidate screen on HeLa and RPE1 cells in which we perturbed motor proteins and other microtubule-associated proteins one by one using siRNA-mediated depletion, small-molecule inhibitors, or overexpression, and measured the resulting spindle twist. As the candidates for this mini-screen, we selected spindle-localized motor proteins for which it has been shown in vitro that they can rotate the microtubule (Eg5/kinesin-5, Kif18A/ kinesin-8, HSET/kinesin-14, MKLP1/kinesin-6, dynein), the main crosslinker of antiparallel microtubules PRC1, and the augmin complex that is responsible for the nucleation of microtubules along existing microtubules. Spindle twist was measured during metaphase, rather than at anaphase onset when twist is most pronounced, because depletion or inhibition of some of the candidate proteins, such as Eg5, Kif18A, and augmin, interferes with anaphase entry [256–258]. Furthermore, the measurement of the twist in metaphase is more reproducible because spindles in metaphase are in a steady state, whereas anaphase spindles undergo extensive changes. All candidate proteins were depleted by siRNA, except Eg5 which was inhibited with S-trityl-L-cysteine (STLC) [259], because siRNA depletion of Eg5 would not allow for spindles to properly assemble, resulting in monoasters [258]. Depletion of each protein was confirmed by measurements of the immunofluorescence signal of that protein on the spindle.

In agreement with our previous work on HeLa cells [43], we found that inhibition of Eg5 with STLC decreased spindle twist in both HeLa and RPE1 cells Figs. 71 to 73 (Tables 3 and 4).

In RPE1 cells, STLC-treated spindles were imaged while in bipolar orientation, before they collapsed into monopolars. Depletion of Kif18A abolished spindle twist in HeLa cells and resulted in right-handed twist in RPE1 cells, causing 65% of RPE1 spindles to twist in the right-handed fashion Figs. 71 to 73 (Tables 3 and 4), although this is not significantly different from 0 ( $p = 0.06$ , Student's t-test). Overexpression of either Eg5 or Kif18A in RPE1 cells did not yield any changes in twist Fig. 73 (Tables 3 and 4). Depletion of HSET/kinesin-14 did not change twist in HeLa or RPE1 cells Figs. 71 to 73; (Tables 3 and 4). We conclude that Eg5 and Kif18A regulate the torques within the spindle, which lead to the twisted shape

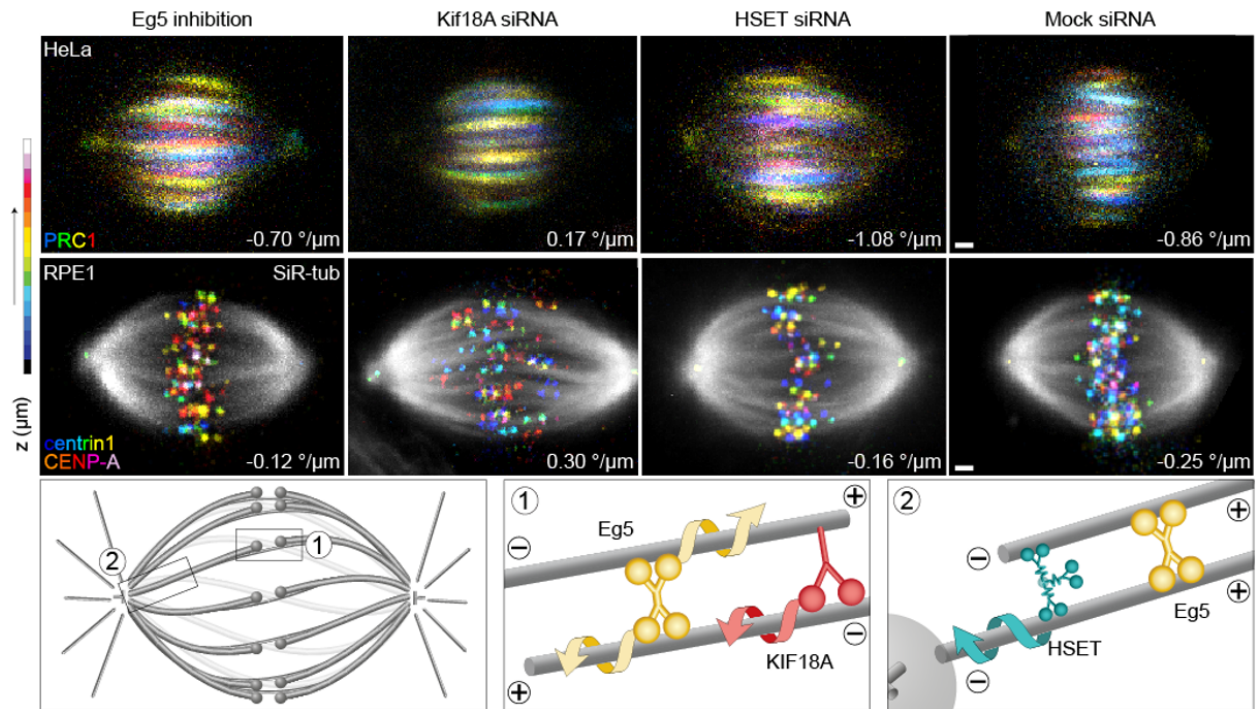


Figure 71: First row, images of the spindles in HeLa-Kyoto BAC cells stably expressing PRC1-GFP after inhibition/depletion of Eg5, Kif18A and HSET motor proteins. Second row, images of the spindles in hTERT-RPE1 cells permanently transfected and stabilized using CENP- $\alpha$ -GFP and centrin1-GFP after inhibition/depletion of Eg5, Kif18A and HSET motor proteins. Third row, simplified schemes showing localization and movement of Eg5, Kif18A and HSET motor proteins in the spindle. Microtubule bundles of HeLa spindles (PRC1-GFP signal) are colour-coded for depth using ImageJ temporal colour coding Lookup Table '16 colors' and microtubules of RPE1 spindles are shown in grey (SiR-tubulin dye) while kinetochores/centrosomes are colour-coded for depth using the same colour coding as described above (see colour bar). Scale bars, 1  $\mu\text{m}$ . Adapted from [2].



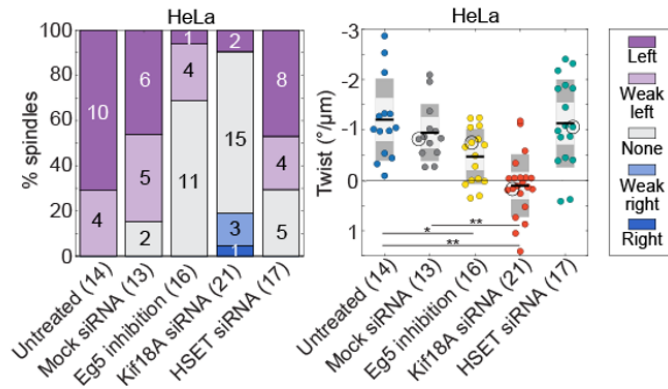


Figure 72: Spindle twist after perturbations of motor proteins in HeLa cells expressing PRC1-GFP. Left, visual assessment graph represents percentages of spindles showing left, right, weak left, weak right or no twist, as described in the legend, after inhibition/depletion of Eg5, Kif18A and HSET (numbers on the graph and in the brackets show the number of cells). Right, graph shows twist values calculated with the optical flow method after inhibition/depletion of Eg5, Kif18A and HSET motor proteins. The black line shows the mean; the light and dark grey areas mark 95% confidence interval on the mean and standard deviation, respectively; one-way ANOVA test showed significant difference between group means ( $p = 3.16 \times 10^{-7}$ );  $*p < 0.05$ ,  $**p < 0.01$  (Tukey's HSD post hoc test); significant difference between Kif18A siRNA and HSET siRNA is not shown on the graph ( $**p < 0.01$ ). Non-significant differences were not shown on the graph. Circled dots represent cells that are shown on the images above. Adapted from [2].

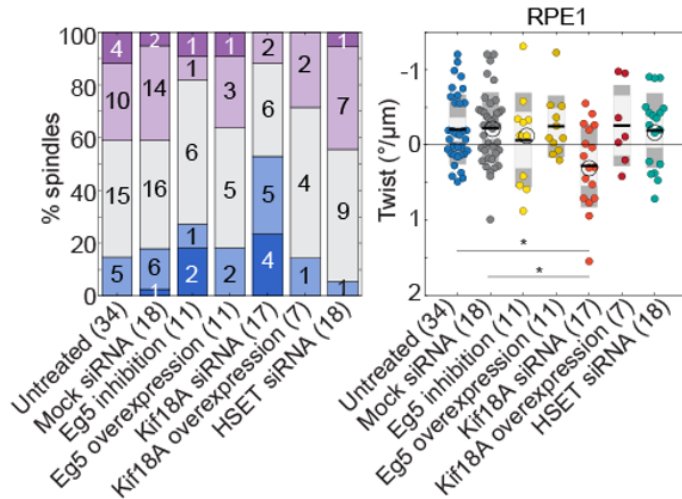


Figure 73: Spindle twist after perturbations of motor proteins in RPE1 cells expressing CENP- $\alpha$ -GFP and centrin1-GFP; legend as in (B). One-way ANOVA test showed significant difference between group means ( $p = 0.02$ );  $*p < 0.05$  (Tukey's HSD post hoc test). Non-significant differences were not shown on the graph. Adapted from [2].

of microtubule bundles.

### 3.3.6 Depletion of PRC1 makes RPE1 spindles twist in a right-handed manner, whereas overexpression of PRC1 abolishes twist

PRC1 protein is a key regulator of cytokinesis [260], but also the main crosslinking protein of antiparallel microtubules within bridging fibres [33, 179]. Without PRC1, bridging fibres are thinner and spindles have less curved and more diamond-like shape [33, 238], which led us to hypothesize that the twist might also be affected. In HeLa cells, depletion of PRC1 did not yield changes in the spindle twist Figs. 74 and 75; (Tables 3 and 4), but, surprisingly, when we depleted PRC1 in RPE1 cells, the spindles had right-handed twist of  $0.21 \pm 0.13 \text{ deg}/\mu\text{m}$  ( $n = 16$ ) Figs. 74 and 76; (Tables 3 and 4). In contrast, overexpression of PRC1 in RPE1 cells resulted in the abolishment of the spindle twist, with a complete lack of rotational movement of microtubule bundles Figs. 74 and 76; (Tables 3 and 4). Taken together, these data suggest that PRC1 regulates torques within the spindle in RPE1 cells, possibly by

limiting free rotation of microtubules within antiparallel bundles.

### **3.3.7 Depletion of augmin leads to zero twist in HeLa cells and right-handed twist in RPE1 cells**

The augmin complex is responsible for the microtubule nucleation from the lateral surface of the pre-existing microtubules [257, 261]. Augmin is thus important for the nucleation of the bridging fibres and, consequentially, the maintenance of the spindle shape [252]. When we depleted the augmin subunit HAUS6 (hDgt6/FAM29A), which binds to  $\gamma$ TuRC through the adaptor protein NEDD145, the spindles in HeLa cells had zero twist on average, whereas those in RPE1 cells had right-handed twist of  $0.49 \pm 0.21 \text{ deg}/\mu\text{m}$  ( $n = 16$ ) Figs. 74 to 76 (Tables 3 and 4). A similar result was observed after the depletion of the augmin subunit HAUS8 (hDgt4/Hice1), which binds to pre-existing microtubules. This resulted in zero average twist in HeLa cells and a strong right-handed twist in RPE1 cells of  $0.85 \pm 0.24 \text{ deg}/\mu\text{m}$  ( $n = 13$ ) Figs. 74 to 76; (Tables 3 and 4). The twist after depletion of HAUS6 or HAUS8 was not significantly different in HeLa ( $p = 0.26$ , Student's t-test) or RPE1 cells ( $p = 0.27$ , Student's t-test), as expected given that they are part of the same complex. Thus, augmin-mediated nucleation of microtubules along the wall of pre-existing microtubules is an important determinant of the direction and amount of spindle twist. As depletion of the augmin complex subunits prolongs metaphase [257], we explored how the twist changes when cells are arrested in metaphase by adding the proteasome inhibitor MG-132. Interestingly, spindles in RPE1 cells arrested in metaphase had right-handed twist of  $0.51 \pm 0.14 \text{ deg}/\mu\text{m}$  ( $n = 15$ ) Fig. 76 (Tables 3 and 4), suggesting that prolonging metaphase may cause a shift in the balance of torque-generating activities resulting in a right-handed twist.

### **3.3.8 Round spindles are more twisted than elongated spindles**

While imaging different types of spindles (phases of mitosis, cell lines, protein perturbation), we noticed that round spindles often have stronger twist than elongated spindles. To quantify

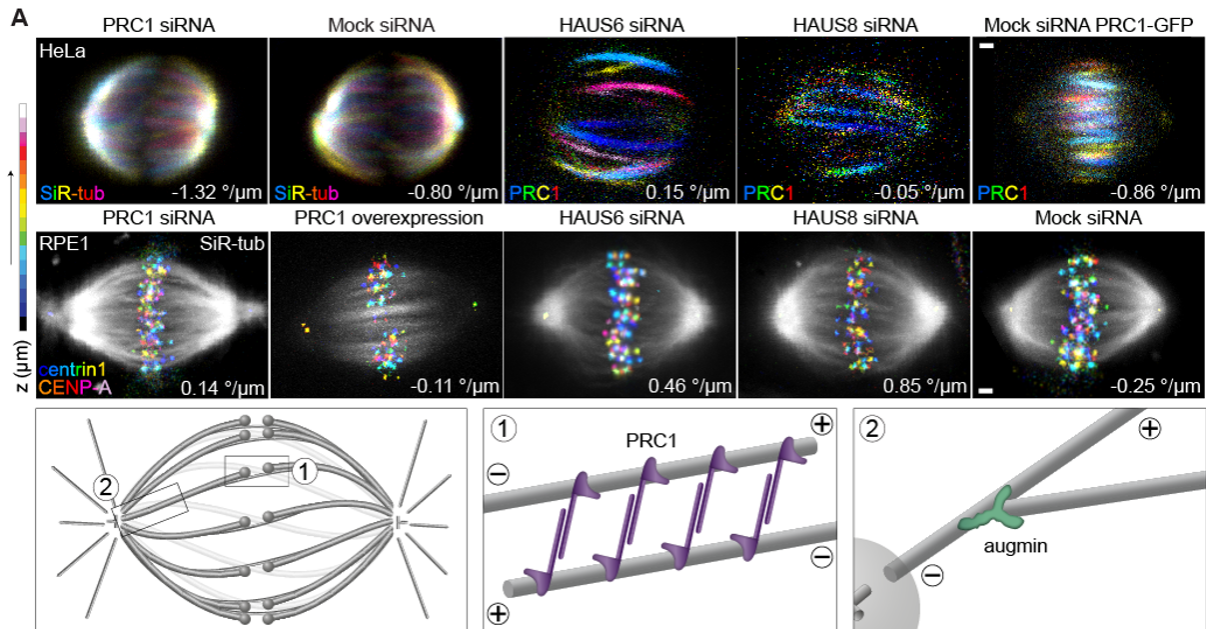


Figure 74: First row, images of spindles in a non-transfected HeLa cell line stained with SiR-tubulin (first 2 spindles) and HeLa-Kyoto BAC cells stably expressing PRC1-GFP (last 3 spindles), after depletion of PRC1 and subunits of the augmin complex HAUS6 and HAUS8. Second row, images of spindles in the hTERT-RPE1 cells, permanently transfected and stabilized using CENP- $\alpha$ -GFP and centrin1-GFP RPE1, after perturbations of PRC1 and depletions of subunits of the augmin complex HAUS6 and HAUS8. Third row, simplified schemes showing the localization of PRC1 and augmin in the spindle. Microtubule bundles in HeLa cells (PRC1-GFP signal in HeLa-Kyoto BAC cells and SiR-tubulin dye in non-transfected HeLa cells) are colour-coded for depth using ImageJ temporal colour coding Lookup Table '16 colors' and microtubules of RPE1 spindles are shown in grey (SiR-tubulin dye, except the cells with overexpressed PRC1 that show PRC1-mCherry signal), while kinetochores/centrosomes are colour-coded for depth using the same colour coding as described above (see colour bar). Scale bars, 1  $\mu\text{m}$ . Adapted from [2].

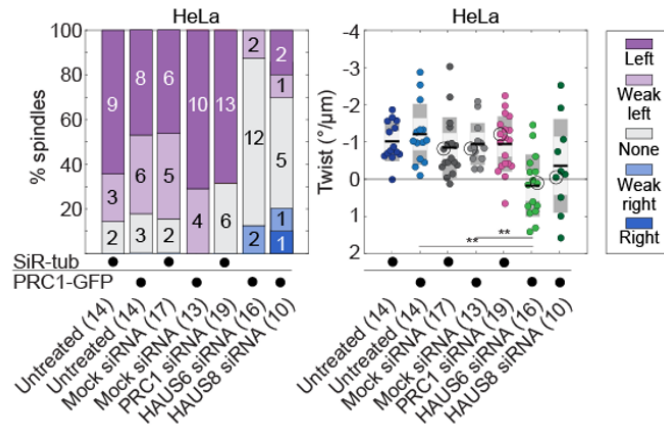


Figure 75: Spindle twist after perturbations of PRC1 and augmin in HeLa cells. Left, visual assessment graph represents percentages of spindles showing left, right, weak left, weak right or none twist, as described in the legend, after depletions of PRC1 protein and subunits of augmin complex HAUS6 and HAUS8 in HeLa cells (numbers on the graph and in the brackets show the number of cells; black dots under the graph denote the cell line/staining used for the corresponding treatment). Right, graph shows twist values calculated with the optical flow method after depletions of PRC1 protein and subunits of augmin complex HAUS6 and HAUS8. The black line shows the mean; the light and dark grey areas mark 95% confidence interval on the mean and standard deviation, respectively; one-way ANOVA test showed significant difference between group means ( $p = 8.06 \times 10^{-5}$ );  $**p < 0.01$  (Tukey's HSD post hoc test). Non-significant differences were not shown on the graph. Circled dots represent cells that are shown on images. Experiments were performed on the non-transfected HeLa cell line (for the depletion of PRC1 and its control) and HeLa-Kyoto BAC cells stably expressing PRC1-GFP (for the depletion of the HAUS6 and HAUS8 and their controls). Adapted from [2].

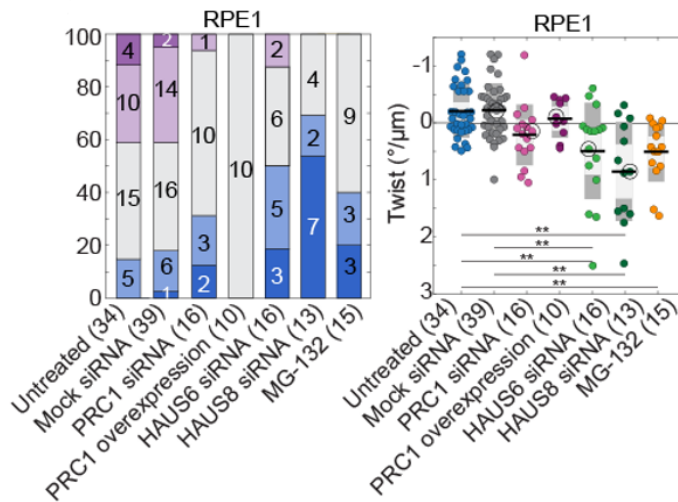


Figure 76: Spindle twist after perturbations of PRC1 and augmin in RPE1 cells expressing CENP- $\alpha$ -GFP and centrin1-GFP; legend as in (B). One-way ANOVA test showed significant difference between group means ( $p = 2.49 \times 10^{-9}$ );  $**p < 0.01$  (Tukey's HSD post hoc test); significant differences between HAUS8 siRNA with PRC1 overexpression ( $**p < 0.01$ ) and PRC1 siRNA ( $*p < 0.05$ ) are not shown on the graph. Non-significant differences were not shown on the graph. Adapted from [2].

this observation, we measured spindle length and width and calculated the width/length ratio as a measure for the roundness of the spindle, where ratios closer to 1 describe round spindles, and smaller values elongated spindles Fig. 80. Higher width/length ratios are a signature of stronger bending moments in the spindle [43] . We tested the correlation between the width/length ratios and twist values in metaphase, and found that in non-transfected HeLa cells, whose width/length ratios were roughly between 0.8 and 1, rounder spindles had a stronger left-handed twist Fig. 80, indicating a correlation between bending and twisting moments. In contrast, no correlation was observed in RPE1 cells, whose width/length ratios were between 0.5 and 0.8 Fig. 80. A weak correlation was found in HeLa cells expressing PRC1-GFP, which had smaller width/length ratios than non-transfected HeLa cells Fig. 77.

A plot of the twist as a function of the width/length ratio for various mitotic phases and treatments indicates that different combinations of twist and bending moments exist in spindles in different phases of mitosis or in which different molecular mechanisms are perturbed (Fig. 80; Figs. 77 to 79 for twist vs. width or length). In HeLa cells, prometaphase and late anaphase spindles are elongated with zero and small left-handed twist values, respectively Fig. 80. Left-handed twist rises during metaphase when spindles are the roundest, and highest twist values are at the beginning of anaphase when spindles are still rather round Fig. 80. In contrast, in RPE1 cells such correlation between twist and roundness over mitotic phases was not observed Fig. 80.

When analysing the twist of metaphase spindles across the treatments, we found that in HeLa cells, the left-handed twist was prevalent in spindles with mild or high width/length ratios (higher than 0.8), whereas right-handed twist was found in spindles with lower width/length ratios (lower than  $\tilde{0}.8$ ; Fig. 80). In RPE1 cells, both left-handed and right-handed twist was found in spindles over the whole range of width/length ratios, which was shifted to smaller values compared to HeLa cells (up to  $\tilde{0}.8$ ; Fig. 80). Taken together, these results suggest that spindles with more round shapes are made of bundles that are more twisted in the left-handed direction than spindles with elongated shapes. Both changes in

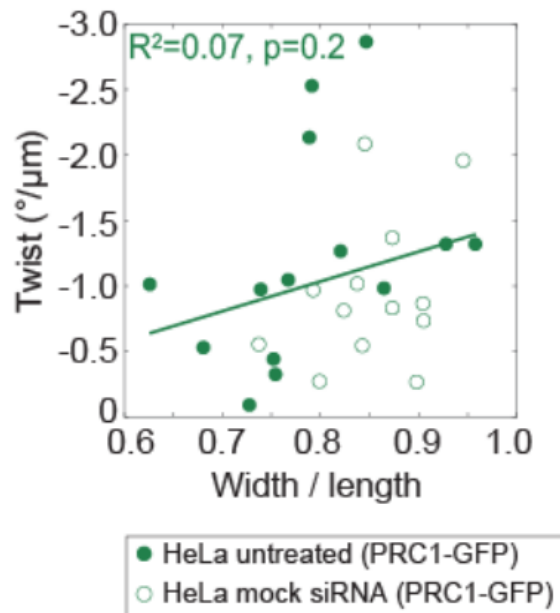


Figure 77: Correlation between spindle length or width and spindle twist in different phases of mitosis and during different protein perturbations in HeLa and RPE1 cells. Round spindles have stronger twist than elongated spindles. Graph shows the correlation between width/length ratio and twist in HeLa cells. Filled circles represent untreated cells while empty circles represent mock siRNA controls. Lines show linear fit (untreated cells together with mock siRNA controls); equation  $y = -2.28x + 0.79$ ; goodness of fit shown in the graph. Experiments were performed on the HeLa-Kyoto BAC cells stably expressing PRC1-GFP. Adapted from [2].



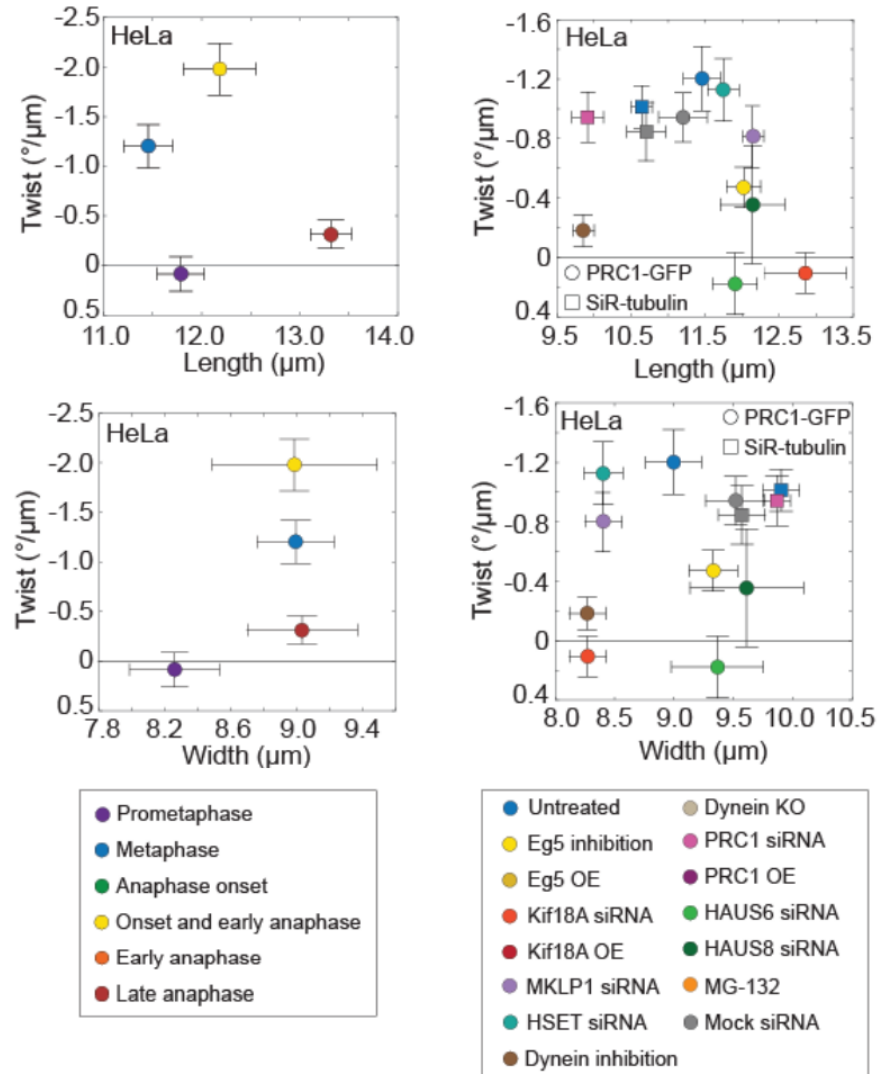


Figure 78: Graphs showing how the spindle twist and length (top) or width (bottom) in HeLa cells vary with the different phases of mitosis (left) or perturbations of spindle-associated proteins (right). Each colour represents different phase of mitosis or protein perturbation, as described in the legend at the bottom; error bars represent SEM. Experiments were performed on the HeLa-Kyoto BAC cells stably expressing PRC1-GFP (dots) and non-transfected HeLa cell line for the depletion of PRC1 and its controls (rectangles). Adapted from [2].

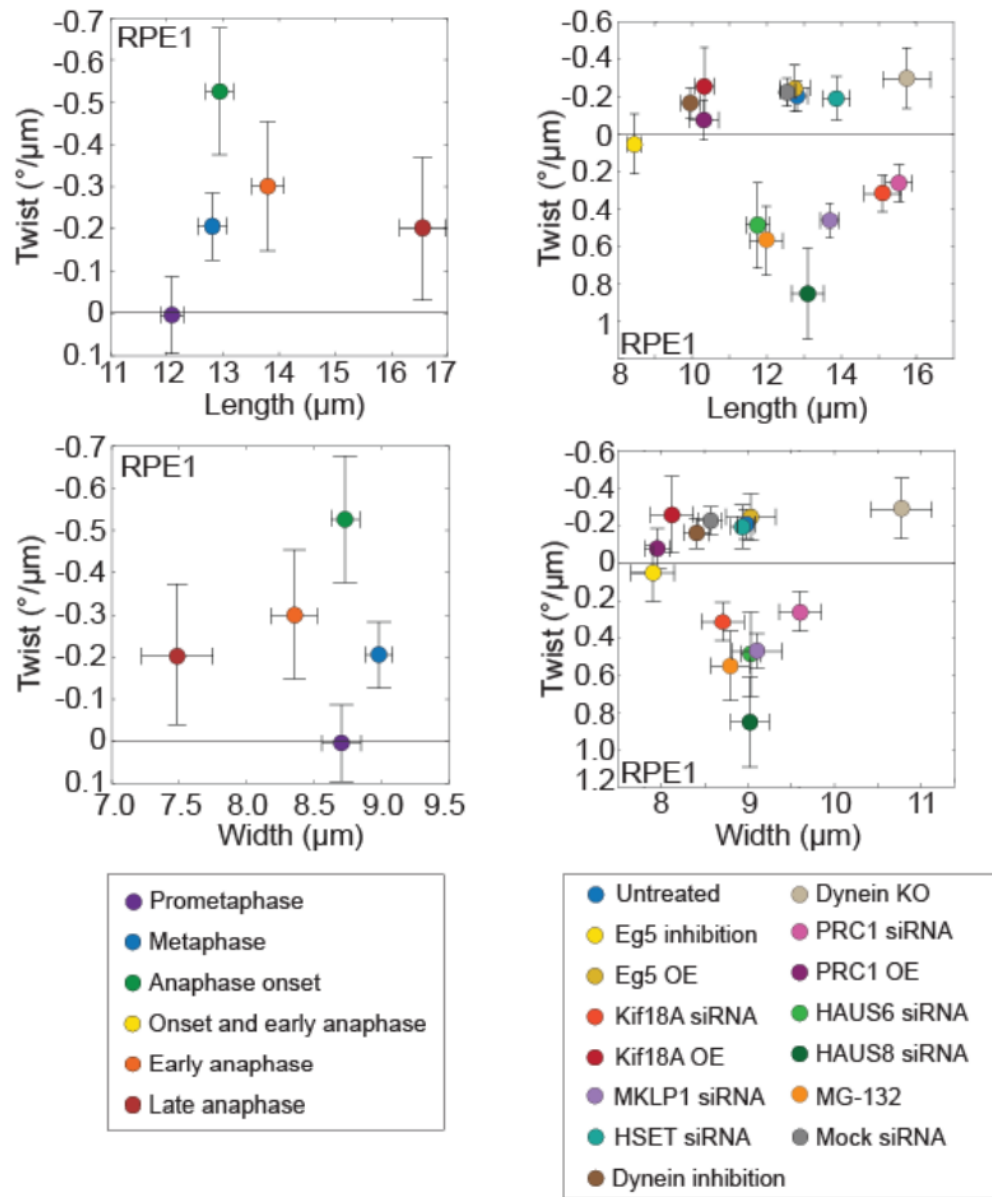


Figure 79: Graphs showing how the spindle twist and length (top) or width (bottom) in RPE1 cells vary depending on the different phases of mitosis (left) or perturbations of spindle-associated proteins (right). Each colour represents different phase of mitosis or protein perturbation, as described in the legend at the bottom; error bars represent SEM. Experiments were performed on hTERT-RPE1 cells, permanently transfected and stabilized using CENP- $\alpha$ -GFP and centrin1-GFP and RPE1 inducible CRISPR/Cas9 DYNC1H1 knockout cells. Adapted from [2].

the twist and in the spindle shape across the treatments are likely caused by the perturbation of the activity of the motor protein or another microtubule-associated protein specific to each treatment.

### **3.3.9 Mechanisms that generate spindle twist**

The chiral shape of the human mitotic spindle, visible as the left-handed twist of microtubule bundles, implies that torques act within the spindle. In this work we reveal biomechanical and molecular mechanisms that regulate the torques within microtubule bundles reflected in the spindle twist. From a biomechanical point of view, we show that forces within or outside the spindle regulate spindle twist Fig. 81 (box 1). Among the spindles in non-transfected HeLa cells during metaphase, round spindles are more twisted than elongated ones. In agreement with this, HeLa cell spindles in metaphase and just after anaphase onset are more round and more twisted than in prometaphase and late anaphase, when the spindles are elongated and twist is largely absent. In RPE1 spindles, which are overall more elongated than HeLa spindles, the twist is weaker and not correlated with the width/length ratio. Moreover, when we squeezed HeLa spindles along the pole-to-pole axis, they became rounder and their twist increased. These findings suggest that spindle roundness, which reflects bending moments within the spindle [43], is correlated with twist. Thus, the molecular mechanisms that generate larger bending moments, causing the spindles to be rounder, may also generate larger twisting moments, visible as stronger twist of the microtubule bundles. It is interesting to see that spindles, as complex and dynamic structures, show a relationship between twisting and bending similar to simple systems from classical beam mechanics [154]

We identified several molecular players involved in the regulation of spindle chirality by performing a candidate screen in which we perturbed motor proteins that step in a chiral manner and other microtubule-associated proteins. Inactivation of Eg5 reduced left-handed twist in HeLa cells, which is consistent with our previous findings [43], and resulted in zero

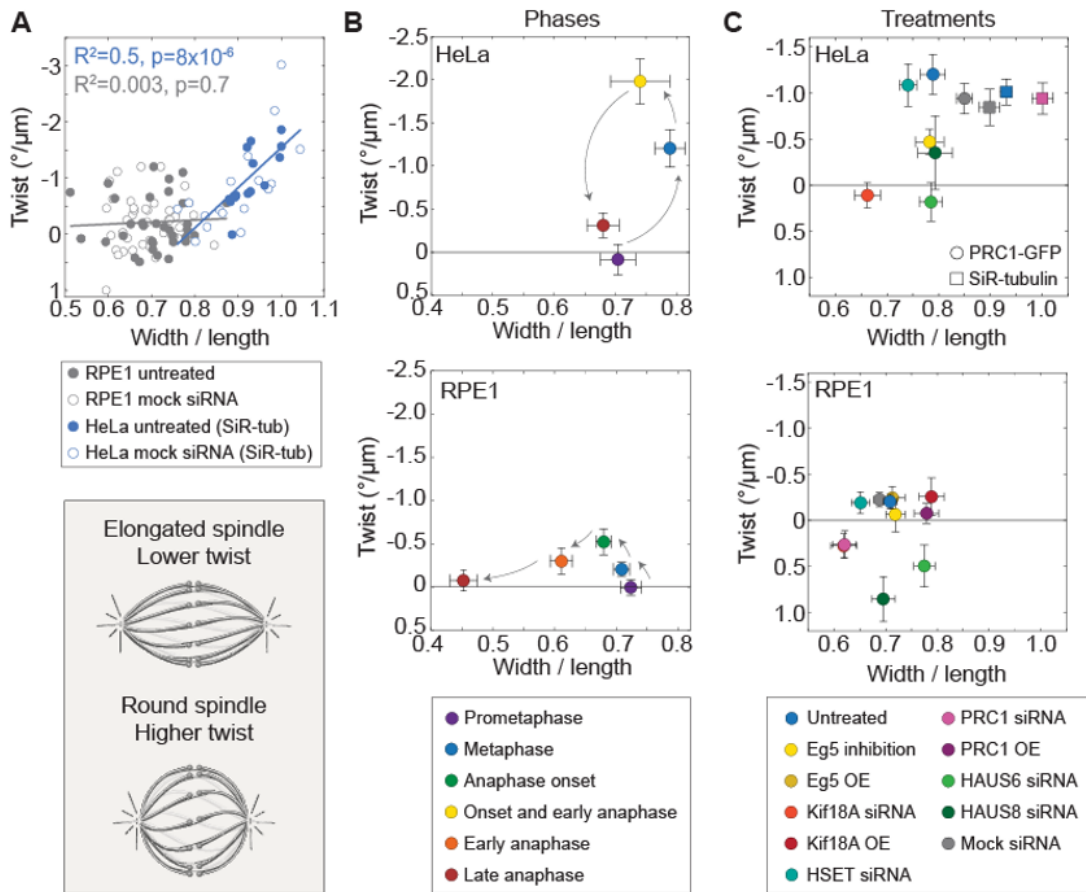


Figure 80: Round spindles have stronger twist than elongated spindles. (A) Graph shows the correlation between width/length ratio and twist in HeLa and RPE1 cells. Filled circles represent untreated cells while empty circles represent mock siRNA controls as indicated in the legend below the graph. Lines show linear fits for each cell line (untreated cells together with mock siRNA controls). Data for HeLa cells were also used in graphs in Fig. 75 The scheme on the bottom shows that elongated and round spindles, with lower and higher width/length ratio, have lower and higher twist, respectively. (B) Graphs showing how the spindle twist and width/length ratio in HeLa (top) and RPE1 cells (bottom) vary over different phases of mitosis. Each colour represents a phase, as described in the legend below the graphs; error bars represent SEM; arrows indicate progression of mitosis. (C) Graphs showing how the spindle twist and width/length ratio in HeLa (top) and RPE1 cells (bottom) vary depending on the perturbations of spindle-associated proteins. Colours represent different protein perturbation, as described in the legend below the graphs; error bars represent SEM. The same data were used in graphs in Figs. 72, 73, 75 and 76. Adapted from [2].

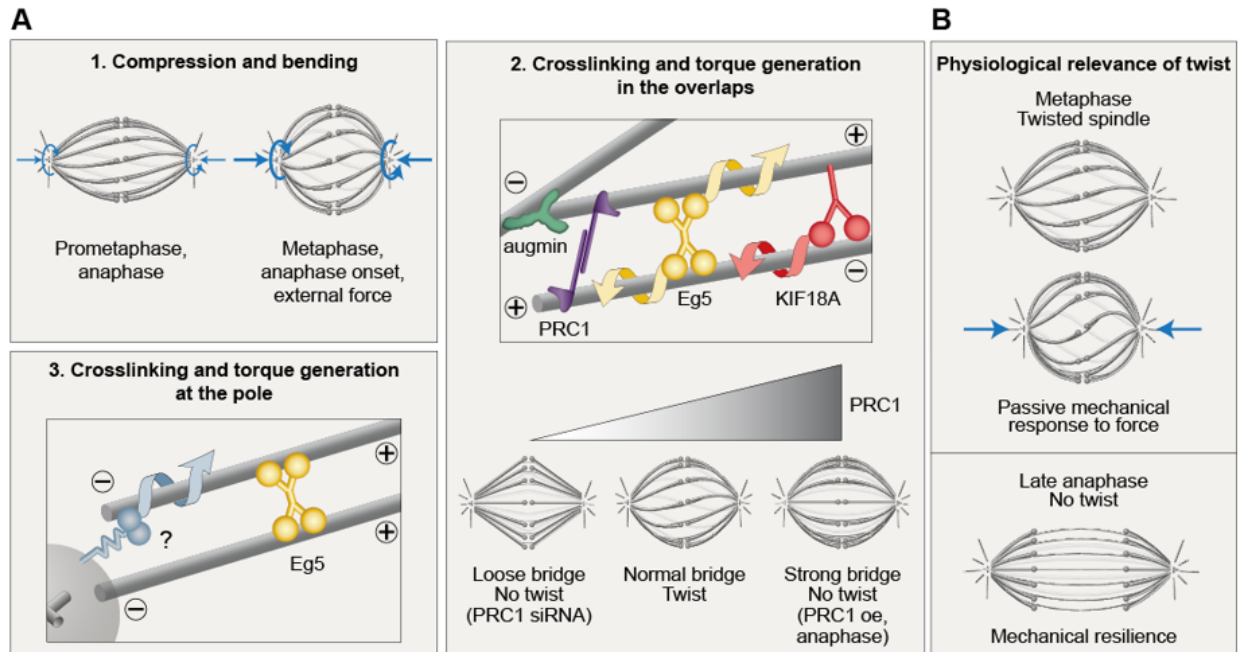


Figure 81: Biomechanical and molecular origins of spindle twist and its biological role. (A) Forces regulate twist (box 1). Round spindles or those compressed by external forces (blue straight arrows) are more twisted than elongated ones, suggesting that larger bending moments (blue curved arrows) are correlated with larger twist. Within the antiparallel overlaps of bridging microtubules (box 2), Eg5 and Kif18A rotate the microtubules around one another, whereas crosslinking by PRC1 constrains the free rotation of microtubules within the bundle, allowing for accumulation of torsional stresses (the triangle represents the amount of PRC1, oe stands for overexpression). Augmin contributes to the twist by nucleating bridging microtubules. At the spindle pole (box 3), Eg5 crosslinks parallel microtubules, which may prevent their free rotation. Eg5 and other motors (question mark) may rotate the microtubules around the pole. (B) Spindle twist allows for a mechanical response to external forces during metaphase (top). In contrast, in late anaphase twist is absent, which promotes force transmission for spindle elongation and maintenance of chromosome separation (bottom). Adapted from [2].

twist in RPE1 cells. Kif18A depletion resulted in no twist in HeLa cells and a switch in twist direction from left to right in RPE1 cells. The twist was not altered by overexpression of these proteins. Both of these motors have been shown *in vitro* to exert torque on microtubules [181, 184, 187], and are found within the antiparallel overlaps of bridging microtubules in the spindle [33, 238, 262]. Thus, it is likely they generate the twisted shape of the bundle by rotating the antiparallel microtubules within the bundle around each other Fig. 81(box 2). Eg5 may also contribute to spindle twist by acting at the spindle pole Fig. 81(box 3), given that the most pronounced localization of Eg5 is in the pole region [33, 262]. Here, Eg5 may crosslink parallel microtubules [263, 264], which would prevent their free rotation within the bundle and promote the accumulation of torsional stresses, but it may also actively generate torques. Other motors at the pole, such as Kif2a58 and Kif2c/MCAK59 from the kinesin-13 family, may also contribute to spindle twist by rotating the microtubules with respect to the spindle pole Fig. 81 (box 3). Surprisingly, depletion of the augmin complex's HAUS6 and HAUS8 subunits, which promote the nucleation of new microtubules from the wall of existing microtubules, had the greatest effect on spindle twist [257, 261, 265]. In HeLa cells, these depletions resulted in zero twist and right-handed twist in RPE1 cells. Given that augmin depletion reduces the number of microtubules within bridging fibres, we hypothesise that the altered twist is due to fewer antiparallel overlaps where torque-generating motors like Eg5 and Kif18A bind. Fig. 81 (box 2). In addition, augmin nucleates new microtubules at an angle with respect to the wall of the old microtubule [266, 267], thus it is tempting to speculate that if the new microtubules extend skewedly from the old microtubules and spiral around them, the entire microtubule bundle may twist. Depletion of the crosslinker of antiparallel microtubules PRC1 caused right-handed twisting in RPE1 cells, similar to augmin perturbation. We propose that in a metaphase spindle, the microtubules crosslinked by PRC1 cannot freely rotate within the bundle, causing torsional stresses to accumulate Fig. 81(box 2). The torsional rigidity of the entire bundle, however, is low enough to allow for twisting. The bundles had completely straight shapes in late anaphase,

when PRC1 is abundant on midzone microtubules, and in metaphase experiments with PRC1 overexpression. A high concentration of PRC1 within the bundles may result in an increased number of bundled microtubules, increasing the bundle's torsional rigidity and making it more difficult to twist. The spindle twist is also affected by the length of metaphase. Arresting RPE1 cells during metaphase resulted in right-handed twist, similar to Kif18A or the augmin complex depletion. Interestingly, these depletions also prolong metaphase [256, 257], which may contribute to the observed effect on twist. The shift in twist direction from left to right suggests the presence of competing mechanisms that promote twist in opposing directions. Various perturbations can tip the balance either way. Protein depletions that resulted in zero twist in HeLa cells largely resulted in right-handed twist in RPE1 cells, so the twist changed by a similar amount in both cell lines. This means that torques in both cell lines are regulated by similar mechanisms, but the torque balance in HeLa spindles is skewed more toward the formation of left-handed twists than in RPE1 spindles. Twist is mostly absent in HeLa and RPE1 spindles during anaphase, in contrast to metaphase. A recent study discovered strong left-handed twisting during anaphase in RPE1 cells after combined Eg5 inhibition and NuMa depletion, implying that opposing motors are required to prevent twisting in the anaphase spindle. [197] .

The twist was tuned in the same direction by all of the different molecular perturbations used in this study, towards more positive values, implying that the corresponding molecular players promote left-handed twist. As a result, we hypothesise that right-handed twisting is caused by the activity of microtubule-associated proteins that were not identified by our candidate screen. Additionally, the helical structure of the microtubule lattice [268, 269] may influence the twist of a bundle of microtubules. In contrast to the left-handed twist of human spindles, spindles in the amoeba *Naegleria gruberi* are twisted in a right-handed fashion [3], which may be due to the differences in kinesins and other microtubule-associated proteins between *Naegleria* and humans. *Naegleria* lacks homologs to subunits of the augmin complex, [253] which is in line with the right-handed twist of spindles in this amoeba and in

RPE1 cells depleted of augmin. Helical structures are also widespread in plants, e.g., lefty mutants in *Arabidopsis thaliana* have cortical microtubule arrays that form right-handed helices, resulting in clockwise bending of leaf petioles and flower petals when viewed from above [270] whereas spiral mutants show counter-clockwise bending [271]. What determines the direction and amount of twist in different organisms' microtubules, and whether there are common elements, remain intriguing areas for future research.

### **3.3.10 Physiological function of spindle twist**

Although spindle chirality may be merely a byproduct of the action of torque-generating motors, the twisted shapes of microtubule bundles may contribute to spindle function. We propose that the twisted shape observed during metaphase is beneficial to the spindle because it allows for mechanical response to external forces to change spindle shape. A twisted spindle can quickly shorten under compressive forces by increasing the twist in the same way that an elastic spring does Fig. 81 (B, top). This response does not necessitate the depolymerization of microtubules during spindle shortening, as it would in non-twisted spindles. Our experiments, in which we compressed the spindle along the pole-to-pole axis and observed an increase in twist while the contour length of microtubule bundles remained largely unchanged, lend support to the model in which the built-in twist helps the spindle respond to forces and reduces the risk of spindle breakage under high load. In contrast to metaphase, the spindle is not chiral during late anaphase because the bundles lose their twist and become straight. This straightening is most likely caused by PRC1 and other midzone proteins accumulating within these bundles. We hypothesise that the straight shapes of the bundles benefit the spindle in late anaphase by allowing force transmission from the central overlap region to the poles, allowing the chromosomes to separate and move apart Fig. 81 (B, bottom). Spindle chirality may also promote physical separation of adjacent bundles during prometaphase or aid in the initiation of spindle elongation at the start of anaphase by releasing elastic energy stored in the twisted bundles. Surprisingly, a recent study discovered that changes in



twist can be linked to chromosome segregation errors [197]. Thus, twist regulation may be important for chromosome segregation fidelity, which requires further investigation. Overall, we anticipate that the findings presented here will spark new interest in the molecular mechanisms and biological roles of rotational forces in the spindle.

## 4 Mean-field model of the mitotic spindle

The mitotic spindle is a complex micro-machine composed of microtubules and associated proteins that must be highly ordered in space and time to function properly. A functional spindle has a distinct shape composed of curved bundles of microtubules twisted around the pole-to-pole axis. It is still unclear how linear and rotational forces define the overall shape of the mitotic spindle, as well as how twisted shapes emerge as a result of interactions between microtubules and motor proteins. To address this, we propose a mean-field approach in which we describe the dominant forces and torques at the poles to model the entire spindle. Motor proteins, which generate forces and torques within the antiparallel overlap region of microtubule bundles, are also included in the model. The model predicts that the shape of the entire spindle is predominately determined by rotational forces, and that a difference in bending forces explains the disparity in the shapes of inner and outer bundles by comparing theoretical results with experimentally observed shapes of bundles in the mitotic spindle. The model's main goal is to investigate the force balance of the entire static spindle using the observed shapes. We intend to describe the spindle's force balance using a mean-field approach in which discrete microtubule bundles in a specific region, as well as the forces and torques exerted by these bundles, will be approximated by an averaged bundle. Averaged microtubule bundles will be described as thin elastic rods that extend between the two spindle poles [43]. The model will predict forces and torques in the spindle, and thus the shape of the entire spindle, including the shapes of the inner and outer bundles. The shapes predicted will be compared to the shapes observed in our experiments. Based on the predicted shapes,

we will provide a mechanical explanation for the shapes of the inner and outer bundles, as well as the major difference(s) between them. This approach will provide comprehensive insight in forces and torques acting in the entire spindle. Though the model will help us understand how forces and torques are distributed in the spindle and how they achieve the delicate balance found in the metaphase spindle, it will not reveal their nature because it does not physically model these forces.

#### 4.1 Theory for force balance of mitotic spindle

To investigate the balance of forces and torques throughout the spindle, we propose a model that includes two centrosomes and interpolar microtubule bundles extending between them. As a first step, we will describe a model for discrete microtubule bundles, similar to how it was done in [43]. In the following step, we will present a *mean-field* description in which discrete microtubule bundles in a specific region, as well as forces and torques, are approximated by averaged physical quantities. The mean-field approach is useful in physics when there are many interacting parties and it is possible to replace these complex interactions with a resultant external field rather than describing each of them individually, which is especially common in solid-state physics, i.e., the Hartree-Fock approximation [272] or the Ginzburg-Landau theory of superconductivity [273]. Because of the large number of microtubules in the spindle [5, 140, 274], the mean-field approach is appropriate for modelling the system [275, 276].

We will first briefly introduce a model for discrete bundles, as it forms the basis for the mean-field model. The centrosomes are described as two spheres of radius  $d$  with centres separated by vector  $\mathbf{L}$  of length  $|L|$  Fig. 82. Microtubule bundles, denoted by index  $i = 1, \dots, n$ , are considered thin elastic rods extending between the spheres. Interactions between the left centrosome and  $i$ -th microtubule bundle are described by the force,  $F_i$ , and the torque,  $M_i$ . This description does not include the molecular basis of this interaction. Because

we consider the shape of the spindle static, the balance of forces for the left centrosome reads

$$\sum_{i=1}^n \mathbf{F}_i = 0, \quad (4.1.1)$$

and the balance of torques reads

$$\sum_{i=1}^n (\mathbf{M}_i + \mathbf{d}_i \times \mathbf{F}_i) = 0. \quad (4.1.2)$$

Balances of forces and torques at the right pole can be obtained by replacing  $\mathbf{F}_i$ ,  $\mathbf{M}_i$ , and  $\mathbf{d}_i$  with  $\mathbf{F}'_i$ ,  $\mathbf{M}'_i$  and  $\mathbf{d}'_i$ , respectively. Here and throughout the text the prime sign corresponds to the right pole. We also introduce a balance of forces for the microtubule bundle

$$\mathbf{F}_i + \mathbf{F}'_i = 0, \quad (4.1.3)$$

and a balance of torques for the microtubule bundle

$$\mathbf{M}_i + \mathbf{M}'_i + \mathbf{d}_i \times \mathbf{F}_i + (\mathbf{L} + \mathbf{d}'_i) \times \mathbf{F}'_i = 0. \quad (4.1.4)$$

Forces and torques acting at the end of a microtubule bundle change its shape, because microtubule bundles are elastic objects [33, 153, 200]. The microtubule bundle can be thought of as a single elastic rod of flexural rigidity  $\kappa$  and torsional rigidity  $\tau$ . The contour of the elastic rod is described by a contour length,  $s$ , and a vector representing the position in space with respect to the initial point at the sphere representing the spindle pole,  $\mathbf{r}(s)$  Fig. 82.

The normalized tangent vector is calculated as  $\mathbf{t} = d\mathbf{r}/ds$ . The torsion angle,  $\phi(s)$ , describes the orientation of the cross-section along the length of the rod. The curvature and the torsion of an elastic rod are described by the static Kirchhoff equation [154], which is a

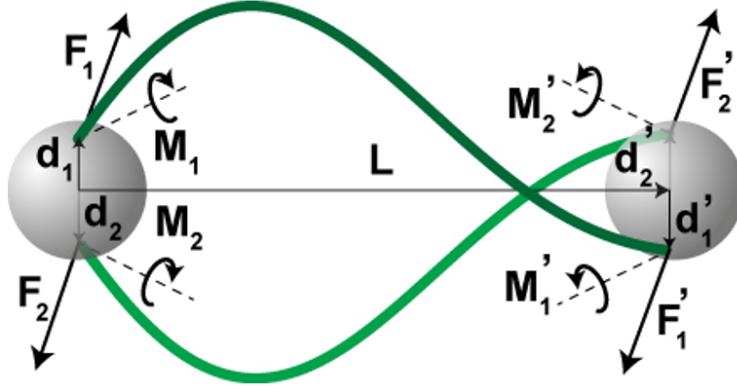


Figure 82: Scheme of the model. Microtubule bundles (green) extend between spindle poles (spheres) at the distance  $L$ . Straight arrows denote forces  $\mathbf{F}_{1,2}$ ,  $\mathbf{F}'_{1,2}$  and positions at the spheres  $\mathbf{d}_{1,2}$ ,  $\mathbf{d}'_{1,2}$ ; curved arrows denote torques  $\mathbf{M}_{1,2}, \mathbf{M}'_{1,2}$ .

generalization of previous models for the curvature of spindle microtubules [33, 153].

$$\kappa \mathbf{t} \times d\mathbf{t}/ds + \tau d\phi/ds \mathbf{t} = \mathbf{r} \times \mathbf{F}_i - \mathbf{M}_i. \quad (4.1.5)$$

The equation Eq. (4.1.5) predicts a unique shape of microtubule bundles for a given boundary conditions. We use this equation to calculate the shapes of microtubule bundles for a set of forces and torques that obey the above equations for the balance of forces and torques.

## 4.2 The mean-field approach

The central idea of our mean-field approach is to generalize the description of the spatial distribution of microtubule bundles by introducing a continuous density of these bundles Fig. 83. The starting point of the model is described below.

Because in our model each microtubule bundle has a unique shape for a given boundary condition, it is convenient to define the surface density of microtubule bundles,  $\rho(\mathbf{d}, \mathbf{d}')$ , as a function of two end points of microtubule bundles,  $\mathbf{d}$  and  $\mathbf{d}'$ , located at the surface of the left and right centrosomes, respectively. The boundary surface of centrosomes are parametrised

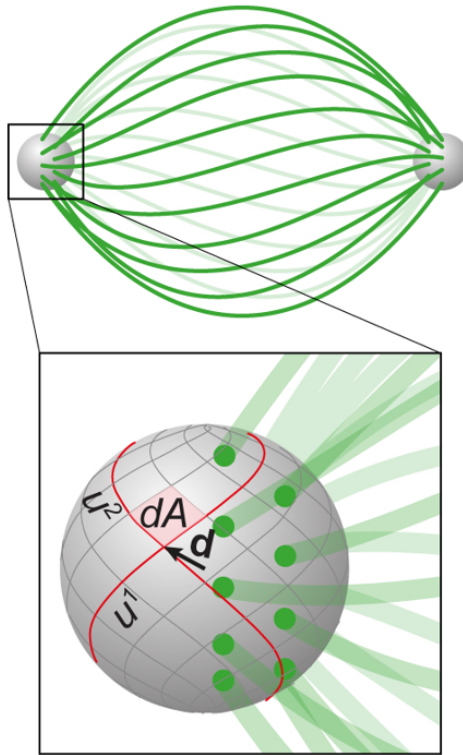


Figure 83: The mean-field model of the spindle. Microtubules (green lines) extend between two centrosomes (grey spheres). The vector  $\mathbf{d}$  points to the surface of the sphere and it is parametrised by parameters  $u^1, u^2$  represented by curved lines (red). The surface element is denoted  $dA$ .

as  $\mathbf{d}(u^1, u^2)$  and  $\mathbf{d}'(u'^1, u'^2)$ , where  $u^1, u^2, (u')^1, (u')^2$  parametrise the left centrosome surface  $dA$  and the right centrosome surface  $dA'$ , respectively. The number of microtubule bundles extending from the surface element at the left centrosome,  $dA$ , and ending at the surface element at the right centrosome,  $dA'$  is calculated as  $dn = \rho dA dA'$ . The total number of microtubule bundles in the spindle is calculated by the surface integral

$$n = \iint_{A, A'} \rho dA dA', \quad (4.2.1)$$

where  $A$  and  $A'$  denote surface of the left and right centrosomes, respectively. Interaction of the left centrosome and a microtubule bundle which connects points  $\mathbf{d}$  and  $\mathbf{d}'$ , is described by the force,  $d\mathbf{F} = \mathbf{f}(\mathbf{d}, \mathbf{d}')dn$ , and the torque,  $d\mathbf{M} = \mathbf{m}(\mathbf{d}, \mathbf{d}')dn$ . Here,  $\mathbf{f}(\mathbf{d}, \mathbf{d}')$  and  $\mathbf{m}(\mathbf{d}, \mathbf{d}')$  denote functions which describe the force and the torque field densities at the left centrosome, respectively. In the mean field approach, we generalise the discrete expressions for the balance of forces Eq. (4.1.3) and torques Eq. (4.1.4). Here, the balance of forces and the balance torques are given by

$$\iint_{A, A'} \mathbf{f} \rho dA dA' = 0, \quad (4.2.2)$$

and

$$\iint_{A, A'} (\mathbf{m} + \mathbf{d} \times \mathbf{f}) \rho dA dA' = 0, \quad (4.2.3)$$

respectively. Balances of forces and torques at the right pole can be calculated by replacing functions  $\mathbf{f}(\mathbf{d}, \mathbf{d}')$ , and  $\mathbf{m}(\mathbf{d}, \mathbf{d}')$ , with functions  $\mathbf{f}'(\mathbf{d}, \mathbf{d}')$  and  $\mathbf{m}'(\mathbf{d}, \mathbf{d}')$ , respectively. In the case of the static spindle, bundles which connect points  $\mathbf{d}$  and  $\mathbf{d}'$  are also in balance

$$\mathbf{f} + \mathbf{f}' = 0. \quad (4.2.4)$$

$$\mathbf{m} + \mathbf{m}' + \mathbf{d} \times \mathbf{f} + (\mathbf{L} + \mathbf{d}') \times \mathbf{f}' = 0. \quad (4.2.5)$$

To solve these equation one needs information about unknown functions  $\rho(\mathbf{d}, \mathbf{d}')$ ,  $\mathbf{f}(\mathbf{d}, \mathbf{d}')$ ,

$\mathbf{m}(\mathbf{d}, \mathbf{d}')$ ,  $\mathbf{f}'(\mathbf{d}, \mathbf{d}')$  and  $\mathbf{m}'(\mathbf{d}, \mathbf{d}')$ . Quantification of these functions is the main aim of this model, which we do by exploring parameter space and comparing the predicted shapes with those observed in our experiments.

### 4.3 Solving the mean-field model

To investigate the shape of the entire spindle, we solve the model as follows. First, we reduce the complexity of the model, by simplifying the geometry of the spindle, so we can determine unknown forces and torques at spindle poles. We identify a minimal number of independent parameters, solve the equations for balance of forces and torques, and obtain predictions for the shapes of all microtubule bundles in the mitotic spindle. To cope with the complex geometry of the model, we impose two symmetries: (i) rotational symmetry of the spindle with respect to the major axis, and (ii) symmetry with respect to exchange of the left and right pole. We also impose that neighbouring bundles remain in the close proximity along their entire length. These symmetries capture, to a large extent, the shapes of typical spindles in HeLa and U2OS cells [2, 3, 43, 197]. We note that these symmetries are imposed, because the model describes already formed metaphase spindles, and therefore the symmetries cannot be an outcome of the model. Our main aim is identification of the unknown functions  $\mathbf{f}$ ,  $\mathbf{m}$ ,  $\mathbf{f}'$  and  $\mathbf{m}'$ . These functions describe the result of interactions between microtubules and molecular motors, and we expect that they will gradually change among neighbouring bundles. Therefore, an appropriate approach in this case is expanding these unknown functions in Taylor series. Finally, comparing our theoretical shape predictions with those from experiments will allow us to identify dominating terms in the series, and subsequently provide insight into how forces and torques are distributed in the mitotic spindle.

We consider the microtubule bundle ends to be continuously distributed across a spherical cap on the centrosome. We can do this because of the large number of microtubules in a spindle [274]. Introducing this microtubule bundle density will make solving the model possible, by allowing us to easily employ additional symmetries and utilise calculus. We can

thus write

$$dN = \rho(A)dA, \quad (4.3.1)$$

where  $dN$  is the number of microtubule bundle ends contained in an infinitesimal area  $dA$ , with  $\rho(A)$  being their density in that area (see Fig. 83). Using the standard spherical coordinate system we can parametrise the above as

$$dN = \rho(\theta, \phi)d^2 \sin \theta d\theta d\phi. \quad (4.3.2)$$

We consider that the bundle end are homogeneously distributed along the spherical cap:

$$\rho(\theta, \phi) = \frac{N_0}{2\pi d^2 \sin \theta}, \quad (4.3.3)$$

which is appropriate as an approximation, and can be seen in, e.g., Fig. 13. The total number of bundles can thus be obtained by integrating over the microtubule bundle end density:

$$N_{tot} = \int_0^{2\pi} \int_{\theta_a}^{\theta_b} \frac{N_0}{2\pi d^2 \sin \theta} d^2 \sin \theta d\theta d\phi = N_0. \quad (4.3.4)$$

Note that a more rigorous derivation of Eq. (4.3.3) can be found in Appendix A.3.1.

The force and torque fields acting on the left end of the microtubule bundle located at  $(r, \theta, \phi)$  are, generally,  $\mathbf{f}(r, \theta, \phi, \rho, \rho')$  and  $\mathbf{m}(r, \theta, \phi, \rho, \rho')$ , with the same relationships holding for the right (') end. Using the density from Eq. (4.3.3) the relations simplify:

$$\rho(\theta, \phi)\mathbf{f}(r, \theta, \phi, \rho, \rho') \propto \mathbf{F}(\theta, \phi), \quad (4.3.5)$$

$$\rho(\theta, \phi)\mathbf{m}(r, \theta, \phi, \rho, \rho') \propto \mathbf{M}(\theta, \phi), \quad (4.3.6)$$

with corresponding equations for the right (') end. The precise nature of these functions, and the dependence of  $\mathbf{f}$  i  $\mathbf{m}$  o  $\rho$  is what we intend to learn about by solving the model and



subsequently comparing the model outputs to real, biological spindles.  $\mathbf{F}(\theta, \phi)$  and  $\mathbf{M}(\theta, \phi)$  represent the force and torque felt by a microtubule bundle end on the left centrosome. Without loss of generality, we set the proportionality constant to be equal to 1 and use the equality sign further on. Furthermore, we must adjust Eq. (4.1.5) for a continuous model, making it read

$$\kappa \mathbf{t} \times d\mathbf{t}/ds + \tau d\phi/ds \mathbf{t} = \mathbf{r} \times \mathbf{F}(\theta, \phi) - \mathbf{M}(\theta, \phi). \quad (4.3.7)$$

$\mathbf{F}(\theta, \phi)$  and  $\mathbf{M}(\theta, \phi)$  represent the total force and torque felt by the microtubules at  $(\theta, \phi)$  on the left centrosome. These equations describe the balance of forces and torques for the entire spindle, which together with the equation Eq. (4.3.7), define the shape of the entire spindle.

#### 4.4 The balance of forces and torques

We proceed by inserting the relationships Eqs. (4.3.5) and (4.3.6) into the balance equations Eqs. (4.1.5) and (4.2.2) to (4.2.5):

$$\int_0^{2\pi} \int_0^{\theta_0} \mathbf{F}(\theta, \phi) \sin \theta d\theta d\phi = \int_0^{2\pi} \int_0^{\theta_0} \mathbf{F}(\theta, \phi) d\Omega = 0. \quad (4.4.1)$$

The corresponding centrosome torque balance is

$$\int_0^{2\pi} \int_0^{\theta_0} (\mathbf{M}(\theta, \phi) + \mathbf{d}(\theta, \phi) \times \mathbf{F}(\theta, \phi)) d\Omega = 0. \quad (4.4.2)$$

The balance for each individual microtubule bundle end must also be satisfied:

$$\mathbf{F}(\theta, \phi) + \mathbf{F}'(\theta', \phi') = 0, \quad (4.4.3)$$

$$\mathbf{M}(\theta, \phi) + \mathbf{M}'(\theta', \phi') + \mathbf{d} \times \mathbf{F}(\theta, \phi) + (\mathbf{d}' + \mathbf{L}) \times \mathbf{F}'(\theta', \phi') = 0, \quad (4.4.4)$$

The resulting shape of microtubule bundles is given by the Eq. (4.1.5) equation:

$$\kappa \mathbf{t} \times d\mathbf{t}/ds + \tau d\Phi/ds \mathbf{t} = \mathbf{r} \times \mathbf{F}(\phi, \theta) - \mathbf{M}(\phi, \theta). \quad (4.4.5)$$

## 4.5 Imposing symmetries

To reduce the degrees of freedom of the model, we will define the symmetries of our resulting mitotic spindle. We proceed by decomposing the forces and torques in the model:

$$\mathbf{F}(\theta, \phi) = \mathbf{F}^\perp(\theta, \phi) + \mathbf{F}^\parallel(\theta, \phi), \quad (4.5.1)$$

$$\mathbf{M}(\theta, \phi) = \mathbf{M}^\perp(\theta, \phi) + \mathbf{M}^\parallel(\theta, \phi). \quad (4.5.2)$$

Here, the ( $\perp$ )  $xy$ -plane is perpendicular to the spindle pole-to-pole axis, while the parallel ( $\parallel$ ) component is along the pole-to-pole axis.

We demand that the forces and torques are symmetric with respect to rotation around the pole-to-pole axis, i.e., they have azimuthal symmetry, like a cylinder. Additionally, we require that the spindle is invariant under exchange of the centrosomes, see Fig. 84. Note that this is not the same as a mirror symmetry along the mid-plane, as exchange of the centrosomes preserves the chirality of the spindle.

We can formulate both of these requirements in terms of the forces and torques acting upon a single bundle end:

$$\mathbf{F}^\perp(\theta, \phi) = -\mathbf{F}^\perp(\theta, \phi + \pi), \quad (4.5.3)$$

$$\mathbf{F}^\parallel(\theta, \phi) = \mathbf{F}^\parallel(\theta, \phi + \pi), \quad (4.5.4)$$

$$|\mathbf{F}(\theta, \phi)| = |\mathbf{F}(\theta)|. \quad (4.5.5)$$

We impose the same symmetry upon the moments:

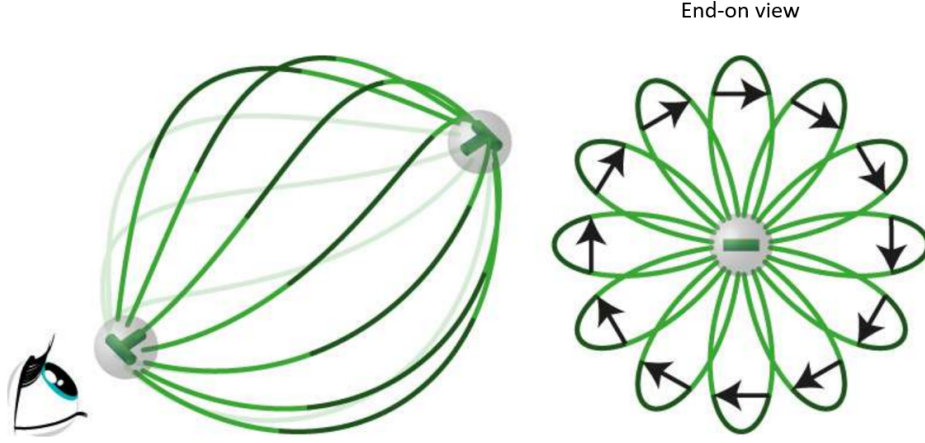


Figure 84: Angled and end-on view of the mean-field mitotic spindle. The system has rotational symmetry around the main axis, and it is invariant under exchange of the centrosomes.

$$\mathbf{M}^\perp(\theta, \phi) = -\mathbf{M}^\perp(\theta, \phi + \pi), \quad (4.5.6)$$

$$\mathbf{M}^\parallel(\theta, \phi) = \mathbf{M}^\parallel(\theta, \phi + \pi), \quad (4.5.7)$$

$$|\mathbf{M}(\theta, \phi)| = |\mathbf{M}(\theta)|. \quad (4.5.8)$$

Note that these symmetries only hold because all microtubule bundles are unnamed, i.e., under rotation around the spindle axis, or upon exchange of the centrosomes, the resulting spindle will be the same, even though the constituent microtubule bundles have been shifted.

## 4.6 The force and torque fields

We will utilise force and torque fields which are as generic as possible, while satisfying all the above requirements:

$$\mathbf{F}(\theta, \phi) = f^\parallel(\theta)\hat{z} + f^\perp(\theta)(\cos(\phi + \delta(\theta))\hat{x} + \sin(\phi + \delta(\theta))\hat{y}), \quad (4.6.1)$$

$$\mathbf{M}(\theta, \phi) = m^{\parallel}(\theta)\hat{z} + m^{\perp}(\theta)(\cos(\phi + \nu(\theta))\hat{x} + \sin(\phi + \nu(\theta))\hat{y}), \quad (4.6.2)$$

where  $f^{\parallel}(\theta)$ ,  $f^{\perp}(\theta)$ ,  $m^{\parallel}(\theta)$  i  $m^{\perp}(\theta)$  are scalar functions of  $\theta$ . Note that these are not the force  $\mathbf{f}$  and torque  $\mathbf{m}$  fields from Eqs. (4.2.2) to (4.2.5). For torques as defined by Eq. (4.6.2), we will impose additional requirements, as defined in Appendix A.3.2. This is necessary because torques act with lever  $\mathbf{d}$  upon a microtubule bundle end, giving them additional degrees of freedom compared to linear forces.

Their direction in the plane perpendicular to the pole-to-pole axis is given by trigonometric functions and the angle  $\delta(\theta)$  for forces and  $\nu(\theta)$  torques. As the microtubule bundle ends are on the surface of a sphere, the angles  $\delta$  and  $\nu$  can be simple understood as the deviation from purely radial forces and torques, for if the angles of deviation were zero, the forces and torques would form an aster-like shape (see Fig. 85).

We note that  $\delta(\theta)$  and  $\nu(\theta)$  have an, as of yet undetermined, dependence on  $\theta$ , which will omit in further considerations to improve readability.

The twist of the microtubule bundle ends is defined by  $\alpha(\theta) = \phi(\theta) - \phi'(\theta)$ .

The total distance between the end of a microtubule bundle changes depending on the angle  $\theta$

$$L = L(\theta) = L_0 - 2d \cos(\theta) \quad (4.6.3)$$

By inserting Eq. (4.6.1) i Eq. (4.6.2) into the force balance equations (for a detailed derivation see Appendix A.3.3) the following set of equations:

$$\int_0^{\theta_0} m^{\parallel}(\theta) \sin \theta + df^{\perp}(\theta) \sin \delta(\theta) (\sin \theta)^2 d\theta = 0 \quad (4.6.4)$$

$$2m^{\perp}(\theta) \cos\left(\frac{\alpha(\theta)}{2} + \nu\right) = f^{\perp}(\theta)(L_0 - 4d \cos(\theta)) \quad (4.6.5)$$

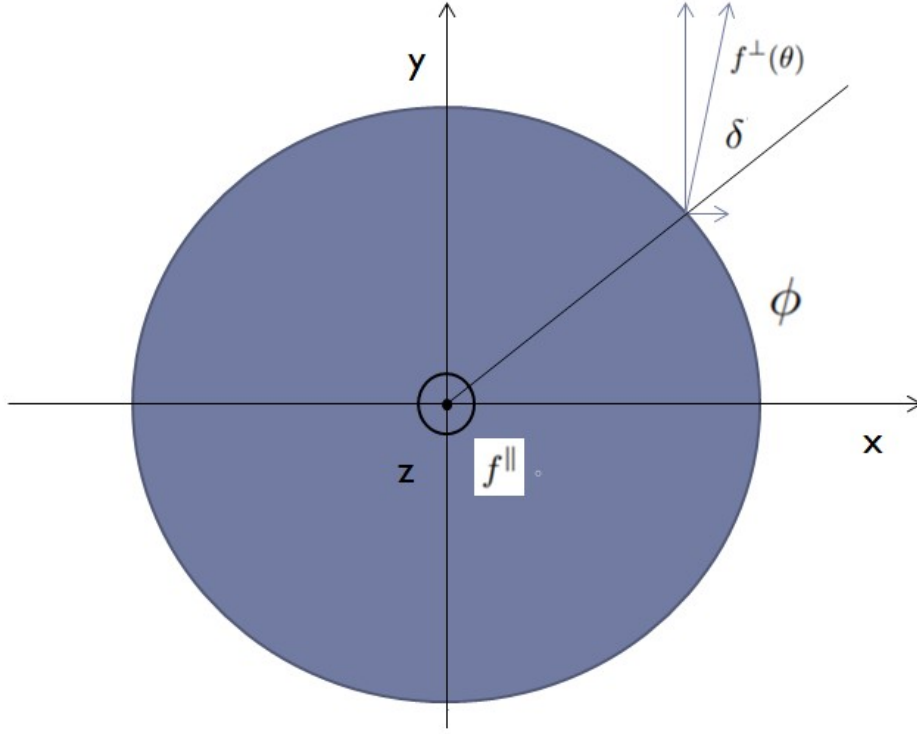


Figure 85: End-on view perspective of the variables used in the mean-field model. The centrosomes are overlapping, and the  $z$ -axis coincides with the pole-to-pole axis of the model spindle. The angle  $\theta$  corresponds to the angle with the  $z$ -axis, as is standard for spherical coordinate systems.

$$\delta(\theta) = \frac{\pi - \alpha(\theta)}{2} \quad (4.6.6)$$

$$\nu(\theta) = \nu = -\nu' = \frac{\pi}{2} \quad (4.6.7)$$

The boundary conditions for the ends of a microtubule bundle are:

$$r(d \cos \theta) = \mathbf{d} = |d|(\sin \theta \cos \phi \hat{x} + \sin \theta \sin \phi \hat{y} + \cos \theta \hat{z}) \quad (4.6.8)$$

$$r(L_0 - 2d \cos \theta) = \mathbf{d}' = |d|(\sin \theta \cos(\phi - \alpha) \hat{x} + \sin \theta \sin(\phi - \alpha) \hat{y} + (\frac{L}{d} - 2 \cos \theta) \hat{z}) \quad (4.6.9)$$

Value	Parameter description
$d = 1\mu\text{m}$	Centrosome radius
$L = 12\mu\text{m}$	Distance between the centrosome centres
$\kappa = 900pN\mu\text{m}^2$	Flexural rigidity

Table 1: Spindle property parameters, whose values are known from the literature [43].

To obtain solutions for these equations, we must describe the dependence of the forces and torques on the angle  $\theta$ . Because we are only looking at the forces and torques phenomenologically, for our purpose it will suffice to expand them in a Taylor series, and then try and determine the unknown coefficients.

#### 4.7 Taylor expansion of forces and torques

We will expand the four scalar functions of theta ( $f^\perp(\theta)$ ,  $f^\parallel(\theta)$ ,  $m^\perp(\theta)$ ,  $m^\parallel(\theta)$ ) from Eqs. (4.6.1) and (4.6.2) in Taylor series. For real spindles, the angle  $\theta$  is small, and thus we are justified in the Taylor expansion. The expanded functions are:

$$f^\perp(\theta) = f_0^\perp + f_1^\perp\theta + f_2^\perp\theta^2 + \dots = \sum_{i=0}^{\infty} f_i^\perp\theta^i \quad (4.7.1)$$

$$f^\parallel(\theta) = f_0^\parallel + f_1^\parallel\theta + f_2^\parallel\theta^2 + \dots = \sum_{i=0}^{\infty} f_i^\parallel\theta^i \quad (4.7.2)$$

$$m^\perp(\theta) = m_0^\perp + m_1^\perp\theta + m_2^\perp\theta^2 + \dots = \sum_{i=0}^{\infty} m_i^\perp\theta^i \quad (4.7.3)$$

$$m^\parallel(\theta) = m_0^\parallel + m_1^\parallel\theta + m_2^\parallel\theta^2 + \dots = \sum_{i=0}^{\infty} m_i^\parallel\theta^i \quad (4.7.4)$$

We will start from the zeroth order term, and add terms until we are satisfied with how the theoretical model predicts the shape of the spindle. The other necessary parameters are shown in Table 1.

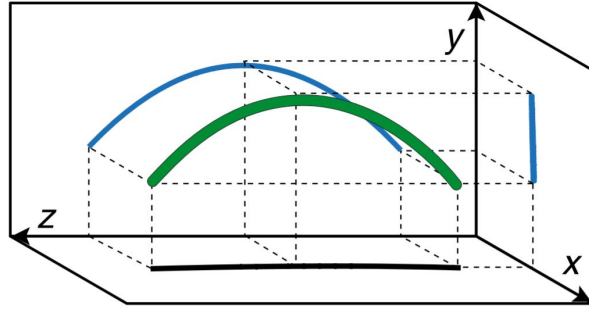


Figure 86: Schematic of the coordinate system in which microtubule bundles are drawn, with one distinguishable microtubule. The ends are attached to the centrosome, which aren't drawn here for the sake of readability.

#### 4.7.1 Zeroth order expansion

The solutions of the zeroth order are degenerate, as can readily be seen from Fig. 87, while a step-by-step solution is available in Appendix A.3.4. The zeroth order has a single solution for the positions of all microtubule bundle ends, on the two closest points of the two centrosomes. Using the solutions of

Using the solutions given in Eqs. (A.3.50) and (A.3.51) obtained from Eq. (4.3.7), it is possible to generate images of the mitotic spindle. On the image Fig. 86 a schematic of the coordinate system in which microtubule bundles are drawn is shown.

A figure of the zeroth order results is given in Fig. 87.

In the zeroth order there is also no twisting of the microtubule bundle end, as a simple consequence of all microtubule bundles being stacked in one point. It is readily apparent that this kind of solution does not provide a sufficiently rich description of the mitotic spindle, so we proceed by adding the linear term.

#### 4.7.2 First order expansion

The first order expansion, unlike the zeroth order expansion, has different solutions for inner vs outer microtubule bundles. All the parameters of the Taylor expanded model, along with

	Parameter description
$f_0^\perp$	Zeroth order Taylor expansion term of the perpendicular forces on the left centrosome
$f_1^\perp$	first-order Taylor expansion term of the perpendicular forces on the left centrosome
$f_0^\parallel$	Zeroth order Taylor expansion term of the parallel forces on the left centrosome
$f_1^\parallel$	first-order Taylor expansion term of the parallel forces on the left centrosome
$m_0^\perp$	Zeroth order Taylor expansion term of the perpendicular torques on the left centrosome
$m_1^\perp$	first-order Taylor expansion term of the perpendicular torques on the left centrosome
$m_0^\parallel$	Zeroth order Taylor expansion term of the parallel torques on the left centrosome
$m_1^\parallel$	first-order Taylor expansion term of the parallel torques on the left centrosome
$\delta_0$	Zeroth order Taylor expansion term of the angular deviation of the force on the left centrosome
$\delta_1$	first-order Taylor expansion term of the angular deviation of the force on the left centrosome
$\nu_0$	Zeroth order Taylor expansion term of the angular deviation of the torque on the left centrosome
$\nu_1$	first-order Taylor expansion term of the angular deviation of the torque on the left centrosome

Table 2: A table of all the Taylor expansion parameters for the left centrosome. For the right centrosome, we have the same parameters, but denoted with ' , leading to a total of 24 parameters.

their descriptions, can be found in Table 2.

In total, we have **24** parameters obtained from the Taylor expansion, two boundary angles  $\theta_a$  and  $\theta_b$ , along with the three structural parameters given in Table 1. Upon solving this as described in Appendix A.3.5, we reduce the amount of free parameters to **4**. These input parameters are  $m_0^\parallel, m_1^\parallel, m_0^\perp, m_1^\perp$ , chosen because they are the most easy to both solve the equations in and to interpret afterwards.

Examples of the model output, along with an experimental spindle, are given in Figs. 88 to 92, with the parameters used being in the figure captions.



Using only linear expansion terms, the model can generate a wide variety of shapes, which cover all shapes that are biologically relevant. By comparing the model outputs to experiments, we will be able to infer the forces and torques acting in the spindle.

### 4.7.3 Higher order terms

It is possible to consider higher order terms. Beginning from Eq. (4.6.5), we can expand the equation in a Taylor series, and group terms of the  $r$ -th order of  $\theta$ :

$$\theta^r : 2 \cos\left(\frac{\alpha(\theta)}{2} + \nu\right) m_r^\perp = L_0 f_r^\perp - 2d \sum_{l=0}^r (f_l^\perp c_{r-l}) \quad (4.7.5)$$

where  $c_n$  denotes only the Taylor terms of  $\cos(\theta)$ .

The integral equation Eq. (4.6.4) is now:

$$\theta^r : \int_{\theta_a}^{\theta_b} \sum_{l=0}^r (m_l^\parallel s_{r-l}) + \sin(\delta(\theta)) d \sum_{l=0}^r \sum_{k=0}^l (f_l^\perp s_{r-l} s_{l-k}), \quad (4.7.6)$$

where similarly  $s_n$  denotes Taylor expansion terms of  $\sin(\theta)$ , and  $\sin(\delta(\theta)) = \sin(\sum_0^r \delta_r \theta^r)$ .

The equation Eq. (4.6.6) is a simple equation between the coefficients of  $\delta_r$  i  $\alpha_r$ .

These relations can be used to consider high order terms. Because the outputs of the first-order model describe biological spindles well, we will not consider such higher order terms, but instead proceed to analysing the predictions of the model and the experimental verification of the model.

### 4.7.4 Predictions of the theoretical model

The predictions of the model consist of the shapes of all microtubule bundles in the mitotic spindle. This information, however, has little value outside of a direct comparison with experiments of biological spindles, as the mean-field model utilises empirical force and torque fields. We can however, examine a particular feature of the microtubule bundle shape, the angle

( $\eta$ ) at which microtubule bundles extend from the centrosomes, in the plane perpendicular to the pole to pole axis.

Our model provides a prediction for this angle, and this can be seen in the biological spindle in Fig. 94. Very little experimental knowledge exists about microtubules near the poles itself [43], because of their density there, and limitations of microscopy.

To understand how the angle  $\eta$  changes with the input parameters of our theoretical model, we calculated  $\eta$  for a variety of input parameters, to see how the angle *eta* changes depending on whether a particular bundle is an inner or outer bundle.

In Figs. 97 to 100, we show how the angle  $\eta$  changes theoretically between inner and outer bundles depending on chosen input parameters.

From this, we see that the angle  $\eta$  varies wildly between inner and outer bundles, but that the precise nature of this dependence depends on the chosen input parameters. This means that, if we are able to infer the forces and torques acting in a biological spindle using our mean-field model, we will obtain predictions for the angle  $\eta$ , which has so far not been experimentally measured to any satisfactory degree.

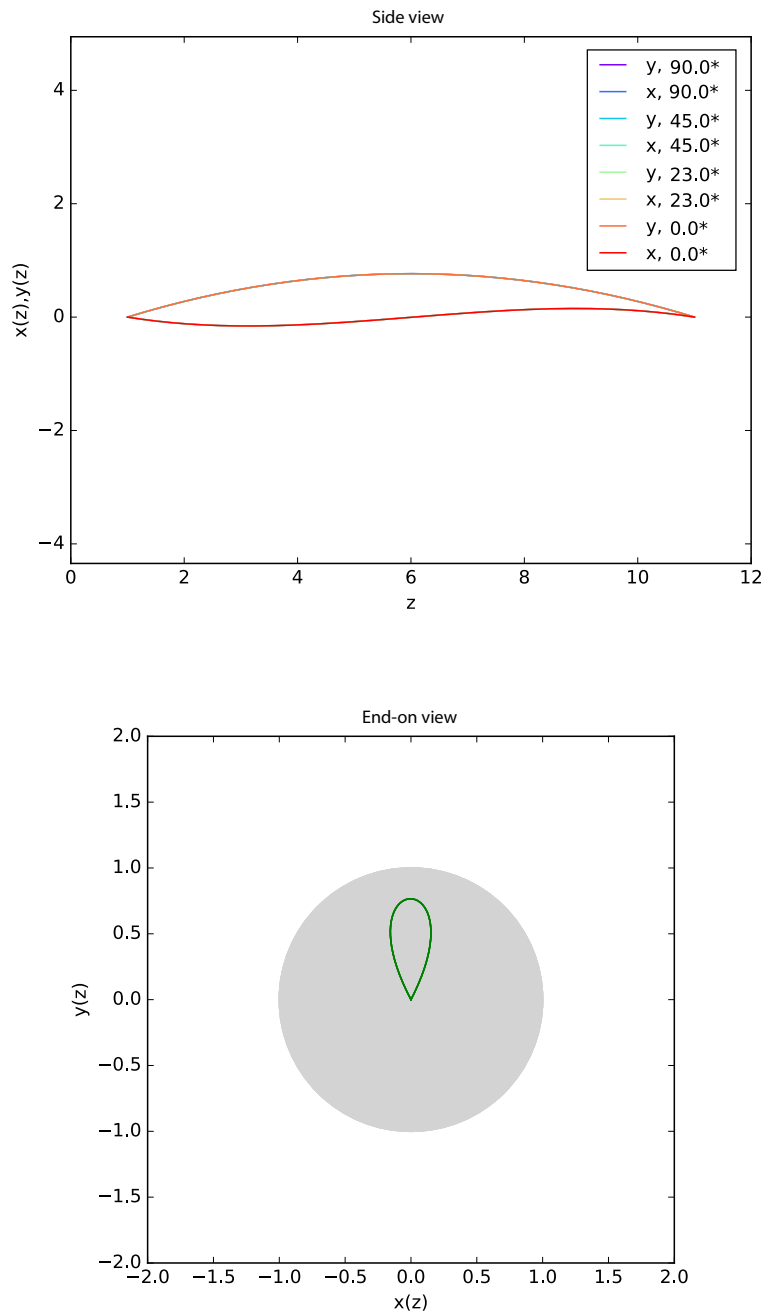


Figure 87: Example of the results of the zeroth order model, from the side-view and end-on view. All microtubules arise from the same point, are essentially stacked on top of each other, which has no relation to how microtubule bundles in a real spindle look like. All units are in  $\mu\text{m}$ .

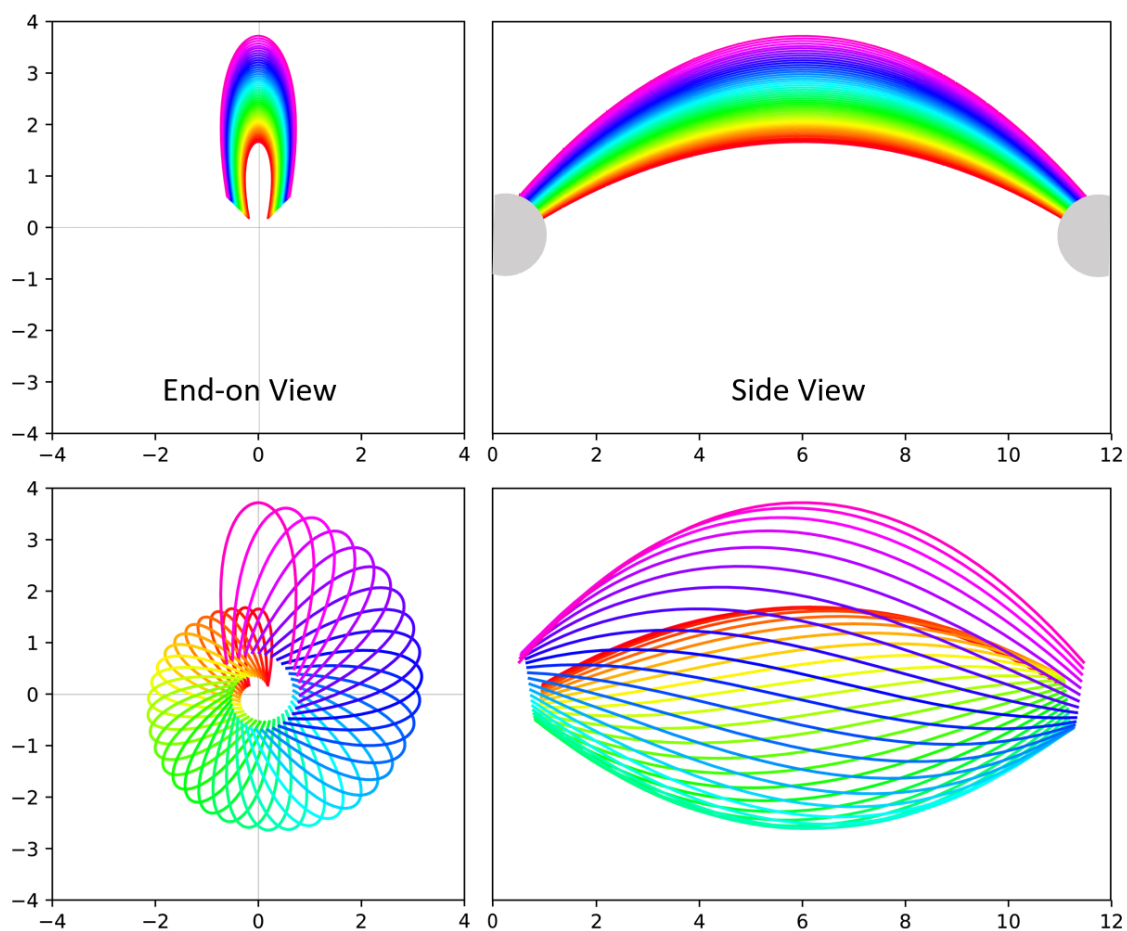


Figure 88: Example of first-order model predictions, end-on and side view. Image shows the rotational symmetry of all model outputs. Different colours correspond to different microtubule bundles, visualised out of the mean-field.  $m_0^\perp = 250.0 \text{ pN}\mu\text{m}$ ,  $m_0^\parallel = -10.0 \text{ pN}\mu\text{m}$ ,  $m_1^\perp = 100 \text{ pN}\mu\text{m}$ ,  $m_1^\parallel = -1 \text{ pN}\mu\text{m}$ ,  $\theta_a = 0.01$ ,  $\theta_b = \pi/3$ . Figure axis units are  $\mu\text{m}$ .

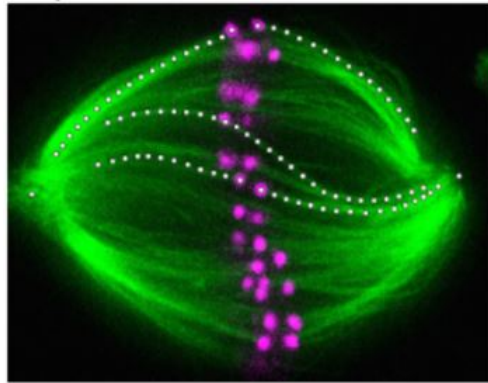
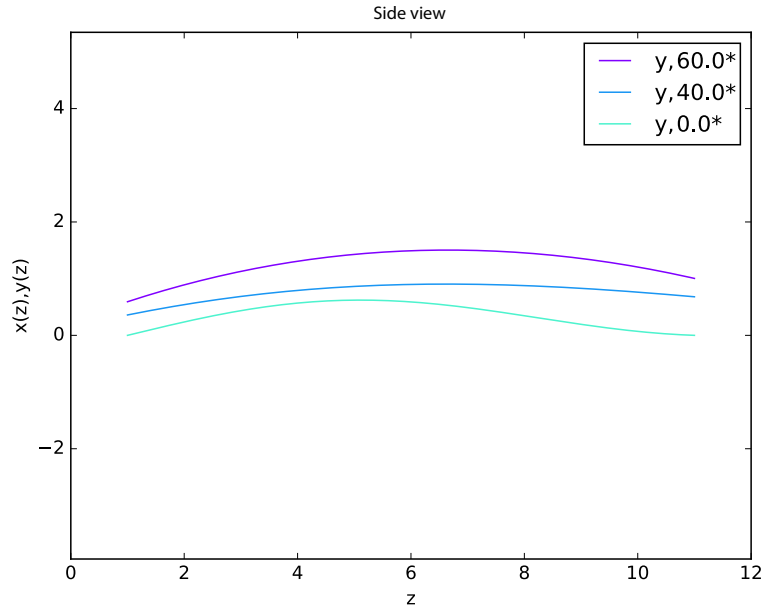


Figure 89: Example of first-order model predictions, side view, along with experimental spindle images ([43]). Obtained for the choice of parameters  $m_0^\perp = -25.0 \text{ pN}\mu\text{m}$ ,  $m_0^\parallel = -10.0 \text{ pN}\mu\text{m}$ ,  $m_1^\perp = 1.0 \text{ pN}\mu\text{m}$ ,  $m_1^\parallel = 350.0 \text{ pN}\mu\text{m}$ ,  $\alpha_0 = \pi/3$ ,  $\theta_a = 0.01$ ,  $\theta_b = \pi/3$ . Figure axis units are  $\mu\text{m}$ .

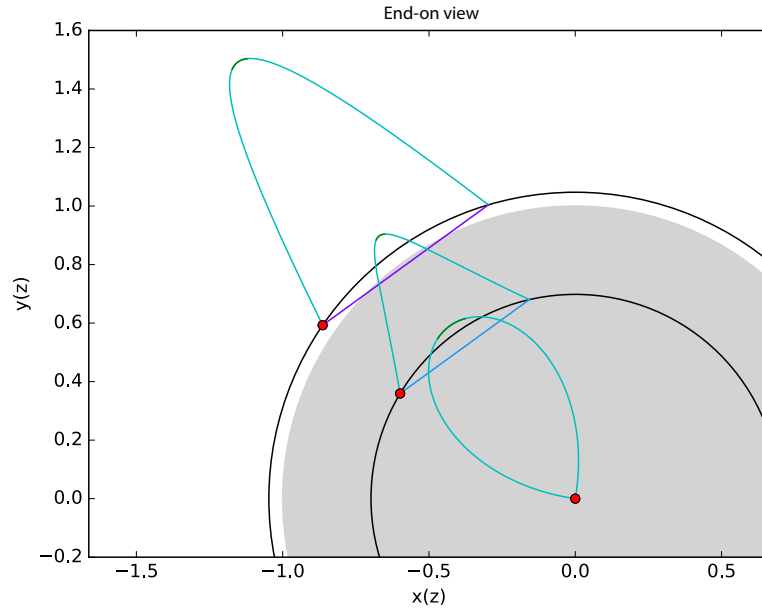


Figure 90: Example of first-order model predictions, end-on view, . The parts of the theoretical bundle highlighted in green correspond to the experimental image. The connection from the red point to the other end of the microtubule bundle corresponds to the twist of the microtubule bundle ends. The black circle corresponds to the particular angle  $\theta$  for which a microtubule has been drawn, from the continuum  $[\theta_a, \theta_b]$ . Images uses the same parameters as in Figs. 89 and 90. Image obtained for parameters  $m_0^\perp = -25.0 \text{ pN}\mu\text{m}$ ,  $m_0^\parallel = -10.0 \text{ pN}\mu\text{m}$ ,  $m_1^\perp = 1.0 \text{ pN}\mu\text{m}$ ,  $m_1^\parallel = 350.0 \text{ pN}\mu\text{m}$ ,  $\alpha_0 = \pi/3$ ,  $\theta_a = 0.01$ ,  $\theta_b = \pi/3$ . Figure axis units are  $\mu\text{m}$ .

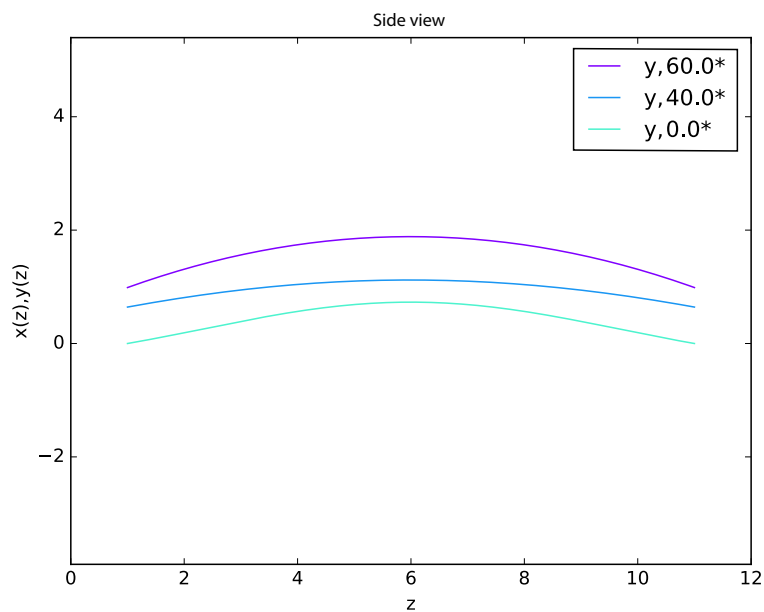


Figure 91: Example of first-order model predictions, for the same parameters as in Figs. 89 and 90 . The model result is three-dimensional, like biological spindles. Image obtained for parameters  $m_0^\perp = -25.0 \text{ pN}\mu\text{m}$ ,  $m_0^\parallel = -10.0 \text{ pN}\mu\text{m}$ ,  $m_1^\perp = 1.0 \text{ pN}\mu\text{m}$ ,  $m_1^\parallel = 350.0 \text{ pN}\mu\text{m}$ ,  $\theta_0 = \pi/3$ . Figure axis units are  $\mu\text{m}$ .

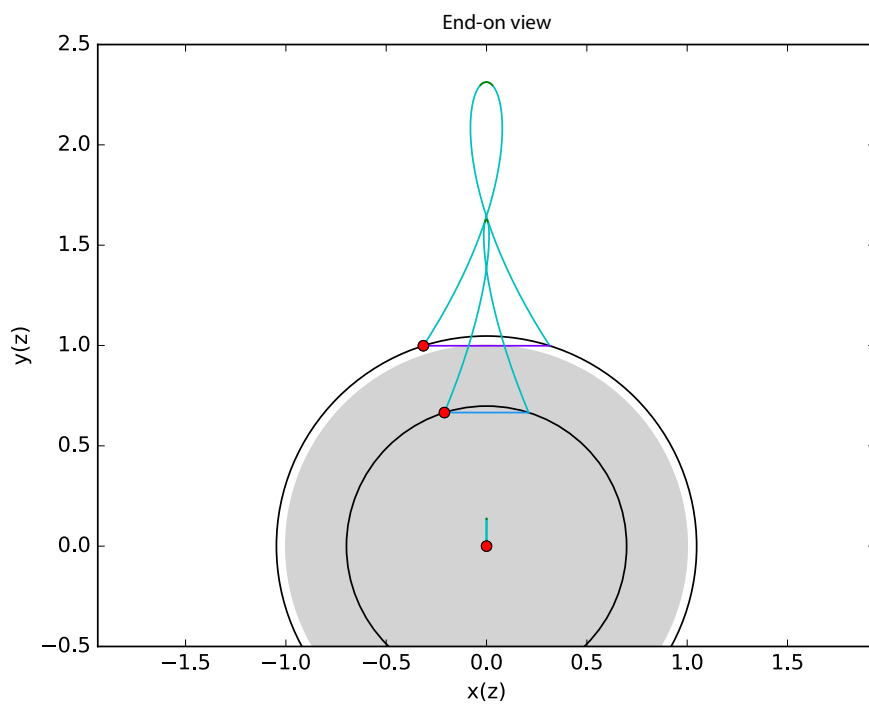


Figure 92: End-on view of the mitotic spindle for parameters.  $m_0^\perp = 1.0 \text{ pN}\mu\text{m}$ ,  $m_1^\perp = 70.0 \text{ pN}\mu\text{m}$ ,  $m_1^\parallel = -250.0 \text{ pN}\mu\text{m}$ ,  $\alpha_0 = \pi/4$ ,  $\alpha_1 = -0.0$ ,  $\theta_0 = \pi/3$ . Figure axis units are  $\mu\text{m}$



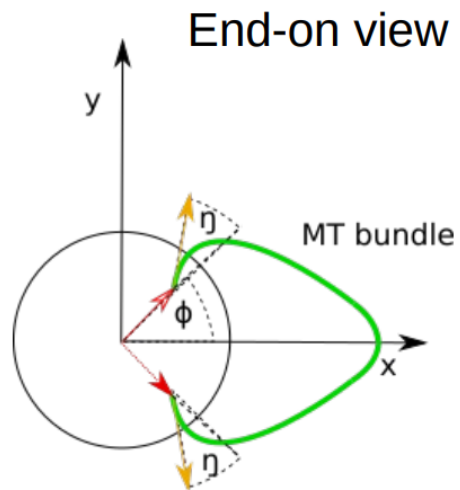


Figure 93: Figure showing the angle  $\eta$  in a schematic of the spindle. The centrosome is centred at the coordinate system origin, and a microtubule bundle is visualised in green. The angle  $\eta$  can be seen from the end-on view, as it is the component of the microtubule bundle that is perpendicular to the pole-to-pole axis.

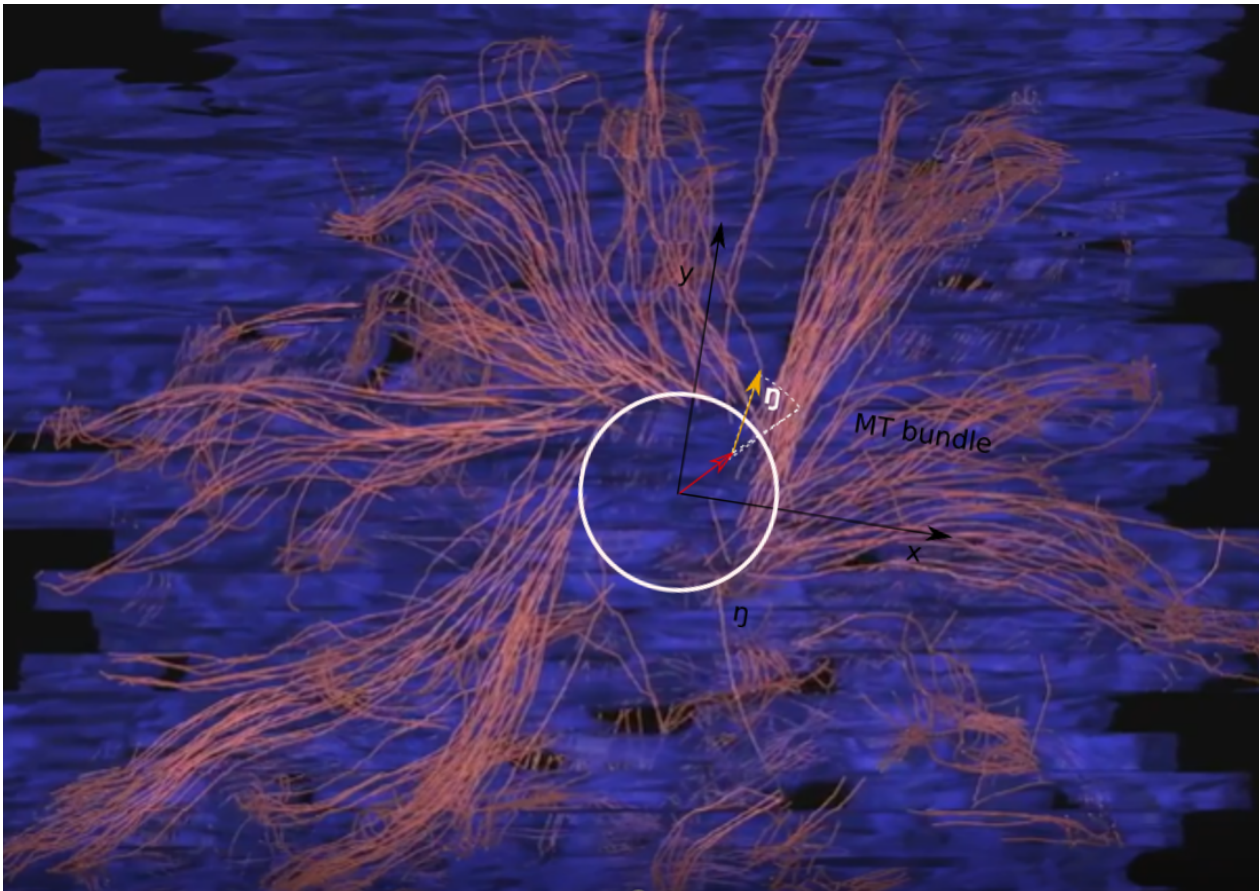


Figure 94: Figure showing the angle  $\eta$  in a biological spindle using electron microscopy. Kinetochore fibres are shown in orange, and the centrosome is invisible, but located at the image centre. Overlaid is the scheme from Fig. 93, showing that  $\eta$ , and we can estimate that the value of  $\eta$  is around 30 degrees. Here, we can clearly see that all microtubule bundles are tilted, in a very uniform manner, to the left. Image adapted from [277]

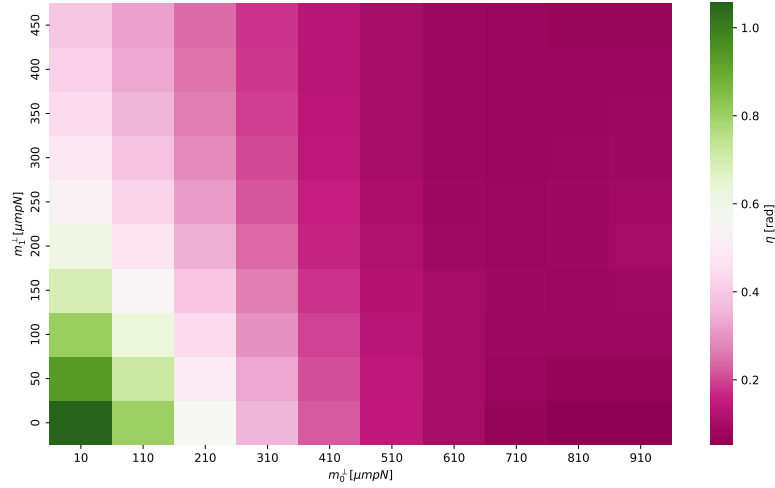


Figure 95: Figure showing the angle  $\eta$  as a function of input parameters  $m_0^\perp$  and  $m_1^\perp$ . The two other input parameters were fixed at  $m_0^\parallel = -10 \text{ pN}\mu\text{m}$  and  $m_1^\parallel = -1 \text{ pN}\mu\text{m}$ . The colour of the heatmap plot shows the value of  $\eta$  at a particular point in the parameters space.

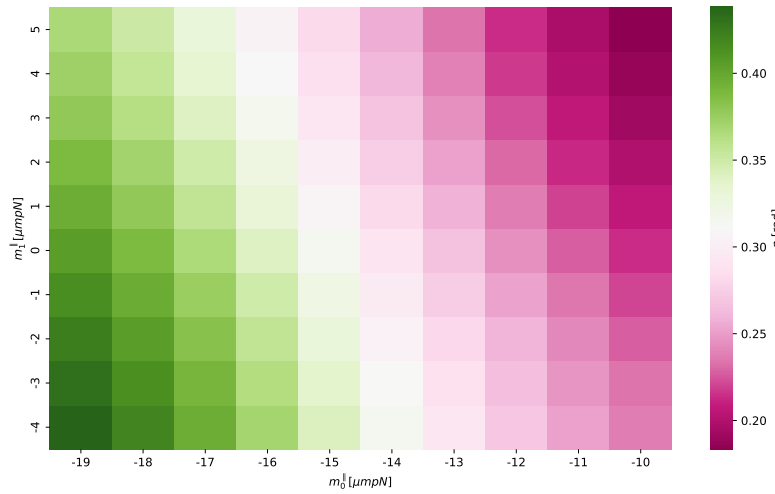


Figure 96: Figure showing the angle  $\eta$  as a function of input parameters  $m_0^\perp$  and  $m_1^\perp$ . The two other input parameters were fixed at  $m_0^\parallel = 210 \text{ pN}\mu\text{m}$  and  $m_1^\parallel = 200 \text{ pN}\mu\text{m}$ . The colour of the heatmap plot shows the value of  $\eta$  at a particular point in the parameters space.

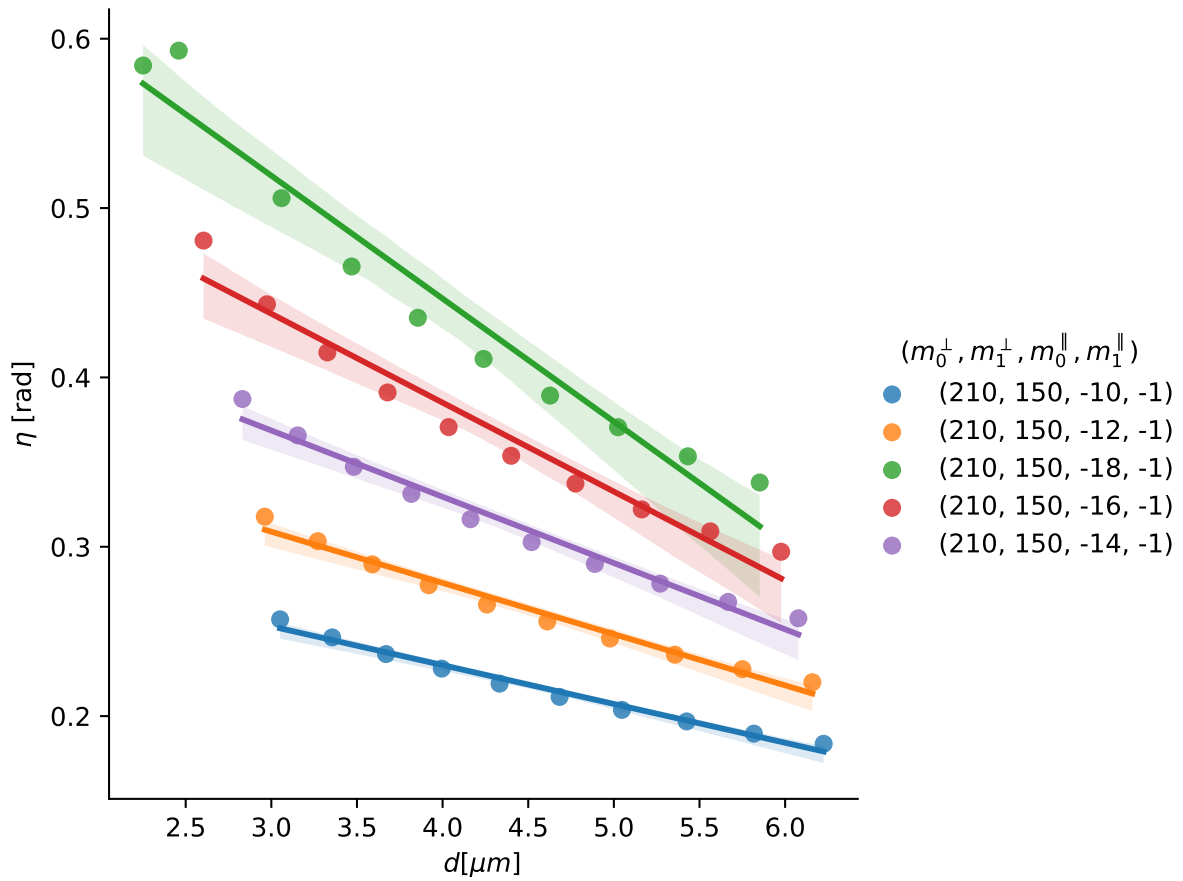


Figure 97: Figure showing the angle  $\eta$  as a function of the distance from the pole-to-pole axis  $d$ . The other input parameters are shown on the legend, and correspond to particular hues.

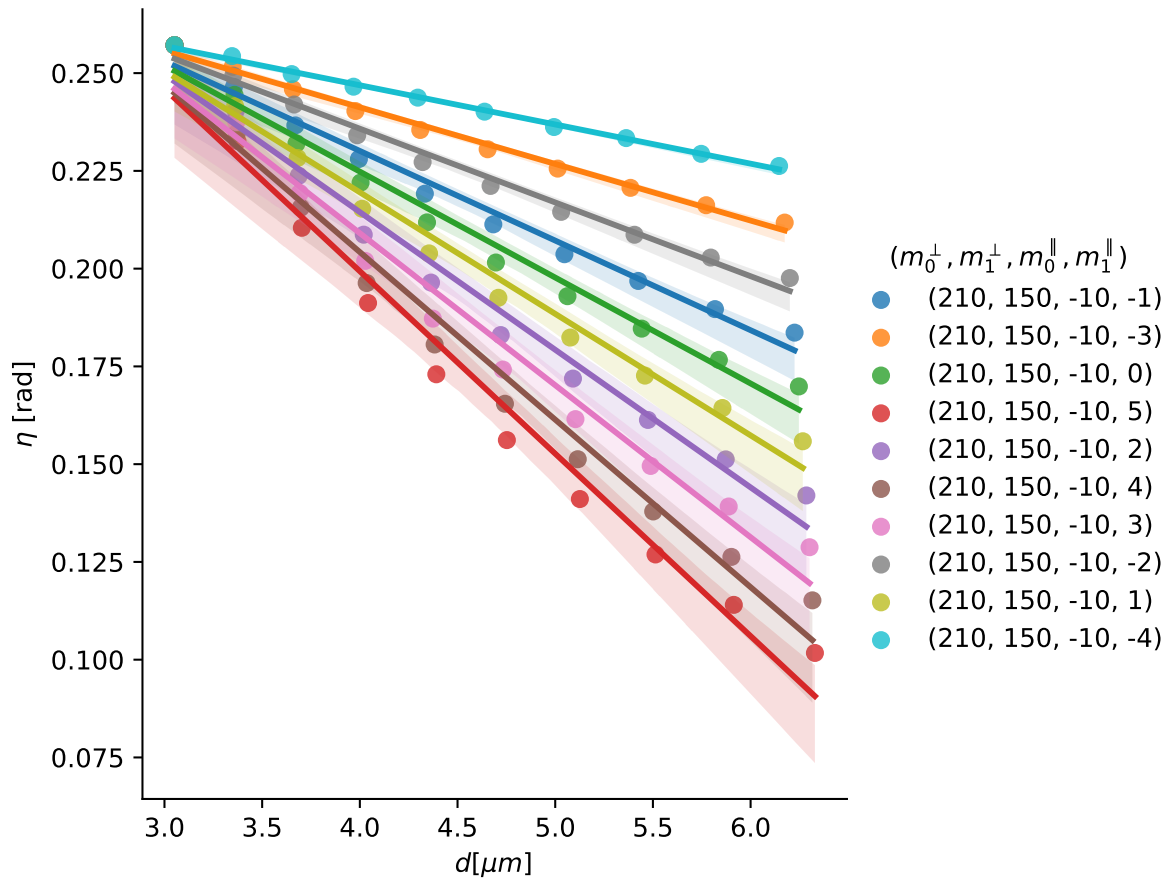


Figure 98: Figure showing the angle  $\eta$  as a function of the distance from the pole-to-pole axis  $d$ . The other input parameters are shown on the legend, and correspond to particular hues.

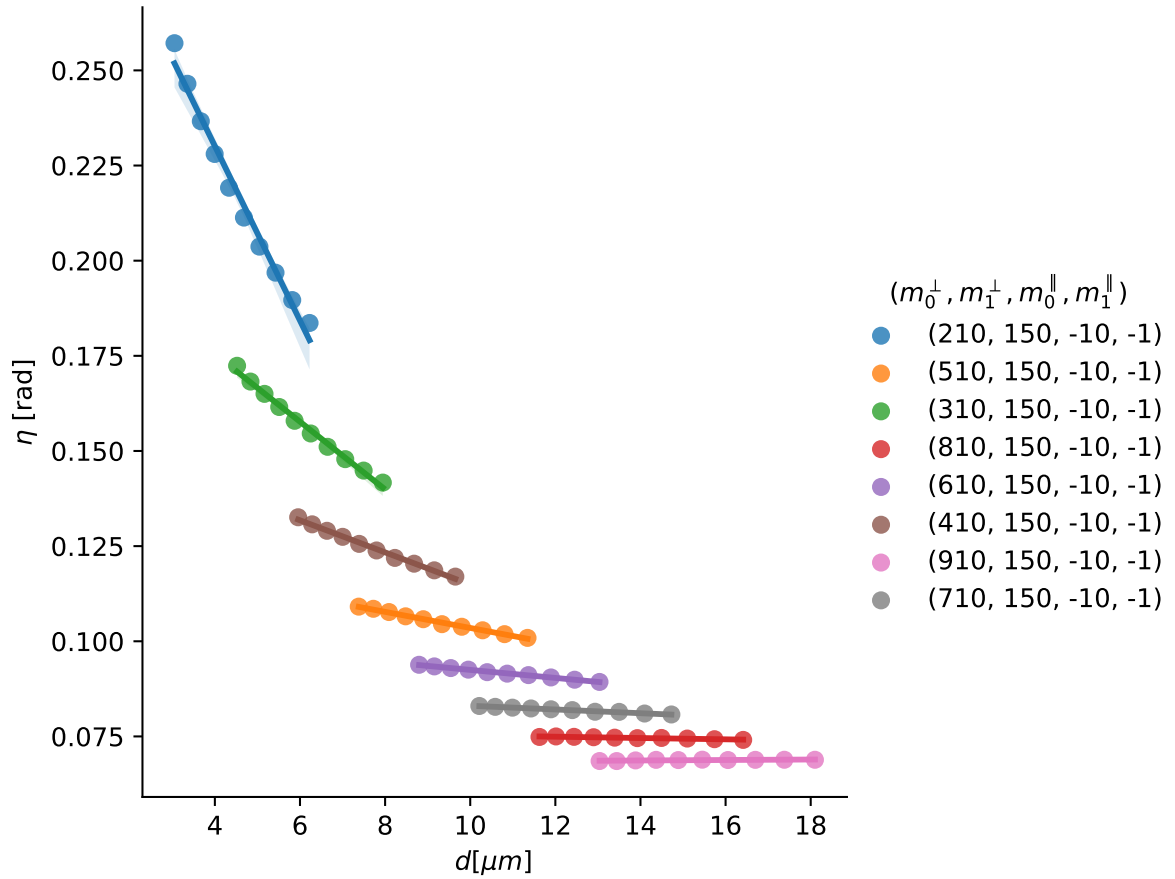


Figure 99: Figure showing the angle  $\eta$  as a function of the distance from the pole-to-pole axis  $d$ . The other input parameters are shown on the legend, and correspond to particular hues.

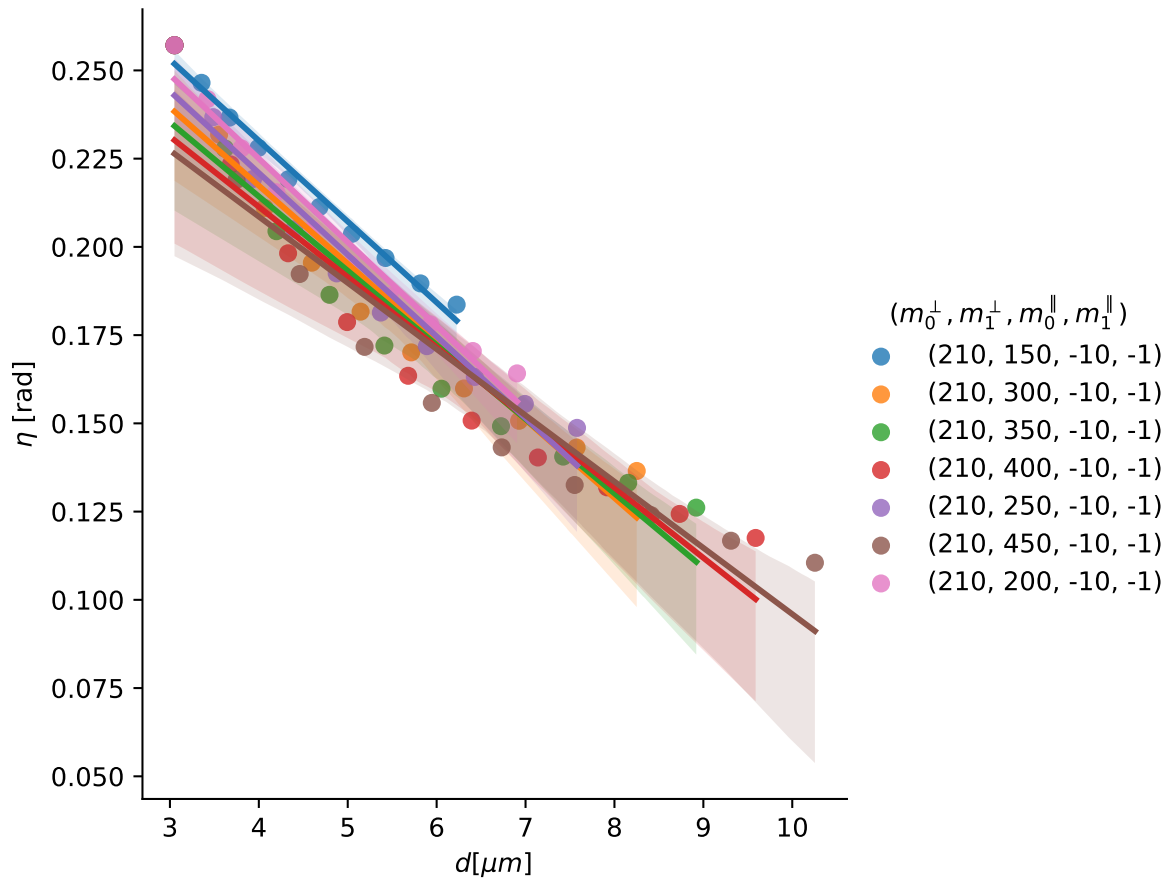


Figure 100: Figure showing the angle  $\eta$  as a function of the distance from the pole-to-pole axis  $d$ . The other input parameters are shown on the legend, and correspond to particular hues.

## 5 Experimental verification of the mean-field model

To find the distribution of forces and torques in the mitotic spindle, it is sufficient to find the optimal input parameters  $m_0^{\parallel}, m_1^{\parallel}, m_0^{\perp}, m_1^{\perp}$  for a biological spindle. To do this, we will perform an exhaustive search through this four-dimensional parameter space, for each individual spindle, and obtain the parameters which describe it optimally.

### 5.1 Comparison criteria and the loss function of choice

To find an optimal parameter choice for a biological spindle, it is necessary to define a loss function. We will utilise the mean squared error [278], summing up the errors in the curvature  $\kappa$  and the twist  $\omega$ , to obtain parameters which best describe the spindle in terms of both variables. The choice of mean square error is appropriate as both errors are of similar scale, and the procedure is outlined in Fig. 101.

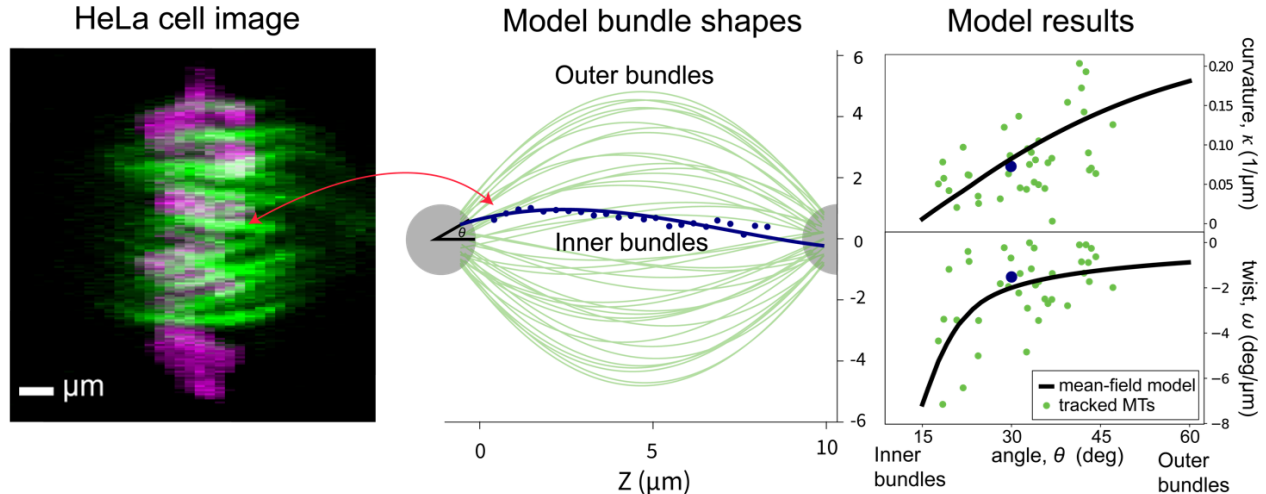


Figure 101: Figure showing the path towards inferring the forces and torques in the spindle using the mean-field model. On the left is an experimental image of a HeLa mitotic spindle obtained through confocal microscopy. In the middle, the data points from a selected microtubule bundle, along with best theoretical prediction, are highlighted in blue, while all other microtubule bundles are shown in green.



## 5.2 Inferring the force and torque distributions in real spindles

To infer the forces and torques in the spindle, we use the procedure from Fig. 101 to obtain optimal values of  $m_0^{\parallel}, m_1^{\parallel}, m_0^{\perp}, m_1^{\perp}$  for a particular spindle. We do this for each spindle from a particular experiment, then we average up the parameters, resulting in a set of parameters describing the experiment itself.

### 5.2.1 Perturbed and unperturbed HeLa cells

We begin by showing optimal model fits to perturbed and unperturbed HeLa cells. We can clearly see there is a difference between STLC treated and wild-type HeLa cells in terms of the measured twist, but also in terms of the acting torques (Fig. 102).

It is interesting to note that even though the optimal twisting moment is nearly constant, there is a change in measured twist. This implies that there might be similar motor concentration between inner and outer bundles, but that the differences in observed twist are due to geometrical reasons, and/or differences in bundle length.

### 5.2.2 Amoeba cells

Next we generate optimal model fits to cells of the Amoeba *N. gruberi* (Fig. 103). We can clearly see there is a difference in the twist sign, because amoeba cells twist in the clock-wise, positive direction.

Otherwise, the results are similar to HeLa cells, even though amoeba cells are very different with regard to their bundle shapes.

### 5.2.3 Compressed HeLa cells

Finally, we look at compressed HeLa cells, squeezed over time using raw mechanical force (Fig. 104)

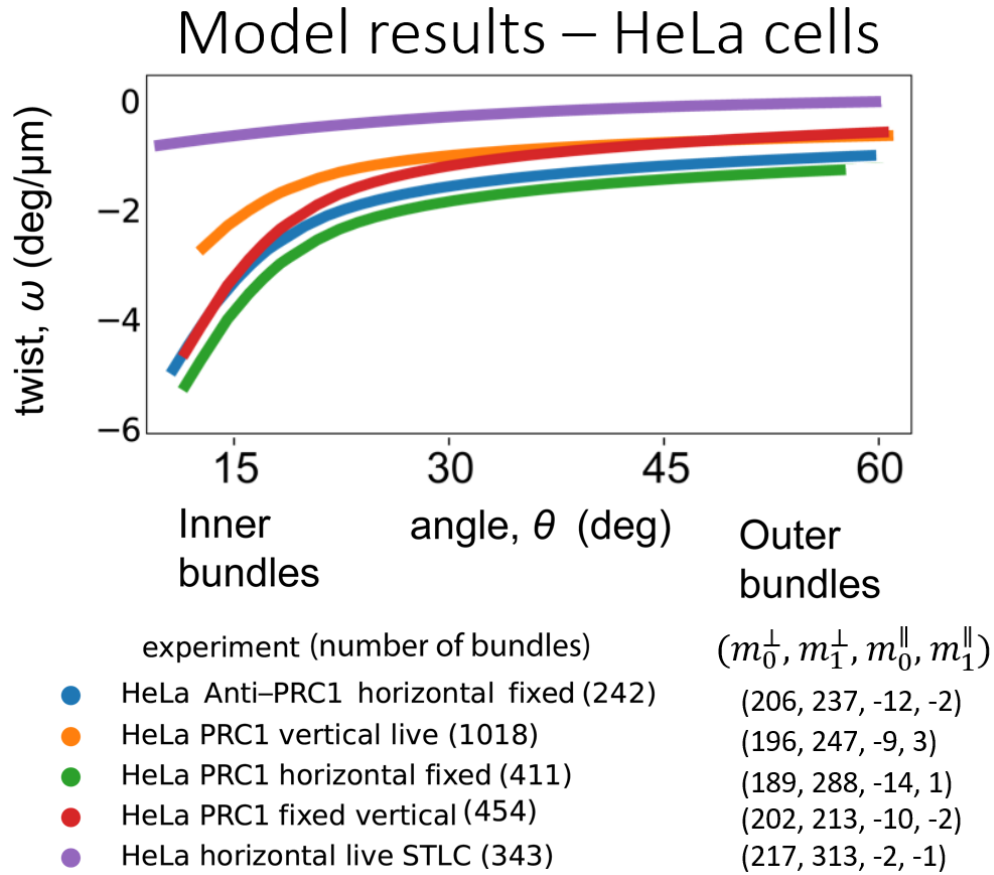


Figure 102: Figure showing the comparison results for a wide variety of HeLa cells, both wild-type and perturbed. The lines show the model fits to a particular experiment, denoted by the hue of the line. The numbers next to the legend show the parameters used.

Here, we can see corresponding increases in bending and twisting moments as compression time increases, which is in-line with experimentally measured observations.

#### 5.2.4 Independent verification of the model

Apart from the optimal distributions of forces and torques in the spindle, we use the model to obtain predictions for the angle  $\eta$ , and how this varies for a particular experiment Fig. 105.

It can be seen that there is a high dependency on the twisting moment, with the prominent example being the HeLa cells which underwent treatment with STLC, corresponding to the

## Model results – Amoeba cells

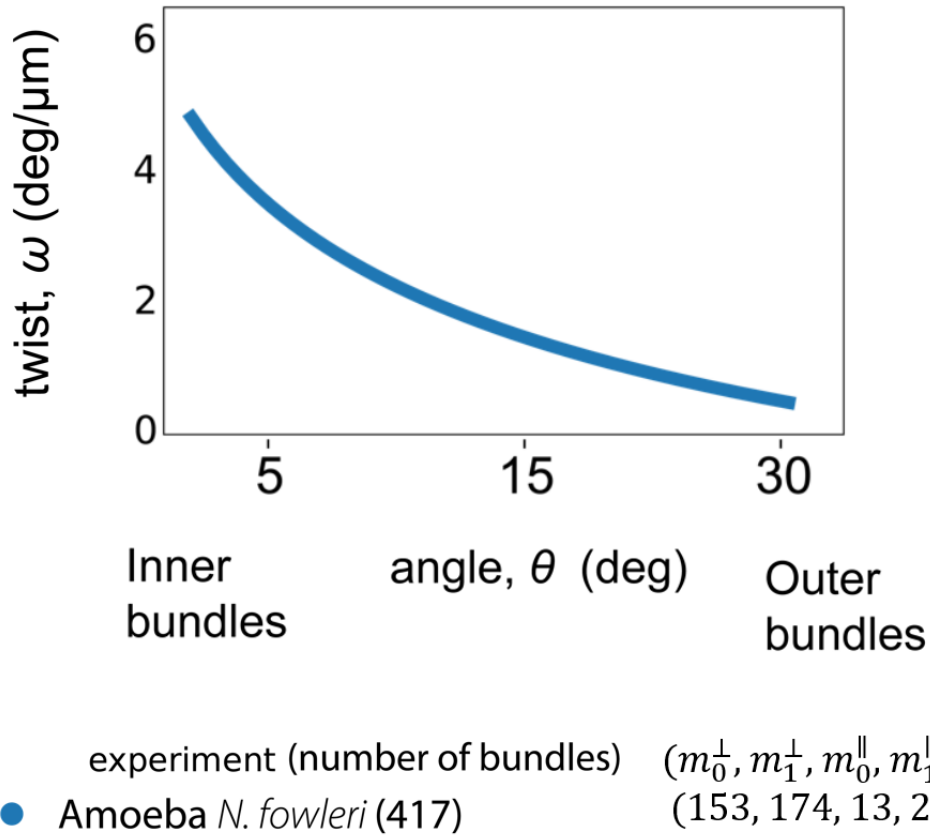


Figure 103: Figure showing the comparison results for a wide variety of Amoeba cells, both wild-type and perturbed. The lines show the model fits to a particular experiment, denoted by the hue of the line. The numbers next to the legend show the parameters used.

orange line in Fig. 105.

## Model results – squeezed HeLa cells

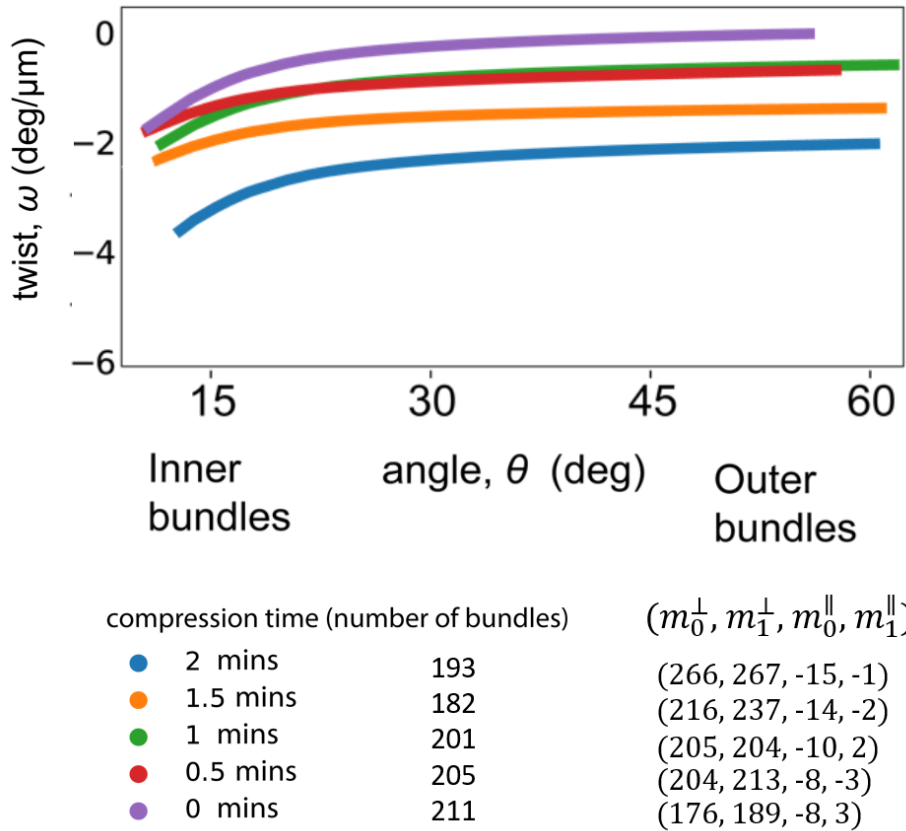


Figure 104: Figure showing the comparison results for a wide variety of squeezed HeLa cells, both wild-type and perturbed. The lines show the model fits to a particular experiment, denoted by the hue of the line. The numbers next to the legend show the parameters used.

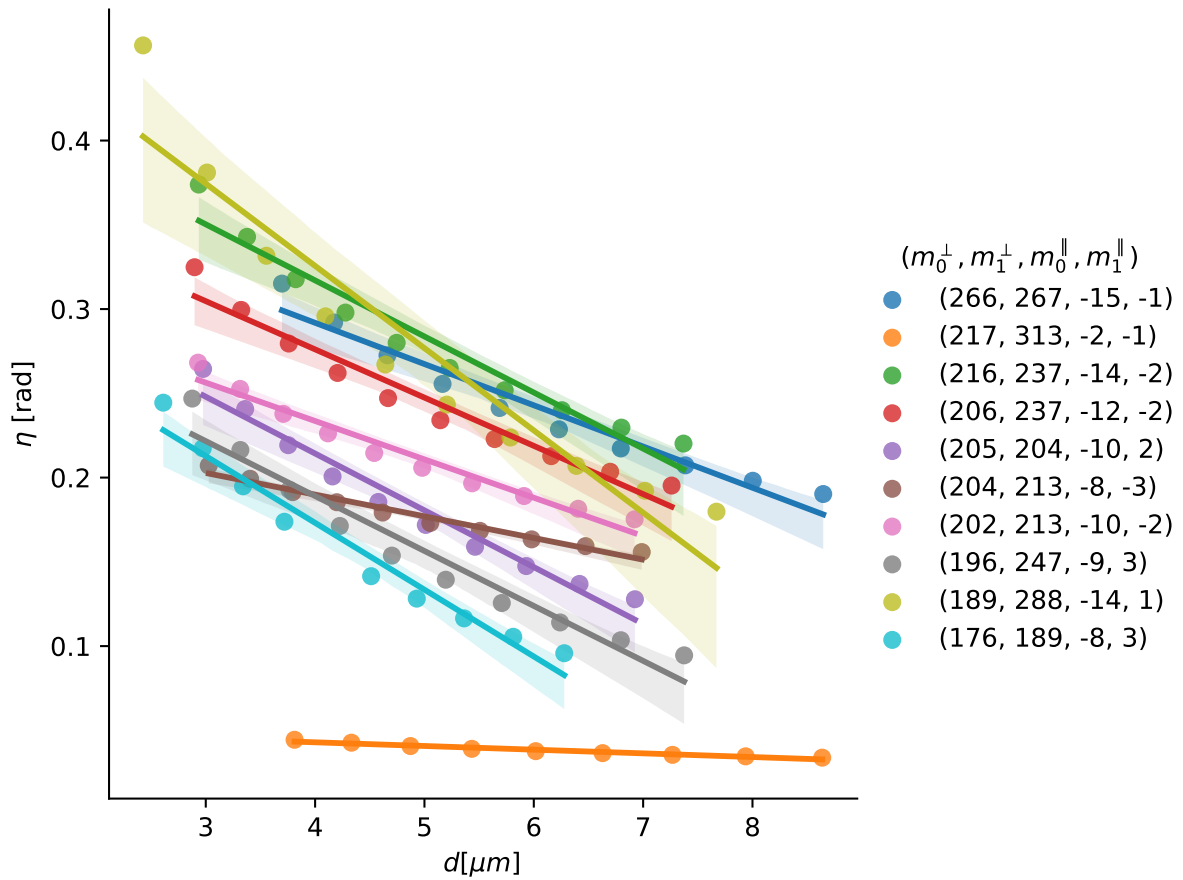


Figure 105: Figure showing the angle  $\eta$  as a function of the distance from the pole-to-pole axis  $d$ . The other input parameters are shown on the legend, for particular hues, and correspond to different experiments from subsection 5.2.

## 6 Summary, conclusions and future expectations

The discovery that microtubule bundles in the mitotic spindle are twisted in a helical manner opened an exciting area of research on the potential biological roles of spindle chirality and the mechanisms generating this curious type of asymmetry, which is why we developed a method to measure the twist and the curvature of microtubule bundles, in order to characterize the shape of the spindle. We used the method for easy extraction of information about the relevant aspects of microtubule bundle geometry. By utilizing the characteristic shape of microtubule bundles in the spindle, we characterized them in a reproducible manner. This approach allowed for the efficient mapping of the similarities and differences between shapes of spindles in various cell types and organisms, which was used to experimentally screen for motor protein candidates which generate forces and torques in the spindle.

Because the spindle shapes reflect the forces within them, and also the forces acting upon constituent microtubule bundles, we further used the Oblique Circle Method to serve as the basis for a theoretical mean-field model of the entire spindle, which is a first in the field. The mean-field model allowed us to obtain theoretical predictions of how the mitotic spindle looks for certain distributions of forces and torques acting upon the bundle ends, then to use these predictions for the shape of the spindle to infer the force and torque distributions in real biological spindles. From these force and torque distributions, we have obtain predictions for the angle  $\eta$  with which microtubule bundles arise out of the centrosomes, which has so far not been studied or documented well.

For future work, we would like to extend the model by including the microscopic origin of forces. Instead of using empirical force and torque field values, and having the input parameters be Taylor series expansion coefficients, we would model the microscopic situation at the overlap region of the spindles and the centrosomes in more detail, allowing us to directly determine motor concentrations from the model, and gain more in-depth insight of how the mitotic spindle functions.

# A Appendix

## A.1 Quantification of spindle chirality

### A.1.1 Cell lines

Experiments were carried out using the following cell lines: He*Lalpha*–Kyoto BAC cell line stably expressing PRC1-GFP courtesy of Ina Poser and Tony Hyman (Max Planck Institute of Molecular Cell Biology and Genetics, Dresden, Germany); unlabeled (non-transfected) He*Lalpha*–TDS cells from the High-Throughput Technology Development Studio (MPI-CBG, Dresden); human hTERT (Wadsworth Center, New York State Department of Health, Albany, NY). Cells were cultured in flasks in Dulbecco’s modified Eagle’s medium (DMEM; Capricorn Scientific GmbH, Germany) supplemented with 10% foetal bovine serum (FBS; Sigma*lpha*–Aldrich, MO, USA), 10000 U/ml penicillin/streptomycin solution (Capricorn Scientific GmbH, Germany), and 50 g/mL geneticin for He*Lalpha*–Kyoto (Life Technologies, Waltham, MA, USA). The cells were kept at 37 degrees Celsius and 5% CO<sub>2</sub> in a Galaxy 170S CO<sub>2</sub> humidified incubator (Eppendorf, Hamburg, Germany) and were regularly passaged at 70-80% confluence.

### A.1.2 Confocal microscopy

The entire spindle must be imaged to assess twist, whether in living or fixed cells. This means that the imaged  $z$ -stack must be large enough to encompass the spindle from the bottom of the dish to the top of the spindle. The analysis is best suited to spindles oriented horizontally (spindle pole-to-pole axis parallel with imaging plane) or vertically (spindle pole-to-pole axis perpendicular to imaging plane). The imaging direction is critical because the direction of twist determines the sign of the chirality. Because the cover slip is usually easy to determine due to surrounding cells in interphase that are attached there, it is convenient to image starting from the cover slip and moving upwards. The imaging direction is critical

for determining the handedness of the twist (right- or left-handed twist). Throughout the cell cycle, an example of a microscopy configuration can be seen in Fig. 106.

### A.1.3 Spindle twist calculation methods

To calculate spindle twist, microscopy images of horizontal spindles were analyzed in Fiji Software (ImageJ, National Institutes of Health, Bethesda, MD, USA) [279, 280]. To avoid unspecific spindle movements in the calculation of spindle twist, only images with both spindle poles in the same plane before and during imaging of the  $z$ -stack were used in analysis. Horizontal spindles were converted to vertical orientation using RStudio code written in the R programming language [43]. Microtubule bundles and poles appear as blobs in the transformed stack. Visual assessment. The spindle is observed end-on in this method, and the rotation of microtubule bundles around the pole-to-pole axis is estimated visually. The twist is left-handed if the bundles rotate clockwise when moving along the spindle axis in the direction of the observer, and vice versa Fig. 57. Our visual assessment yields a spindle twist score, which indicates whether the spindle is left-handed, weakly left-handed, right-handed, weakly right-handed, or has no visible twist. In the bundle tracing method, weak left-handed or weak right-handed twists correspond to a range of approximately  $-1$  to  $-2 \text{ deg}/\mu\text{m}$ . This is visible as a total rotation of  $5 - 10 \text{ deg}$  in the clockwise (left-handed) or counter-clockwise (right-handed) direction when moving towards the observer along the bundle length, where bundles are typically  $5 \mu\text{m}$  long. Twists to the left or right correspond to a rotation of more than  $10 \text{ deg}$  in the end-on view. The main advantage of this method is its dependability because coarse classification of spindles into five groups is accurate, whereas the main disadvantage is that the results are semi-quantitative rather than quantitative. Optical flow. The optical flow method estimates the movement of the signal from microtubule bundles automatically by comparing the signal from one  $z$ -plane to the next.(Fig. 57). This method yields a value for the average twist of all bundles in a spindle. It is the preferred choice for experiments on a large number of spindles because it is automated. Disadvantages are that it



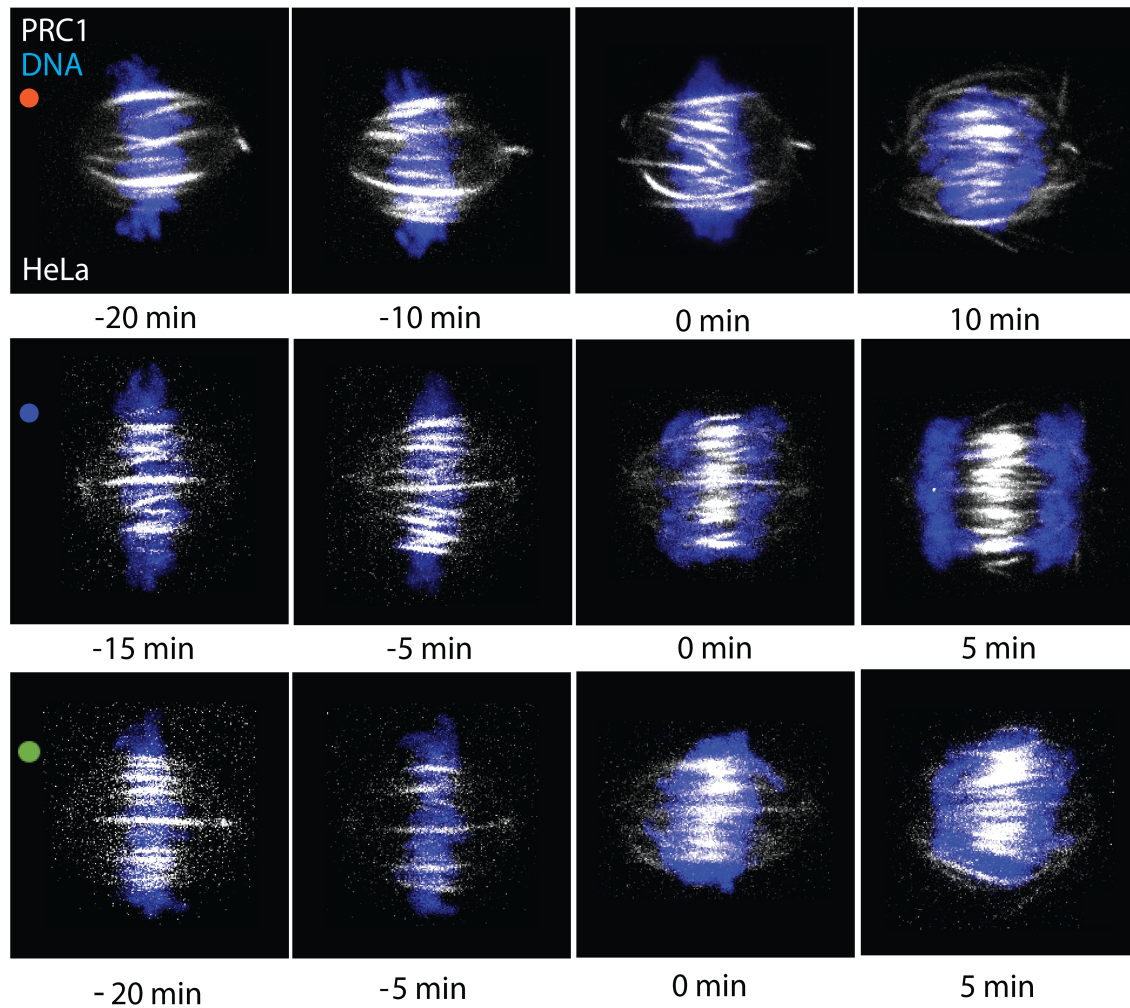


Figure 106: Microscope images of the spindles of HeLa cells over time. Each coloured dot represents one spindle’s progression through mitosis over time, and each colour corresponds to the colour of the data for that spindle in the graph Fig. 61. Three distinct examples are provided. Microtubule bundles (PRC1-GFP) are shown in grey, and DNA is shown in blue (SiR-DNA dye). Maximum  $z$ -projections are used to display the images. Experiments were carried out on HeLa $\alpha$ –Kyoto BAC cells that were stably expressing PRC1-GFP. Adapted from [2].

provides only the average twist value rather than the twist of each bundle, and that the results are sensitive to unspecific signal in the images, individual bundles with atypical behavior, and imperfect alignment of the spindle axis with the  $z$ -axis. First, parts of the images containing the blobs were selected for analysis using Rectangle tool in ImageJ [279, 280]. In all transformed stacks only images between spindle poles were used for analysis. Transformed spindle images contained a lot of noise that was removed by using the Mexican hat filter and a threshold. The Mexican hat filter, also called the Laplacian of Gaussian filter, was used for detection of blobs [281, 282]. After applying the Mexican hat filter, a threshold was applied to the image. It removes all the pixels with intensity lower than the given threshold. Microtubule bundles of transformed spindles were detected and traced automatically using optical flow for calculating the movement of pixels between two consecutive images. Farnebäck's two-frame motion estimation algorithm (dense optical flow algorithm) was used [283]. The spindle poles were manually tracked in ImageJ using the Multipoint tool. Mitotic spindle twists were calculated using the All pixels weighted twist algorithm. The total twist is calculated as the average twist of all pixels in the spindle, weighted by their normalised intensity. Using the tracked spindle poles, the tilt of the spindle with respect to the imaging plane is taken into account, and the twist measurement is corrected by this tilt angle. In Fiji, we used the Line tool to measure spindle length and width. The length of the spindle was measured by drawing a line from pole to pole. Width was measured in HeLa cells expressing PRC1-GFP by drawing a line across the equatorial plane of the spindle and terminating at the spindle's outer edges. The width of RPE1 cells expressing CENP- $\alpha$ -GFP and centrin1-GFP was measured by drawing a line across the spindle's equatorial plane, ending at the outer kinetochore pairs. The fluorescence intensity signal of the protein of interest was measured on the entire spindle region using the ImageJ Polygon Selection tool on the sum-intensity projection of the entire  $z$ -stack to quantify protein expression. The mean background fluorescence intensity measured in the cytoplasm was subtracted from the mean value obtained on the spindle, and the resulting value was divided by the number of  $z$ -slices used in the sum projection. A

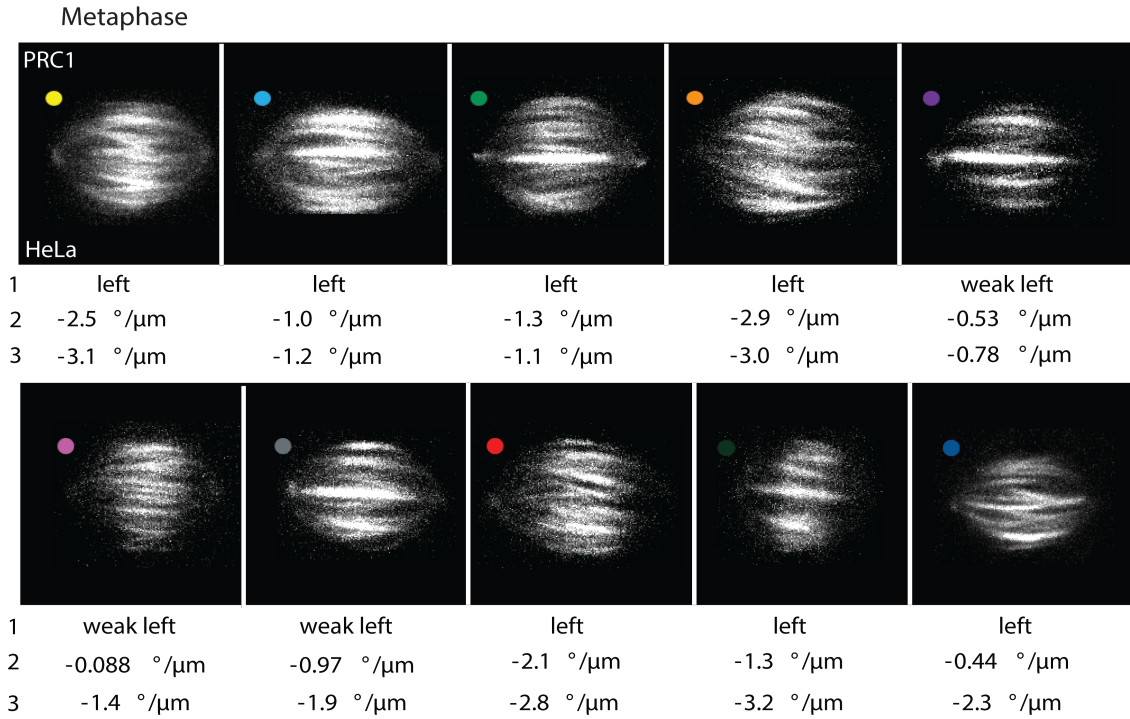


Figure 107: Microscope images of individual spindles of HeLa cells in metaphase (E) and anaphase (F) are shown with their twist values. Twist was determined with the visual assessment method, optical flow and the Oblique Circle Method, marked by 1, 2, and 3, respectively. Data from these cells was used in the graphs in Fig. 61 and Fig. 59. Microtubule bundles are shown in grey (PRC1-GFP) and DNA in blue (SiR-DNA dye). Images are shown in maximum  $z$ -projections. Experiments were performed on the HeLa-Kyoto BAC cells stably expressing PRC1-GFP. Adapted from [2].

comparison of the values obtained from the different methods can be seen in Fig. 107.

#### A.1.4 Tables with data breakdown from chirality quantification

Cell type	HeLa		
	Twist ( deg/ $\mu\text{m}$ )	Length ( $\mu\text{m}$ )	Width ( $\mu\text{m}$ )
Prometaphase	$0.09 \pm 0.18(12)$	$11.8 \pm 0.2$	$8.3 \pm 0.3$
Metaphase	$-1.20 \pm 0.22 (14)$ $*-1.01 \pm 0.14 (14)$	$11.5 \pm 0.3$ $*10.6 \pm 0.1(6)$	$9.0 \pm 0.2$ $*9.9 \pm 0.2$
Anaphase onset Early anaphase	$-1.98 \pm 0.26$	$12.2 \pm 0.4$	$9.0 \pm 0.5$
Late anaphase	$-0.31 \pm 0.14 (12)$	$13.3 \pm 0.2$	$9.0 \pm 0.3$
Mps1 inhibition	$-0.17 \pm 0.21 (17)$	$11.9 \pm 0.4$	$8.4 \pm 0.2$
Eg5 inhibition	$-0.47 \pm 0.14 (16)$	$12.0 \pm 0.2$	$9.3 \pm 0.2$
Eg5 overexpression	n.d.	n.d.	n.d.
Kif18A siRNA	$0.11 \pm 0.14 (21)$	$12.8 \pm 0.6$	$8.3 \pm 0.2$
Kif18A overexpression	n.d.	n.d.	n.d.
HSET siRNA	$-1.13 \pm 0.21 (17)$	$11.7 \pm 0.2$	$8.4 \pm 0.2$
PRC1 siRNA	$*-0.94 \pm 0.17 (19)$	$*9.9 \pm 0.2$	$*9.9 \pm 0.1$
PRC1 overexpression	n.d.	n.d.	n.d.
HAUS6 siRNA	$0.18 \pm 0.21 (16)$	$11.9 \pm 0.3$	$9.4 \pm 0.4$
HAUS8 siRNA	$-0.35 \pm 0.40 (10)$	$12.1 \pm 0.4$	$9.6 \pm 0.5$
Mock siRNA	$*-0.85 \pm 0.20 (17)$ $-0.94 \pm 0.16 (13)$	$*10.7 \pm 0.3$ $11.2 \pm 0.3$	$*9.6 \pm 0.2$ $9.5 \pm 0.3$
MG-132	n.d.	n.d.	n.d.

Table 3: Full spindle geometry analysis data for HeLa cells.

Cell type	RPE1		
Parameter	Twist (deg/ $\mu\text{m}$ )	Length ( $\mu\text{m}$ )	Width ( $\mu\text{m}$ )
Prometaphase	$0.004 \pm 0.09$ (20)	$12.1 \pm 0.2$	$8.7 \pm 0.1$
Metaphase	$-0.21 \pm 0.08$ (34)	$12.8 \pm 0.3$	$9.0 \pm 0.1$
Anaphase onset	$-0.53 \pm 0.15$ (26)	$12.9 \pm 0.2$	$8.7 \pm 0.1$
Early anaphase	$-0.30 \pm 0.15$ (22)	$13.8 \pm 0.3$	$8.4 \pm 0.2$
Late anaphase	$-0.20 \pm 0.17$ (16)	$16.6 \pm 0.4$	$7.5 \pm 0.3$
Mps1 inhibition	n.d.	n.d.	n.d.
Eg5 inhibition	$-0.06 \pm 0.19$ (11)	$12.3 \pm 0.4$	$8.8 \pm 0.1$
Eg5 overexpression	$-0.25 \pm 0.12$ (11)	$12.7 \pm 0.4$	$9.0 \pm 0.3$
Kif18A siRNA	$0.28 \pm 0.13$ (17)	$14.0 \pm 0.5$	$8.4 \pm 0.1$
Kif18A overexpression	$-0.26 \pm 0.20$ (7)	$10.3 \pm 0.3$	$8.1 \pm 0.2$
HSET siRNA	$-0.19 \pm 0.12$ (18)	$13.9 \pm 0.4$	$8.9 \pm 0.1$
PRC1 siRNA	$0.21 \pm 0.13$ (16)	$15.1 \pm 0.5$	$9.3 \pm 0.2$
PRC1 overexpression	$-0.08 \pm 0.11$ (10)	$10.3 \pm 0.4$	$8.0 \pm 0.1$
HAUS6 siRNA	$0.49 \pm 0.21$ (16)	$11.7 \pm 0.3$	$9.0 \pm 0.1$
HAUS8 siRNA	$0.85 \pm 0.24$ (13)	$13.1 \pm 0.4$	$9.0 \pm 0.2$
Mock siRNA	$-0.22 \pm 0.08$ (39)	$12.5 \pm 0.2$	$8.6 \pm 0.1$
MG-132	$0.51 \pm 0.14$	$12.0 \pm 0.4$	$8.8 \pm 0.2$

Table 4: Full spindle geometry analysis data for RPE cells.

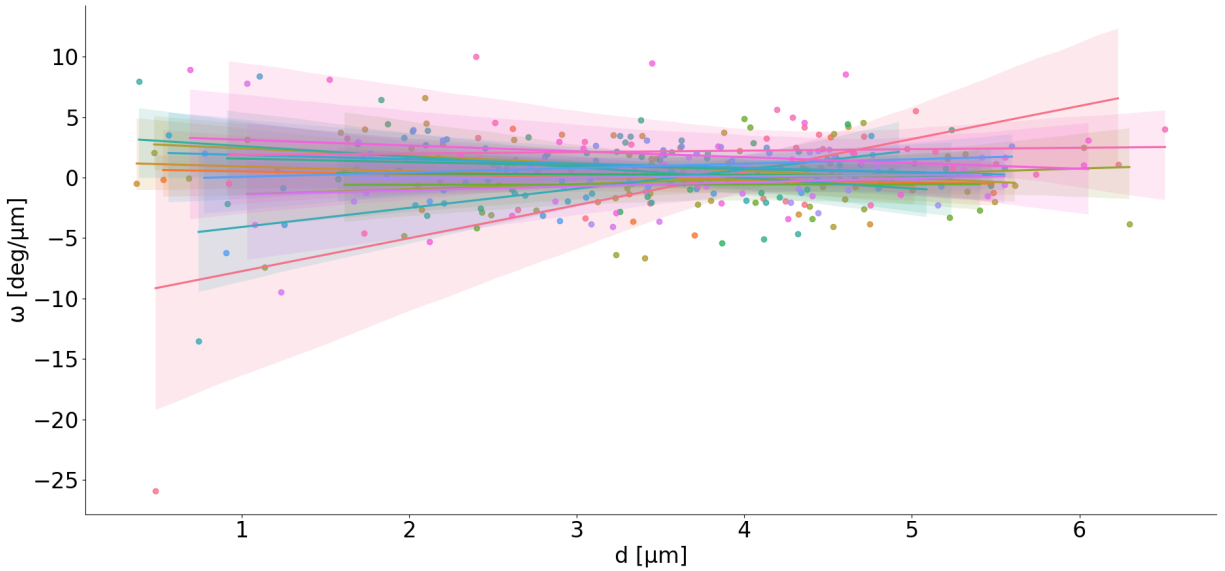


Figure 108: Calculation of the twist of spindles in STLC cells using the OCM ( $N_{\text{spindles}} = 16$  and  $N_{\text{bundles}} = 343$ ). Data corresponds to the last bar in Fig. 46. Dots show the measured twist (y-axis) and distance from the pole-to-pole axis (x-axis) from each bundle. The line is a linear regression fit, with the shaded region corresponding to a confidence interval of 95%. Colours corresponds to different cells from the experiment.

### A.1.5 Detailed STLC analysis

We show a bundle-by-bundle breakdown of HeLa cells treated using STLC, which has been shown to remove spindle twist [43], in Figs. 108 to 110.

We can see that twist is reduced, but the curvature and length of bundles in the cells does not exhibit a significant change.

## A.2 Additional Naegleria gruberi images

We show three-dimensional reconstructions of the amoeba *Naegleria gruberi* in Figs. 111 and 112. From the images we can see that its microtubule bundles extend from pole-to-pole, and that they form a continuous elastic rod, suitable for both the Oblique Circle Method, and our further theoretical models.

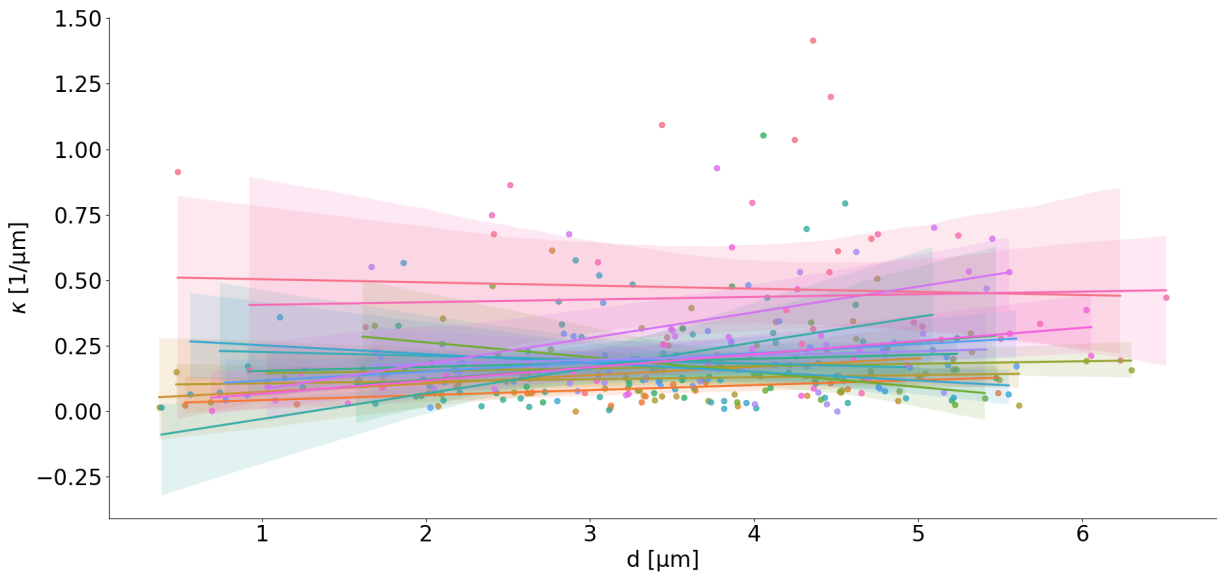


Figure 109: Calculation of the curvature of spindles in STLC cells using the OCM ( $N_{\text{spindles}} = 16$  and  $N_{\text{bundles}} = 343$ ). Data corresponds to the last bar in Fig. 46. Dots show the measured curvature (y-axis) and distance from the pole-to-pole axis (x-axis) from each bundle. The line is a linear regression fit, with the shaded region corresponding to a confidence interval of 95%. Colours corresponds to different cells from the experiment.

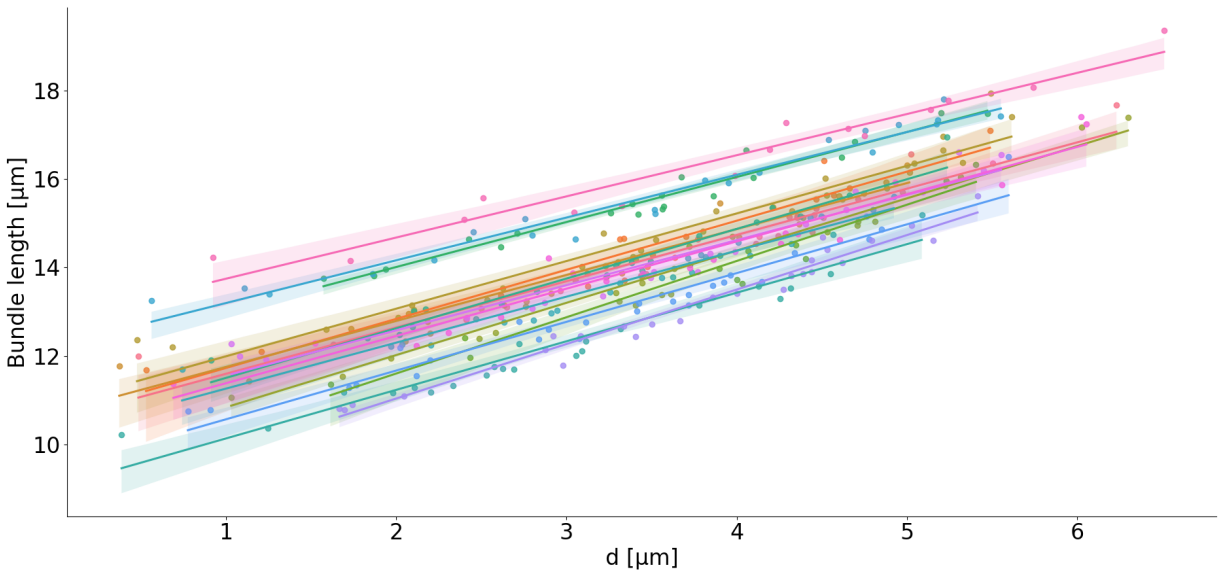


Figure 110: Calculation of the twist of spindles in STLC cells ( $N_{\text{spindles}} = 16$  and  $N_{\text{bundles}} = 343$ ). Data corresponds to the last bar in Fig. 46. Dots show the measured bundle length (y-axis) and distance from the pole-to-pole axis (x-axis) from each bundle. The line is a linear regression fit, with the shaded region corresponding to a confidence interval of 95%. Colours corresponds to different cells from the experiment.



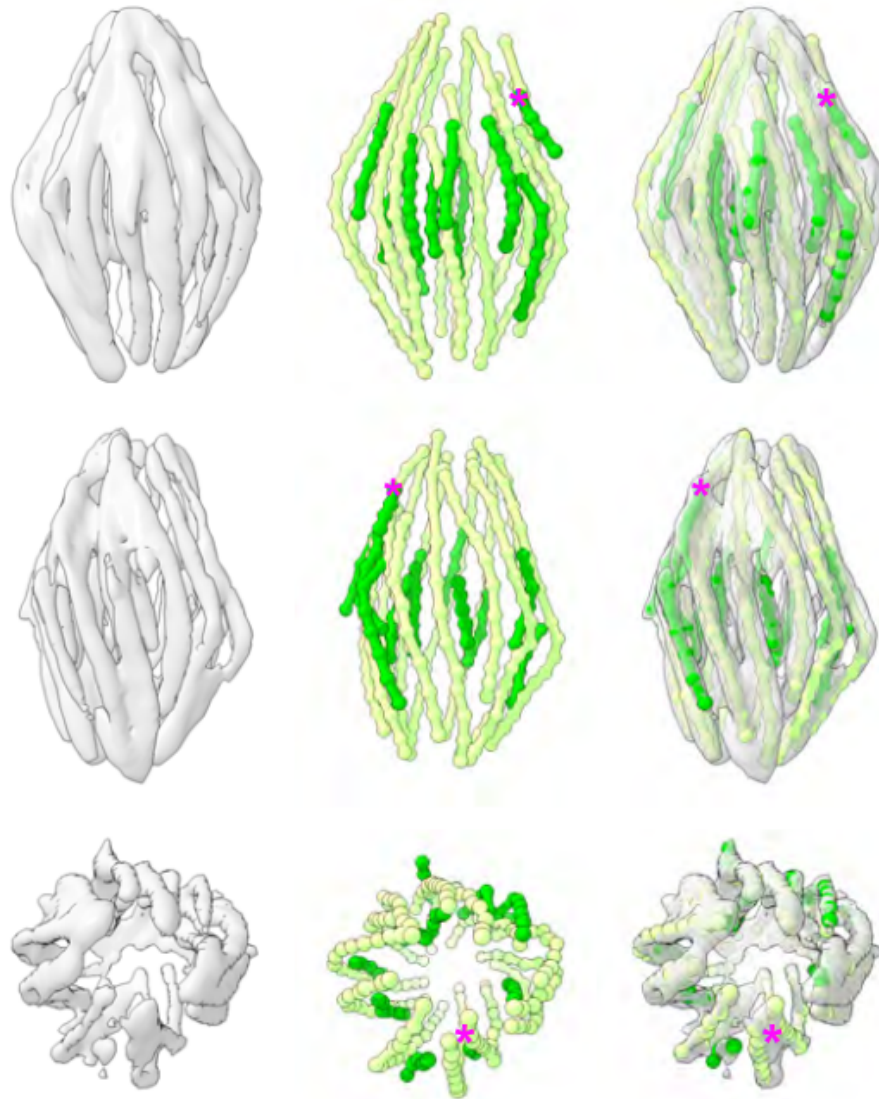


Figure 111: A spindle from Fig. 62 was rendered using ChimeraX, and primary and secondary bundles were traced using markers placed inside the 3D volume of each bundle. Longer bundles that persisted to the poles ( primary bundles) were labelled with light green markers, while shorter bundles present at the spindle midzone (secondary bundles) were labelled with dark green markers. Three angles of the same spindle are shown (top, middle, bottom) as volume renderings (left), markers (middle) and an overlay (right). Adapted from [3].

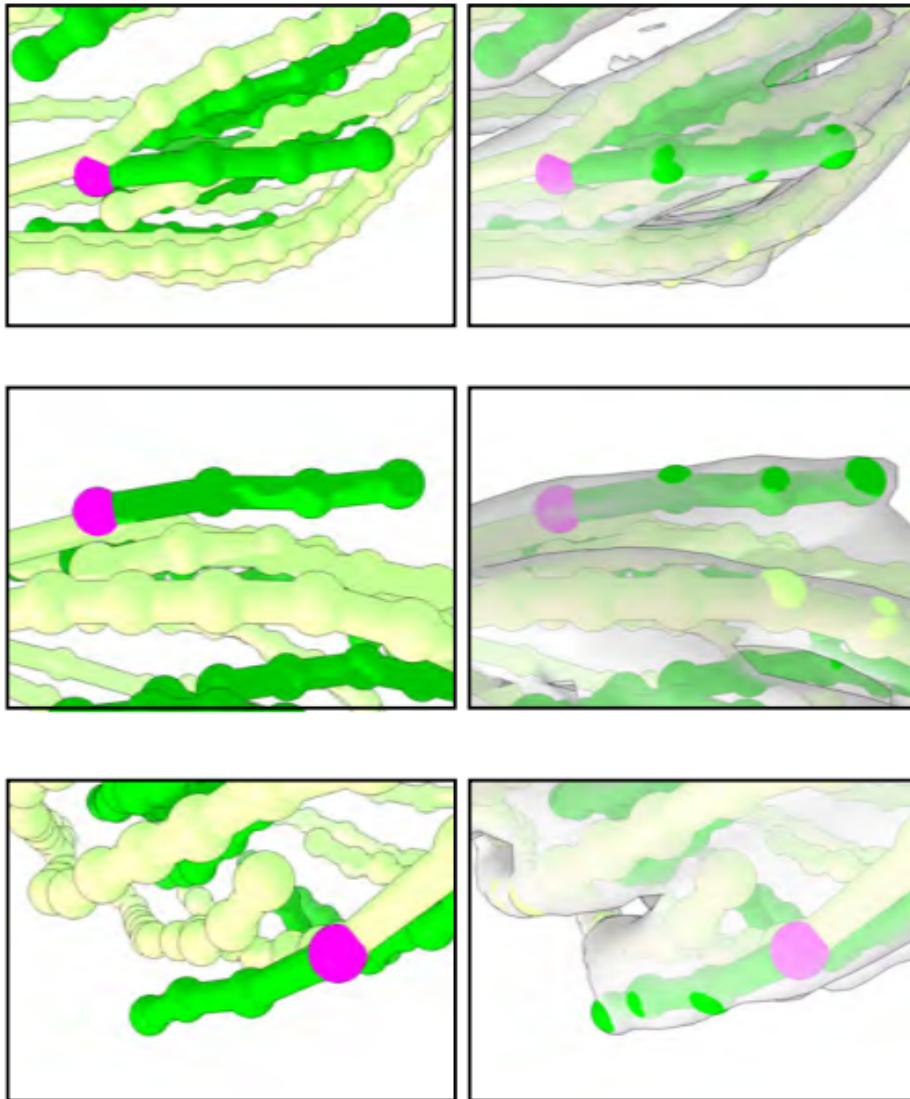


Figure 112: One point of close proximity between a secondary and primary bundle is highlighted as an example (the secondary bundle contains a magenta marker at this site, also see the magenta asterisk in panel A for context). Views from a variety of angles reveal that this secondary bundle also approaches other primary microtubule bundles. Adapted from [3].

## A.3 Mean-field model

### A.3.1 Microtubule bundle density

In the mean-field approximation we introduce the volume density of microtubule bundles  $\rho_{\text{MT}} = \rho_V$ , which is connected to the total number of microtubule bundles, which is connected to the total number of microtubule bundles  $N_{\text{MT}}$  as follows:

$$N_{\text{MT}} = \int_S \rho_V dV, \quad (\text{A.3.1})$$

where  $S$  is the entirety of space, and  $dV$  is the differential volume element.

We will use the standard spherical coordinate system  $(r, \phi, \theta)$ , where the origin is at the centre of the left centrosome. The  $z$ -axis, which is closed by the angle  $\theta$ , is also the pole-to-pole axis between the centrosomes, where the vector  $\mathbf{L}$  lies. The same ' variables  $(r', \phi', \theta')$  hold for the right centrosome.

Generally, the density of microtubules on one centrosome will depend on the microtubule bundle end density on the other centrosome. Every microtubule bundle end has its partner.

$$\rho = \rho(r, \phi, \theta, \rho'), \quad (\text{A.3.2})$$

$$\rho' = \rho'(r', \phi', \theta', \rho). \quad (\text{A.3.3})$$

The microtubule bundle end are located on the centrosomes, meaning that  $N_{\text{MT}} = N'_{\text{MT}}$ , or rather

$$\int_S \rho_V dV = \int_S \rho'_V dV'. \quad (\text{A.3.4})$$

For the density on the left centrosome we can write:

$$\rho = \rho(r, \phi, \theta, r', \phi', \theta'). \quad (\text{A.3.5})$$

We want our system to be rotationally invariant around the central pole-to-pole axis and invariant under exchange of the centrosomes. These two requirements boil down to  $r = r'$  and  $\theta = \theta'$ , leading us to

$$\rho_V = \rho_V(r, \phi, \theta, \phi'). \quad (\text{A.3.6})$$

Furthermore, the only sources of forces and torques will be located at the bundle ends, meaning that the density can only have a functional dependence on the surface of the centrosome  $r = d$ , where  $d$  is the radius of both centrosomes. From this we obtain

$$\rho_V = \delta(r - d)\rho_\Omega(\phi, \theta, \phi'), \quad (\text{A.3.7})$$

where  $\delta$  is the Dirac delta function, and  $\rho_\Omega$  is the part of the volume microtubule bundle density which only has an angular component.

The relationship between  $\phi = \phi(\theta, \phi')$  is what determines the twisting of the microtubule bundle ends  $\alpha(\theta) = \phi(\theta) - \phi'(\theta)$ , or rather which bundle ends are paired, and its dependency on  $(\theta)$  is of particular interest as a prediction of the model.

For the density we can furthermore assume that the angular part is homogeneous  $\rho_0$ , and that the microtubule bundle ends only fill a spherical cap between the angles  $\theta_a$  and  $\theta_b$ . The volume density then becomes, using  $\theta_a = 0$  and  $\theta_b = \theta_0$  for simplicity:

$$\rho_V = \delta(r - d)\Theta(\theta - \theta_a)\Theta(\theta_b - \theta)\rho_0, \quad (\text{A.3.8})$$

where  $\Theta(\theta_0)$  is the Heavyside step function.

We can determine the factor  $\rho_0$  through the total number of microtubule bundles by inserting Eq. (A.3.8) into Eq. (A.3.1). This means that the total volume density becomes

$$\rho_V(r) = \frac{N_{\text{MT}}\delta(r - d)\Theta(\theta - \theta_a)\Theta(\theta_b - \theta)}{2\pi d^2(\cos \theta_a - \cos \theta_b)}, \quad (\text{A.3.9})$$

where from the entirety of the mitotic spindle volume we restrict ourselves to the centrosome sphere via  $\delta(r - d)$ . We can write this more succinctly

$$\rho = \rho_\Omega = \frac{N_{\text{MT}}\Theta(\theta - \theta_a)\Theta(\theta_b - \theta)}{2\pi(\cos \theta_a - \cos \theta_b)}, \quad (\text{A.3.10})$$

bearing in mind that we are constricted to the surface of the centrosome sphere.

Because we assumed symmetry around the pole-to-pole axis, the density must be independent of  $\phi$

$$\rho(\theta, \phi) = \rho(\theta). \quad (\text{A.3.11})$$

### A.3.2 Additional symmetries for the torques

For the torques, we impose additional symmetry requirements, to allow for easier solving of the model. The requirements are necessary because the azimuthal symmetry and the centrosome exchange symmetry do not specify the geometry to the same degree as for linear forces. The first requirement is for the parallel torques to be of opposite sign:

$$\mathbf{M}^{\parallel} = -\mathbf{M}^{\parallel'} \quad (\text{A.3.12})$$

Additionally, we impose the requirement that all microtubules at the same angle  $\theta$  have the same magnitude of the torque:

$$\int_0^{2\pi} |\mathbf{M}(\theta, \phi)| d\phi = \int_0^{2\pi} |\mathbf{M}'(\theta, \phi)| d\phi. \quad (\text{A.3.13})$$

We can then insert Eq. (4.6.2) here, leading to:

$$\begin{aligned}
\int_0^{2\pi} \sqrt{m^{\parallel 2} + m^{\perp 2}(\cos(\phi + \delta)^2 + \sin(\phi + \delta)^2)} &= \\
&= \int_0^{2\pi} \sqrt{m^{\parallel \prime 2} + m^{\perp \prime 2}(\cos(\phi' + \delta')^2 + \sin(\phi' + \delta')^2)}, \quad (\text{A.3.14})
\end{aligned}$$

and

$$m^{\parallel 2} + m^{\perp 2} = m^{\parallel \prime 2} + m^{\perp \prime 2}. \quad (\text{A.3.15})$$

Utilising the above equation for the parallel torque components:

$$m^{\perp} = \pm m^{\perp \prime} \quad (\text{A.3.16})$$

The final requirement is that the perpendicular components of the torques are perpendicular to the position vector of a microtubule bundle end  $\mathbf{d}$ :

$$\mathbf{d} \cdot \mathbf{M}^{\perp} = \mathbf{d}' \cdot \mathbf{M}^{\perp \prime}, \quad (\text{A.3.17})$$

from which we have

$$m^{\perp} \cos(\nu) = m^{\perp \prime} \cos(\nu') = 0. \quad (\text{A.3.18})$$

This equation has as solutions  $\nu = \pm\nu'$  or  $\nu = \frac{\pi}{2}$  and  $\nu' = -\frac{\pi}{2}$ . The physical situation is unchanged, so we use the sign  $\nu = -\nu'$ .

### A.3.3 Derivation of the force-balance equations

To derive the balance equations in the mean-field approximations we insert Eqs. (A.3.50) and (A.3.51) into the force-balance equation. Starting from the parallel( $\parallel$ ) direction:

$$\hat{z} : \int_0^{2\pi} \int_0^{\theta^0} f^{\parallel}(\theta) d\Omega = 4\pi \int_0^{\theta^0} f^{\parallel}(\theta) \sin \theta d\theta = 0. \quad (\text{A.3.19})$$

For the perpendicular direction we, bearing in mind that we have two components, obtain:

$$\hat{x} : \int_0^{2\pi} \int_0^{\theta^0} f^\perp(\theta) \cos(\phi + \delta) d\Omega = 0 \times \int_0^{\theta^0} f^\perp(\theta) \sin \theta d\theta = 0, \quad (\text{A.3.20})$$

$$\hat{y} : \int_0^{2\pi} \int_0^{\theta^0} f^\perp(\theta) \sin(\phi + \delta) d\Omega = 0 \times \int_0^{\theta^0} f^\perp(\theta) \sin \theta d\theta = 0. \quad (\text{A.3.21})$$

Next we insert the parallel term:

$$\hat{z} : f^\parallel(\theta) = -f^\parallel'(\theta'). \quad (\text{A.3.22})$$

Followed by the perpendicular direction:

$$\hat{x} : f^\perp(\theta) \cos(\phi + \delta) = -f^\perp'(\theta) \cos(\phi' + \delta'), \quad (\text{A.3.23})$$

$$\hat{y} : f^\perp(\theta) \sin(\phi + \delta) = -f^\perp'(\theta) \sin(\phi' + \delta'). \quad (\text{A.3.24})$$

From squaring equations Eq. (A.3.23) and Eq. (A.3.24) we obtain:

$$f^\perp(\theta) = \mp f^\perp'(\theta), \quad (\text{A.3.25})$$

By defining the shorthand  $\Delta \equiv \delta - \delta'$ :

$$\phi'_1 = \phi + (\delta(\theta) - \delta'(\theta)) = \phi + \Delta, \quad (\text{A.3.26})$$

$$\phi'_2 = \phi + \pi + (\delta(\theta) - \delta'(\theta)) = \phi + \pi + \Delta. \quad (\text{A.3.27})$$

These two solutions, though at first glance different, reduce to the same one, as will be shown explicitly later. The value of  $\Delta$  will depend on a case by case basis.

We introduce the twist of microtubule bundle ends as  $\alpha \equiv \phi - \phi'$ .

We proceed with the balance equations, switching now to the torque balance. For the

parallel direction

$$\begin{aligned}\hat{z} : \int_0^{2\pi} \int_0^{\theta_0} (m^{\parallel}(\theta) + |d|(f^{\perp}(\theta) \sin \theta \sin \delta) \sin \theta d\theta d\phi \\ \rightarrow \int_0^{\theta_0} (m^{\parallel}(\theta) + |d|(f^{\perp}(\theta) \sin \theta \sin \delta) \sin \theta d\theta = 0, \quad (\text{A.3.28})\end{aligned}$$

followed by the perpendicular direction:

$$\hat{x} : \int_0^{2\pi} \int_0^{\theta_0} (m^{\perp}(\theta) \cos(\phi + \nu) + |d|(f^{\parallel}(\theta) \sin \theta \sin \phi - f^{\perp}(\theta) \cos \theta \sin(\phi + \delta)) d\Omega = 0, \quad (\text{A.3.29})$$

$$\hat{y} : \int_0^{2\pi} \int_0^{\theta_0} (m^{\perp}(\theta) \sin(\phi + \nu) + |d|(f^{\perp}(\theta) \cos \theta \cos(\phi + \delta) - f^{\parallel}(\theta) \sin \theta \cos \phi) d\Omega = 0. \quad (\text{A.3.30})$$

The remaining equation for the parallel direction is

$$\hat{z} : m^{\parallel}(\theta) + m^{\parallel \prime}(\theta) + d(f^{\perp} \sin \theta \sin \delta + f^{\perp \prime} \sin \theta \sin \delta') = 0. \quad (\text{A.3.31})$$

The perpendicular direction is:

$$\begin{aligned}\hat{x} : m^{\perp}(\theta) \cos(\phi + \nu) + m^{\perp \prime}(\theta) \cos(\phi' + \nu') \\ + d(f^{\parallel}(\theta) \sin(\theta) \sin(\phi) + f^{\parallel \prime}(\theta) \sin(\theta) \sin(\phi')) \\ - d(f^{\perp}(\theta) \cos(\theta) \sin(\phi + \delta) - f^{\perp \prime}(\theta) \cos(\theta) \sin(\phi' + \delta')) \\ - f^{\perp \prime}(\theta) L \sin(\phi' + \delta') = 0, \quad (\text{A.3.32})\end{aligned}$$



$$\begin{aligned}
\hat{y} : m^\perp(\theta) \sin(\phi + \nu) + m^{\perp'}(\theta) \sin(\phi' + \nu') \\
- d(f^\parallel(\theta) \sin(\theta) \cos(\phi) + f^{\parallel'}(\theta) \sin(\theta) \cos(\phi')) \\
+ d(f^\perp(\theta) \cos(\theta) \cos(\phi + \delta) - f^{\perp'}(\theta) \cos(\theta) \cos(\phi' + \delta')) \\
+ f^{\perp'}(\theta) L \cos(\phi' + \delta') = 0, \quad (\text{A.3.33})
\end{aligned}$$

From the symmetries we used we immediately know that  $f^\parallel = 0$ . The above equation correctly transform into one another for  $\phi = \phi + \frac{\pi}{2}$ , as expected from the axial symmetry. Furthermore we have

$$\begin{aligned}
\hat{x} : m^\perp(\theta) \cos(\phi + \nu) + m^{\perp'}(\theta) \cos(\phi + \nu' - \alpha) \\
- 2d(f^\perp(\theta) \cos(\theta) \sin(\phi + \delta) \\
+ f^\perp(\theta) L(\theta) \sin(\phi + \delta) = 0, \quad (\text{A.3.34})
\end{aligned}$$

or

$$\begin{aligned}
\hat{x} : m^\perp(\theta) \cos(\phi + \nu) + m^{\perp'}(\theta) \cos(\phi + \nu' - \alpha) \\
+ 2d(f^\perp(\theta) \cos(\theta) \cos(\phi + \delta + \frac{\pi}{2})) \\
- f^\perp(\theta) L(\theta) \cos(\phi + \delta + \frac{\pi}{2}) = 0, \quad (\text{A.3.35})
\end{aligned}$$

Using all torque symmetries from Appendix A.3.2 we obtain:

$$\begin{aligned} \hat{x} : 2m^\perp(\theta) \cos\left(\frac{\phi + \phi'}{2} + \frac{\nu + \nu'}{2}\right) \cos\left(\frac{\phi - \phi'}{2} + \frac{\nu - \nu'}{2}\right) \\ - 2d(f^\perp(\theta) \cos(\theta) \sin(\phi + \delta) \\ + f^\perp(\theta)L(\theta) \sin(\phi + \delta)) = 0, \end{aligned} \quad (\text{A.3.36})$$

Using the definition of  $\alpha$ :

$$\begin{aligned} \hat{x} : 2m^\perp(\theta) \cos\left(\phi - \frac{\alpha}{2} + \frac{\nu + \nu'}{2}\right) \cos\left(\frac{\alpha}{2} + \frac{\nu - \nu'}{2}\right) \\ = (2d(f^\perp(\theta) \cos(\theta) + f^\perp(\theta)L(\theta)) \sin(\phi + \delta), \end{aligned} \quad (\text{A.3.37})$$

For the  $\hat{y}$  direction we obtain

$$\begin{aligned} \hat{y} : 2m^\perp(\theta) \sin\left(\phi - \frac{\alpha}{2} + \frac{\nu + \nu'}{2}\right) \cos\left(\frac{\alpha}{2} + \frac{\nu - \nu'}{2}\right) \\ = -(2d(f^\perp(\theta) \cos(\theta) + f^\perp(\theta)L(\theta)) \cos(\phi + \delta). \end{aligned} \quad (\text{A.3.38})$$

We split the equation into the  $\hat{y}$  i  $\hat{x}$  directions

$$\tan\left(\phi - \frac{\alpha}{2} + \frac{\nu + \nu'}{2}\right) = -\cot(\phi + \delta) = \tan\left(\phi + \delta - \frac{\pi}{2}\right) \quad (\text{A.3.39})$$

$$\frac{\nu + \nu'}{2} + \frac{\pi - \alpha}{2} = \delta \quad (\text{A.3.40})$$

The first term is zero because  $\nu = -\nu'$ , meaning that

$$\delta(\theta) = \frac{\pi - \alpha(\theta)}{2}. \quad (\text{A.3.41})$$

We note that  $\delta$ ,  $\alpha$  i  $\phi$  do depend on  $\theta$ , but it was dropped in the notation for the sake of

brevity. Alternatively from Eq. (A.3.35) we can obtain:

$$\begin{aligned}
& -tg(\phi) \left( m^\perp(\theta) \sin(\nu) + m^{\perp'}(\theta) \sin(\nu' - \alpha) + 2df^\perp(\theta) \cos(\theta) \sin\left(\delta + \frac{\pi}{2}\right) \right. \\
& \quad \left. - f^\perp(\theta)L(\theta) \sin\left(\delta + \frac{\pi}{2}\right) \right) \\
& + \left( m^\perp(\theta) \cos(\nu) + m^{\perp'}(\theta) \cos(\nu' - \alpha) + 2df^\perp(\theta) \cos(\theta) \cos\left(\delta + \frac{\pi}{2}\right) \right. \\
& \quad \left. - f^\perp(\theta)L(\theta) \cos\left(\delta + \frac{\pi}{2}\right) \right) = 0, \quad (\text{A.3.42})
\end{aligned}$$

from which the same conclusion for  $\delta$  holds.

By eliminating the trigonometric functions we get:

$$\hat{x} : m^\perp(\theta) + m^{\perp'}(\theta) + 2df^\perp(\theta) \cos(\theta) - f^\perp(\theta)(L_0 - 2d \cos(\theta)) = 0, \quad (\text{A.3.43})$$

$$\hat{x} : m^\perp(\theta) + m^{\perp'}(\theta) + 4df^\perp(\theta) \cos(\theta) - f^\perp(\theta)L_0 = 0. \quad (\text{A.3.44})$$

$$\hat{x} : 2m^\perp(\theta) = f^\perp(\theta)(L_0 - 4d \cos(\theta)) \quad (\text{A.3.45})$$

We have thus eliminated all dependency on  $\phi$ , leaving only  $\theta$  as the angular variable. This is expected, because we do suppose axial symmetry.

The final equations are:

$$\int_0^{\theta_0} m^\parallel(\theta) \sin \theta + df^\perp(\theta) \sin \delta(\theta) (\sin \theta)^2 d\theta = 0 \quad (\text{A.3.46})$$

$$2m^\perp(\theta) \cos\left(\frac{\alpha(\theta)}{2} + \nu\right) = f^\perp(\theta)(L_0 - 4d \cos(\theta)) \quad (\text{A.3.47})$$

$$\delta(\theta) = \frac{\pi - \alpha(\theta)}{2} \quad (\text{A.3.48})$$

$$\nu = -\nu' = \frac{\pi}{2} \quad (\text{A.3.49})$$

The solutions of the Eq. (4.3.7), which give us the bundle shape using known forces at the end, will be used in the small-angle approximations. Though generally there are analytical solutions to large angle shapes [284], they are complicated and not easy to interpret. Because biological spindles are largely in the small-angle regime, the use of the approximation is justified. The solutions are:

$$\begin{aligned} y(z) = & A \sin((\omega_1 z + \phi_1)/2) \cos((\omega_2 z + \phi_2)/2) \\ & + B \cos((\omega_1 z + \phi_1)/2) \sin((\omega_2 z + \phi_2)/2) \\ & + \frac{M_x}{F_z} - \frac{F_y z}{F_z} - \frac{M_z F_x}{F_z^2} \end{aligned} \quad (\text{A.3.50})$$

$$\begin{aligned} x(z) = & A \sin((\omega_1 z + \phi_1)/2) \cos((\omega_2 z + \phi_2)/2) \\ & + B \cos((\omega_1 z + \phi_1)/2) \sin((\omega_2 z + \phi_2)/2) \\ & - \frac{M_y}{F_z} + \frac{F_x z}{F_z} + \frac{M_z = t w F_y}{F_z^2} \end{aligned} \quad (\text{A.3.51})$$

$$\omega_1 = \frac{\sqrt{M_z M_z + 4\kappa F_z}}{\kappa} \quad (\text{A.3.52})$$

$$\omega_2 = \frac{M_z}{\kappa} \quad (\text{A.3.53})$$

Forces and torques are just the x, y and z components of Eqs. (4.6.1) and (4.6.2), evaluated

at coordinates  $(\theta, \phi)$  of a particular microtubule bundle

$L, d$  i  $\kappa$  are determined experimentally, and given in Table 1.

A,B, and  $\phi_{1/2}$  are determined from the boundary conditions in  $\mathbf{d}$  i  $\mathbf{L} + \mathbf{d}' - (\mathbf{d}' \cdot \hat{z})\hat{z}$ ,

$$r(d \cos \theta) = \mathbf{d} = |d|(\sin \theta \cos \phi \hat{x} + \sin \theta \sin \phi \hat{y} + \cos \theta \hat{z}) \quad (\text{A.3.54})$$

$$r(L - d \cos \theta) = \mathbf{d} = |d|(\sin \theta \cos(\phi - \alpha) \hat{x} + \sin \theta \sin(\phi - \alpha) \hat{y} + (\frac{L}{d} - \cos \theta) \hat{z}) \quad (\text{A.3.55})$$

Table 5: Function expansion up to the zeroth order term.

$f^\perp = f_0^\perp$
$f^\parallel = f_0^\parallel$
$m^\perp = m_0^\perp$
$m^\parallel = m_0^\parallel$
$f^{\perp'} = f_0^{\perp'}$
$f^{\parallel'} = f_0^{\parallel'}$
$m^{\perp'} = m_0^{\perp'}$
$m^{\parallel'} = m_0^{\parallel'}$
$\delta(\theta) = \delta_0$
$\alpha(\theta) = \alpha_0$
$\sin(\theta) = \theta$
$\cos(\theta) = 1$

### A.3.4 Zeroth order

To specify the form of the unknown scalar functions, we expand the functions in a Taylor series around zero. This is justified because we are in the small angle regime, which we are already using to describe the shapes of the bundles. Starting from the zeroth order, where we only have constant terms, we expand all undefended functions into power series and insert them into the force balance equations.

$$\theta^0 : 2m_0^\perp \cos\left(\nu + \frac{\alpha_0}{2}\right) = f_0^\perp(L_0 - 2d) \quad (\text{A.3.56})$$

$$f_0^\perp = \frac{2m_0^\perp \cos\left(\nu + \frac{\alpha_0}{2}\right)}{(L_0 - 2d)} \quad (\text{A.3.57})$$

The integral equation becomes:

$$\int_0^{\theta_0} m_0^\parallel(\sin \theta) + df_0^\perp \sin(\delta_0)(\sin \theta)^2 d\theta = 0, \quad (\text{A.3.58})$$

which can easily be integrated, becoming:

$$m_0^{\parallel}(1 - \cos \theta_0) + df_0^{\perp} \sin(\delta_0) \frac{1}{2}(\theta_0 - \frac{1}{2} \sin(2\theta_0)) = 0. \quad (\text{A.3.59})$$

The boundary conditions also transform:

$$r(d \cos \theta) = \mathbf{d} = |d|(0\hat{x} + 0\hat{y} + 1\hat{z}), \quad (\text{A.3.60})$$

$$r(L - d \cos \theta) = \mathbf{d} = (0\hat{x} + 0\hat{y} + (L - d)\hat{z}). \quad (\text{A.3.61})$$

The zeroth order does not lead to solutions, which can readily be seen from the boundary conditions. It only allows solutions in the closest points of the two spheres, on the pole-to-pole axis, which does not describe reality. Thus, we have to proceed to the first-order term.

Table 6: Function expansion up to the first-order term.

$f^\perp = f_0^\perp + f_1^\perp \theta$
$f^\parallel = f_0^\parallel + f_1^\parallel \theta$
$m^\perp = m_0^\perp + m_1^\perp \theta$
$m^\parallel = m_0^\parallel + m_1^\parallel \theta$
$f^{\perp'} = f_0^{\perp'} + f_1^{\perp'} \theta$
$f^{\parallel'} = f_0^{\parallel'} + f_1^{\parallel'} \theta$
$m^{\perp'} = m_0^{\perp'} + m_1^{\perp'} \theta$
$m^{\parallel'} = m_0^{\parallel'} + m_1^{\parallel'} \theta$
$\delta(\theta) = \delta_0 + \delta_1 \theta$
$\alpha(\theta) = \alpha_0 + \alpha_1 \theta$
$\sin(\theta) = \theta$
$\cos(\theta) = 1$

### A.3.5 first-order terms

We expand the unknown scalar function in a Taylor series, but this time we continue up until the first term. The balance equations in this case are:

$$\theta^0 : 2m_0^\perp \cos\left(\nu + \frac{\alpha_0}{2}\right) = f_0^\perp (L_0 - 4d), \quad (\text{A.3.62})$$

$$\theta^1 : 2\left(m_1^\perp \cos\left(\nu + \frac{\alpha_0}{2}\right) - m_0^\perp \sin\left(\nu + \frac{\alpha_0}{2}\right) \frac{\alpha_1}{2}\right) = f_1^\perp (L_0 - 4d), \quad (\text{A.3.63})$$

$$\theta^0 : \delta_0 = \frac{\pi - \alpha_0}{2}, \quad (\text{A.3.64})$$

$$\theta^1 : \delta_1 = \frac{-\alpha_1}{2}. \quad (\text{A.3.65})$$



$$\sin(\delta_0 + \delta_1\theta) = \sin(\delta_0) \cos(\delta_1\theta) + \cos(\delta_0) \sin(\delta_1\theta). \quad (\text{A.3.66})$$

Which brings us to the equation:

$$\int_0^{\theta_0} \left( (m_0^{\parallel} + m_1^{\parallel}\theta) \sin \theta + (\sin(\delta_0) \cos(\delta_1\theta) + \cos(\delta_0) \sin(\delta_1\theta))(f_0^{\perp} + f_1^{\perp}\theta)(\sin(\theta))^2 \right) \theta = 0. \quad (\text{A.3.67})$$

This integral can be easily evaluated analytically, which however leads to a high amount of terms:

$$\begin{aligned}
& m_0^{\parallel}(1 - \cos \theta_0) + m_1^{\parallel} \sin(\theta_0) - m_1^{\parallel} \theta_0 \cos(\theta_0) + \\
& + 1/4df_0^{\perp} \cos(\delta_0) \left( (\cos((-2 + \delta_1)\theta_0)/(-2 + \delta_1) - (2\cos(\delta_1\theta_0))/\delta_1 + \cos((2 + \delta_1)\theta_0)/(2 + \delta_1)) \right. \\
& \quad \left. + 1/(-2 + \delta_1) - 1/\delta_1 + 1/(2 + \delta_1) \right) \\
& + 1/4df_0^{\perp} \sin(\delta_0) \left( (\sin((-2 + \delta_1)\theta_0)/(-2 + \delta_1) - (2\sin(\delta_1\theta_0))/\delta_1 + \sin((2 + \delta_1)\theta_0)/(2 + \delta_1)) \right) \\
& + 1/4df_1^{\perp} \sin(\delta_0) \left( (2\cos(\delta_1\theta_0))/\delta_1^2 - (\theta_0\sin((\delta_1 - 2)\theta_0))/(\delta_1 - 2) + (2\theta_0\sin(\delta_1\theta_0))/\delta_1 - \right. \\
& \quad (\theta_0\sin((\delta_1 + 2)\theta_0))/(\delta_1 + 2) - \cos((\delta_1 - 2)\theta_0)/(\delta_1 - 2)^2 - \cos((\delta_1 + 2)\theta_0)/(\delta_1 + 2)^2 \\
& \quad \left. - \left( (2)/\delta_1^2 - 1/(\delta_1 - 2)^2 - 1/(\delta_1 + 2)^2 \right) \right) \\
& + 1/4df_1^{\perp} \cos(\delta_0) \left( (2\sin(\delta_1\theta_0))/\delta_1^2 - (\theta_0\cos((\delta_1 - 2)\theta_0))/(\delta_1 - 2) + (2\theta_0\cos(\delta_1\theta_0))/\delta_1 - \right. \\
& \quad (\theta_0\sin((\delta_1 + 2)\theta_0))/(\delta_1 + 2) - \sin((\delta_1 - 2)\theta_0)/(\delta_1 - 2)^2 - \sin((\delta_1 + 2)\theta_0)/(\delta_1 + 2)^2) = 0
\end{aligned} \tag{A.3.68}$$

These equations correctly reduce to the zeroth order terms in the limit when when the first-order terms go to zero.

The boundary conditions are:

$$r(d \cos \theta) = \mathbf{d} = |d|(\theta \cos \phi \hat{x} + \theta \sin \phi \hat{y} + 1 \hat{z}) \tag{A.3.69}$$

$$r(L - d \cos \theta) = \mathbf{d} = |d|(\theta \cos(\phi + \Delta) \hat{x} + \theta \sin(\phi + \Delta) \hat{y} + (\frac{L}{d} - 1) \hat{z}) \tag{A.3.70}$$

In this case, unlike the zeroth order expansion, we have a distribution of microtubule bundle ends on a spherical cap, instead of all of them being located in a single point. In the

end these equations give us five free/fitting parameters, chosen from the Taylor expansion coefficients given in Appendix A.3.5. For simplicity, we will set  $\delta_1$  to be equal to zero, leaving us with only four parameters.

### A.3.6 Mid-zone density

Similarly, we can define the mid-point (the point of the bundle in the metaphase plane) density of bundles.

$$dN = \sigma(A)dA. \quad (\text{A.3.71})$$

Instead of a spherical cap, the mid-points are located on a disk

$$dN = \sigma(r, \phi)rdrd\phi, \quad (\text{A.3.72})$$

where we can once again remove the dependence on  $d\phi$  due to the symmetry of our system.

$$dN = 2\pi\sigma(r)rdr \quad (\text{A.3.73})$$

The same relationship in regard to the total number of bundles in a spindle must hold:

$$N_{tot} = \int_0^{2\pi} \int_{r_a}^{r_b} \sigma(r)rdrd\phi = N_0 \quad (\text{A.3.74})$$

The density of microtubule ends on the pole are explicitly connected to the mid-point density of bundles through the shape of the bundle, which is, in our model, given by the static equation (using the orientation where  $y(L/2) = r$  for simplicity)

$$y(L/2; \theta) = 2d + \frac{M(\theta)}{2\kappa} \frac{L^2}{4}, \quad (\text{A.3.75})$$

where  $M(\theta)$  is the torque acting on the microtubule bundle, ends, which are located along the centrosome. This gives us a one-to-one relationship between the angle  $\theta$  on the

centrosome and the position of the bundle in the equatorial plane of the spindle.

This relation also allows the calculation the limit values of  $\theta_a$ ,  $\theta_b$ ,  $r_a$  and  $r_b$ .

If we use a Taylor expansion  $M = m_0 + m_1\theta$

$$dr = dy = \frac{dM(\theta)d\theta}{2\kappa} \frac{L^2}{4} \quad (\text{A.3.76})$$

$$= \frac{m_1}{4\kappa} \frac{L^2}{4} d\theta \quad (\text{A.3.77})$$

$$\sigma(\theta) = \frac{\rho(\theta)d^2 \sin \theta}{\left(\frac{m_0+m_1\theta}{2\kappa}\right)\left(\frac{L^2}{4}\right)\left(\frac{m_1}{2\kappa}\right)\left(\frac{L^2}{4}\right)} \quad (\text{A.3.78})$$

### A.3.7 Contour length of the bundle

The contour length of the bundle can be calculated from its definition:

$$\mathcal{L} = \int_{\mathbf{d}}^{\mathbf{d}'} \sqrt{\left(\frac{dx}{dt}\right)^2 + \left(\frac{dy}{dt}\right)^2 + \left(\frac{dz}{dt}\right)^2} dt \quad (\text{A.3.79})$$

Here, we must insert the equations Eq. (A.3.51), Eq. (A.3.50) and  $z = t$  to obtain an expression of the torque. There is no analytical expression for the general case, but it is simple enough to evaluate numerically after input parameters and boundary conditions are chosen. If we expand the expression in a Taylor series, and keep the lowest order terms, we obtain

$$\mathcal{L}(\theta) \approx C\theta^2, \quad (\text{A.3.80})$$

where the constant  $C$  depends on the mentioned input parameters.

$$\frac{dN}{d\mathcal{L}}(\theta) = \frac{\pi d^2}{C} \frac{\rho(\theta) \sin \theta}{\theta} \quad (\text{A.3.81})$$

## B Curriculum vitae

Arian Ivec was born on the 3rd of October in 1994. He finished his high school education at V. Gimnazija, Zagreb in 2012. He obtained his master's degree at the Department of Physics at the Faculty of Science of the University of Zagreb in 2018. Since 2019, he has worked as a research and teaching assistant at the Department of Theoretic Physics, at the Faculty of Science at the University of Zagreb, as a member of Nenad Pavin's group for theoretical biophysics. He has worked at the project Balance of forces and torques in the mitotic spindle of the Croatian Science Foundation, as well as the Scientific Center of Excellence for Quantum and Complex Systems, and Representations of Lie Algebras - QuantiXLie. He has published 3 articles in CC journals, and presented his work in numerous domestic and international conferences. He has received the award for the best short talk at the 5. Symposium of doctoral students of the Faculty of Science, 2021.

### B.1 Papers

1. A. Ivec, M. Trupinić, I.M. Tolić and N. Pavin Oblique circle method for measuring the curvature and twist of mitotic spindle microtubule bundles. *Biophys J* 120, 3641-3648 (2021).
2. M. Trupinić, B. Kokanović, I. Ponjavić, I. Barišić, S. Šegvić, A. Ivec, I.M. Tolić The chirality of the mitotic spindle provides a mechanical response to forces and depends on microtubule motors and augmin. *Curr Biol* 32 , 2480–2493 (2022).
3. K. B. Velle, A. S. Kennard, M. Trupinić, A. Ivec, A. J. M. Swafford, E. Nolton, L. M. Rice, I. M. Tolić, L. K. Fritz-Laylin, P. Wadsworth Naegleria's mitotic spindles are built from unique tubulins and highlight core spindle features. *Curr Biol* 32, 1247–1261 (2022).

## B.2 Conferences

1. Biophysics of Spindle Assembly Workshop, Zagreb, Croatia; talk; 2022
2. 85. Annual Meeting of DPG and DPG-Tagung (DPG Meeting) of the Condensed Matter Section (SKM), Regensburg, Germany; talk; 2022
3. 9th World Congress of Biomechanics; online; talk; 2022
4. Meeting of the American Physical Society, Chicago, United States; talk; 2022
5. 84. Annual Meeting of DPG and DPG-Tagung (DPG Meeting) of the Condensed Matter Section (SKM); online; talk; 2021
6. Mitotic spindle: From living and synthetic systems to theory; online; talk; 2021
7. 5. Symposium of doctoral students of the Faculty of Science, Zagreb, Croatia; poster & talk; 2021
8. 4. Symposium of doctoral students of the Faculty of Science, Zagreb, Croatia; poster & talk; 2020
9. Seminar at ICTP Trieste; Trieste, Italy; talk; 2019
10. Biophysical conference, Hvar, Croatia; talk; 2019
11. Mitotic spindle: From living and synthetic systems to theory, Split, Croatia; poster; 2019

## References

1. Ivec, A., Trupinić, M., Tolić, I. M. & Pavin, N. Oblique circle method for measuring the curvature and twist of mitotic spindle microtubule bundles. *Biophysical Journal* **120**, 3641–3648 (Sept. 2021).
2. Trupinić, M. *et al.* The chirality of the mitotic spindle provides a mechanical response to forces and depends on microtubule motors and augmin. *eng. Current biology : CB* **32**, 2480–2493.e6 (11 June 2022).
3. Velle, K. B. *et al.* Naegleria’s mitotic spindles are built from unique tubulins and highlight core spindle features. *Current Biology* **32**, 1247–1261.e6. ISSN: 0960-9822. <https://doi.org/10.1016/j.cub.2022.01.034> (Mar. 2022).
4. Paweletz, N. Walther Flemming: pioneer of mitosis research. *Nature reviews Molecular cell biology* **2**, 72–75 (2001).
5. McIntosh, J. R., Molodtsov, M. I. & Ataullakhanov, F. I. Biophysics of mitosis. *Q Rev Biophys* **45**, 147–207. ISSN: 1469-8994 (Electronic) 0033-5835 (Linking). <https://www.ncbi.nlm.nih.gov/pubmed/22321376> (2012).
6. Lodish, H. *Molecular Cell Biology (9th edition): Harvey Lodish, Arnold Berk, S. Lawrence Zipursky, Paul Matsudaira, David Baltimore and James Darnell; ISBN 0-7167-3136-3* 1084 (Freeman & Co., New York, 2021).
7. Worrall, J. T. *et al.* Non-random mis-segregation of human chromosomes. *Cell reports* **23**, 3366–3380 (2018).
8. Joglekar, A. P. *et al.* Molecular architecture of the kinetochore-microtubule attachment site is conserved between point and regional centromeres. *The Journal of cell biology* **181**, 587–594 (2008).
9. Nagaoka, S. I., Hassold, T. J. & Hunt, P. A. Human aneuploidy: mechanisms and new insights into an age-old problem. *Nature Reviews Genetics* **13**, 493–504 (2012).

10. Aguirre, A. J. *et al.* Genomic Copy Number Dictates a Gene-Independent Cell Response to CRISPR/Cas9 Targeting Genomic Copy Number Affects CRISPR/Cas9 Screens. *Cancer discovery* **6**, 914–929 (2016).
11. Alberts, B. *et al.* *Molecular cell biology* (New York: Garland Science, 2008).
12. Cooper, G. M., Hausman, R. E. & Hausman, R. E. *The cell: a molecular approach* (ASM press Washington, DC, 2007).
13. Godinho, S. A. *et al.* Oncogene-like induction of cellular invasion from centrosome amplification. *Nature* **510**, 167–171 (2014).
14. Mogilner, A. & Craig, E. Towards a quantitative understanding of mitotic spindle assembly and mechanics. *Journal of cell science* **123**, 3435–3445 (2010).
15. Kaseda, K., McAinsh, A. D. & Cross, R. A. Dual pathway spindle assembly increases both the speed and the fidelity of mitosis. *Biology Open* **1**, 12–18 (Oct. 2011).
16. Musacchio, A. & Desai, A. A molecular view of kinetochore assembly and function. *Biology* **6**, 5 (2017).
17. Kirschner, M. & Mitchison, T. Beyond self-assembly: from microtubules to morphogenesis. *Cell* **45**, 329–342 (1986).
18. Maiato, H., Gomes, A. M., Sousa, F. & Barisic, M. Mechanisms of chromosome congression during mitosis. *Biology* **6**, 13 (2017).
19. Dumont, S. & Mitchison, T. J. Force and length in the mitotic spindle. *Current Biology* **19**, R749–R761 (2009).
20. Cheeseman, I. M. & Desai, A. Molecular architecture of the kinetochore–microtubule interface. *Nature reviews Molecular cell biology* **9**, 33–46 (2008).
21. Pavin, N. & Tolic, I. M. Self-Organization and Forces in the Mitotic Spindle. *Annual Review of Biophysics, Vol 45* **45**, 279–298. ISSN: 1936-122x (2016).



22. Prosser, S. L. & Pelletier, L. Mitotic spindle assembly in animal cells: a fine balancing act. *Nat Rev Mol Cell Biol* **18**, 187–201. ISSN: 1471-0080 (Electronic) 1471-0072 (Linking). <https://www.ncbi.nlm.nih.gov/pubmed/28174430> (2017).
23. Wittmann, T., Hyman, A. & Desai, A. The spindle: a dynamic assembly of microtubules and motors. *Nature cell biology* **3**, E28–E34 (2001).
24. Howard, J. *Mechanics of Motor Proteins and the Cytoskeleton* ISBN: 9780878933341. <https://books.google.hr/books?id=-mmnQgAACAAJ> (Sinauer Associates, Publishers, 2001).
25. Inoue, S. Polarization optical studies of the mitotic spindle. *Chromosoma* **5**, 487–500 (1953).
26. Sato, T., Inoue, H. & Hata, K. The Photochemical Oxidation Reaction of Benzylic Alcohols in Dimethyl Sulfoxide. *Bulletin of the Chemical Society of Japan* **40**, 1502–1506 (1967).
27. Mohri, H. Amino-acid composition of 'Tubulin' constituting microtubules of sperm flagella. *Nature* **217**, 1053–1054 (1968).
28. Walczak, C. E. & Heald, R. Mechanisms of mitotic spindle assembly and function. *International review of cytology* **265**, 111–158 (2008).
29. Amano, S. The Structure of the Centrioles and Spindle Body as Observed Under the Electron and Phase Contrast Microscope SA New Extension-fiber Theory Concerning Mitotic Mechanism in Animal Cells. *Cytologia* **22**, 193–212 (1957).
30. Rieder, C. L. & Khodjakov, A. Mitosis through the microscope: advances in seeing inside live dividing cells. *Science* **300**, 91–96 (2003).
31. Dumont, S. & Mitchison, T. J. Compression regulates mitotic spindle length by a mechanochemical switch at the poles. *Current Biology* **19**, 1086–1095 (2009).

32. Recouvreux, P. & Dogterom, M. Dissecting Spindle Architecture with a Laser. *Cell* **149**, 507–509. ISSN: 0092-8674. <https://www.sciencedirect.com/science/article/pii/S0092867412004655> (2012).
33. Kajtez, J. *et al.* Overlap microtubules link sister k-fibres and balance the forces on bi-oriented kinetochores. *Nature Communications* **7**, 10298 (2016).
34. Vukušić, K. *et al.* Microtubule Sliding within the Bridging Fiber Pushes Kinetochore Fibers Apart to Segregate Chromosomes. *Developmental Cell* **43**, 11–23.e6 (Oct. 2017).
35. Lampson, M. A. & Kapoor, T. M. Unraveling cell division mechanisms with small-molecule inhibitors. *Nature chemical biology* **2**, 19–27 (2006).
36. Shimamoto, Y., Maeda, Y. T., Ishiwata, S., Libchaber, A. J. & Kapoor, T. M. Insights into the Micromechanical Properties of the Metaphase Spindle. *Cell* **145**, 1062–1074 (June 2011).
37. McIntosh, J. R. & Hays, T. A brief history of research on mitotic mechanisms. *Biology* **5**, 55 (2016).
38. Müller-Reichert, T., Kiewisz, R. & Redemann, S. Mitotic spindles revisited-new insights from 3D electron microscopy. *Journal of Cell Science* **131**, jcs211383 (2018).
39. Nigg, E. A. & Stearns, T. The centrosome cycle: Centriole biogenesis, duplication and inherent asymmetries. *Nature cell biology* **13**, 1154–1160 (2011).
40. Vleugel, M., Kok, M. & Dogterom, M. Understanding force-generating microtubule systems through in vitro reconstitution. *Cell adhesion & migration* **10**, 475–494 (2016).
41. VanBuren, V., Cassimeris, L. & Odde, D. J. Mechanochemical model of microtubule structure and self-assembly kinetics. *Biophysical journal* **89**, 2911–2926 (2005).
42. Wendell, K. L., Wilson, L. & Jordan, M. A. Mitotic block in HeLa cells by vinblastine: ultrastructural changes in kinetochore-microtubule attachment and in centrosomes. *Journal of Cell Science* **104**, 261–274 (1993).

43. Novak, M. *et al.* The mitotic spindle is chiral due to torques within microtubule bundles. *Nature Communications* **9**, 63–70. ISSN: 2041-1723. %3CGo%20to%20ISI%3E : //WOS:000443466700011 (2018).
44. Redemann, S. *et al.* C. elegans chromosomes connect to centrosomes by anchoring into the spindle network. *Nature Communications* **8** (May 2017).
45. Svitkina, T. in *Cytoskeleton Methods and Protocols* 187–206 (Springer, 2009).
46. Sabatini, D. D., Bensch, K. & Barnett, R. J. Cytochemistry and electron microscopy: the preservation of cellular ultrastructure and enzymatic activity by aldehyde fixation. *The Journal of cell biology* **17**, 19–58 (1963).
47. Ledbetter, M. & Porter, K. A” microtubule” in plant cell fine structure. *The Journal of cell biology* **19**, 239–250 (1963).
48. Wohlfarth-Bottermann, K. Weitreichende, fibrilläre Protoplasmaidifferenzierungen und ihre Bedeutung für die Protoplasmaströmung. *Protoplasma* **54**, 514–539 (1962).
49. Kreis, T. & Vale, R. *Guidebook to the extracellular matrix, anchor, and adhesion proteins* (Sambrook and Tooze Publications, 1999).
50. Pierre, P., Scheel, J., Rickard, J. E. & Kreis, T. E. CLIP-170 links endocytic vesicles to microtubules. *Cell* **70**, 887–900 (1992).
51. Navone, F. *et al.* Cloning and expression of a human kinesin heavy chain gene: interaction of the COOH-terminal domain with cytoplasmic microtubules in transfected CV-1 cells. *The Journal of cell biology* **117**, 1263–1275 (1992).
52. Scherer, W. F., Syverton, J. T. & Gey, G. O. Studies on the propagation in vitro of poliomyelitis viruses: IV. Viral multiplication in a stable strain of human malignant epithelial cells (strain HeLa) derived from an epidermoid carcinoma of the cervix. *The Journal of experimental medicine* **97**, 695–710 (1953).

53. Hartwell, L. H., Culotti, J. & Reid, B. Genetic control of the cell-division cycle in yeast, I. Detection of mutants. *Proceedings of the National Academy of Sciences* **66**, 352–359 (1970).
54. Conde, C. & Cáceres, A. Microtubule assembly, organization and dynamics in axons and dendrites. *Nature Reviews Neuroscience* **10**, 319–332 (May 2009).
55. Pawley, J. ( *Handbook of Biological Confocal Microscopy* 985 pp. ISBN: 038725921X. [https://www.ebook.de/de/product/5270101/handbook\\_of\\_biological\\_confocal\\_microscopy.html](https://www.ebook.de/de/product/5270101/handbook_of_biological_confocal_microscopy.html) (Springer-Verlag New York Inc., June 2, 2006).
56. Mitchison, T. & Kirschner, M. Dynamic instability of microtubule growth. *nature* **312**, 237 (1984).
57. Al-Bassam, J. & Chang, F. Regulation of microtubule dynamics by TOG-domain proteins XMAP215/Dis1 and CLASP. *Trends in cell biology* **21**, 604–614 (2011).
58. Walker, R. *et al.* Dynamic instability of individual microtubules analyzed by video light microscopy: rate constants and transition frequencies. *The Journal of cell biology* **107**, 1437–1448 (1988).
59. Brouhard, G. J. Dynamic instability 30 years later: complexities in microtubule growth and catastrophe. *Molecular biology of the cell* **26**, 1207–1210 (2015).
60. Salmon, E., Leslie, R., Saxton, W., Karow, M. & McIntosh, J. Spindle microtubule dynamics in sea urchin embryos: analysis using a fluorescein-labeled tubulin and measurements of fluorescence redistribution after laser photobleaching. *The Journal of cell biology* **99**, 2165–2174 (1984).
61. Amos, L. A., Amos, W. B. & Amos, L. *Molecules of the Cytoskeleton* (Springer, 1991).
62. Mastronarde, D. N., McDonald, K. L., Ding, R. & McIntosh, J. R. Interpolar spindle microtubules in PTK cells. *The Journal of cell biology* **123**, 1475–1489 (1993).

63. Burbank, K. S., Groen, A. C., Perlman, Z. E., Fisher, D. S. & Mitchison, T. J. A new method reveals microtubule minus ends throughout the meiotic spindle. *Journal of Cell Biology* **175**, 369–375 (Nov. 2006).
64. Gatlin, J. C. & Bloom, K. *Microtubule motors in eukaryotic spindle assembly and maintenance* in *Seminars in cell & developmental biology* **21** (2010), 248–254.
65. Ems-McClung, S. C. & Walczak, C. E. Kinesin-13s in mitosis: Key players in the spatial and temporal organization of spindle microtubules. **21**, 276–282 (2010).
66. Pearson, C. G. & Bloom, K. Dynamic microtubules lead the way for spindle positioning. *Nature reviews Molecular cell biology* **5**, 481–492 (2004).
67. Mitchison, T. & Salmon, E. Poleward kinetochore fiber movement occurs during both metaphase and anaphase-A in newt lung cell mitosis. *The Journal of Cell Biology* **119**, 569–582 (1992).
68. Tao, L. *et al.* A homotetrameric kinesin-5, KLP61F, bundles microtubules and antagonizes Ncd in motility assays. *Current Biology* **16**, 2293–2302 (2006).
69. Dogterom, M., Kerseemakers, J. W., Romet-Lemonne, G. & Janson, M. E. Force generation by dynamic microtubules. *Current opinion in cell biology* **17**, 67–74 (2005).
70. Pavin, N. & Tolic, I. M. Mechanobiology of the Mitotic Spindle. *Developmental Cell*. ISSN: 1878-1551 (Electronic) 1534-5807 (Linking). <https://www.ncbi.nlm.nih.gov/pubmed/33238148> (2020).
71. Sprague, B. L. *et al.* Mechanisms of microtubule-based kinetochore positioning in the yeast metaphase spindle. *Biophysical journal* **84**, 3529–3546 (2003).
72. Klemm, A. H., Bosilj, A., Gluncic, M., Pavin, N. & Tolic, I. M. Metaphase kinetochore movements are regulated by kinesin-8 motors and microtubule dynamic instability. *Molecular Biology of the Cell* **29**, 1332–1345 (2018).

73. Skibbens, R. V., Skeen, V. P. & Salmon, E. Directional instability of kinetochore motility during chromosome congression and segregation in mitotic newt lung cells: a push-pull mechanism. *The Journal of cell biology* **122**, 859–875 (1993).
74. Wise, D., Cassimeris, L., Rieder, C. L., Wadsworth, P. & Salmon, E. D. Chromosome fiber dynamics and congression oscillations in metaphase PtK2 cells at 23 C. *Cell motility and the cytoskeleton* **18**, 131–142 (1991).
75. Civelekoglu-Scholey, G. *et al.* Dynamic bonds and polar ejection force distribution explain kinetochore oscillations in PtK1 cells. *Journal of Cell Biology* **201**, 577–593 (2013).
76. Tran, P., Marsh, L., Doye, V., Inoue, S. & Chang, F. A mechanism for nuclear positioning in fission yeast based on microtubule pushing. *The Journal of cell biology* **153**, 397–412 (2001).
77. Hays, T. S. *The force-balance mechanism of chromosome congression* PhD thesis (University of North Carolina at Chapel Hill, 1985).
78. INOUÉ, S. in *Collected Works Of Shinya InouÉ: Microscopes, Living Cells, and Dynamic Molecules (With DVD-ROM)* 89–102 (World Scientific, 2008).
79. Inoué, S., Fuseler, J., Salmon, E. D. & Ellis, G. W. Functional organization of mitotic microtubules. Physical chemistry of the in vivo equilibrium system. *Biophysical journal* **15**, 725–744 (1975).
80. Inoué, S. & Sato, H. Cell motility by labile association of molecules: the nature of mitotic spindle fibers and their role in chromosome movement. *The Journal of general physiology* **50**, 259–292 (1967).
81. Itabashi, T. *et al.* Probing the mechanical architecture of the vertebrate meiotic spindle. *Nature methods* **6**, 167–172 (2009).

82. Salmon, E. Pressure-induced depolymerization of spindle microtubules. I. Changes in birefringence and spindle length. *The Journal of cell biology* **65**, 603–614 (1975).
83. Flemming, W. *Zellsubstanz, kern und zelltheilung* (Vogel, 1882).
84. Inoue, S. & Sato, H. The nature of mitotic spindle fibers and their role in chromosome movement. *J. gen. Physiol* **50**, 259 (1967).
85. Borisy, G. G. & Taylor, E. W. The Mechanism of Action of Colchicine. *Journal of Cell Biology* **34**, 525–533 (Aug. 1967).
86. Sharp, D. J., Rogers, G. C. & Scholey, J. M. Microtubule motors in mitosis. *Nature* **407**, 41–47 (2000).
87. Manning, A. L. & Compton, D. A. Structural and regulatory roles of nonmotor spindle proteins. *Current Opinion in Cell Biology* **20**, 101–106 (Feb. 2008).
88. Cheerambathur, D. K. & Desai, A. Linked in: formation and regulation of microtubule attachments during chromosome segregation. *Current opinion in cell biology* **26**, 113–122 (2014).
89. Novak, M. *The role of bridging microtubules in the force balance of mitotic spindle* (Doctoral thesis) Doctoral thesis (2017).
90. Chang, P., Jacobson, M. K. & Mitchison, T. J. Poly (ADP-ribose) is required for spindle assembly and structure. *Nature* **432**, 645–649 (2004).
91. Blower, M. D., Feric, E., Weis, K. & Heald, R. Genome-wide analysis demonstrates conserved localization of messenger RNAs to mitotic microtubules. *The Journal of cell biology* **179**, 1365–1373 (2007).
92. Inoué, S. & Salmon, E. D. Force generation by microtubule assembly/disassembly in mitosis and related movements. *Collected Works Of Shinya Inoué: Microscopes, Living Cells, and Dynamic Molecules*, 749–770 (2008).

93. Nicklas, R. B. Measurements of the force produced by the mitotic spindle in anaphase. *The Journal of cell biology* **97**, 542–548 (1983).
94. Nicklas, R. B. & Koch, C. A. CHROMOSOME MICROMANIPULATION: III. Spindle Fiber Tension and the Reorientation of Mal-Oriented Chromosomes. *The Journal of cell biology* **43**, 40–50 (1969).
95. Nicklas, R. B. & Ward, S. C. Elements of error correction in mitosis: microtubule capture, release, and tension. *The Journal of cell biology* **126**, 1241–1253 (1994).
96. Li, X. & Nicklas, R. B. Mitotic forces control a cell-cycle checkpoint. *Nature* **373**, 630–632 (1995).
97. Tolić-Nørrelykke, I. M. Push-me-pull-you: how microtubules organize the cell interior. *European biophysics journal* **37**, 1271–1278 (2008).
98. Manneville, J.-B. & Etienne-Manneville, S. Positioning centrosomes and spindle poles: looking at the periphery to find the centre. *Biology of the Cell* **98**, 557–565 (2006).
99. Grill, S. W. & Hyman, A. A. Spindle positioning by cortical pulling forces. *Developmental cell* **8**, 461–465 (2005).
100. Kapoor, T. M. & Compton, D. A. Searching for the middle ground: mechanisms of chromosome alignment during mitosis. *The Journal of cell biology* **157**, 551 (2002).
101. Conway, W. *et al.* Self-organization of kinetochore-fibers in human mitotic spindles. *eLife* **11** (July 2022).
102. McEwen, B. F. *et al.* CENP-E is essential for reliable bioriented spindle attachment, but chromosome alignment can be achieved via redundant mechanisms in mammalian cells. *Molecular biology of the cell* **12**, 2776–2789 (2001).
103. Begg, D. A. & Ellis, G. W. Micromanipulation studies of chromosome movement. I. Chromosome-spindle attachment and the mechanical properties of chromosomal spindle fibers. *The Journal of cell biology* **82**, 528–541 (1979).



104. McDonald, K. L., O'toole, E. T., Mastronarde, D. N. & McIntosh, J. R. Kinetochore microtubules in PTK cells. *The Journal of cell biology* **118**, 369–383 (1992).
105. Kiewisz, R. *et al.* Three-dimensional structure of kinetochore-fibers in human mitotic spindles. *Elife* **11**, e75459 (2022).
106. O'Toole, E., Morphew, M. & McIntosh, J. R. Electron tomography reveals aspects of spindle structure important for mechanical stability at metaphase. *Molecular Biology of the Cell* **31**, 184–195 (2020).
107. Oriola, D., Jülicher, F. & Brugués, J. Active forces shape the metaphase spindle through a mechanical instability. *Proceedings of the National Academy of Sciences* **117**, 16154–16159 (2020).
108. McEwen, B. F., Ding, Y. & Heagle, A. B. *Chromosome Research* **6**, 123–132 (1998).
109. Dudka, D. *et al.* Complete microtubule-kinetochore occupancy favours the segregation of merotelic attachments. *Nature Communications* **9**, 2042. ISSN: 2041-1723. <https://doi.org/10.1038/s41467-018-04427-x> (2018).
110. Nicklas, R. B., Kubai, D. F. & Hays, T. S. Spindle microtubules and their mechanical associations after micromanipulation in anaphase. *Journal of Cell Biology* **95**, 91–104 (Oct. 1982).
111. Nicklas, R. B. & Staehly, C. A. Chromosome micromanipulation. *Chromosoma* **21**, 1–16 (1967).
112. Hayden, J. H., Bowser, S. S. & Rieder, C. L. Kinetochores capture astral microtubules during chromosome attachment to the mitotic spindle: direct visualization in live newt lung cells. *Journal of Cell Biology* **111**, 1039–1045 (Sept. 1990).
113. Maiato, H., Rieder, C. L. & Khodjakov, A. Kinetochore-driven formation of kinetochore fibers contributes to spindle assembly during animal mitosis. *Journal of Cell Biology* **167**, 831–840 (Nov. 2004).

114. Zhai, Y., Kronebusch, P. J. & Borisy, G. G. Kinetochore microtubule dynamics and the metaphase-anaphase transition. *Journal of Cell Biology* **131**, 721–734 (Nov. 1995).
115. Mitchison, T. J. Polewards microtubule flux in the mitotic spindle: evidence from photoactivation of fluorescence. *Journal of Cell Biology* **109**, 637–652 (Aug. 1989).
116. Cameron, L. A. *et al.* Kinesin 5-independent poleward flux of kinetochore microtubules in PtK1 cells. *The Journal of cell biology* **173**, 173–179 (2006).
117. Heald, R. *et al.* Self-organization of microtubules into bipolar spindles around artificial chromosomes in *Xenopus* egg extracts. *Nature* **382**, 420–425 (Aug. 1996).
118. Mahoney, N. M., Goshima, G., Douglass, A. D. & Vale, R. D. Making Microtubules and Mitotic Spindles in Cells without Functional Centrosomes. *Current Biology* **16**, 564–569 (Mar. 2006).
119. Saxton, W. M. *et al.* Tubulin dynamics in cultured mammalian cells. *Journal of Cell Biology* **99**, 2175–2186 (Dec. 1984).
120. Yang, G. *et al.* Architectural dynamics of the meiotic spindle revealed by single-fluorophore imaging. *Nature Cell Biology* **9**, 1233–1242 (Oct. 2007).
121. Burbank, K. S., Mitchison, T. J. & Fisher, D. S. Slide-and-cluster models for spindle assembly. *Current Biology* **17**, 1373–1383 (2007).
122. Grill, S. W., Howard, J., Schäffer, E., Stelzer, E. H. K. & Hyman, A. A. The Distribution of Active Force Generators Controls Mitotic Spindle Position. *Science* **301**, 518–521 (July 2003).
123. O’Toole, E. T. *et al.* Morphologically distinct microtubule ends in the mitotic centrosome of *Caenorhabditis elegans*. *Journal of Cell Biology* **163**, 451–456 (Nov. 2003).
124. Rusan, N. M., Fagerstrom, C. J., Yvon, A.-M. C. & Wadsworth, P. Cell Cycle-Dependent Changes in Microtubule Dynamics in Living Cells Expressing Green Fluorescent Protein- $\alpha$  Tubulin. *Molecular Biology of the Cell* **12** (ed Salmon, T.) 971–980 (Apr. 2001).

125. Waterman-Storer, C. M., Desai, A., Bulinski, J. C. & Salmon, E. Fluorescent speckle microscopy, a method to visualize the dynamics of protein assemblies in living cells. *Current Biology* **8**, 1227–S1 (Nov. 1998).
126. Brust-Mascher, I., Sommi, P., Cheerambathur, D. K. & Scholey, J. M. Kinesin-5–dependent Poleward Flux and Spindle Length Control in *Drosophila* Embryo Mitosis. *Molecular biology of the cell* **20**, 1749–1762 (2009).
127. Saunders, A. M., Powers, J., Strome, S. & Saxton, W. M. Kinesin-5 acts as a brake in anaphase spindle elongation. *Current Biology* **17**, R453–R454 (2007).
128. Bloom, K. S. Beyond the code: the mechanical properties of DNA as they relate to mitosis. *Chromosoma* **117**, 103–110 (2008).
129. Howard, J. & Hyman, A. A. Microtubule polymerases and depolymerases. *Current opinion in cell biology* **19**, 31–35 (2007).
130. Maiato, H., DeLuca, J., Salmon, E. & Earnshaw, W. C. The dynamic kinetochore–microtubule interface. *Journal of cell science* **117**, 5461–5477 (2004).
131. Tanaka, T. U. & Desai, A. Kinetochore–microtubule interactions: the means to the end. *Current opinion in cell biology* **20**, 53–63 (2008).
132. Compton, D. A. Focusing on spindle poles. *Journal of cell science* **111**, 1477–1481 (1998).
133. Rogers, G. C. *et al.* Two mitotic kinesins cooperate to drive sister chromatid separation during anaphase. *Nature* **427**, 364–370 (2004).
134. Waters, J. C., Mitchison, T. J., Rieder, C. L. & Salmon, E. The kinetochore microtubule minus-end disassembly associated with poleward flux produces a force that can do work. *Molecular Biology of the Cell* **7**, 1547–1558 (1996).

135. Levesque, A. A. & Compton, D. A. The chromokinesin Kid is necessary for chromosome arm orientation and oscillation, but not congression, on mitotic spindles. *The Journal of cell biology* **154**, 1135–1146 (2001).
136. Rieder, C. L., Davison, E. A., Jensen, L., Cassimeris, L. & Salmon, E. D. Oscillatory movements of monooriented chromosomes and their position relative to the spindle pole result from the ejection properties of the aster and half-spindle. *The Journal of cell biology* **103**, 581–591 (1986).
137. O’Connell, C. B. & Wang, Y.-l. Mammalian spindle orientation and position respond to changes in cell shape in a dynein-dependent fashion. *Molecular biology of the cell* **11**, 1765–1774 (2000).
138. Matos, I. *et al.* Synchronizing chromosome segregation by flux-dependent force equalization at kinetochores. *Journal of Cell Biology* **186**, 11–26 (July 2009).
139. Pereira, A. J. & Maiato, H. Maturation of the kinetochore-microtubule interface and the meaning of metaphase. *Chromosome Research* **20**, 563–577 (July 2012).
140. McIntosh, J. R., Hepler, P. K. & Wie, D. G. V. Model for Mitosis. *Nature* **224**, 659–663 (Nov. 1969).
141. Goode, D. Microtubule turnover as a mechanism of mitosis and its possible evolution. *Biosystems* **14**, 271–287 (Jan. 1981).
142. Margolis, R. L., WILSON, L. & KIEFER, B. I. Mitotic mechanism based on intrinsic microtubule behaviour. *Nature* **272**, 450–452 (Mar. 1978).
143. Tolic, I. M. & Pavin, N. Bridging the gap between sister kinetochores. *Cell Cycle* **15**, 1169–1170. ISSN: 1538-4101. %3CGo%20to%20ISI%3E://WOS:000378725300001 (2016).
144. Milas, A. & Tolić, I. Relaxation of interkinetochore tension after severing of a k-fiber depends on the length of the k-fiber stub. *Matters Select* (Mar. 2016).

145. Elting, M. W., Hueschen, C. L., Udy, D. B. & Dumont, S. Force on spindle microtubule minus ends moves chromosomes. *Journal of Cell Biology* **206**, 245–256 (July 2014).
146. Sikirzhytski, V. *et al.* Direct kinetochore-spindle pole connections are not required for chromosome segregation. *Journal of Cell Biology* **206**, 231–243 (July 2014).
147. Walczak, C. E., Cai, S. & Khodjakov, A. Mechanisms of chromosome behaviour during mitosis. *Nature Reviews Molecular Cell Biology* **11**, 91–102 (Jan. 2010).
148. Barisic, M., Aguiar, P., Geley, S. & Maiato, H. Kinetochore motors drive congression of peripheral polar chromosomes by overcoming random arm-ejection forces. *Nature Cell Biology* **16**, 1249–1256 (Nov. 2014).
149. Cai, S., O’Connell, C. B., Khodjakov, A. & Walczak, C. E. Chromosome congression in the absence of kinetochore fibres. *Nature Cell Biology* **11**, 832–838 (June 2009).
150. Magidson, V. *et al.* The Spatial Arrangement of Chromosomes during Prometaphase Facilitates Spindle Assembly. *Cell* **146**, 555–567 (Aug. 2011).
151. Paul, R. *et al.* Computer simulations predict that chromosome movements and rotations accelerate mitotic spindle assembly without compromising accuracy. *Proceedings of the National Academy of Sciences* **106**, 15708–15713 (Sept. 2009).
152. Jensen, C. G. Dynamics of spindle microtubule organization: kinetochore fiber microtubules of plant endosperm. *Journal of Cell Biology* **92**, 540–558 (Feb. 1982).
153. Rubinstein, B., Larripa, K., Sommi, P. & Mogilner, A. The elasticity of motor-microtubule bundles and shape of the mitotic spindle. *Physical biology* **6**, 016005–016005. ISSN: 1478-3975 1478-3967. <https://pubmed.ncbi.nlm.nih.gov/19193975/><https://www.ncbi.nlm.nih.gov/pmc/articles/PMC2723726/> (2009).
154. L. D. Landau, E. M. L. *Theory of Elasticity* 7 195 pp. ISBN: 075062633X. [https://www.ebook.de/de/product/3240398/1\\_d\\_landau\\_e\\_m\\_lifshitz\\_theory\\_of\\_elasticity\\_7.html](https://www.ebook.de/de/product/3240398/1_d_landau_e_m_lifshitz_theory_of_elasticity_7.html) (Elsevier LTD, Oxford, Jan. 11, 2004).

155. Loughlin, R., Heald, R. & Nédélec, F. A computational model predicts *Xenopus* meiotic spindle organization. *Journal of Cell Biology* **191**, 1239–1249 (Dec. 2010).
156. Brugués, J. & Needleman, D. Physical basis of spindle self-organization. *Proceedings of the National Academy of Sciences* **111**, 18496–18500 (Dec. 2014).
157. Brugués, J., Nuzzo, V., Mazur, E. & Needleman, D. J. Nucleation and Transport Organize Microtubules in Metaphase Spindles. *Cell* **149**, 554–564 (Apr. 2012).
158. Wollman, R., Civelekoglu-Scholey, G., Scholey, J. M. & Mogilner, A. Reverse engineering of force integration during mitosis in the *Drosophila* embryo. *Molecular Systems Biology* **4**, 195 (Jan. 2008).
159. Sawin, K. E. & Mitchison, T. J. Poleward microtubule flux mitotic spindles assembled in vitro. *The Journal of cell biology* **112**, 941–954 (1991).
160. Miyamoto, D. T., Perlman, Z. E., Burbank, K. S., Groen, A. C. & Mitchison, T. J. The kinesin Eg5 drives poleward microtubule flux in *Xenopus laevis* egg extract spindles. *The Journal of cell biology* **167**, 813–818 (2004).
161. Goshima, G., Wollman, R., Stuurman, N., Scholey, J. M. & Vale, R. D. Length control of the metaphase spindle. *Current Biology* **15**, 1979–1988 (2005).
162. Brinkley, B. Microtubule organizing centers. *Annual review of cell biology* **1**, 145–172 (1985).
163. Rogers, G. C., Rogers, S. L. & Sharp, D. J. Spindle microtubules in flux. *Journal of Cell Science* **118**, 1105–1116 (2005).
164. Sawin, K. E., LeGuellec, K., Philippe, M. & Mitchison, T. J. Mitotic spindle organization by a plus-end-directed microtubule motor. *Nature* **359**, 540–543 (Oct. 1992).
165. Höök, P. & Vallee, R. B. The dynein family at a glance. *Journal of cell science* **119**, 4369–4371 (2006).

166. McDonald, H. B., Stewart, R. J. & Goldstein, L. S. The kinesin-like ncd protein of *Drosophila* is a minus end-directed microtubule motor. *Cell* **63**, 1159–1165 (1990).
167. Sharp, D. J., Rogers, G. C. & Scholey, J. M. Roles of motor proteins in building microtubule-based structures: a basic principle of cellular design. *Biochimica et Biophysica Acta (BBA)-Molecular Cell Research* **1496**, 128–141 (2000).
168. Kapitein, L. C. *et al.* The bipolar mitotic kinesin Eg5 moves on both microtubules that it crosslinks. *Nature* **435**, 114–118 (2005).
169. Goshima, G., Nédélec, F. & Vale, R. D. Mechanisms for focusing mitotic spindle poles by minus end-directed motor proteins. *The Journal of cell biology* **171**, 229–240 (2005).
170. Nédélec, F. Computer simulations reveal motor properties generating stable antiparallel microtubule interactions. *The Journal of cell biology* **158**, 1005–1015 (2002).
171. Gatlin, J. C. *et al.* Spindle fusion requires dynein-mediated sliding of oppositely oriented microtubules. *Current Biology* **19**, 287–296 (2009).
172. Tirnauer, J. S., Salmon, E. D. & Mitchison, T. J. Microtubule plus-end dynamics in *Xenopus* egg extract spindles. *Molecular biology of the cell* **15**, 1776–1784 (2004).
173. Needleman, D. & Bruges, J. Determining physical principles of subcellular organization. *Developmental cell* **29**, 135–138 (2014).
174. Mickey, B. & Howard, J. Rigidity of microtubules is increased by stabilizing agents. *The Journal of cell biology* **130**, 909–917 (1995).
175. Odde, D. J., Ma, L., Briggs, A. H., DeMarco, A. & Kirschner, M. W. Microtubule bending and breaking in living fibroblast cells. *Journal of cell science* **112**, 3283–3288 (1999).
176. Rieder, C. L. Formation of the astral mitotic spindle: ultrastructural basis for the centrosome-kinetochore interaction. *Electron microscopy reviews* **3**, 269–300 (1990).

177. Claessens, M. M., Bathe, M., Frey, E. & Bausch, A. R. Actin-binding proteins sensitively mediate F-actin bundle stiffness. *Nature materials* **5**, 748–753 (2006).
178. Tolic, I. M., Novak, M. & Pavin, N. Helical Twist and Rotational Forces in the Mitotic Spindle. *Biomolecules* **9**. ISSN: 2218-273x. %3CGo%20to%20ISI%3E : // WOS : 000467318400015 (2019).
179. Polak, B., Risteski, P., Lesjak, S. & Tolić, I. M. PRC1-labeled microtubule bundles and kinetochore pairs show one-to-one association in metaphase. *EMBO reports* **18**, 217–230 (Dec. 2016).
180. Vale, R. D. & Toyoshima, Y. Y. Rotation and translocation of microtubules in vitro induced by dyneins from *Tetrahymena* cilia. *Cell* **52**, 459–469 (Feb. 1988).
181. Mitra, A., Ruhnaw, F., Girardo, S. & Diez, S. Directionally biased sidestepping of Kip3/kinesin-8 is regulated by ATP waiting time and motor–microtubule interaction strength. *Proceedings of the National Academy of Sciences* **115**, E7950–E7959 (2018).
182. Mitra, A. *et al.* Kinesin-14 motors drive a right-handed helical motion of antiparallel microtubules around each other. *Nature communications* **11**, 1–11 (2020).
183. Walker, R. A., Salmon, E. D. & Endow, S. A. The *Drosophila* claret segregation protein is a minus-end directed motor molecule. *Nature* **347**, 780–782 (Oct. 1990).
184. Yajima, J., Mizutani, K. & Nishizaka, T. A torque component present in mitotic kinesin Eg5 revealed by three-dimensional tracking. *Nature structural & molecular biology* **15**, 1119–1121. ISSN: 1545-9985 (2008).
185. Yajima, J. & Cross, R. A. A torque component in the kinesin-1 power stroke. *Nature chemical biology* **1**, 338–341 (2005).
186. Brunnbauer, M. *et al.* Torque generation of kinesin motors is governed by the stability of the neck domain. *Molecular cell* **46**, 147–158 (2012).



187. Bormuth, V. *et al.* The highly processive kinesin-8, Kip3, switches microtubule protofilaments with a bias toward the left. *Biophysical journal* **103**, L4–L6. ISSN: 0006-3495 (2012).
188. Can, S., Dewitt, M. A. & Yildiz, A. Bidirectional helical motility of cytoplasmic dynein around microtubules. *E-life* **3**, e03205. ISSN: 2050-084X (2014).
189. Bugiel, M., Böhl, E. & Schäffer, E. The Kinesin-8 Kip3 switches protofilaments in a sideward random walk asymmetrically biased by force. *Biophysical journal* **108**, 2019–2027 (2015).
190. Ramaiya, A., Roy, B., Bugiel, M. & Schäffer, E. Kinesin rotates unidirectionally and generates torque while walking on microtubules. *Proceedings of the National Academy of Sciences* **114**, 10894–10899. ISSN: 0027-8424 (2017).
191. Maruyama, Y. *et al.* CYK4 relaxes the bias in the off-axis motion by MKLP1 kinesin-6. *Communications biology* **4**, 1–15 (2021).
192. Hagan, I. & Yanagida, M. Novel potential mitotic motor protein encoded by the fission yeast cut7 gene. *Nature* **347**, 563–566 (Oct. 1990).
193. Gayek, A. S. & Ohi, R. Kinetochores-microtubule stability governs the metaphase requirement for Eg5. *Molecular Biology of the Cell* **25** (ed Bloom, K. S.) 2051–2060 (July 2014).
194. Ding, R., McDonald, K. L. & McIntosh, J. R. Three-dimensional reconstruction and analysis of mitotic spindles from the yeast, *Schizosaccharomyces pombe*. *The Journal of cell biology* **120**, 141–151 (1993).
195. Winey, M. *et al.* Three-dimensional ultrastructural analysis of the *Saccharomyces cerevisiae* mitotic spindle. *The Journal of cell biology* **129**, 1601–1615 (1995).

196. Nitzsche, B. *et al.* Working stroke of the kinesin-14, *ncd*, comprises two substeps of different direction. *Proceedings of the National Academy of Sciences* **113**, E6582–E6589 (2016).
197. Neahring, L., Cho, N. H. & Dumont, S. Opposing motors provide mechanical and functional robustness in the human spindle. *Developmental Cell* **56**, 3006–3018.e5 (Nov. 2021).
198. Nicklas, R. B. Measurements of the force produced by the mitotic spindle in anaphase. *J Cell Biol* **97**, 542–8. ISSN: 0021-9525 (Print) 0021-9525 (Linking). <https://www.ncbi.nlm.nih.gov/pubmed/6885908> (1983).
199. Dogterom, M. & Yurke, B. Measurement of the force-velocity relation for growing microtubules. *Science* **278**, 856–860. ISSN: 0036-8075 (1997).
200. Gittes, F., Mickey, B., Nettleton, J. & Howard, J. Flexural rigidity of microtubules and actin filaments measured from thermal fluctuations in shape. *J Cell Biol* **120**, 923–934. ISSN: 0021-9525 (1993).
201. Smith, M. B. *et al.* Segmentation and tracking of cytoskeletal filaments using open active contours. *Cytoskeleton* **67**, 693–705. ISSN: 1949-3584 (2010).
202. Xu, T., Vavylonis, D. & Huang, X. 3D actin network centerline extraction with multiple active contours. *Medical image analysis* **18**, 272–284. ISSN: 1361-8415 (2014).
203. Xu, T. *et al.* SOAX: a software for quantification of 3D biopolymer networks. *Scientific reports* **5**, 1–10. ISSN: 2045-2322 (2015).
204. Jikeli, J. F. *et al.* Sperm navigation along helical paths in 3D chemoattractant landscapes. *Nature Communications* **6**, 7985. ISSN: 2041-1723 (Electronic) 2041-1723 (Linking). <https://www.ncbi.nlm.nih.gov/pubmed/26278469> (2015).
205. Frenet, F. Sur les courbes a double courbure. *Journal de mathématiques pures et appliquées*, 437–447 (1852).

206. Crowder, M. E. *et al.* A comparative analysis of spindle morphometrics across metazoans. *Current Biology* **25**, 1542–1550. ISSN: 0960-9822 (2015).
207. Walsh, C. J. The structure of the mitotic spindle and nucleolus during mitosis in the amebo-flagellate *Naegleria*. *PloS one* **7**, e34763. ISSN: 1932-6203 (2012).
208. Zhang, H. & Dawe, R. K. Mechanisms of plant spindle formation. *Chromosome Research* **19**, 335–344. ISSN: 0967-3849 (2011).
209. McCully, E. K. & Robinow, C. F. Mitosis in the fission yeast *Schizosaccharomyces pombe*: a comparative study with light and electron microscopy. *Journal of cell science* **9**, 475–507. ISSN: 0021-9533 (1971).
210. Rodrigues, O. Des lois geometriques qui regissent les desplacements d’un systeme solide dans l’espace et de la variation des coordonnees provenant de deplacements consideres independamment des causes qui peuvent les produire. *J Mathematiques Pures Appliquees* **5**, 380–440 (1840).
211. Golub, G. H. & Reinsch, C. in *Linear Algebra* 134–151 (Springer, 1971).
212. Kanatani, K. & Rangarajan, P. Hyper least squares fitting of circles and ellipses. *Computational Statistics & Data Analysis* **55**, 2197–2208. ISSN: 0167-9473. %3CGo%20to%20ISI%3E://WOS:000289015500014 (2011).
213. Taubin, G. Estimation of Planar Curves, Surfaces, and Nonplanar Space Curves Defined by Implicit Equations with Applications to Edge and Range Image Segmentation. *IEEE Trans. Pattern Anal. Mach. Intell.* **13**, 1115–1138. ISSN: 0162-8828. <https://doi.org/10.1109/34.103273> (1991).
214. Friedrich, B. frenet\_robust. *MATLAB Central File Exchange*. [https://www.mathworks.com/matlabcentral/fileexchange/47885-frenet\\_robust-zip](https://www.mathworks.com/matlabcentral/fileexchange/47885-frenet_robust-zip) (2021).
215. Friedrich, B. powersmooth. *MATLAB Central File Exchange*. <https://www.mathworks.com/matlabcentral/fileexchange/48799-powersmooth> (2021).

216. Kuzmic, B. *The mitotic spindle is chiral due to torques within microtubule bundles* 2018.
217. Liu, X. & Winey, M. The MPS1 family of protein kinases. *Annual review of biochemistry* **81**, 561 (2012).
218. Nurse, P. A long twentieth century of the cell cycle and beyond. *Cell* **100**, 71–78 (2000).
219. Raff, E. C. Genetics of microtubule systems. *The Journal of cell biology* **99**, 1–10 (1984).
220. Vemu, A., Atherton, J., Spector, J. O., Moores, C. A. & Roll-Mecak, A. Tubulin isoform composition tunes microtubule dynamics. *Molecular biology of the cell* **28**, 3564–3572 (2017).
221. Johnson, K. A. The axonemal microtubules of the Chlamydomonas flagellum differ in tubulin isoform content. *Journal of cell science* **111**, 313–320 (1998).
222. Matthews, K. A., Rees, D. & Kaufman, T. C. A functionally specialized  $\alpha$ -tubulin is required for oocyte meiosis and cleavage mitoses in Drosophila. *Development* **117**, 977–991 (1993).
223. Hoyle, H. D. & Raff, E. C. Two Drosophila beta tubulin isoforms are not functionally equivalent. *The Journal of cell biology* **111**, 1009–1026 (1990).
224. Savage, C. *et al.* mec-7 is a beta-tubulin gene required for the production of 15-protofilament microtubules in Caenorhabditis elegans. *Genes & development* **3**, 870–881 (1989).
225. Wilson, P. G. & Borisy, G. G. Evolution of the multi-tubulin hypothesis. *Bioessays* **19**, 451–454 (1997).
226. Fulton, C. & Simpson, P. A. Selective synthesis and utilization of flagellar tubulin. The multi-tubulin hypothesis. *Cell motility* **3**, 987–1005 (1976).

227. Fulton, C. Amebo-flagellates as research partners: the laboratory biology of Naegleria and Tetramitus. *Methods Cell Physiol* **4**, 341–476 (1970).
228. Fritz-Laylin, L. K., Assaf, Z. J., Chen, S. & Cande, W. Z. Naegleria gruberi de novo basal body assembly occurs via stepwise incorporation of conserved proteins. *Eukaryotic cell* **9**, 860–865 (2010).
229. FULTON, C. Naegleria: A Research Partner For Cell and Developmental Biology 1. *Journal of Eukaryotic Microbiology* **40**, 520–532 (1993).
230. Lee, J. & Walsh, C. J. Transcriptional regulation of coordinate changes in flagellar mRNAs during differentiation of Naegleria gruberi amebae into flagellates. *Molecular and cellular biology* **8**, 2280–2287 (1988).
231. Chung, S., Cho, J., Cheon, H., Paik, S. & Lee, J. Cloning and characterization of a divergent  $\alpha$ -tubulin that is expressed specifically in dividing amebae of Naegleria gruberi. *Gene* **293**, 77–86 (2002).
232. Walsh, C. J. The role of actin, actomyosin and microtubules in defining cell shape during the differentiation of Naegleria amebae into flagellates. *European journal of cell biology* **86**, 85–98 (2007).
233. Fulton, C. & Dingle, A. D. Basal bodies, but not centrioles, in Naegleria. *The Journal of cell biology* **51**, 826–836 (1971).
234. Inoué, S. Mitotic organization and force generation by assembly/disassembly of microtubules. *Cell structure and function* **21**, 375–379 (1996).
235. Yu, C.-H. *et al.* Central-spindle microtubules are strongly coupled to chromosomes during both anaphase A and anaphase B. *Molecular biology of the cell* **30**, 2503–2514 (2019).
236. Asbury, C. L. Anaphase A: disassembling microtubules move chromosomes toward spindle poles. *Biology* **6**, 15 (2017).

237. Vukušić, K., Ponjavić, I., Buđa, R., Risteski, P. & Tolić, I. M. Microtubule-sliding modules based on kinesins EG5 and PRC1-dependent KIF4A drive human spindle elongation. *Developmental Cell* **56**, 1253–1267.e10 (May 2021).
238. Jagrić, M., Risteski, P., Martinčić, J., Milas, A. & Tolić, I. M. Optogenetic control of PRC1 reveals its role in chromosome alignment on the spindle by overlap length-dependent forces. *Elife* **10**, e61170 (2021).
239. Vukušić, K., Ponjavić, I., Buđa, R., Risteski, P. & Tolić, I. M. Microtubule-sliding modules based on kinesins EG5 and PRC1-dependent KIF4A drive human spindle elongation. *Developmental cell* **56**, 1253–1267 (2021).
240. Drechsler, H. & McAinsh, A. D. Exotic mitotic mechanisms. *Open biology* **2**, 120140 (2012).
241. Sazer, S., Lynch, M. & Needleman, D. Deciphering the evolutionary history of open and closed mitosis. *Current Biology* **24**, R1099–R1103 (2014).
242. Pickett-Heaps, J. D. The evolution of the mitotic apparatus: an attempt at comparative ultrastructural cytology in dividing plant cells. *Cytobios* **1**, 257–280 (1969).
243. Lüders, J. & Stearns, T. Microtubule-organizing centres: a re-evaluation. *Nature Reviews Molecular Cell Biology* **8**, 161–167 (2007).
244. Ito, D. & Bettencourt-Dias, M. Centrosome remodelling in evolution. *Cells* **7**, 71 (2018).
245. Heath, I. B. Variant mitoses in lower eukaryotes: indicators of the evolution of mitosis? *International review of cytology* **64**, 1–80 (1980).
246. Dumont, J., Oegema, K. & Desai, A. A kinetochore-independent mechanism drives anaphase chromosome separation during acentrosomal meiosis. *Nature cell biology* **12**, 894–901 (2010).

247. Schuster, F. L. Ultrastructure of mitosis in the amoebflagellate *Naegleria gruberi*. *Tissue and Cell* **7**, 1–11 (1975).
248. Akiyoshi, B. & Gull, K. Discovery of unconventional kinetochores in kinetoplastids. *Cell* **156**, 1247–1258 (2014).
249. D’Archivio, S. & Wickstead, B. Trypanosome outer kinetochore proteins suggest conservation of chromosome segregation machinery across eukaryotes. *Journal of Cell Biology* **216**, 379–391 (2017).
250. Drinnenberg, I. A. & Akiyoshi, B. Evolutionary lessons from species with unique kinetochores. *Centromeres and Kinetochores*, 111–138 (2017).
251. Van Hooff, J. J., Tromer, E., van Wijk, L. M., Snel, B. & Kops, G. J. Evolutionary dynamics of the kinetochore network in eukaryotes as revealed by comparative genomics. *EMBO reports* **18**, 1559–1571 (2017).
252. Štimac, V., Koprivec, I., Manenica, M., Simunić, J. & Tolić, I. M. Augmin prevents merotelic attachments by promoting proper arrangement of bridging and kinetochore fibers. *bioRxiv*, 2020–09 (2022).
253. Fritz-Laylin, L. K. *et al.* The genome of *Naegleria gruberi* illuminates early eukaryotic versatility. *Cell* **140**, 631–642 (2010).
254. Fritz-Laylin, L. K. & Cande, W. Z. Ancestral centriole and flagella proteins identified by analysis of *Naegleria* differentiation. *Journal of cell science* **123**, 4024–4031 (2010).
255. Siddiqui, R., Ali, I. K. M., Cope, J. R. & Khan, N. A. Biology and pathogenesis of *Naegleria fowleri*. *Acta tropica* **164**, 375–394 (2016).
256. Stumpff, J., Von Dassow, G., Wagenbach, M., Asbury, C. & Wordeman, L. The kinesin-8 motor Kif18A suppresses kinetochore movements to control mitotic chromosome alignment. *Developmental cell* **14**, 252–262 (2008).

257. Uehara, R. *et al.* The augmin complex plays a critical role in spindle microtubule generation for mitotic progression and cytokinesis in human cells. *Proceedings of the National Academy of Sciences* **106**, 6998–7003 (2009).
258. Zhu, C. *et al.* Functional analysis of human microtubule-based motor proteins, the kinesins and dyneins, in mitosis/cytokinesis using RNA interference. *Molecular biology of the cell* **16**, 3187–3199 (2005).
259. Skoufias, D. A. *et al.* S-trityl-L-cysteine is a reversible, tight binding inhibitor of the human kinesin Eg5 that specifically blocks mitotic progression. *Journal of biological chemistry* **281**, 17559–17569 (2006).
260. Jiang, W. *et al.* PRC1: a human mitotic spindle-associated CDK substrate protein required for cytokinesis. *Molecular cell* **2**, 877–885 (1998).
261. David, A. F. *et al.* Augmin accumulation on long-lived microtubules drives amplification and kinetochore-directed growth. *Journal of Cell Biology* **218**, 2150–2168 (2019).
262. Mann, B. & Wadsworth, P. Distribution of Eg5 and TPX2 in mitosis: Insight from CRISPR tagged cells. *Cytoskeleton* **75**, 508–521 (2018).
263. Valentine, M. T., Fordyce, P. M. & Block, S. M. Eg5 steps it up! *Cell Division* **1**, 1–8 (2006).
264. Walczak, C. E., Vernos, I., Mitchison, T. J., Karsenti, E. & Heald, R. A model for the proposed roles of different microtubule-based motor proteins in establishing spindle bipolarity. *Current biology* **8**, 903–913 (1998).
265. Goshima, G., Mayer, M., Zhang, N., Stuurman, N. & Vale, R. D. Augmin: a protein complex required for centrosome-independent microtubule generation within the spindle. *The Journal of cell biology* **181**, 421–429 (2008).
266. Kamasaki, T. *et al.* Augmin-dependent microtubule nucleation at microtubule walls in the spindle. *Journal of Cell Biology* **202**, 25–33 (2013).



267. Petry, S., Groen, A. C., Ishihara, K., Mitchison, T. J. & Vale, R. D. Branching microtubule nucleation in *Xenopus* egg extracts mediated by augmin and TPX2. *Cell* **152**, 768–777 (2013).
268. Amos, L. A. & Hirose, K. in *Methods in Molecular Medicine*<sup>TM</sup> 65–91 (Humana Press, 2007).
269. Sept, D., Baker, N. A. & McCammon, J. A. The physical basis of microtubule structure and stability. *Protein Science* **12**, 2257–2261 (2003).
270. Thitamadee, S., Tuchiara, K. & Hashimoto, T. Microtubule basis for left-handed helical growth in *Arabidopsis*. *Nature* **417**, 193–196 (2002).
271. Furutani, I. *et al.* The SPIRAL genes are required for directional control of cell elongation in *Arabidopsis thaliana*. *Development* **127**, 4443–4453 (Oct. 2000).
272. Echenique, P. & Alonso, J. L. A mathematical and computational review of Hartree–Fock SCF methods in quantum chemistry. *Molecular Physics* **105**, 3057–3098 (Dec. 2007).
273. Cyrot, M. Ginzburg-Landau theory for superconductors. *Reports on Progress in Physics* **36**, 103–158 (Feb. 1973).
274. McIntosh, J. R. & Landis, S. C. The distribution of spindle microtubules during mitosis in cultured human cells. *The Journal of cell biology* **49**, 468–497. ISSN: 0021-9525 (2 May 1971).
275. Tolić, I. M. & Pavin, N. Mitotic spindle: lessons from theoretical modeling. *Molecular Biology of the Cell* **32** (ed Kozminski, K.) 218–222 (Feb. 2021).
276. Matković, J. *et al.* Kinetochore-and chromosome-driven transition of microtubules into bundles promotes spindle assembly. *bioRxiv* (2022).
277. Kiewisz, R. *et al.* Three-dimensional structure of kinetochore-fibers in human mitotic spindles. *eLife* **11** (July 2022).

278. Shcherbakov, M. V. *et al.* A survey of forecast error measures. *World applied sciences journal* **24**, 171–176 (2013).
279. Abràmoff, M. D., Magalhães, P. J. & Ram, S. J. Image processing with ImageJ. *Bio-photonics international* **11**, 36–42 (2004).
280. Collins, T. J. ImageJ for microscopy. *Biotechniques* **43**, S25–S30 (2007).
281. Lowe, D. G. Distinctive image features from scale-invariant keypoints. *International journal of computer vision* **60**, 91–110 (2004).
282. Jin, F. & Feng, D. Image registration algorithm using Mexican hat function-based operator and grouped feature matching strategy. *PloS one* **9**, e95576 (2014).
283. Farneäck, G. *Two-frame motion estimation based on polynomial expansion in Scandinavian conference on Image analysis* (2003), 363–370.
284. Nizette, M. & Goriely, A. Towards a classification of Euler–Kirchhoff filaments. *Journal of Mathematical Physics* **40**, 2830–2866 (June 1999).